Philosophy Dissertations   **Philosophy**

11-2017

Design of Telescopic Beams Based On Parametric Studies Using FEA and Statistical Optimization

Neha Arieckal Jacob

جامعة الإمارات العربية المتحدة
United Arab Emirates University

UAEU

United Arab Emirates University

College of Engineering

DESIGN OF TELESCOPIC BEAMS BASED ON PARAMETRIC STUDIES USING FEA AND STATISTICAL OPTIMIZATION

Neha Arieckal Jacob

This dissertation is submitted in partial fulfilment of the requirements for the degree of Doctor of Philosophy

Under the Supervision of Dr. Sangarappillai Sivaloganathan

November 2017

Declaration of Original Work

I, Neha Arieckal Jacob, the undersigned, a graduate student at the United Arab Emirates University (UAEU), and the author of this dissertation entitled *"Design of Telescopic Beams Based on Parametric Studies using FEA and Statistical Optimization"*, hereby, solemnly declare that this dissertation is my own original research work that has been done and prepared by me under the supervision of Dr. Sangarappillai Sivaloganathan, in the College of Engineering at UAEU. This work has not previously been presented or published, or formed the basis for the award of any academic degree, diploma or a similar title at this or any other university. Any materials borrowed from other sources (whether published or unpublished) and relied upon or included in my dissertation have been properly cited and acknowledged in accordance with appropriate academic conventions. I further declare that there is no potential conflict of interest with respect to the research, data collection, authorship, presentation and/or publication of this dissertation.

Student's Signature: _____   Date: __18-12-2017__
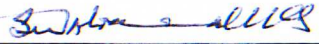
Approval of the Doctorate Dissertation

This Doctorate Dissertation is approved by the following Examining Committee Members:

1) Advisor (Committee Chair): Dr. Sangarappillai Sivaloganathan

   Title: Associate Professor

   Department of Mechanical Engineering

   College of Engineering

   Signature _____   Date 14 | 11 | 2017

2) Member: Dr. Tariq Darabseh

   Title: Associate Professor

   Department of Mechanical Engineering

   College of Engineering

   Signature _____   Date 14 / 11 / 2017

3) Member: Dr. Bilal El-Ariss

   Title: Associate Professor

   Department of Civil and Environmental Engineering

   College of Engineering

   Signature _____   Date Nov. 14, 2017

4) Member (External Examiner): Prof. Shaker A. Meguid

   Title: Professor

   Department of Mechanical Engineering

   Institution: University of Toronto

   Signature _____   Date 14 | 11 | 2017

This Doctorate Dissertation is accepted by:

Dean of the College of Engineering: Professor Sabah Alkass

Signature _Scebett_   Date _27/12/2017_

for Dean of the College of Graduate Studies: Professor Nagi T. Wakim

Signature _Ali Hassan_   Date _27/12/2017_

Copy _8_ of _9_

Advisory Committee

1) Advisor: Dr. Sangarappillai Sivaloganathan

Title: Associate Professor

Department of Mechanical Engineering

College of Engineering

2) Co-advisor: Dr. Kilani Ghoudi

Title: Professor

Department of Statistics

College of Business and Economics

3) Member: Dr. Mousa Hussein

Title: Associate Professor

Department of Electrical Engineering

College of Engineering

Abstract

This dissertation describes an investigation on the behavior of the overlap area in telescopic cantilevers under tip loads.

The main aim of this research is to address the question of 'how the overlap region of a telescopic beam behaves under a tip load' and to develop a new generic approach to the design of telescopic beams based on parametric studies using FEA and statistical optimization.

Experimental investigations and exploratory analyses were carried out to study the behavior of RHS (Rectangular Hollow Section) rings and RHS pieces. Based on these observations, theoretical explanations were developed and a methodology for the design of the inner beam assembly based on FEA and design of experiments was recommended. The recommended methodology was also implemented on a case study.

Results showed that the overlap area can be treated as an assembly of RHS rings and a middle section or an assembly of RHS pieces and a middle section. Further, the region near the bottom wearpads of the overlap area of the inner beam is identified as most vulnerable.

RHS rings are treated as an assemblage of horizontal beams and vertical columns whereas RHS pieces are treated as an assemblage of vertical and horizontal plates. When compressed transversely between platens, the constituent beams, columns, and plates in both RHS rings and pieces, are subjected to corner moments. Further, when compressed between wearpads, an additional corner moment is introduced which in effect reduces the maximum load carrying capacity further. Because of the nature of the assembly, the end conditions of the constituent members of the RHS ring and pieces are unknown and hence complete theoretical solutions are

not derived. Therefore, FEA and experimental designs were used to establish a design methodology for telescopic beams.

Significant contributions from this study involve the explanation of the behavior of RHS rings and RHS pieces when compressed transversely and the development of a new generic approach to the design of telescopic beams based on parametric studies using FEA and statistical optimization.

Keywords: Telescopic cantilevers, Overlap area, FEA, Design of Experiments, RHS rings, RHS pieces, Inner beam assembly, Design Methodology.

Title and Abstract (in Arabic)

تصميم دعامات منظارية تستند إلى دراسات قياسية باستخدام طريقة تحليل العناصر المنتهية و التحسين الإحصائي

الملخص

في هذه الأطروحة تم دراسة سلوك منطقة التداخل في الدعامات المنظارية نتيجة ثقل طرفي.

الهدف الرئيسي من هذا البحث هو معالجة مسألة كيف تتصرف منطقة تداخل الدعامات المنظارية تحت حمولة طرفية، وتطوير نهج عام جديد لتصميم الدعامات المنظارية استنادا إلى الدراسات القياسية، باستخدام طريقة تحليل العناصر المنتهية والطرق الإحصائية.

أجريت الالفحوصات التجريبية والتحليلات الاستكشافية لدراسة سلوك الحلقات المستطيلة الشكل المجوفة، و القطع مستطيلة الشكل المجوفة. واستنادا إلى هذه الملاحظات، وضعت تفسيرات نظرية، وتم توصية منهجية لتصميم تجميع الدعامة الداخلية على أساس طريقة تحليل العناصر المنتهية، وتصميم التجارب. ونفذت المنهجية الموصى بها أيضا في دراسة حالة.

وأظهرت النتائج أن منطقة التداخل يمكن أن تعامل على أنها تجميع من حلقات مستطيلة الشكل مجوفة وقسم أوسط، أو مجموعة من القطع مستطيلة الشكل المجوفة وقسم أوسط. وعلاوة على ذلك، يتم تحديد المنطقة بالقرب من التبطين السفلي، في منطقة التداخل، من الدعامة الداخلية على أنها الأكثر ضعفا.

يتم التعامل مع الحلقات مستطيلة الشكل المجوفة كتجميع من الدعامات الأفقية والأعمدة الرأسية، في حين يتم التعامل مع القطع مستطيلة الشكل المجوفة كتجميع من الألواح الرأسية والأفقية. عندما يتم ضغطها بشكل عرضي بين الاسطوانات، فإن الدعامات المكونة، والأعمدة، والألواح في كل من الحلقات و القطع مستطيلة الشكل المجوفة، تتعرض لقوة عزم عند الزاوية . وعلاوة على ذلك، عندما يتم ضغطها بين الاسطوانات، يتم إدخال قوة عزم الزاوية الإضافية، الذي في الواقع يقل من سعة الحمولة القصوى. أكثر من ذلك، ونظرا لطبيعة التجميع، فإن الشروط النهائية لتكوين الحلقات و القطع مستطيلة الشكل المجوفة غير معروفة. وبالتالي لم يتم اشتقاق حلول نظرية كاملة. ولذلك، استخدمت طريقة تحليل العناصر المنتهية والتصاميم التجريبية لوضع منهجية تصميم للدعامات المنظارية.

وتشمل المساهمات الهامة من هذه الدراسة شرح سلوك الحلقات و القطع مستطيلة الشكل المجوفة عند ضغطها بشكل عرضي وتطوير نهج عام جديد لتصميم الدعامات المنظارية، استنادا إلى الدراسات القياسية باستخدام طريقة تحليل العناصر المنتهية والطرق الإحصائية.

مفاهيم البحث الرئيسية: دعامات منظارية، منطقة متداخلة، تحليل العناصر المنتهية، تصميم التجارب، حلقات مستطيلة الشكل مجوفة، قطع مستطيلة الشكل مجوفة، التجميع الداخلي للدعامة، منهجية التصميم.

Acknowledgements

Dedication

To my wonderful, beloved parents

Table of Contents

List of Tables

List of Figures

List of Abbreviations

A	Cross-sectional Area
BMD	Bending Moment Diagram
CCD	Central Composite Design
CRCA	Cold Rolled Cold Annealed
DOE	Design of Experiments
FBD	Free-Body Diagram
FEA	Finite Element Analysis
FEM	Finite Element Method
IB	Inner Beam
MRO	Maintenance, Repair and Operations
MS	Mild Steel
MTS	Material Testing System
RHS	Rectangular Hollow Section
RSD	Response Surface Design
SFD	Shear Force Diagram
SHS	Square Hollow Sections
WP	Wearpad
E	Modulus of Elasticity
I	Second Moment of Area
q	Distributed load
Q	First Moment of Area
V	Shear Force
c	Distance from the neutral axis

b	Width of beam cross-section
R_A, R_B, R_C	Reaction forces at A, B and C respectively
$\dfrac{dv}{dx}$	Slope of beam
$u(x, y, z)$	Displacement in x- direction
$v(x, y, z)$	Displacement in y- direction
$w(x, y, z)$	Displacement in z- direction
e_{xx}, e_{yy}, e_{zz}	Direct strains in x, y and z-directions respectively
e_{xy}	Shear strain on x plane acting in y-direction
e_{xz}	Shear strain on x plane acting in z-direction
e_{yz}	Shear strain on y plane acting in z-direction
e_{ij}	Shear stress on i plane acting in j-direction
$\sigma_{xx}, \sigma_{yy}, \sigma_{zz}$	Direct stresses in x, y and z-directions respectively
σ_{xy}	Shear stress on x plane acting in y-direction
σ_{xz}	Shear stress on x plane acting in z-direction
σ_{yz}	Shear stress on y plane acting in z-direction
σ_{ij}	Shear stress on i plane acting in j-direction
$\sigma_1, \sigma_2, \sigma_3$	Principal stresses in x,y and z-directions
σ_f, σ_y	Yield stress
σ_b	Bending stress
σ_{pr}	Proportional stress

σ_{ult}	Ultimate stress
υ	Poisson's ratio
k	Constant where $k^2 = \dfrac{P}{EI}$
k_1	Boundary condition dependent constant for columns
k_2	Boundary condition dependent constant for plates
λ	Slenderness ratio
λ_{cr}	Critical slenderness ratio
P	Applied Vertical load
P_{cr}	Critical buckling load
L, l	Length of column
a/h	Plate length to thickness ratio
w/h	Plate deflection to thickness ratio
e	Load Eccentricity distance
y	Lateral deflection of column
x	Distance along the column length 'l'
l_1	Flange length
δ_1	Deflection at mid-length of flange
b	Plate height
t, h	Plate thickness
N_x, N_y	Plate in plane normal forces
N_{xy}, N_{yx}	Plate in plane shear forces
Q_x, Q_y	Plate transverse shearing forces

M_x, M_y	Bending moments
M_{xy}, M_{yx}	Twisting Moments
$\bar{\tau}_{xy}, \bar{\tau}_{yx}, \bar{\sigma}_x, \bar{\sigma}_y$	Stress components at any point through plate thickness
$\tau_{xy}, \tau_{yx}, \sigma_x, \sigma_y$	Stress components at plate mid-surface
k_{xx}, k_{yy}, k_{xy}	Plate curvature at mid-surface
D	Flexural rigidity of plate
$(N_x)_{cr}$	Critical buckling load (per unit length) for plate
$(\sigma_x)_{cr}$	Critical buckling stress for plate
a_0, a_n, b_n	Fourier series constants
$\{f\}$	Vector of elemental nodal forces
$[k]$	Element Stiffness Matrix
$\{d\}$	Vector of unknown elemental degrees of freedom
$\{F\}$	Vector of global nodal forces
$[K]$	Global Stiffness Matrix
K_0^{NM}	is the stiffness matrix corresponding to the base state, which includes the effects of the preloads (if any)
K_Δ^{NM}	is the differential initial stress and load stiffness matrix due to the incremental loading pattern
λ_i	are the eigenvalues
υ_i^M	are the buckling mode shapes (eigenvectors)
M and N	refer to degrees of freedom M and N of the whole model

i	refers to the ith buckling mode
Q^N	Incremental loading pattern
P_{total}	Dead load value
P_{ref}	Reference load vector
λ_p	Load proportionality factor
Δl_{in}	Initial increment in Arc length
l_{period}	Total arc length scale factor
$\Delta l_{min}, \Delta l_{max}$	Minimum and maximum arc lengths
η	Response
$(x_1, x_2 ......x_n)$	Active or influencing factors
$\beta_0, \beta_j, \beta_{ij}$	Response surface constants
n	Number of variables in a quadratic polynomial
α	Axial points in central composite design
M_0	Corner Moment
M_x	Moment at x-distance away from column end

Chapter 1: Introduction

1.1 Overview

Telescopic Cantilevers are used in machinery including cranes, access platforms, truck mounted cranes and loaders. They find multiple applications in the MRO (Maintenance, Repair and Operations) industry where they are used to access structures like aircrafts, in material handling equipment at harbors and infrastructure building sites, and complex machinery including automated welding plants, aircrafts and off-shore pipe-laying vessels. Published material to assist designing these thin and complex structures is limited. Modern scientific trends in design and manufacturing of complex components takes an integrated approach based on integrated parametric multi-computational assessment that leads to simplified formulae, which can be utilized by field engineers to optimize their designs. Engineering software developers like Simulia have started linking FEA of specific engineering problems with 'Statistical Analyses' resulting in design formulas that can be utilized by practicing engineers.

This research addresses the question of 'how the overlap region in a telescopic beam behaves under a tip load' and establishes a new generic approach to the design of telescopic beams based on parametric studies using FEA and statistical optimization.

1.2 Background

This section briefly outlines the necessary background to understand the problem and the approach taken towards finding a solution. It describes the structure, the design parameters and the motivation for this study.

1.2.1 Telescopic Cantilever

A telescopic cantilever is a structural assembly consisting of two or more beam sections with the outermost beam section fixed at one end, supporting the entire beam assembly while one or more inner sections of beam are stacked inside. The inner beams move outwards when a full or partial extension is needed. The main parts of a single stage telescopic beam assembly are given in Figure 1.
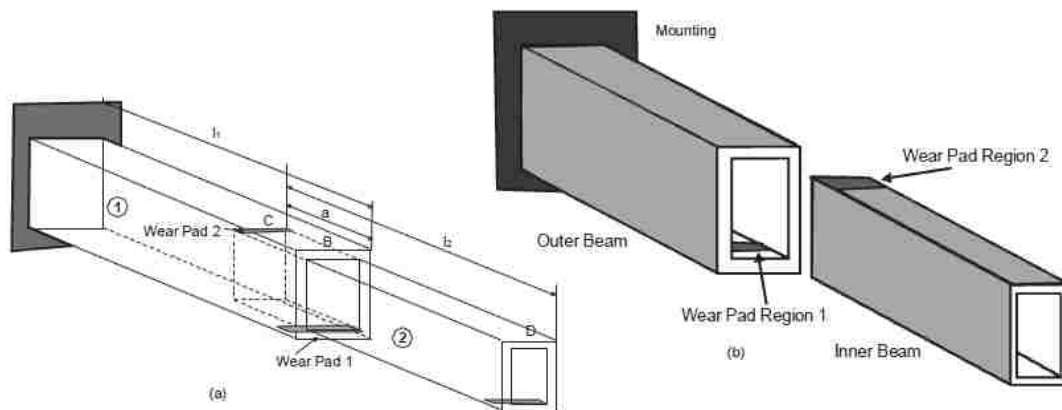
Figure 1: Single stage telescopic cantilever

The inner beams are pushed out and pulled in as and when required. In order to reduce the contact area between the inner side of the outer beam and the outer side of the inner beam, contact between the inner and outer beams are provided through wearpads. The inner beam slides on the wearpads. At any given position, part of the inner beam will be inside the outer beam. This portion is called the overlap. Manufacturers see the overlap as wasted material and often try to reduce this overlap to save material, reduce weight and make manufacturing easy. But reducing the overlap increases the tip reactions at the wearpad areas and the inner beam is under high compression in this region. This may lead to buckling in the overlap area.

In applications such as in the telescopic boom of a crane, an important requirement is the minimum deflection at the innermost beam tip. Large tip-deflection makes the user in the cage at the tip feel uncomfortable. In order to minimize the tip deflection which requires high rigidity or second moment of area, designers tend to increase the height of the beam. But this makes the beam vulnerable to buckling in the overlap area. Structural members fail resisting tension, shear or torsion, when the stress in the member reaches a certain limiting strength of the material. Buckling on the other hand does not take place as a result of the resisting stress reaching a limiting strength of the material. In general, the stress at which buckling occurs depends on a variety of factors such as the dimensions of the member, boundary conditions and the properties of the material of the member. In other words, buckling behavior is project-dependent.

1.2.2 Parameters Involved

The overlap area of the inner beam is minimal in the fully extended position. It is the most vulnerable area of a telescopic beam assembly and therefore is the focus of this study. Consider a two-section telescopic cantilever beam assembly. For simplicity, neglect the self-weight of the structure. Assume that the interactions between the inner beam and outer beam are through the wearpads that are located at the corresponding tips of the beams. These interactions give rise to tip-reactions at these tips. With this tip-reaction model, free body diagrams can be considered to analyze the equilibrium of the inner beam. Figure 2 illustrates the beam and the free body diagrams under the tip reaction model.
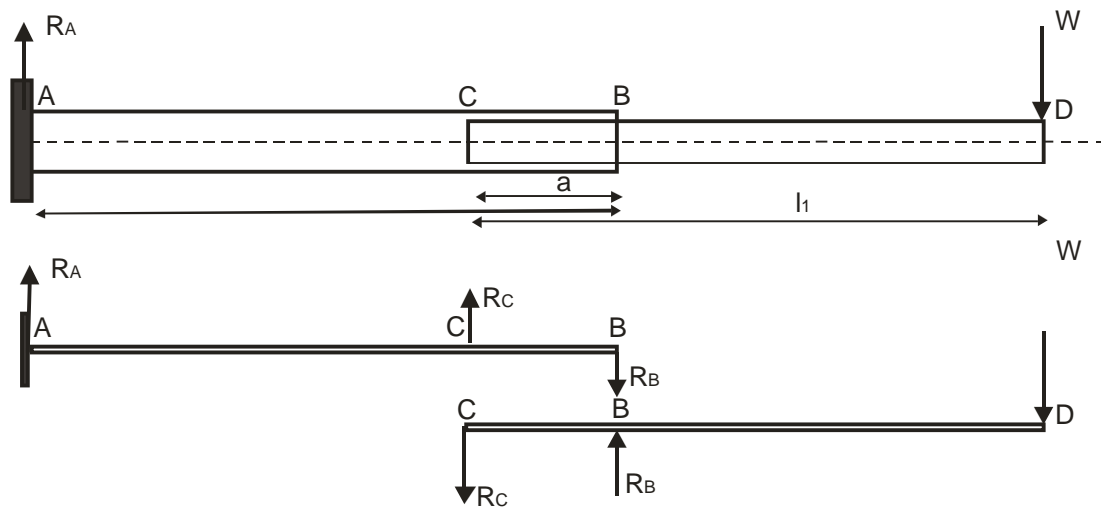
Figure 2: Free-body diagram of the telescopic cantilever beam sections

Consider the inner beam CBD as shown in Figure 2.

Considering the equilibrium of the system, it can be said that $R_A = W$

Taking moments about C for the beam CD gives $R_B = \dfrac{l_1}{a}W$

Similarly taking moments about B gives $R_C = \dfrac{(l_1 - a)}{a}W$

Normally $l_1 >> a$ and thus the overlap area is subjected to large multiples of the tip load W. Since these large forces are compressive in nature they can cause buckling. A combination of geometric factors of the inner beam, the wearpads, and the overall assembly geometric factors affects the behavior of the beam in this overlap area. The inner beam and the wearpads are considered as an assembly as shown in Figure 3.
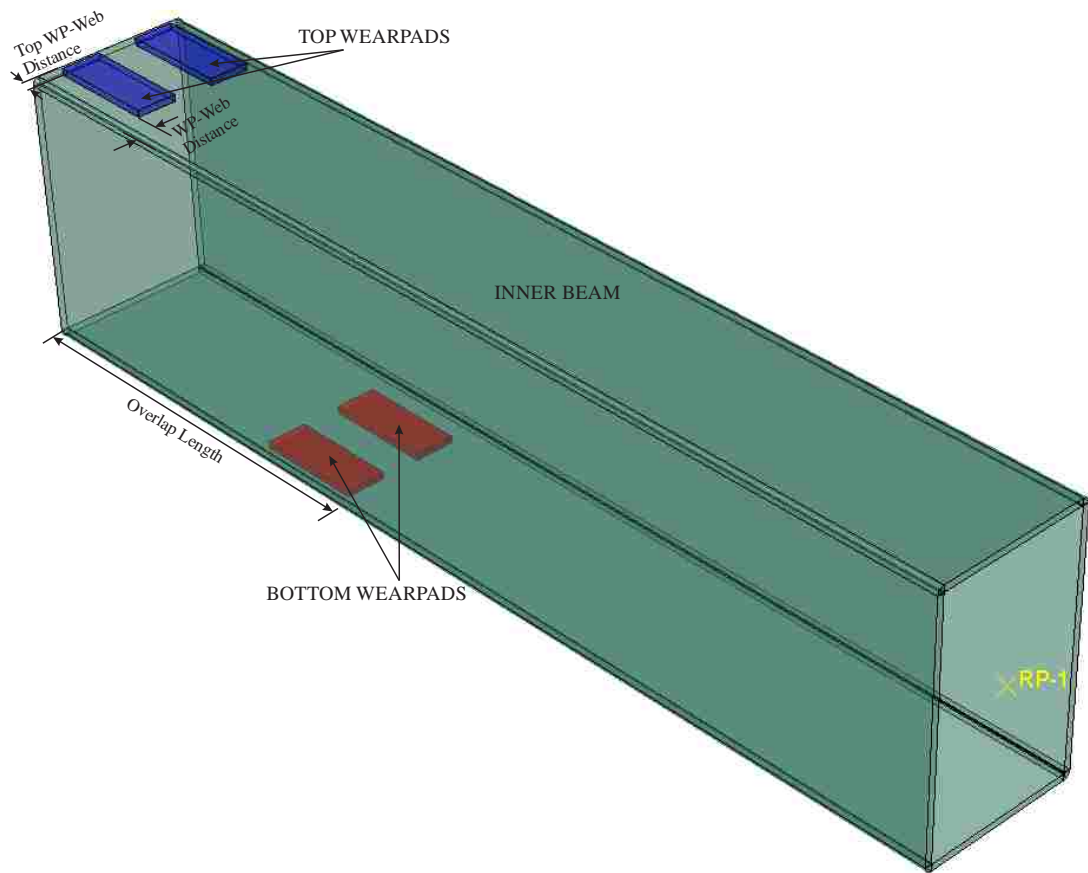
Figure 3: Inner beam assembly of a telescopic cantilever

The geometric factors are listed in Table 1. Some of the geometric factors listed in Table 1 is shown in Figure 3.

Table 1: Geometric factors of the inner beam assembly

Geometry of Inner Beam	Geometry of Wearpads	Geometry of assembly
Thickness	WP Length	WP-Web Distance
Height (web)	WP Width	Overlap Length
Width (flange)	WP Height	Top WP-End Distance
Length		
Corner radius		

1.2.3 The Motivation

This research was initially undertaken as an extension to my design project at Brunel University, UK which involved the validation of a telescopic crane boom FE model for one of the leading manufacturers of access platforms and boom lifts in Europe.

To understand the criticality of the overlap area design, consider the analysis of a telescopic beam shown in Figure 4 and consider the stresses at two points P_1 and P_2 in the outside of the inner beam located 25 mm from the ends of the inner and outer beams. This means that when the overlap 'a' changes, the point P_1 will also change its location on the inner beam. An FE analysis carried out in ABAQUS for five different overlaps; 1200 mm, 1100 mm, 1000 mm, 900 mm and 800 mm is executed and the stresses (Mises) at points P_1 and P_2 observed. Figure 5 shows them in the form of two graphs.
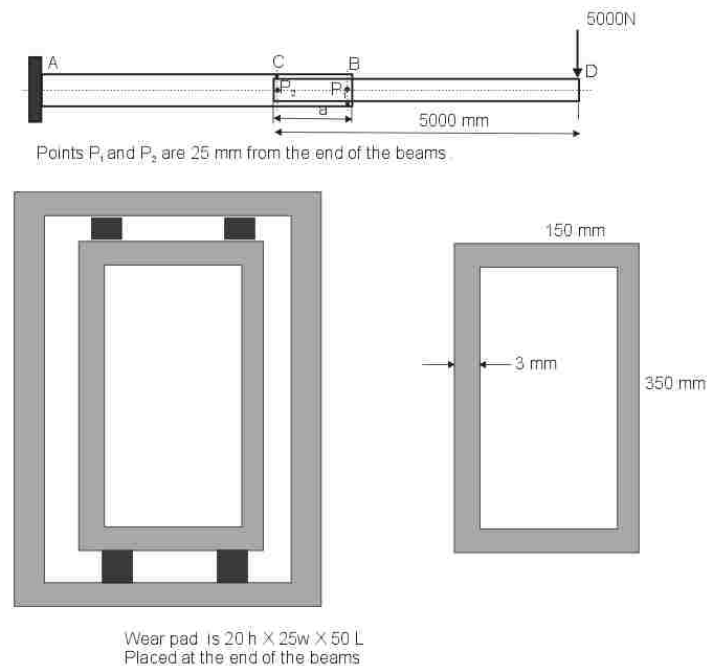
Figure 4: A telescopic beam

Stress Plot at 5000 N
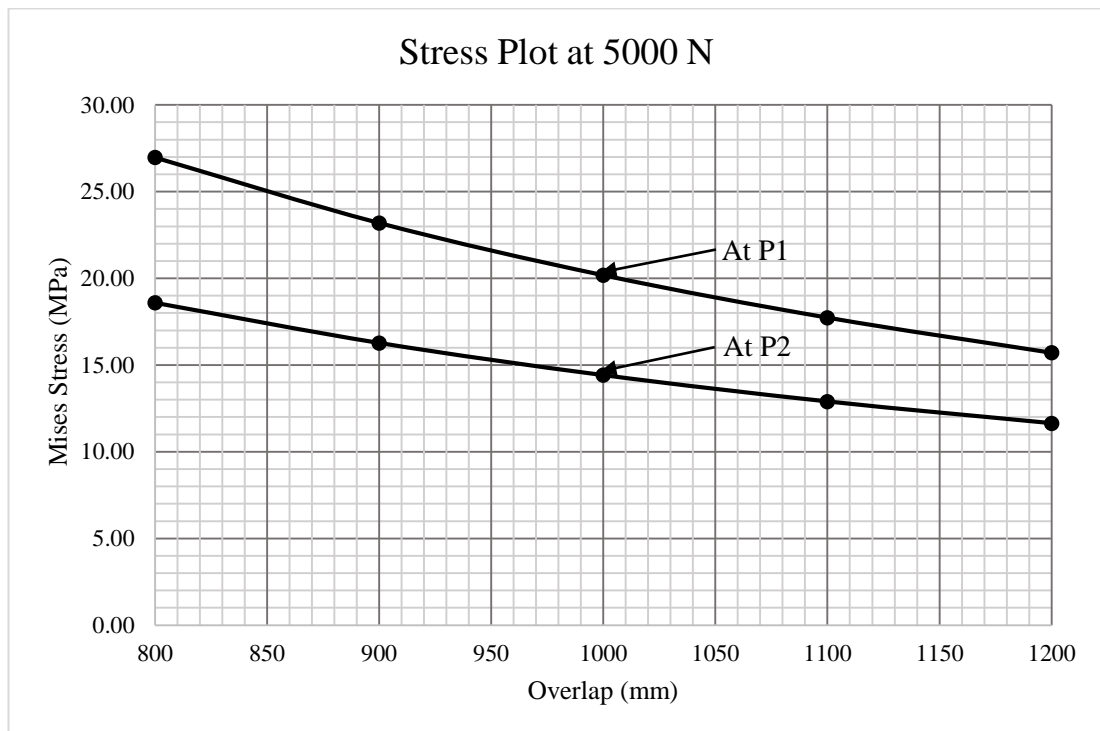
Figure 5: Stress variation under the wearpads with varying overlap

The graph in Figure 5 shows that the stress varies substantially, from 15.72 MPa to 26.97 MPa at P_1 with the reduction of 400 mm in overlap while the load at the tip remains the same. Also, it shows that the magnitude of stress at P_1 is always greater than that at P_2. This highlights the fact that, chances of buckling are high in the vicinity of P_1.

Figure 6 shows the stress distribution in the entire assembly for an 800 mm overlap. In general, the stresses are high near the overlap and were very minimal in all other areas of the assembly. This observation together with the amplification of the tip loads as explained in section 1.2.2 raised the curiosity to investigate the overlap area in detail in connection with the telescopic beam design.
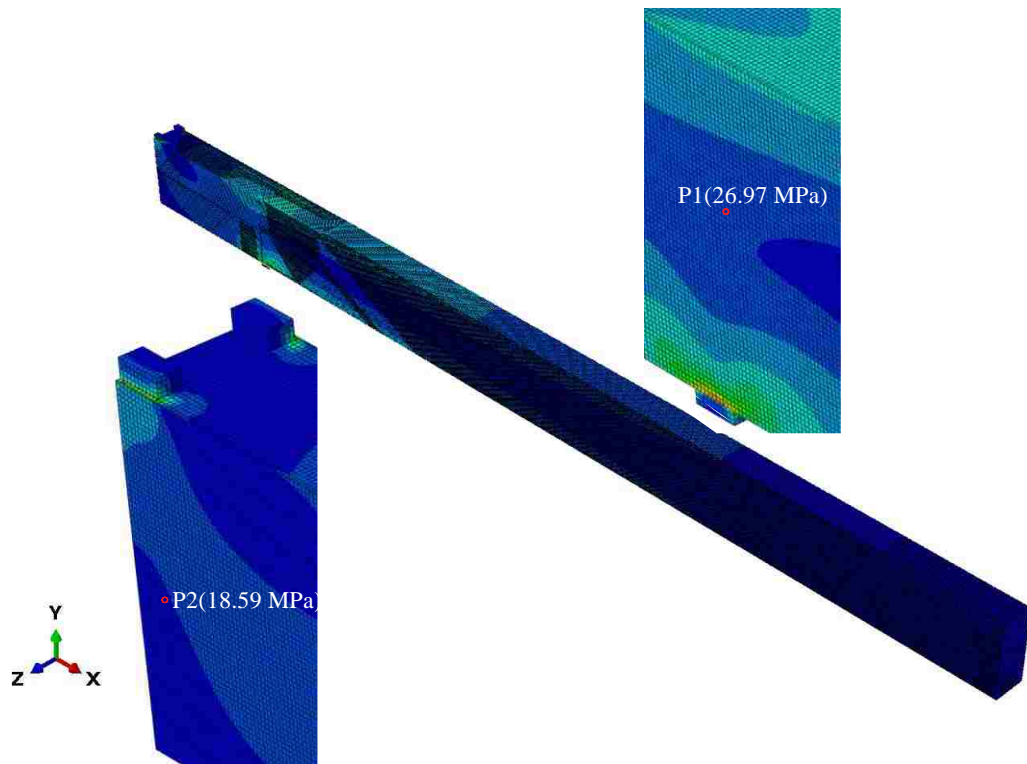
Figure 6: Stress distribution in the entire telescope assembly

The research question therefore addresses the question of 'how the overlap region of the inner beam assembly in a telescopic beam behaves under a tip load' and establishes a new generic approach to the design of telescopic beams based on parametric studies using FEA and statistical optimization.

1.3 Situation Analysis

In order to start the investigation, the following topics were visited and reviewed:

- Beam theory

- Stresses and strains at a point

- Failure theories

- Buckling of columns

- Finite Element Analysis Using ABAQUS software

1.3.1 Beam Theory

Beam theory can be summarized under the eight headings namely assumptions, implications of the assumptions on beam behavior, shear force and bending moment diagrams, deflection curve, flexure equation, bending stress, shear stress and governing set of differential equations.

Table 2 borrows from [1] and [2] and summarizes the beam theory.

Table 2: Beam theory highlights

Beam Definition	A structural member designed to support transverse loads, having one of its dimensions (the axis) much larger than the other two [3].
Assumption 1	The beam has a longitudinal plane of symmetry (x-z), with the cross section symmetric about this plane. Load is applied in the plane x-z and is transverse to the long axis (the x-axis) [1].
Implication of Assumption 1	All loads in y – direction are zero. Therefore, all stresses in y-direction are zero: $\sigma_{yy} = \sigma_{xy} = \sigma_{yz} = 0$ The only significant stresses are in the x- direction: σ_{xx}, σ_{xz}
Assumption 2	During deformation, plane sections remain plane and perpendicular to the midplane after deformation.
Implication of Assumption 2	The implication of this assumption on displacements are: $u(x, y, z) = -z \dfrac{dw}{dx}$ $v(x, y, z) = 0$ $w(x, y, z) = w(x)$
Flexure Equation/ Bending Stress	Stresses calculated from the flexure formula are called bending stresses or flexural stresses. $\sigma_{xx} = -\dfrac{Mc}{I}$
Shear Stress	$\tau = \dfrac{VQ}{Ib}$ For a specific cross section, the shear force V, moment of inertia I, and width b are constants. However, the first moment Q varies with the distance c from the neutral axis
SFD and BMD	Information relating to beam shear forces and bending moments is provided by graphs in which the shear force and bending moment are plotted as ordinates and the distance x along the axis of the beam is plotted as the abscissa. These graphs are called shear force diagrams and bending moment diagrams.

Table 2: Beam Theory highlights (Continued)

Deflection Curve	When a beam with a straight longitudinal axis is loaded by lateral forces, the axis is deformed into a curve, called the deflection curve of the beam. The basic differential equation of the deflection curve of a beam is: $\dfrac{d^2w}{dx^2} = \dfrac{M}{EI}$ (where $\dfrac{dw}{dx}$ is the slope)
Governing set of Differential equations	$z\dfrac{dw}{dx} = -u \qquad EI\dfrac{d^2w}{dx^2} = M$ $\dfrac{dM}{dx} = -V \qquad EI\dfrac{d^3w}{dx^3} = -V \qquad EI\dfrac{d^4w}{dx^4} = q(x)$

1.3.2 Stress and Strain at a Point

In general, a body can be subjected to point and surface forces, body forces, contact forces and constraints. Chadrupatla and Belgundu [4] represent this in a figure which is adapted and reproduced here as Figure 7.
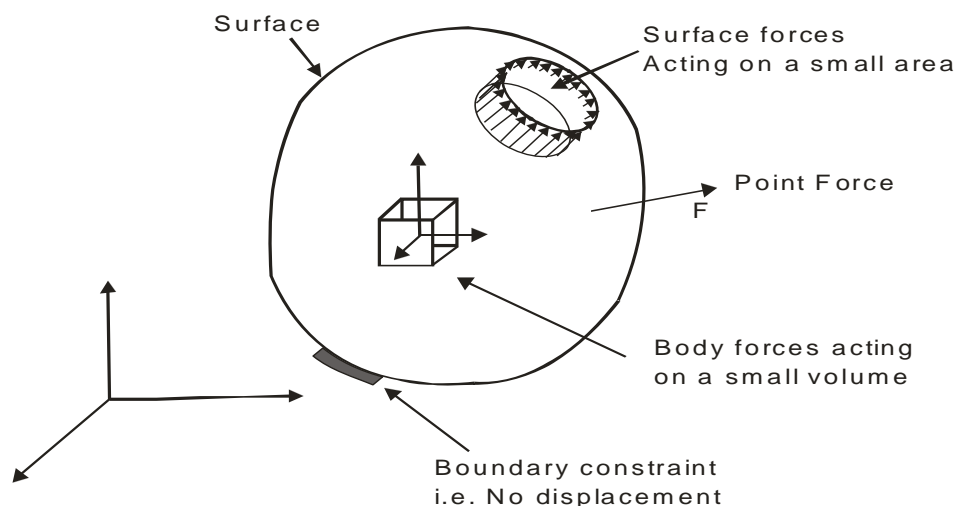
Figure 7: Forces and constraints in a body

As a result of these forces, three dimensional stresses and strains are produced in the body. There are fifteen such variables which are represented by the stress tensor (six variables), strain tensor (six variables) and displacements (three variables) [5].

The components of the displacement vector in x, y, and z directions are denoted respectively by (u, v, w).

Stress Tensor: Stresses acting on a plane, are typically decomposed into three mutually orthogonal components – one normal and two shear [6]. As shown in Figure 8(a), the stress at a point needs nine components to be completely specified. Each component is defined by the direction in which it acts and the orientation of the surface upon which it is acting. Therefore, the ith component of the force acting on a surface whose outward normal points in the jth direction is σ_{ij} [6].
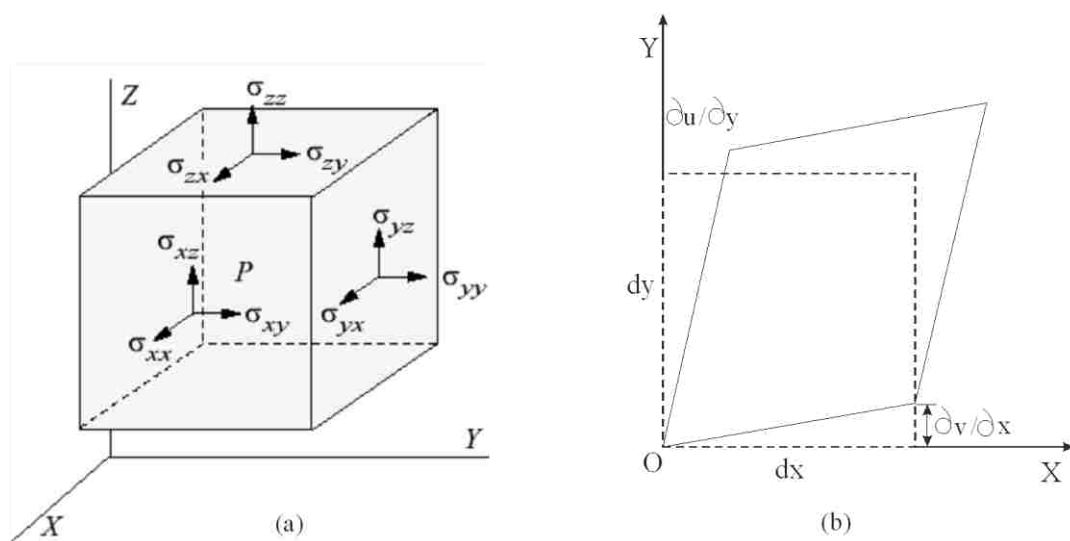
Figure 8: (a) Stresses on an infinitesimal cube whose surface are parallel to the coordinate system (b) Shear strain [7]

These nine components can be organized into the matrix:

$$\sigma_{ij} = \begin{bmatrix} \sigma_{xx} & \sigma_{xy} & \sigma_{xz} \\ \sigma_{yx} & \sigma_{yy} & \sigma_{yz} \\ \sigma_{zx} & \sigma_{zy} & \sigma_{zz} \end{bmatrix} \tag{1.1}$$

where shear stresses on either side of the diagonal are identical (i.e. $\sigma_{xy} = \sigma_{yx}$, $\sigma_{yz} = \sigma_{zy}$, and $\sigma_{zx} = \sigma_{xz}$) as a result of static equilibrium (no net moment), thereby effectively reducing the stress tensor to six components. This grouping of the stress components is known as the stress tensor (or stress matrix) [8].

Strain Tensor: As in the case of stress tensors, there are a total of nine strain measures. The non-diagonal components are the shear strains that are defined as the change in an angle that was originally at a right angle before deformation occurred. The shear strain e_{xy} is the average of the shear strain on the x face along the y direction, and on the y face along the x direction [9]. The shear strain for the element in the x-y plane is as shown in Figure 8(b). All nine measures can be organized into a matrix (similar in form to the stress matrix), shown here:

$$e_{ij} = \begin{bmatrix} e_{xx} & e_{xy} & e_{xz} \\ e_{yx} & e_{yy} & e_{yz} \\ e_{zx} & e_{zy} & e_{zz} \end{bmatrix} = \begin{bmatrix} \dfrac{\partial u}{\partial x} & \dfrac{1}{2}\left(\dfrac{\partial u}{\partial y} + \dfrac{\partial v}{\partial x}\right) & \dfrac{1}{2}\left(\dfrac{\partial u}{\partial z} + \dfrac{\partial w}{\partial x}\right) \\ \dfrac{1}{2}\left(\dfrac{\partial u}{\partial y} + \dfrac{\partial v}{\partial x}\right) & \dfrac{\partial v}{\partial y} & \dfrac{1}{2}\left(\dfrac{\partial v}{\partial z} + \dfrac{\partial w}{\partial y}\right) \\ \dfrac{1}{2}\left(\dfrac{\partial u}{\partial z} + \dfrac{\partial w}{\partial x}\right) & \dfrac{1}{2}\left(\dfrac{\partial v}{\partial z} + \dfrac{\partial w}{\partial y}\right) & \dfrac{\partial w}{\partial z} \end{bmatrix} \tag{1.2}$$

1.3.3 Failure Theories

Behavior of materials like steel when subjected to tensile load in only one direction can be determined experimentally, and conforming failure theories can be, and are formulated. However, when the material is loaded in three dimensions the behavior cannot be experimentally determined. Failure theories have been developed

to fill this gap and there are several of them. Table 3 gives a summary of the failure theories.

Table 3: Failure theories [10]

Sr. No.	Theory Name	Statement	Limiting Condition
1	Maximum principal stress theory (Rankine theory)	Yield occurs when one of the principal stresses at a point in the structure subjected to the combined stresses reaches the yield strength in simple tension or compression of the material.	$\sigma_1 = \sigma_f$ $\sigma_2 = \sigma_f$
2	Maximum principal strain theory (St. Venant's theory)	Failure is predicted to occur in the multi-axial state of stress when the maximum principal normal strain become equal to or exceeds the maximum normal strain at the time of failure in a simple uniaxial stress test using a specimen of the same material.	$\sigma_1 - \upsilon\sigma_2 \geq \pm\sigma_f$ $\sigma_2 - \upsilon\sigma_1 \geq \pm\sigma_f$
3	Maximum shear stress theory (Tresca theory)	Failure is predicted to occur in the multiaxial state of stress when the maximum shearing stress magnitude becomes equal to or exceeds the maximum shearing stress magnitude at the time of failure in a simple uniaxial stress test using a specimen of the same material.	$\sigma_1 - \sigma_2 \geq \pm\sigma_f$ $\sigma_2 - \sigma_3 \geq \pm\sigma_f$ $\sigma_3 - \sigma_1 \geq \pm\sigma_f$
4	Maximum strain energy theory (Beltrami's theory)	Failure would occur when the total strain energy absorbed at a point per unit volume exceeds the strain energy absorbed per unit volume at the tensile yield point.	$\left(\dfrac{\sigma_1}{\sigma_f}\right)^2 + \left(\dfrac{\sigma_2}{\sigma_f}\right)^2$ $- 2\upsilon\left(\dfrac{\sigma_1\sigma_2}{\sigma_f^2}\right) = 1$
5	Distortion energy theory (Von Mises yield criterion)	Failure is predicted to occur in the multi-axial state of stress when the distortion energy per unit volume becomes equal to or exceeds the distortion energy per unit volume at the time of failure in a simple uniaxial stress test using a specimen of the same material	$(\sigma_1 - \sigma_2)^2$ $+ (\sigma_2 - \sigma_3)^2$ $+ (\sigma_3 - \sigma_1)^2 \geq 2\sigma_f^2$

The five failure theories are compared graphically in Figure 9. When the third principal stress σ_3 is zero, each yield criterion describes a closed boundary condition in principal stress axes σ_1 and σ_2 [11].
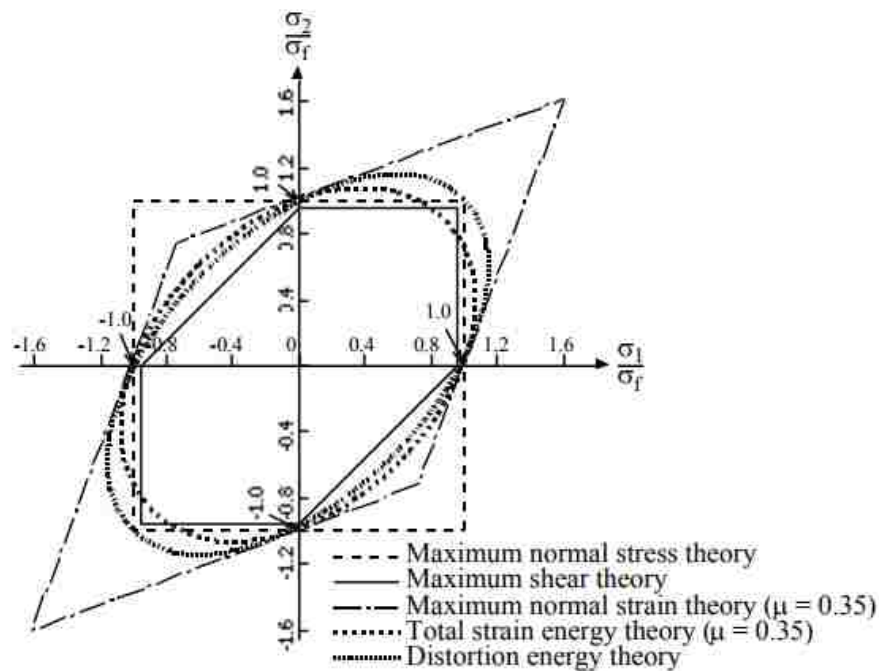
Figure 9: Comparison of different failure theories [10], [12]

Each of the boundaries predicted by the theory is called a yield locus. Elastic conditions prevail within the interior region. Plastic behavior occurs to the external of each locus [11]. The Tresca locus is mostly conservative and therefore safe. The Von Mises ellipse is the most representative for ductile materials, and the Rankine the best fit for brittle materials [13].

1.3.4 Buckling of Columns

Buckling is a physical phenomenon of a straight and slender member abruptly bending laterally from its longitudinal position due to compressive loading [14]. Buckling study called Stability Analysis is explained using the stable, unstable and marginally stable conditions of a ball. It demonstrates that there can be several equilibrium positions in the marginally stable condition since there is no energy change. This means there can be several equilibrium paths [15]. A column when

subjected to a compressive load, shrinks due to the load. The load deflection curve describes an equilibrium path for this behavior. As the load is increased there comes a point where the column can also bend and maintain its equilibrium. This bending behavior is described by another equilibrium path. At the point where the loads corresponding to each equilibrium path are the same, the column can switch from one equilibrium path to the other. The load deflection behavior can be estimated using any one of these behaviors. This method is called the method of adjacency equilibrium and the analysis of a column using the bent position makes use of this equality.

Using the method of adjacency equilibrium, a column can be analysed in the following way [16]:
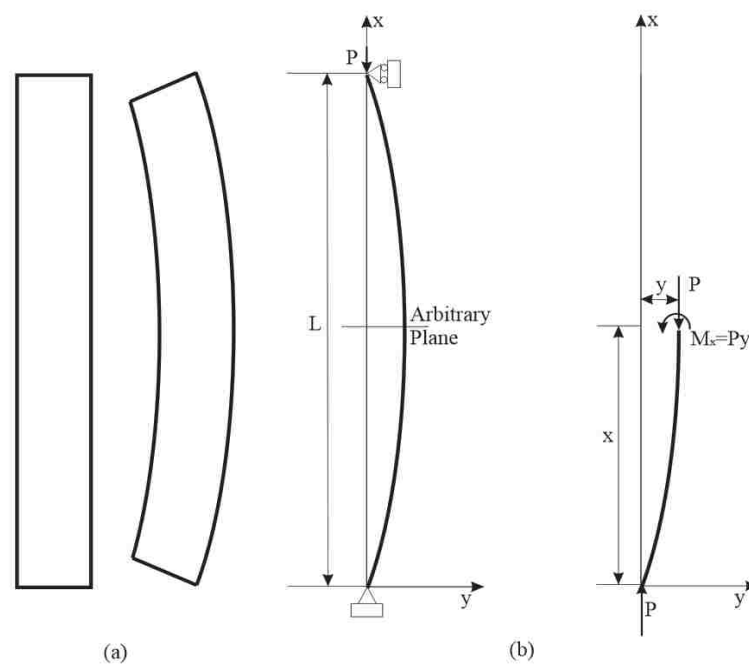
Figure 10: (a) Column in bent position and (b) Free body diagram of an arbitrary section

The free body diagram shown in Figure 10(b) shows the bending moment in a section at a distance x from the y axis along the x axis.

The governing differential equation is

$$EI\frac{d^2y}{dx^2} + Py = 0 \tag{1.3}$$

Substituting $k^2 = \frac{P}{EI}$ the differential equation is

$$\frac{d^2y}{dx^2} + k^2y = 0 \tag{1.4}$$

It is a second-order linear differential equation with constant coefficients. Its

boundary conditions are

$$y = 0 \text{ when } x = 0 \text{ and } x = l$$

The general solution for this differential equation is
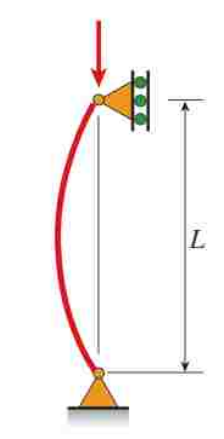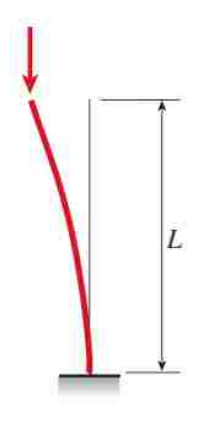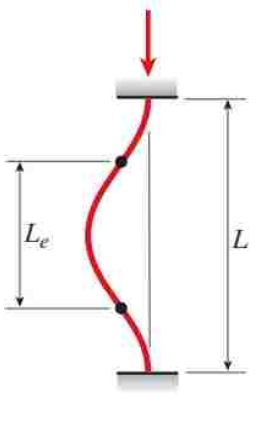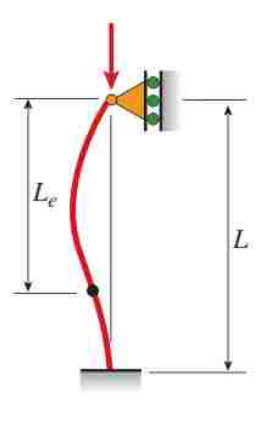
$$y = A\cos kx + B\sin kx \tag{1.5}$$

The integration constants are found by substituting boundary conditions and

using which the critical load or buckling load is found. Table 4 gives a summary of the

buckling loads for some specific boundary conditions. It is sufficient to say here that

the buckling load,

$$P_{cr} = \frac{k_1\pi^2 EI}{L^2} \tag{1.6}$$

where the value of k_1 is dependent on the boundary conditions. This theory is

attributed Euler and is called the Euler buckling analysis.

Table 4: Summary of buckling loads for different boundary conditions [1]

Pinned-Pinned Column	Fixed-Free Column	Fixed-Fixed Column	Fixed-Pinned Column
$P_{cr} = \dfrac{\pi^2 EI}{L^2}$	$P_{cr} = \dfrac{\pi^2 EI}{4L^2}$	$P_{cr} = \dfrac{4\pi^2 EI}{L^2}$	$P_{cr} = \dfrac{2.046\pi^2 EI}{L^2}$
$L_e = L$	$L_e = 2L$	$L_e = 0.5L$	$L_e = 0.7L$
$k_1 = 1$	$k_1 = 0.25$	$k_1 = 4$	$k_1 = 2.046$

There are situations where the load is not axial but is away from the axis. Mathematically, this is equivalent to having an additional moment Pe with the axial load as shown in Figure 11. Columns under eccentric loading can be treated as columns under axial loading with an additional external moment acting on the loading end [17] as shown in Figure 11.
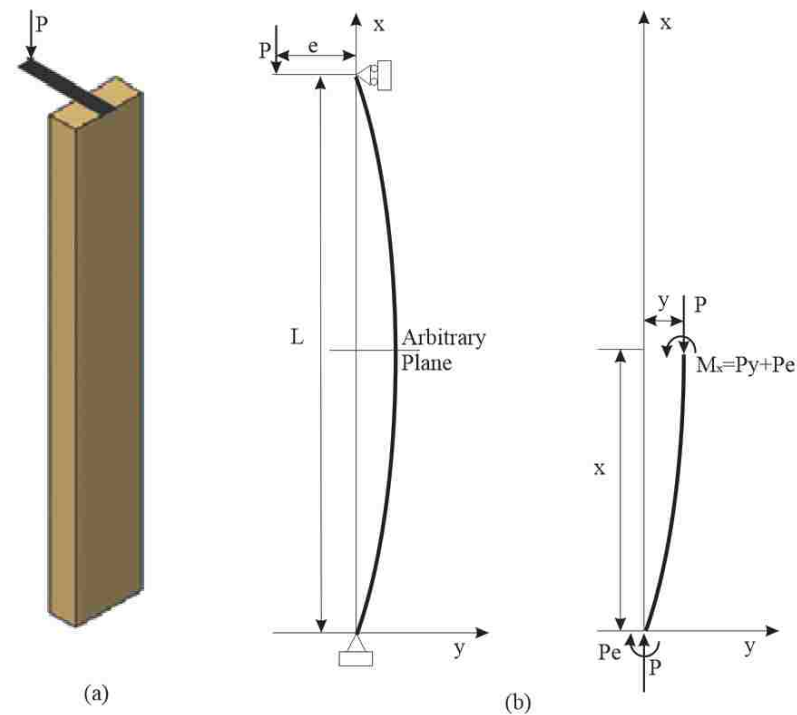
Figure 11: (a) Column under eccentric loading (b) FBD at an arbitrary plane

The governing differential equation is

$$EI\,\frac{d^2y}{dx^2} + P(y+e) = 0 \tag{1.7}$$

Substituting $k^2 = \dfrac{P}{EI}$, the differential equation is $\dfrac{d^2y}{dx^2} + k^2y = -k^2e$

The solution to this equation is

$$y = A\sin kx + B\cos kx - e \tag{1.8}$$

Substituting the initial condition when $x = 0$, $y = 0$ gives $B = e$

Substituting the initial condition when $x = l$, $y = 0$ gives $A = e\left(\dfrac{1 - \cos kl}{\sin kl}\right)$

The complete solution is

$$y = e\left(\cos kx + \frac{1 - \cos kl}{\sin kl}\sin kx - 1\right) \tag{1.9}$$

But $\dfrac{1-\cos kl}{\sin kl} = \dfrac{1-\left(1-2\sin^2\left(kl/2\right)\right)}{2\sin\left(kl/2\right)\cos\left(kl/2\right)} = \tan\left(\dfrac{kl}{2}\right)$

Therefore,

$$y = e\left(\cos kx + \tan\left(\dfrac{kl}{2}\right)\sin kx - 1\right) \tag{1.10}$$

Equation (1.10) has two consequences:

a) y becomes infinity when $\dfrac{kl}{2} = \dfrac{\pi}{2}$ because $\tan\dfrac{kl}{2}$ becomes infinity. This leads

to finding the critical load P_{cr} which becomes equal to $\dfrac{\pi^2 EI}{l^2}$.

b) Bending moment found earlier is $M_x = P(e+y)$. This means as y increases

M_x also will increase. But for a bending beam the maximum bending stress at a

section $\sigma_b = \dfrac{Mc}{I}$. This means the bending stress will increase and reach the yield point

as y increases.

1.3.5 Finite Element Analysis

During the design of a product, it is quite often required to deal with field

variables such as displacements and stresses to

- Calculate the displacements at certain points

- Calculate the entire distribution of the displacement field

- Determine the stress distribution and hence predict the strength

- Determine the natural frequencies and associated modes of vibration

- Determine the critical buckling loads

- Predict the response for forced vibrations etc.

Three methods are normally employed to perform these analyses. They are the use of (a) analytical methods (b) experimental methods and (c) numerical methods. Analytical methods use only simple geometries and idealized loading and support conditions. Therefore, they are not well suited for the complex structures of modern days. Experimental methods are expensive and time consuming and not possible for complex objects. Numerical methods, require very few restrictive assumptions, can treat complex geometries and realistic support and loading conditions, and are cost effective. Finite Element Method is such a Numerical Method employed for Engineering Analysis and can be described in the following way:

(a) In engineering problems, there are some basic unknowns. If they are found the behavior of the entire structure can be predicted. These basic unknowns are called the Field Variables [18]. The field variables encountered in solid mechanics are displacements and stresses. Field variables in other areas of study are velocities in fluid mechanics, electric and magnetic potentials in electrical engineering and temperatures in heat flow problems.

(b) In a continuum (a thing of continuous structure) these unknowns are infinite (values at the infinite number of points). The finite element method reduces this number of unknowns to a finite number by describing the variables at chosen points called the 'Nodes' [19]. A portion of the continuum is defined by the connection of these nodes and the region is called an 'Element' [19]. The field variables at points within the element are found by interpolation using the values at the nodes and interpolating function is called the 'Shape Function' [19].

Thus, the Finite Element Method can be described as a method where (a) the Field Variables at the infinite number of points in a continuum is represented by those

at a chosen finite number of points called nodes (b) their values are then calculated using some engineering principles and other governing relationships and (c) finally the values of the field variables at all intermediate points are calculated by interpolation using the shape functions.

In ABAQUS for example this is achieved by following a set procedure as shown in Figure 12.
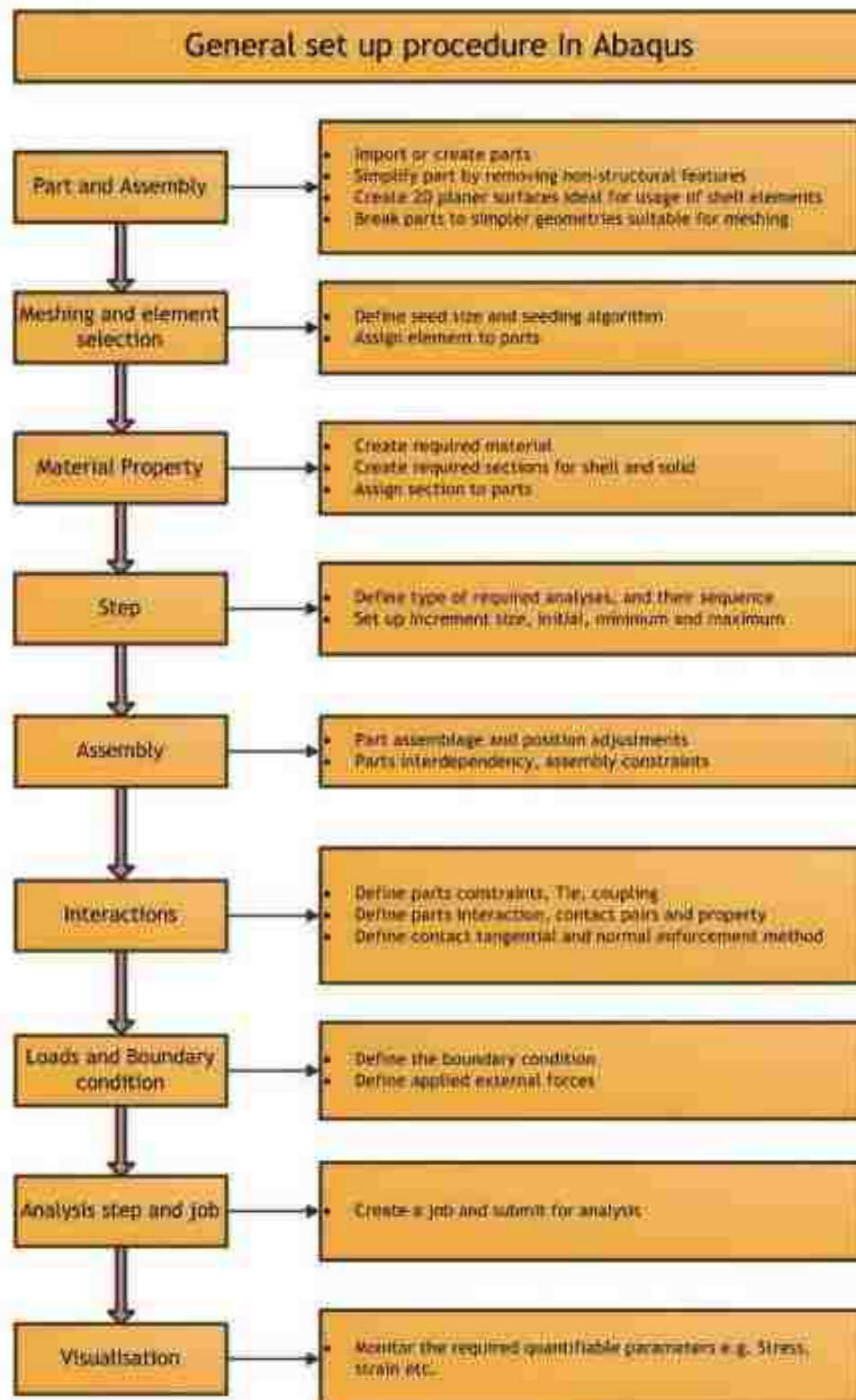
Figure 12: Finite element analysis using ABAQUS [20]

1.4 Parametric Analysis

Consider a cuboid which has a length 'a', width 'b' and height 'c'. Then the cube can be represented by a vector [a b c]. Now the vector [a b c] can be used to represent all cuboids by changing the values of the elements a, b and c. This representation of cuboids as a vector of three elements is a parametric representation. In general, an engineering design can have several such variables. For example, earlier in Table 1, eleven parameters were identified to represent the inner beam assembly of a telescopic cantilever. This means that an eleven-element vector can represent each of the inner beam assemblies and in an eleven dimensional co-ordinate system, an inner beam assembly can be represented by a vector, will be a single point. But each of the parameters (like WP length for example) can take values within a given range and all the designs would lie within an 11-dimensional hyperspace. An optimal design would lie as a point within this hyperspace. Analysis that varies the parametric values to find the optimal design is called Parametric Analysis.

Scientists conduct experiments, make observations and analyze the data to draw conclusions. Consider the eleven-dimensional hyperspace where each of the design variables are allowed to take just two values. These values are called levels. Then there will be 2^{11} designs to consider in the hyperspace. It is impossible to conduct experiments with all these 2^{11} designs, and the statistical method that systematically chooses the design points (or parameter combinations) is called Experimental Design. There are several methods for Experimental Design. Taguchi [21] provides a set of orthogonal arrays using indicator variables 1 and 2 for this purpose. For example, the array L_{12} has eleven columns which can be assigned to eleven factors while the number of experiments is limited to only 12. Table 5 gives Taguchi's L_{12} array.

Table 5: Taguchi L$_{12}$ array [21]

Experiment Number	Column										
	1	2	3	4	5	6	7	8	9	10	11
1	1	1	1	1	1	1	1	1	1	1	1
2	1	1	1	1	1	2	2	2	2	2	2
3	1	1	2	2	2	1	1	1	2	2	2
4	1	2	1	2	2	1	2	2	1	1	2
5	1	2	2	1	2	2	1	2	1	2	1
6	1	2	2	2	1	2	2	1	2	1	1
7	2	1	2	2	1	1	2	2	1	2	1
8	2	1	2	1	2	2	2	1	1	1	2
9	2	1	1	2	2	2	1	2	2	1	1
10	2	2	2	1	1	1	1	2	2	1	2
11	2	2	1	2	1	2	1	1	1	2	2
12	2	2	1	1	2	1	2	1	2	2	1

When the number of levels or the number of factors to be studied is increased the number of experimental runs also increases. At the beginning of an experimental investigation, to understand a phenomenon, one may find that there are too many factors to study. This would result in a large experiment that would be difficult to manage. In this situation, it would be better to conduct a small experiment with just two levels that would identify the factors that have little or no effect on the chosen response so that they can be eliminated from the main study. Such an initial experiment is called a 'Screening Experiment'. After identifying the sensitive parameters from the screening experiment a second experiment with high number of levels is conducted to fit a response surface and use the fitted surface to optimize the design.

Physical experiments are costly and cumbersome, and the current trend is to conduct computer experiments. In a computer experiment, computer code is used in lieu of a physical experiment to obtain the value of the response variable. In order to obtain reliable results from experimentation, the computer model should be a true

representation of the physical object and ensuring this truthfulness is called validation. Normally, computer models are validated by physical experiments.

1.5 Problem Statement and Research Objectives

The broad aim of this research is to explain 'how the overlap region of the inner beam assembly in a telescopic beam behaves under a tip load' and establishes a new generic approach to the design of telescopic beams based on parametric studies using FEA and statistical optimization.

The preceding sections highlighted that the critical area of concern is the overlap area of the inner beam and its behavior depends on multiple factors. Further, the behavior varies from case to case as it depends on the numeric values of the geometric factors. The overlap section, when looked at separately, can be divided into three sections, two sections under the wearpads and the connecting middle region as shown in Figure 13. At the extreme ends, two RHS rings or RHS pieces (depending on the length of the wearpad) receive the thrusting compressive forces from the outer beam through the wearpads. These forces balance the tip load and the moment created by it. The rings or pieces are connected by the middle portion and the magnitudes of the forces increase as the length of the middle portion decreases.
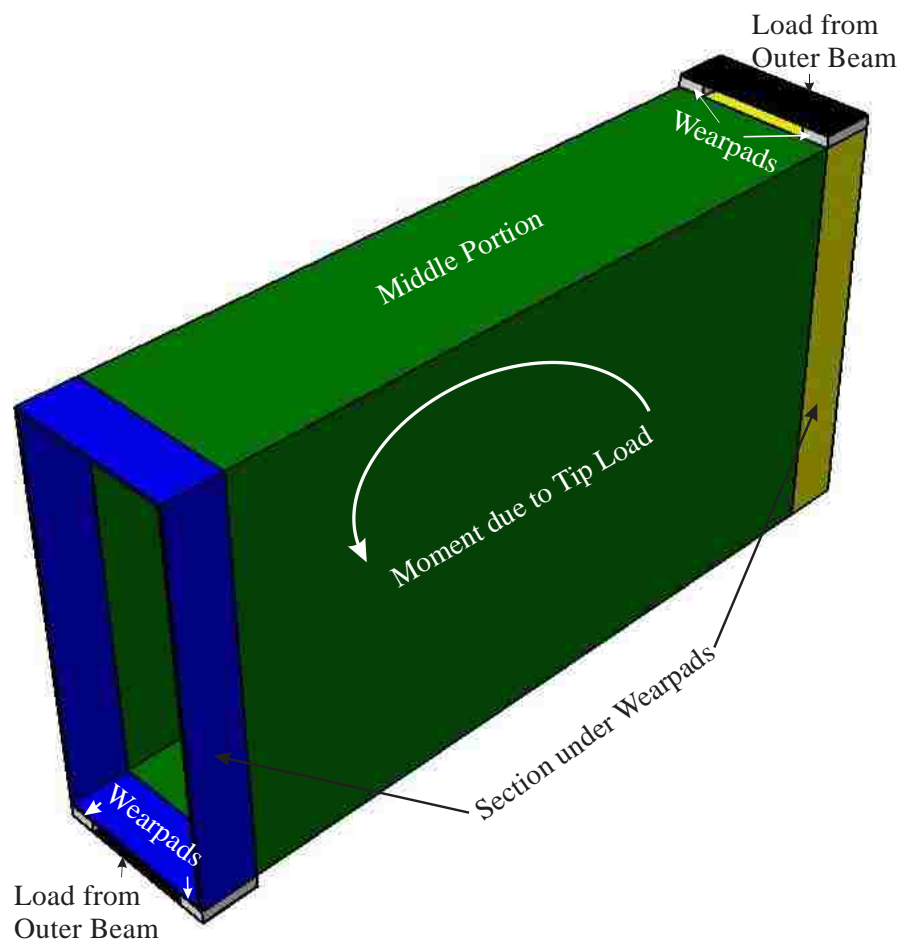
Figure 13: Division of the overlap section

The research objectives drawn in this background therefore are as follows:

1. Establish the behavior of RHS rings, RHS pieces and telescopic beams under transverse loading through qualitative investigations and experiments.

2. Establish the status of the current knowledge in this and the relevant areas through a literature survey.

3. Establish validated FEA methods using ABAQUS software to analyze RHS rings, RHS pieces and telescopic beams

4. Establish statistical optimization method using computer experiments and validate with case study

5. Establish a design methodology to design telescopic beams using computer experiments.

Methods used to achieve these objectives include physical experimentation, FEA and theoretical developments.

1.6 Research Methodology

The research methodology adopted can be described as shown in Table 6.

Table 6: Research methodology

Objective	Method	Description
Establish the behavior of RHS rings, pieces and under transverse compressive loading	Transverse loading of RHS rings between • Platens • Wearpads	RHS rings of 3 mm thickness, with a height of 350mm, width of 150 mm and length of 10 mm were compressed between platens and wearpads
	Transverse loading of RHS pieces between • Platens • Wearpads	RHS pieces of 3mm thickness of the following outer dimensions were compressed between platens and wearpads • 350 mm height, 150 mm width and 150 mm length • 150 mm height, 100 mm width and 100 mm length
Establish the status of the current knowledge in relevant areas	Literature Survey	Chapter 3 begins with explanation of scientific method adopted. Additionally, four topics were reviewed; buckling, RHS, FEM and experimental design
Establish theoretical development and define methodology to design telescope inner beam assembly	Use experimental observations to establish theoretical developments theory	RHS Ring explained as an assemblage of columns and beams. RHS pieces explained as an assemblage of plates. Analysis was done for RHS Rings and pieces between platens and wearpads
Establish influencing factors for RHS Rings, RHS pieces between wearpads	Use experimental designs to acquire influencing factors	Validate FE models of RHS Rings and RHS pieces against experimental data. Used screening experiments and response surface design to acquire influencing factors

Table 6: Research methodology (Continued)

Validate design methodology for inner beam assembly, establish mathematical model for case study and optimize design	Apply step by step method to design and optimize the inner beam assembly of a telescopic cantilever assembly	Using screening experiments, list the influencing factors. Conduct a Central Composite Design (CCD to establish the mathematical model. Use model to optimize design for the given constraints.

1.7 Summary of Results

The behavior of the overlap region of the inner beam was analysed as (i) two RHS rings or RHS pieces and a middle connecting part and (ii) as a whole piece. The following behavior was established for the RHS rings, RHS pieces and the Overlap region as a whole.

- Exploratory experimentation with RHS rings between platens suggested that the flanges behaved as beams under end moments and the webs behaved as columns under axial loads and end moments. Experiments with RHS rings loaded through the wearpads suggested that the wearpads contributed an additional end moment compared to the RHS Ring behavior under loading between platens. Under both loading conditions, the flanges curved inside while the webs curved outside and the webs formed hinges in the middle. Theoretical model suggested that the critical load $P_{cr} = \dfrac{k_1 \pi^2 EI}{L^2}$ with a value for k_1 between 1 and 4 because of the degree of constraints at the corner joints.

- Exploratory experimentation with RHS pieces between platens suggested that the RHS piece behaved as assembly of four plates – two vertical (webs) and two horizontal (flanges). In contrast to the RHS Rings, the flanges in the RHS pieces acted as plates instead of beams under end moments and the webs

behaved as plates under axial loads and end moments. Experiments with RHS pieces loaded between the wearpads also suggested that the wearpads contributed an additional moment compared to the RHS piece behavior under loading between platens. In the specimens of both experiments the flanges curved inside while the webs curved outside and the webs formed hinges in the middle.

For a rectangular plate of height 'b' and thickness 't', the critical stress

$(\sigma_x)_{cr} = k_2 \dfrac{\pi^2 E}{12(b/t)^2(1-\upsilon^2)}$ with a value for k_2 between 4 and 6.97 because of

the degree of constraints at the edges.

- Exploratory FEA suggested that the maximum stress occurs in the overlap region of the inner beam in the vicinity of the bottom wearpad. In the bottom flange of this region, high stresses occur due to the bending stress due to the tip load and due to the bending stress due to the corner moments from the loads through the wearpads. The webs in this region suffers the maximum compressive stress near the bottom that may also lead to buckling. The magnitudes and the buckling behavior are case dependent and a methodology for the design is suggested as shown in Figure 14 below.
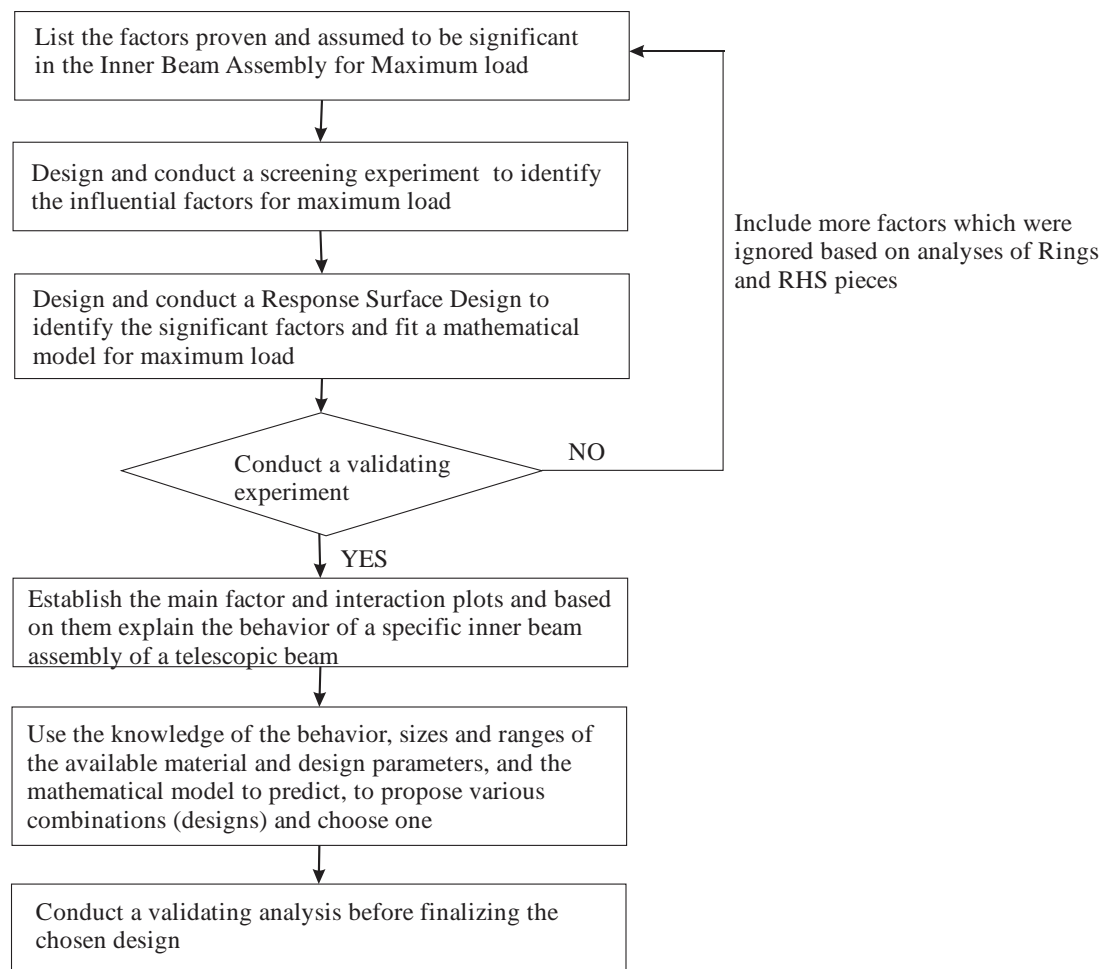
Figure 14: Design methodology flowchart

1.8 Structure of Thesis

The thesis consists of eight chapters. Chapter 1 introduces the background and the research question and establishes the objectives of the research.

Chapter 2 describes the literature survey segregated in five sections; Scientific Method, Buckling, Rectangular hollow sections, FEM (Finite Element Method) and Experimental Design.

Chapter 3 describes the exploratory Finite Element Analyses on telescopic beams and experimental investigations on RHS rings and RHS pieces.

Chapter 4 describes the theoretical developments based on the results of the qualitative experiments in Chapter 3 and the literature survey in Chapter 2.

Chapter 5 is a case study on RHS rings. It determines the influencing geometric factors affecting the maximum load carrying capacity of RHS rings using validated FE Models and design of experiment methods.

Chapter 6 is a case study on RHS pieces. It determines the influencing geometric factors affecting the maximum load carrying capacity of RHS pieces using validated FE models and design of experiment methods.

Chapter 7 is a case study on the inner beam assembly of a telescopic cantilever assembly. It implements the methodology established in Chapter 4 to establish a mathematical model and optimize the design of the inner beam assembly of a telescopic beam assembly.

Chapter 8 describes the discussion and conclusions drawn from the research.

Appendix I shows the material test report for the RHS ring sample.

Appendix II lists the DOE tables for the case study of the RHS rings.

Appendix III lists the DOE tables for the case study of the RHS pieces.

Appendix IV lists the DOE tables for the case study of the inner beam assembly of the telescopic beam.

Chapter 2: Literature Survey

This chapter describes the summary of the current frontiers of knowledge, which is needed to build the knowledge further. It categorizes them under seven groups for easy comprehension and each category is described by each of the following subsections.

2.1 Scientific Method

Science is a determination of what is most likely to be correct at the current time with the evidence at hand. Scientific explanations can be inferred from confirmable data only, and observations and experiments leading to science must be reproducible and verifiable by other individuals. Scientific method is a methodological approach to the process of inquiry – in which empirically grounded theory of nature is constructed and verified [22]. The origin of modern scientific method occurred in Europe in the 1600s: involving a chain of research events from Copernicus to Newton [22]. The scientific method may include some or all of the following "steps" in one form or another: observation, defining a question or problem, research (planning, evaluating current evidence), forming a hypothesis, prediction from the hypothesis (deductive reasoning), experimentation (testing the hypothesis), evaluation and analysis, peer review and evaluation, and publication [23], [24].

The trigger for this research was the observation of magnification of the tip reactions (explained in section 1.2.2). The curiosity from this observation led to an exploratory FEA and experimental investigations on RHS rings and RHS pieces as described in Chapter 3. This chapter describes the literature survey carried out to know the current frontiers of knowledge in relevant topics. This will assist to formulate the hypothesis to establish knowledge that can help to explain or design the overlap areas of telescopic cantilever beams.

2.2 Buckling

Buckling is a physical phenomenon of a straight and slender member abruptly bending laterally from its longitudinal position due to compressive loading [20]. Structural members fail resisting tension, shear or torsion when the stress in the member reaches a certain limiting strength of the material. Buckling on the other hand does not take place as a result of the resisting stress reaching a limiting strength of the material. In thin-walled structures, because of the low thickness to width ratio, it is likely that the structure will buckle under compressive, bearing, and shear bending forces [25]. Therefore, for structural members consisting of thin-walled profiles, the ultimate strength is greatly influenced by its buckling capacity [26].

As discussed in section 1.2.1, the stress at which buckling occurs depends on a variety of factors such as the dimensions of the member, boundary conditions and the properties of the material of the member. Determining it is complicated and is analysed under the heading Stability Analysis.

2.2.1 Stability Analysis

The concept of the stability of various forms of equilibrium of a compressed bar is frequently explained in literature [27] by considering the equilibrium of a ball in various positions, as shown in Figure 15. Consider the equilibrium of the ball in Figure 15(a). Any slight displacement of the ball from its position of equilibrium will raise the center of gravity and work is required to produce such a displacement. In other words energy input is required.
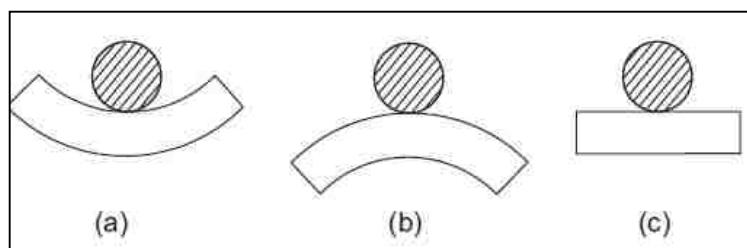
Figure 15: Equilibrium positions of a ball (a) Stable (b) Unstable (c) Neutral [28]

Now consider the equilibrium of the ball in Figure 15(b). If it is disturbed slightly from its equilibrium position it will continue to move down. The equilibrium of the ball in Figure 15(b) is called unstable equilibrium. Any slight displacement from the position of equilibrium will lower the center of gravity of the ball and consequently will decrease the potential energy of the ball. Thus in the case of stable equilibrium, the energy of the system is a minimum (local), and in the case of unstable equilibrium it is a maximum (local).

Now consider the equilibrium of the ball in Figure 15(c). If displaced slightly, it neither returns to its original equilibrium position nor continues to move away upon removal of the disturbing force. It finds another equilibrium position. This type of equilibrium is called neutral equilibrium. If the equilibrium is neutral, there is no change in energy during a displacement in a conservative force system.

A column under axial compression responds in a very similar manner to that of the ball in Figure 15. The straight configuration of the column is stable at small loads, but it is unstable at large loads. A state of neutral equilibrium exists at the transition from stable to unstable equilibrium in the column. Then the load at which the straight configuration of the column ceases to be stable is the load at which neutral equilibrium is possible. This load is usually referred to as the critical load.

At critical load, the member can be in equilibrium, both in the straight and in a slightly bent configuration. The method that bases this slightly bent configuration for evaluating the critical loads is called the method of neutral equilibrium, neighboring equilibrium, or adjacent equilibrium. At critical loads, the primary equilibrium path or stable equilibrium, reaches a bifurcation point and branches into neutral equilibrium paths.
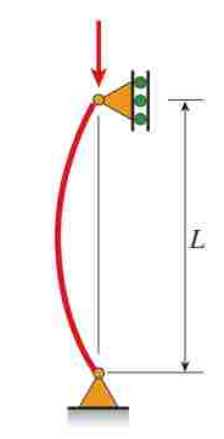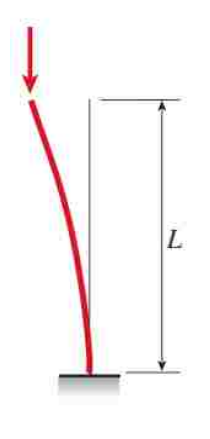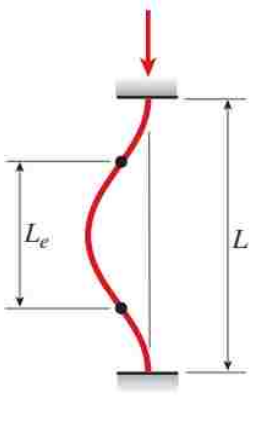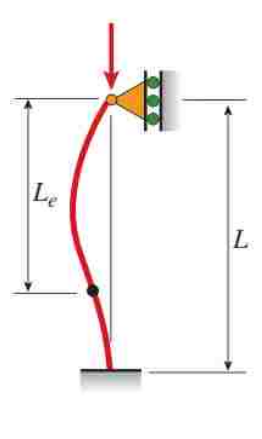
The bifurcation-type buckling is a purely conceptual one that occurs in a perfectly straight (geometry) homogeneous (material) member subjected to a compressive loading of which the resultant must pass through the centroidal axis of the member [14]. The importance attached to and the considerably large amounts of research devoted to bifurcation-type loading is justified in that the bifurcation-type buckling load or the critical buckling load gives the upper bound solution for practical columns [29].

As explained in section 1.3.4, for an axially loaded pin-ended column, the smallest buckling load for a pinned prismatic column corresponding to $k_1 = 1$ is

$$P_{cr} = \frac{\pi^2 EI}{L^2}.$$

Table 4 in Chapter 1 gives a summary of the buckling loads for some specific boundary conditions and is repeated here again as Table 7. The value of k_1 is dependent on the boundary conditions.

Table 7: (Repeated) Buckling loads for different boundary conditions

Pinned-Pinned Column	Fixed-Free Column	Fixed-Fixed Column	Fixed-Pinned Column
$P_{cr} = \dfrac{\pi^2 EI}{L^2}$	$P_{cr} = \dfrac{\pi^2 EI}{4L^2}$	$P_{cr} = \dfrac{4\pi^2 EI}{L^2}$	$P_{cr} = \dfrac{2.046\pi^2 EI}{L^2}$
$L_e = L$	$L_e = 2L$	$L_e = 0.5L$	$L_e = 0.7L$
$k_1 = 1$	$k_1 = 0.25$	$k_1 = 4$	$k_1 = 2.046$

Considering P_{cr} for the pinned-pinned column gives

$$\sigma_{cr} = \frac{P_{cr}}{A} = \frac{\pi^2 EI}{L^2 A} = \frac{\pi^2 E}{\lambda^2} \tag{3.1}$$

Where λ is the slenderness ratio.

2.2.2 Eccentric Loading

Columns designed for axial load are discussed in section 2.2.1 above. However, for situations where the load is eccentric, columns are analyzed differently. When a column is eccentrically loaded, bending can be a severe problem and may be more important than the compression stress or buckling.

Columns under eccentric loading can be treated as columns under axial loading with an additional external moment acting on the loading end as shown in Figure 11 and repeated in Figure 16 below. As the load is increased, the moment will increase

and cause the beam to bend further. Viewed this way, the problem of buckling is not a question of determining how long the column can remain straight and stable under the increasing load, but rather how much the column can be permitted to bend under the increasing load, if the allowable stress is not to be exceeded and if the deflection 'y' is not to be excessive.
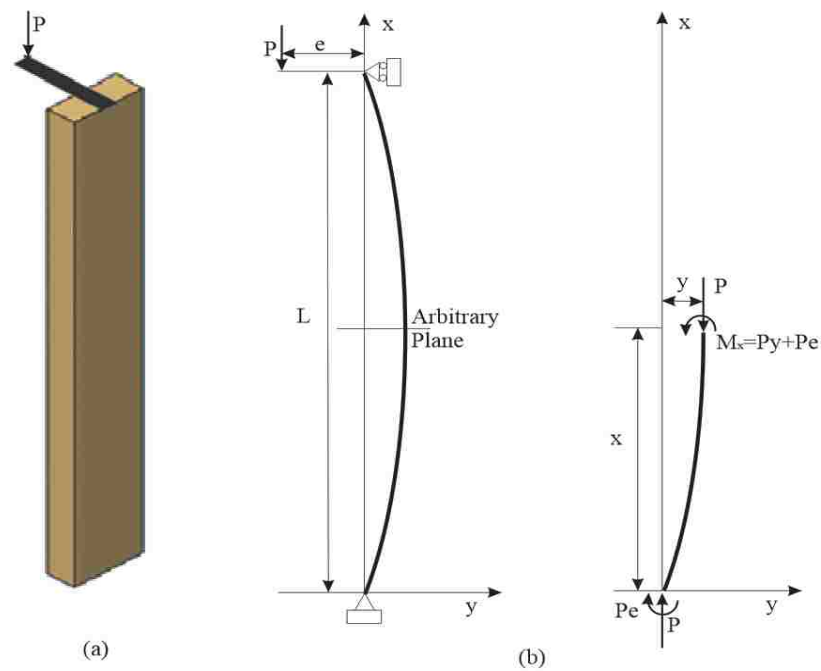
Figure 16: (Repeated) (a) Column under eccentric loading (b) FBD at an arbitrary plane

Consider bent column shown in Figure 17(a). At the midpoint of the beam the deflection will be maximum. Hence the bending moment will also be at a maximum. This follows that the bending stress also will be at a maximum.
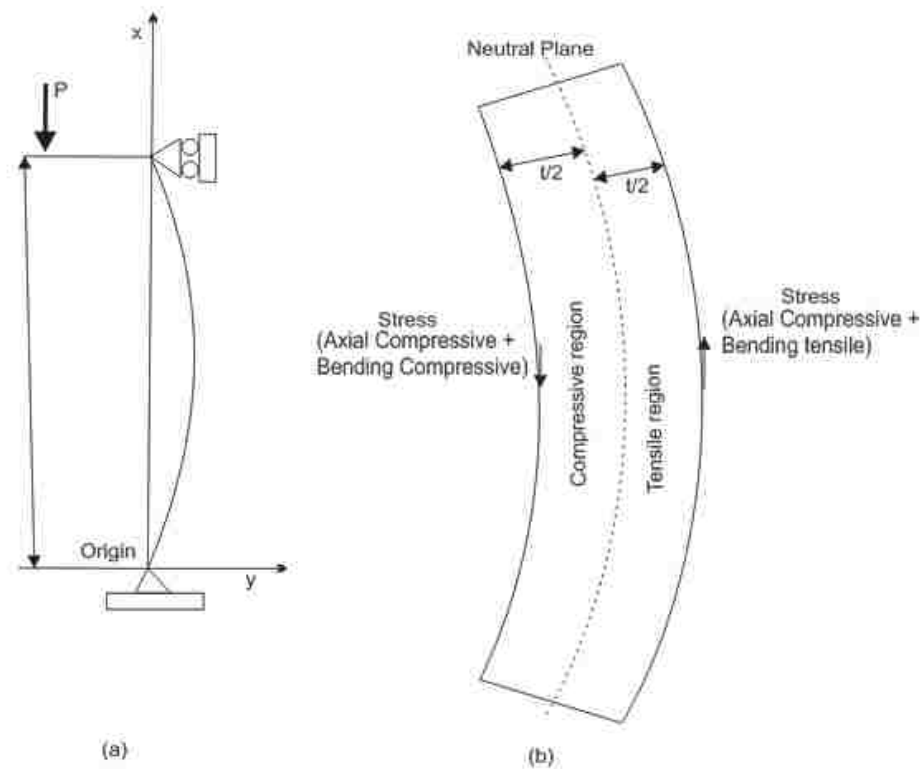
Figure 17: Combined axial and bending stresses

Axial stress P/A due to the compressive load P will be distributed uniformly throughout the cross section. But the major addition is the bending stresses, which reach very high values when the deflection increases. The stresses in the extreme fibers are maximum within each section. The stress in the inner section is compressive and is maximum at the inner most fiber. This combined with the axial stress makes the stress in the inner most fiber at mid-height of the beam to reach the maximum at $-\sigma_b - \dfrac{P}{A}$ first to trigger yielding. The outer most fiber will be under tensile stress and the magnitude is $\sigma_b - \dfrac{P}{A}$.

2.2.3 Load Deflection Behaviour of Steel under Compression

Steel being a ductile material has a stress – strain diagram in compression test similar to its tensile test. It has an elastic region, proportional limit and a plastic region that follows.
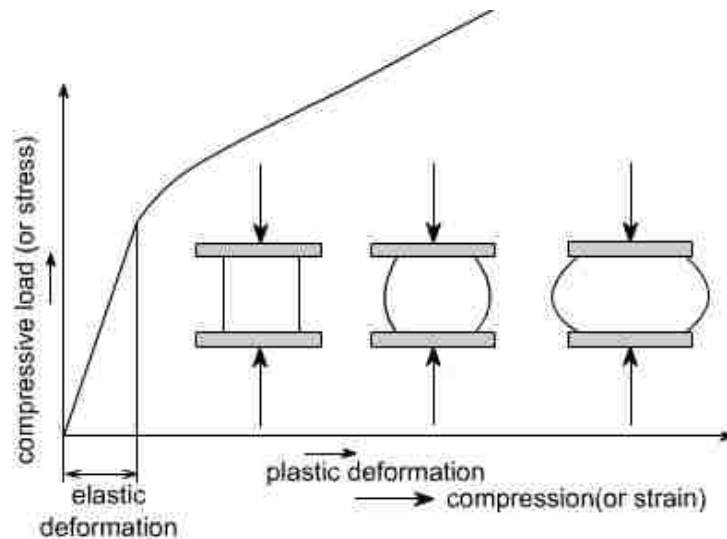
Figure 18: Compressive stress vs compressive strain diagram

In tension test, a specimen is being stretched, necking may occur, and ultimately fracture takes place. On the other hand, when a small specimen of steel is compressed, it begins to bulge on sides and becomes barrel shaped as shown in Figure 18 before it fails. The graph shows that the material's strength to carry load still increases in the plastic region even though it produces a higher increase in strain for a small increase in stress.

2.2.4 Collapse Load with Columns with Various Slenderness Ratios
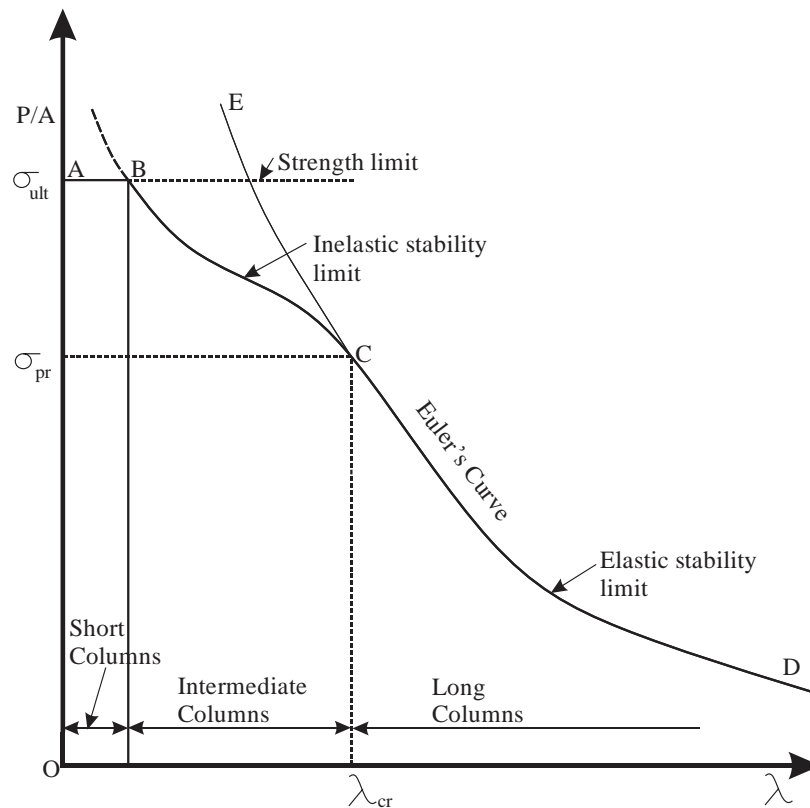
Figure 19: Average stress in columns versus slenderness ratio[1]

Gere [1] explains the behavior of steel columns with various slenderness ratios in the form of a graph as shown in Figure 19. The curve ABCD shows the collapse load of the columns with small to large slenderness ratios. The short columns fail due to the collapse of the material represented by the region AB in the curve. The intermediate columns fail due to inelastic buckling. The long columns represented by the region CD fails due to elastic buckling. He estimates λ_{cr} of steel as

$\sqrt{\dfrac{\pi^2 \times 210000}{300}} = 83.07$ by considering yield strength and Young's modulus of steel.

For short steel columns, the slenderness ratio should be less than ten. The columns, which have slenderness ratio in the range between 10 and 83 are classified

as intermediate columns. They lose their stability by inelastic buckling. Inelastic buckling is characterized by its occurrence after yielding has started and it occurs between the yield strength σ_y and ultimate strength σ_{ult} ..

2.2.5 Buckling and Buckling Modes

As explained above, buckling can occur both elastically and inelastically. Elastically, three kinds of buckling can occur in a member; local, distortional and global [30]. In case of local or distortional buckling there exists a post-buckling reserve capacity, which allows extra load to be applied. If the member buckles globally there is no allowance for additional load and the member collapses [26]. Global buckling can further be classified into flexural, torsional and flexural-torsional buckling.

The buckling phenomenon classified in terms of the buckling modes are as shown in Table 8.

Table 8: Modes of buckling classification [7], [8]
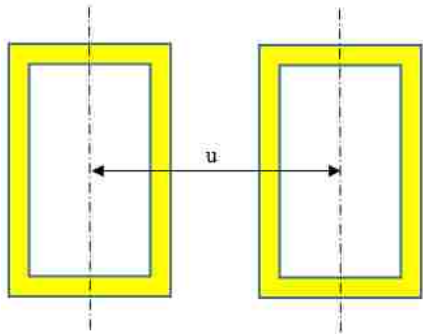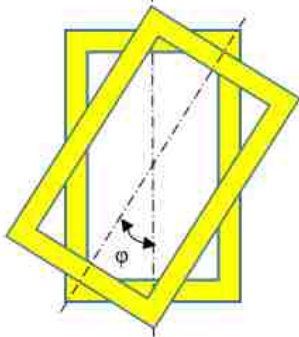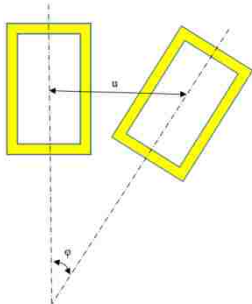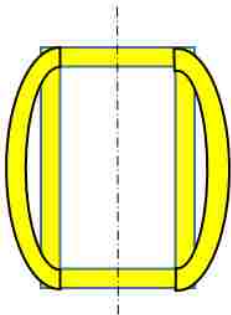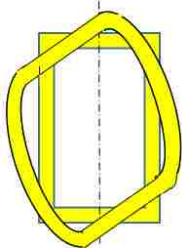
MODE	DESCRIPTION	VISUALIZATION
Flexural	It may involve transverse displacement of the member cross-section and is resisted by the flexural rigidity of the member. It occurs when the second-order moment caused by the product of the axial compression forces with the displacements are equal to the internal bending resistance at any point in the structure.	

Table 8: Modes of buckling classification (Continued)

MODE	DESCRIPTION	VISUALIZATION
Torsional	This involves twist of the member cross-section, and is resisted by the tensional rigidity and the warping rigidity. It occurs when second-order torque caused by the axial compression force and the twist are equal to the sum of the internal torsion resistances at any point in the structure.	
Flexural-Torsional	This involves the mixture of two above phenomena and therefore resisted by the combination of the bending resistance and the torsional resistance.	
Local	This mode involves deflection of a thin plate out of its original plane. This mode occurs when the second-order actions caused by the in-plane compressions and the out of plane deflections are equal to the internal resistances of the plate elements to bend and twist at any point in the structure.	
Distortional	This is an intermediate mode between local and member buckling. It often involves web flexure and corresponding rotations of the flanges which vary slowly along the member length.	

It is worth noting that local buckling involves plate-like deformations alone, without the translation of the intersection lines of adjacent plate elements, whereas

distortional buckling is a mode with cross-sectional distortion that involves the translation of some of the fold lines (intersection lines of adjacent plate elements) [31].

2.2.6 Plate Buckling

Plates are initially flat members bounded by two parallel planes called faces and a cylindrical surface called an edge or boundary [32]. The generators of the cylindrical surface are perpendicular to the plane faces. Distance between the faces is the thickness h of the plate and for thin plates assumed it is small compared to other dimensions. The thickness h is divided into two halves by a plane parallel to the faces and this plane is called the midplane. When the plate bends, the midplane also bends and the bent form is called the mid surface. Plates may be classified into three groups according to the ratio a/h where a is a typical dimension and h is the thickness [32].

i.   *Thick plates having an a/h ratio less than 8 to 10*

Their analysis include all the components of stresses, strains, and displacements as for solid bodies using the general equations of three-dimensional elasticity.

ii.   *Membranes having a/h greater than 80 to 100*

They carry the lateral loads by axial tensile forces N (and shear forces) acting in the plate middle surface. These forces are called the membrane forces.

iii.   *Thin Plate with a/h between 8 to 10 and 80 to 100*

Depending on the value of the ratio, maximum deflection to thickness *w/h*, the part of flexural and membrane forces here may be different. Therefore they are classified into two classes called *stiff* (w/h up to 0.2) and *flexible* ($w/h \geq 0.3$) plates.

Majority of the plates considered here falls in the membrane or thin category.

In column buckling adjacency equilibrium method was used and the bent column was analysed as a bent beam to derive the critical load for buckling. In a similar fashion a bent plate can be analysed to establish the buckling load for an axially loaded plate. Bending of a plate, however, involves bending in two planes and from a mathematical point of view, the quantities such as deflections and bending moments, become functions of two independent variables [33]. As a consequence of this, the behavior of plates is governed by partial differential equations, which increases the complexity of the analysis. Plate buckling is usually referred to as local buckling [14]. Structural shapes composed of plate elements may not necessarily terminate their load-carrying capacity at the instance of local buckling of individual plate elements and this adds further difficulty [34].

2.2.7 Theory of Plates

The objective of thin-plate theory is to reduce a three-dimensional (complex) problem to an approximate (practical) one based on the following simplifying assumptions known as Kirchoff's assumptions [35]:

i. Normals to the undeformed middle plane are assumed to remain normal to the deflected middle plane and in extensional during deformations, so that transverse normal and shearing strains may be ignored in deriving the plate kinematic relations.

ii. Transverse normal stresses are assumed to be small compared with the other normal stresses, so that they may be ignored.

The resulting forces and moments acting on a plate element according to these assumptions are shown in Figure 20. With these the following three sets of equations can be derived:

i. *Kinematic Equations* relating deflection and curvatures

ii. *Constitutive Equations* relating curvatures and bending moments

iii. *Equilibrium Equations* relating transverse load and bending moments
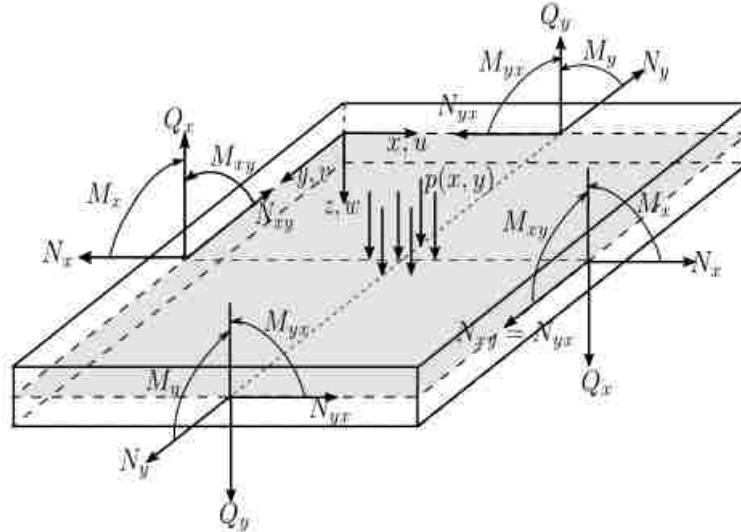
Figure 20: Forces and moments acting on a plate element

Internal forces (generalized) acting on the edges of a plate element *dxdy* are related to the internal stresses by the equations in Table 9 [14].

Table 9: Plate forces and moment equations

$N_x = \int_{-h/2}^{+h/2} \overline{\sigma}_x dz$	$N_y = \int_{-h/2}^{+h/2} \overline{\sigma}_y dz$	In plane normal forces
$N_{xy} = \int_{-h/2}^{+h/2} \overline{\tau}_{xy} dz$	$N_{yx} = \int_{-h/2}^{+h/2} \overline{\tau}_{yx} dz$	In plane shear forces
$Q_x = \int_{-h/2}^{+h/2} \overline{\tau}_{xz} dz$	$Q_y = \int_{-h/2}^{+h/2} \overline{\tau}_{yz} dz$	Transverse shearing forces
$M_x = \int_{-h/2}^{+h/2} \overline{\sigma}_x z dz$	$M_y = \int_{-h/2}^{+h/2} \overline{\sigma}_y z dz$	Bending moments
$M_{xy} = \int_{-h/2}^{+h/2} \overline{\tau}_{xy} z dz$	$M_{yx} = \int_{-h/2}^{+h/2} \overline{\tau}_{yx} z dz$	Twisting moments

The barred quantities $\overline{\tau}_{xy}, \overline{\sigma}_x$ etc. are components at any point through thickness. τ_{xy}, σ_x are quantities in the mid-surface.

The kinematic equations relating the curvature of the mid-surface to deflection are:

$$k_{xx} = \frac{\partial^2 w}{\partial x^2}$$
$$k_{yy} = \frac{\partial^2 w}{\partial y^2} \tag{3.2}$$
$$k_{xy} = \frac{\partial^2 w}{\partial x \partial y}$$

The constitutive equations relating curvature of the mid-surface and bending moments are

$$M_{xx} = D[k_{xx} + \upsilon k_{yy}]$$
$$M_{yy} = D[k_{yy} + \upsilon k_{xx}] \tag{3.3}$$
$$M_{xy} = D\left[\frac{1}{2} k_{xy}(1+\upsilon)\right]$$

where $D = \dfrac{Eh^3}{12(1-\upsilon^2)}$ the isotropic plate rigidity.

The equilibrium equation relating moments and the applied load is

$$\frac{\partial^2 M_{xx}}{\partial x^2} + \frac{\partial^2 M_{xy}}{\partial x \partial y} + \frac{\partial^2 M_{yy}}{\partial y^2} = p \tag{3.4}$$

Combining these three sets of equations give the partial differential equation of the deflection surface given by

$$D\left[\frac{\partial^4 w}{\partial x^4} + \frac{\partial^4 w}{\partial x^2 \partial y^2} + \frac{\partial^4 w}{\partial y^4}\right] = p \tag{3.5}$$

This equation is called the biharmonic equation. This is similar to the equation

$EI \dfrac{d^2 y}{dx^2} = M$ in the beam.

2.2.8 Plate under Axial Loading

Consider a plate simply supported on four edges and subjected to compressive load N_x per unit length uniformly distributed at the edges $x = 0, a$ as shown in Figure 21.
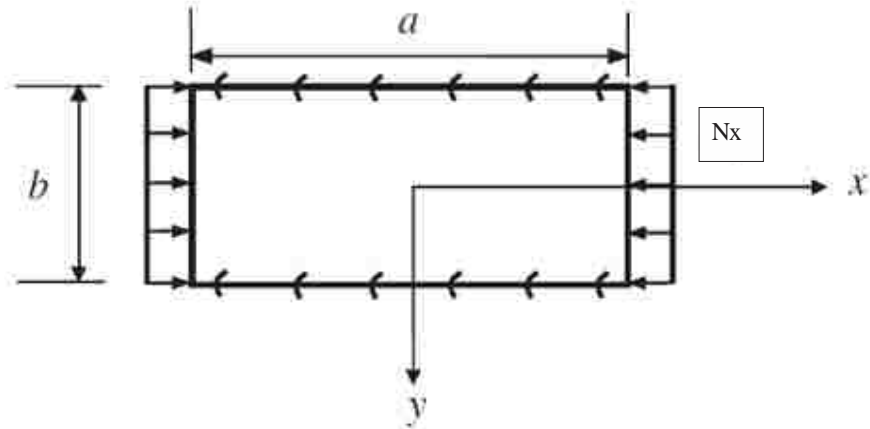
Figure 21: Simply supported plate in all four sides

The critical buckling load, $(N_x)_{cr}$, and the critical buckling stress, $(\sigma_x)_{cr}$ for the simply supported plated is calculated as shown [7], [27], [36]:

The harmonic equation for a plate in general is

$$\frac{\partial^4 w}{\partial x^4} + 2\frac{\partial^4 w}{\partial x^2 \partial y^2} + \frac{\partial^4 w}{\partial y^4} = \frac{1}{D}\left(N_x \frac{\partial^2 w}{\partial x^2} + N_y \frac{\partial^2 w}{\partial y^2} + 2N_{xy}\frac{\partial^2 w}{\partial x \partial y}\right) \qquad (3.6)$$

When subjected to a uniform compressive force N_x per unit length in the x direction, the harmonic equation becomes

$$\frac{\partial^4 w}{\partial x^4} + 2\frac{\partial^4 w}{\partial x^2 \partial y^2} + \frac{\partial^4 w}{\partial y^4} = -\frac{1}{D}\left(N_x \frac{\partial^2 w}{\partial x^2}\right) \qquad (3.7)$$

Any function f(x) can be defined by a Fourier series

$$f(x) = \frac{a_0}{2} + \sum_{n=1}^{\infty}\left(a_n \cos\frac{n\pi x}{L} + b_n \sin\frac{n\pi x}{L}\right)$$

For functions where the domain is $0 \le x \le L$, only the sine series is used.

$$\therefore f(x) = \frac{a_0}{2} + \sum_{n=1}^{\infty} b_n \sin \frac{n\pi x}{L} \tag{3.8}$$

where $b_n = \dfrac{1}{L} \displaystyle\int_{-L}^{L} f(x) \sin \frac{n\pi x}{L} \, dx = \dfrac{2}{L} \displaystyle\int_{0}^{L} f(x) \sin \frac{n\pi x}{L} \, dx$

From (3.8), for L=a,

$$w(x, y) = \sum_{m=1,2}^{\infty} W_m(y) \sin \frac{m\pi x}{a}$$

$$w(x, y) = \sum_{m=1,2}^{\infty} \left(\sum_{n=1,2}^{\infty} W_{mn} \sin \frac{n\pi y}{b} \right) \sin \frac{m\pi x}{a}$$

$$\therefore w(x, y) = \sum_{m}^{\infty} \sum_{n}^{\infty} \sin \frac{m\pi x}{a} \sin \frac{n\pi y}{b} \tag{3.9}$$

Substituting (3.9) in (3.7)

$$\frac{\partial^4}{\partial x^4} \sum_{m}^{\infty} \sum_{n}^{\infty} \sin \frac{m\pi x}{a} \sin \frac{n\pi y}{b} = \left(\sum_{m}^{\infty} \sum_{n}^{\infty} \sin \frac{n\pi y}{b} \right) \frac{\partial^4}{\partial x^4} \sin \frac{m\pi x}{a}$$

$$\frac{\partial^4}{\partial x^4} \sum_{m}^{\infty} \sum_{n}^{\infty} \sin \frac{m\pi x}{a} \sin \frac{n\pi y}{b} = \sum_{m} \sum_{n} \left(\frac{m\pi}{a} \right)^4 \sin \frac{n\pi y}{b} \sin \frac{m\pi x}{a}$$

Therefore, LHS of (3.7) is

$$\sum_{m} \sum_{n} \left[\left(\frac{m\pi}{a} \right)^4 + 2 \left(\frac{m\pi}{a} \right)^2 \left(\frac{n\pi}{b} \right)^2 + \left(\frac{n\pi}{b} \right)^4 \right] W_{mn} \sin \frac{n\pi y}{b} \sin \frac{m\pi x}{a} \tag{3.10}$$

Now, $\dfrac{\partial^2 w}{\partial x^2} = \left(\dfrac{m\pi}{a} \right)^2 \displaystyle\sum_{m} \sum_{n} W_{mn} \sin \frac{n\pi y}{b} \sin \frac{m\pi x}{a}$

Therefore, RHS of (3.7) is

$$\frac{1}{D} N_x \sum_{m} \sum_{n} \left(\frac{m\pi}{a} \right)^2 W_{mn} \sin \frac{m\pi x}{a} \sin \frac{n\pi y}{b} \tag{3.11}$$

Equating (3.10) and (3.11), we get

$$\left(\frac{m\pi}{a} \right)^4 + 2 \left(\frac{m\pi}{a} \right)^2 \left(\frac{n\pi}{b} \right)^2 + \left(\frac{n\pi}{b} \right)^4 = \frac{1}{D} N_x \left(\frac{m\pi}{a} \right)^2 \tag{3.12}$$

$$\therefore (N_x)_{cr} = D\frac{(m^2/a^2 + n^2/b^2)^2}{m^2/a^2} = \frac{\pi^2 Et^3}{12(1-\upsilon^2)}\left[\frac{m}{a} + \frac{a}{mb^2}\right]^2$$

$$= \frac{\pi^2 Et^3}{12b^2(1-\upsilon^2)}\left[\frac{mb}{a} + \frac{a}{mb}\right]^2$$

$$\text{Let } k_2 = \left[\frac{m}{a} + \frac{a}{mb^2}\right]^2 \text{ and } (N_x)_{cr} = (\sigma_x)_{cr}.t$$

(3.13)

$$\therefore (\sigma_x)_{cr} = k_2 \frac{\pi^2 E}{12(b/t)^2(1-\upsilon^2)}$$

(3.14)

Where,

$(N_x)_{cr}$ is the critical buckling load

$(\sigma_x)_{cr}$ is the critical buckling stress

Figure 22 shows a segment of a long plate having thickness 't' and length 'b'.
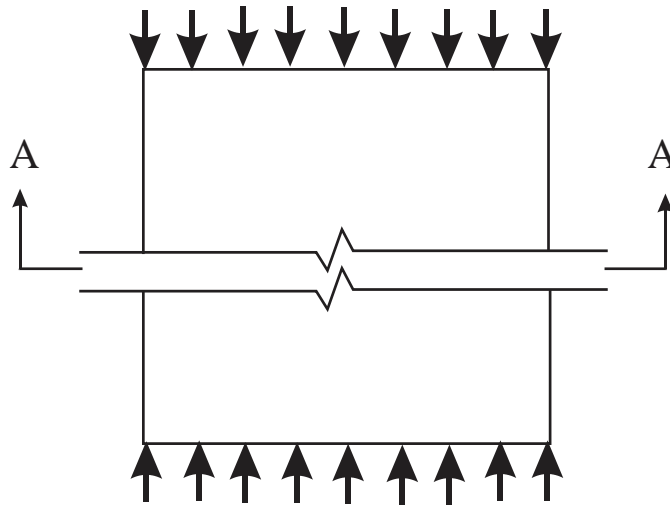
Figure 22: Segment of a long plate with thickness t and width b [37]

The local plate buckling co-efficient, k_2, for plate in compression at section A-A shown in Figure 22 with varied boundary conditions is given in Table 10.

Table 10: Local plate buckling co-efficient, k_2, for plates in compression with varied boundary conditions [37]

Case	Description of edge support	k_2	At Section A-A
1	Both edges simply supported	4.0	
2	One edge simply supported, the other fixed	5.42	
3	Both edges fixed	6.97	
4	One edge simply supported, the other free	0.425	
5	One edge fixed, the other free	1.277	

2.3 Rectangular Hollow Sections

- *Definition:*

Square Hollow Sections (SHS) and rectangular hollow sections (RHS), are types of hollow tubular sections that are widely used due to the recognition of the inherent aesthetic and structural advantages [38]. It is now well recognized that for thin-walled hollow section, the longitudinal residual stresses are in tension at outer surface and in compression at inner surface, and the distribution is assumed to be linear through the thickness [39]. These types of structural members are the fundamental constituents of the telescopic cantilever beams and the literature therefore is analyzed in detail in the following sub-sections.

2.3.1 Hollow under Axial Compression and Bending

Four types of tests: (a) four point bending tests (b) three point bending tests (c) axial compression tests and (d) combine loading tests are reported in this category.

Four Point Bending Tests: The papers involving the four point bending tests involve experimental investigations carried out on flexural behavior of specimens under pure bending brought about by four-point bending tests. Four-point bending tests involve placing a simply supported specimen at a set distance apart. Loading is applied at two loading points on the specimen at an equal distance around the center. The load is applied at a constant rate until the failure of the sample. Hollow sections of different shapes and sizes were investigated for their flexural behavior under four-point bending tests: Chen et al. [40] tested concrete filled stainless steel SHS and RHS tubes. Zhao and Bock [41]–[43], tested SHS and RHS stainless steel tubes under bending. Zhao and Young [44], tested normal strength and high strength steel SHS and RHS tubes. Zheng et al. [45] tested cold formed stainless steel CHS and RHS tubes. Huang and Young [46] tested SHS and RHS tubes cold rolled from flat plates of lean duplex stainless steel. In addition to SHS and RHS tubes, Theofanous et al. [47] also conducted experiments on I-section tubes. Typical data from these experimental tests showed ultimate moment, failure modes and bending moment-midspan deflection curves. Chen et al. [40] also showed overall deflection curves, strain distribution curves, and flexural stiffness obtained from the bending moment-midspan deflection curves. Typical bending moment versus midspan deflection curves show elastic stage, elasto-plastic stage, post-ultimate stage and unloading stage [40]. The failure mode in all these papers was local buckling. Zheng and Huang et al. [48], [49] developed Finite element models in ABAQUS and validated them using the experimental test data. In

Zhao and Huang et al. [42], [46] assigned S4R elements to the tube in the FE model and used a Riks analysis. Similarly, Zheng et al. [45], built an FE model using S9R5 elements and conducted an Eigen value analysis. Using the validated FE models, parameter studies were conducted to expand test data with different material properties and geometric parameters.

All these tests suggest appropriate design rules improvements for incorporation in steel design standards.

Three Point Bending Tests: In this section, papers highlight experimental investigations carried out on flexural behavior of specimens subjected to three-point bending tests. A three-point bend test consists of the specimen simply supported between rollers and the force applied to the top of the sample through a single point.

Theofanous and Bock et al. [50], [51] showed testing of lean duplex stainless steel SHS and RHS tubes. For the experiments, Theofanous et al. [50] rolled the SHS and RHS tubes into shape and welded them on the bottom flange. In addition to SHS and RHS tubes, Theofanous [47] also tested I-section austenitic and stainless steel tubes. Gardner et al. [52] also conducted tests on SHS, RHS and CHS cold formed stainless steel tubes.

Typical data from these experimental tests showed ultimate moment, failure modes and bending moment-rotation curves and bending moment-vertical displacement at mid-span. The failure mode in all these papers was local buckling.

Theofanous et al. [50] developed FE models in ABAQUS and validated the models using the test data. S4R elements were used in the model and analysis type was Riks analysis. Using the validated FE models, parameter studies were conducted to expand test data with different material properties and geometric parameters.

All these tests were conducted to assess design guidelines and suggest improvements or validate current codes.

Axial Compression Tests: In this section, long columns and stub columns were compressed to obtain cross-sectional load carrying capacity under pure compression.

Specimens tested included SHS and RHS tubes [41]–[43], [53]–[55], CHS tubes [52] and I-sections [47].

Typical test data acquired involved obtaining load-carrying capacity under pure compression and Load-end shortening curves. All specimens tested by Zhao et al. [41], failed by inelastic local buckling. Experimental tests conducted by Zhao, Block and Theofanous et al. [42], [51], [47] showed local buckling. Wang et al. [56], conducted experiments showing failure modes of local buckling, elephant-foot buckling and global buckling triggered by initial local buckling. Gardner [52] tests on columns with slender cross-sections first showed elastic buckling, then plastic buckling and then reached ultimate load at relatively small lateral deflections, whereas the columns with stocky cross-sections reached ultimate load at higher lateral deflections. Failure modes observed included overall flexural buckling and global local buckling interaction.

As explained for the four-point bending tests by Zhao et al. [42], FE models using S4R elements with the Riks analysis in ABAQUS were validated against test data and used further for parametric studies.

Again, load–deformation histories helped assess design guidelines.

Combined Loading: Combined loading involves testing specimens under uniaxial bending plus compression. To provide the bending moment, loading eccentricities were provided.

Zhao et al. [41], [42] and Arrayago [57], tested SHS and RHS tubes under combined loads. Failures modes involved in-plane bending and flexural buckling for all. The more slender sections displayed an additional local buckling. Results included load vs mid-height deflection curves [41] and load-end rotation curves [42].

Again, experimental data (deformation shape and load-mid height deflection curve) was used to validate FE model and the validated FE model used further for parametric studies [41].

Obtained results were used to prove improvements needed on existing standards.

Zhao et. al [58], reviewed the current beam-column design methods and established methodologies for overcoming the shortcomings by deriving new beam-column design proposals involving the derivation of new beam-column interaction factors resulting in improving capacity predictions. The reliability of the new proposals was confirmed by statistical analyses.

2.3.2 Hollow Sections under Transverse Compressive Loading

Reddy and Reid [59] report large deformations of circular metal tubes compressed between platens. Measured strain values and those predicted by the plastica theory were compared and the difference attributed mainly to strain hardening. An attempt to rectify the error was made unsuccessfully. They also introduce the concept of plastic hinges to determine collapse load. Sinha and Chitkara [60] report experiments on square rings to determined theoretically its plastic collapse load when compressed between rigid plates. They made assumptions: (1) the vertical members of the rings treated as columns subjected to axial loads (2) formation of plastic hinges at mid-points of the member arms and (3) constant co-efficient of friction between the

platens and rings. The accuracy of the developed theory diminished as the length of the ring increased and this was attributed to the deformation of the ring changing with the length. Gupta and Ray [61] analyzed the collapse of empty and filled square tubes laterally compressed between platens. They presented experimentally obtained load-compression curves and tube shape at various deformation stages. They considered plastic hinges formation for obtaining peak load and frictional force between platen and tube and equated slopes of webs and flanges for theoretical analysis. Gupta and Khullar [62] describe an improved analysis for collapse load of square and rectangular tubes, by considering the initial out of straightness of the arms and corner roundness of the sections. The results obtained compared well with the theory. They identified that eccentricities in loading caused by the corner radius and out-of-straightness resulted in large bending stresses at mid-height of the vertical arms compared to a direct compressive stress. Eccentricities caused the tubes to collapse at loads much lower than the buckling loads.

Gupta and Sinha [63], [64] describe plastic collapse of square and rectangular tubes laterally compressed between indenters experimentally. Gupta and Khullar [65], [66] investigated lateral compression of rectangular tubes placed compressed between orthogonally and non-orthogonally placed indenters. The load versus compression obtained was analysed in both these sets of papers. They considered stationary and rolling plastic hinges in their theoretical collapse load analysis the computed results and experiments were in agreement. Although the placements of indenters vary, these papers develop the theory to predict the collapse behavior based on experiments.

Gupta and Khullar [67] and Gupta and Sinha [68] describe experimental study of compression of square section tubes placed orthogonally in two and multiple layers

between platens. Load-compression curves were obtained and theoretical analysis based on stationary and travelling plastic hinges were carried out. The results were found to be in agreement.

Gupta et al [69] report an experimental and FE analysis study of SHS and RHS subjected to lateral quasi-static loading. They experimentally obtained deformed shapes, load-compression curves, energy-compression curves and compared FEA results. Again, plastic hinge formation was explained.

Lateral compression of hollow tubes allow for efficient energy absorption, and have hence been the subject of extensive research with respect to their plastic collapse and energy absorption capacity. While this group of papers concentrate on the analysis of tubes (square/ rectangular/ circular/ triangular) in the plastic area, the behavior of the RHS tubes is not detailed before the maximum load. Therefore, the theoretical developments shown in Chapter 4 concentrates on the behavior of the RHS tubes before the maximum load capacity is reached. The recommended theoretical analysis in this thesis is adapted from the 'collapse load of empty tubes' given by Gupta and Ray in [61].

2.3.3 Hollow Sections under Impact and Crushing Loads

In this section, the investigation of the crushing behavior of hollow tubes is studied. Tran and Ton [70] investigate the lateral crushing behavior of RHS and SHS tubes through experimental testing and theoretical analysis. A comparison between the two tube types show average crushing force of the RHS is smaller than that of the SHS. However, the crushing mechanism is identical. Experimental data obtained involves force–stroke curves and deformed shape of tubes. The average crushing force at each stage was done by using plastic hinge formation and deformed shape experimentally

obtained. Bambach, Liu and Jilin et al. [71]–[73] conducted experimental and analytical investigations of SHS beams subjected to static and transverse impacts at the beam mid-span. Here, elastic–plastic theoretical methods were developed to establish force–displacement and energy absorption relationships for hollow and concrete filled sections.

This section again highlights how experimental observations and data are used to formulate theoretical explanations and models. This method of using experimental observations to develop theoretical models is followed in this research and detailed in Chapter 4 of this thesis.

2.4 Finite Element Method

2.4.1 Introduction

Finite Element Method is a Numerical Method employed for Engineering Analysis and can be described in the following way [74], [75]:

Finite Element Method can be described as a method where (a) the Field Variables at the infinite number of points in a continuum is represented by those at a chosen finite number of points called nodes (b) their values are then calculated using some engineering principles and other governing relationships and (c) finally the values of the field variables at all intermediate points are calculated by interpolation using the shape functions.

2.4.2 Steps in FEA

Logan [75] describes that a typical analysis is made up of the following eight steps:

- Discretize and select the element types

This involves dividing the body into a system of finite elements with associated nodes and building the model based on choosing the most appropriate element type to represent the actual physical behavior. The element size should be small enough to give usable results yet large enough to reduce computational effort.

- Select a displacement function

This step involves choosing a displacement function within each element. Within each element, the function is defined using the nodal values of the element. Most often, linear, quadratic, and cubic polynomials are used and occasionally trigonometric series can be used. The FEM is one in which a continuous quantity (example: displacement), is approximated by a discrete model composed of piecewise-continuous functions defined within each finite element.

- Define the strain/displacement and stress/strain relationships

Strain/displacement and stress/strain relationships are necessary for deriving the equations for each finite element. The strain is derived from the displacements and the stresses are related to the strains through the stress/strain law – generally called the constitutive law.

- Derive the element stiffness matrix and equations

The following methods are used to derive the element stiffness matrix and equations:

- o Direct equilibrium Method:

Force equilibrium conditions for a basic element, along with force/deformation relationships are used to obtain the stiffness matrix and element equations relating

nodal forces to nodal displacements. This method is used for one-dimensional elements.

    o   Work or Energy methods:

For two-and-three dimensional elements, it is much easier to apply a work or energy method to develop the stiffness matrix. The principle of virtual work, the principle of minimum potential energy, and Castigliano's theorem are methods frequently used for the derivation of element equations. All three principles yield similar element equations for linear-elastic materials; thus the choice of method is a matter of convenience.

    o   Methods of Weighted Residuals:

These methods allow the FEM to be applied directly to any differential equation. Galerkin's method is the most popular of these methods. The Galerkin Method is useful for solving differential equations in solid mechanics, fluid mechanics, heat flow and electrical engineering [76]. These methods yield equations to describe the behaviour of an element which are written in a matrix form as

$$\{f\} = [k]\{d\} \tag{3.15}$$

where $\{f\}$ is a vector of element nodal forces, $[k]$ is the element stiffness matrix and $\{d\}$ is the vector of unknown element nodal degrees of freedom or generalised displacements, n. Here, generalised displacements may include such quantities as actual displacements, slopes or even curvatures.

- Assemble the element equations to obtain the global or total equations and introduce the boundary conditions

In this step, the individual element nodal equilibrium equation generated previously are assembled the global nodal equilibrium equation written in the matrix form as

$$\{F\} = [K]\{d\} \qquad\qquad (3.16)$$

where $\{F\}$ is a vector of global nodal forces, $[K]$ is the structure global stiffness matrix and $\{d\}$ is the vector of known and unknown structure nodal degrees of freedom or generalised displacements.

The global stiffness matrix $[K]$ is a singular matrix. To remove the singularity problem, the boundary conditions are invoked so that the structure remains in place.

- Solve the unknown degrees of freedom

After modifying the global nodal equation for the boundary conditions, the equations can now be solved for the d's by using an elimination method such as Gauss's method.

- Solve for the element strains and stresses

Typical relationships between strain and displacements can be used to determine secondary quantities of strain and stress (or moment and shear force) in terms of the displacements determined in the previous step.

- Interpret the results

The final goal is to interpret and analyze the results for use in the design/analysis process. Postprocessor computer programs help the user to interpret the results by displaying them in graphical form.

2.4.3 Types of Analyses

- Static Stress Analysis

A static stress analysis does not depend on time and is used when inertia effects can be neglected. It can be linear or nonlinear.

In a linear static analysis displacements, strains, stresses, and reaction forces under the effect of applied loads are calculated. Here, the relationship between the load applied to an object and the response of the object is linear.

Nonlinearities can arise from large-displacement effects, material nonlinearity, and/or boundary nonlinearities such as contact and friction and must be accounted for. These non-linearities are accounted for in a non-linear static stress analysis.

- Eigen Value Analysis for buckling

Eigenvalue buckling is generally used to estimate the critical buckling loads of stiff structures (classical eigenvalue buckling) [77]. The response of stiff structures usually involves very little deformation prior to buckling. A simple example of a stiff structure is the Euler column, which responds very stiffly to a compressive axial load until a critical load is reached, when it bends suddenly and exhibits a much lower stiffness. Thus, for example, when minimizing weight of the telescopic beam structure used as a lift and reach device, its stiffness and load carrying capacity are to be preserved [78]. Even when the response of a structure is nonlinear before collapse, a general eigenvalue buckling analysis can provide useful estimates of collapse mode shapes.

An incremental loading pattern, Q^N, is defined in the eigenvalue buckling prediction step. The magnitude of this loading is not important; it is scaled by the load multipliers, λ_i, found in the eigenvalue problem [77]:

$$\left(K_0^{NM} + \lambda_i K_\Delta^{NM}\right)\upsilon_i^M = 0 \qquad (3.17)$$

where,

K_0^{NM} is the stiffness matrix corresponding to the base state, which includes the effects of the preloads (if any)

K_Δ^{NM} is the differential initial stress and load stiffness matrix due to the incremental loading pattern

λ_i are the eigenvalues

υ_i^M are the buckling mode shapes (eigenvectors)

M and N   refer to degrees of freedom M and N of the whole model

i refers to the ith buckling mode

The critical buckling loads are then

$$P^N + \lambda_i Q^N \qquad (3.18)$$

Normally, the lowest value of λ_i is of interest.

The buckling mode shapes, υ_i^M, are normalized vectors and do not represent actual magnitudes of deformation at critical load. The buckling mode shapes are often the most useful outcome of the eigenvalue analysis, since they predict the likely failure mode of the structure [77].

- Riks Analysis

Obtaining nonlinear static equilibrium solutions for unstable problems is often necessary, where during periods of the load displacement response, the load and/or the displacement may decrease as the solution evolves. The modified Riks method used in ABAQUS is an algorithm that allows effective solution of such cases.

In this method, the solution is viewed as the discovery of a single equilibrium path in a space defined by the nodal variables and the loading parameter. The basic

algorithm is the Newton method; therefore, at any time there will be a finite radius of convergence. Further, many of the materials (and possibly loadings) of interest will have path-dependent response. For these reasons, it is essential to limit the increment size.

In the modified Riks algorithm, as it is implemented in ABAQUS, the increment size is limited by moving a given distance (determined by the automatic incrementation algorithm) along the tangent line to the current solution point and then searching for equilibrium in the plane that passes through the point thus obtained and that is orthogonal to the same tangent line [77].

The Riks method uses the load magnitude as an additional unknown; it solves simultaneously for loads and displacements. Therefore, another quantity must be used to measure the progress of the solution; ABAQUS uses the "arc length," l, along the static equilibrium path in load-displacement space.

If the Riks step is a continuation of a previous history, any loads that exist at the beginning of the step and are not redefined are treated as "dead" loads with constant magnitude. A load whose magnitude is defined in the Riks step is referred to as a "reference" load. All prescribed loads are ramped from the initial (dead load) value to the reference values specified.

The loading during a Riks step is always proportional. The current load magnitude, P_{total}, is defined by:

$$P_{total} = P_0 + \lambda_p (P_{ref} - P_0) \tag{3.19}$$

where P_0 is the "dead load", P_{ref} is the reference load vector, and λ_p is the "load proportionality factor." The load proportionality factor is found as part of the solution.

2.4.4 FEA Applications

The FEM can be used to analyse both structural and non-structural problems. Typical structural areas include:

- Stress analysis

- Buckling

- Vibration Analysis

Non-structural problems include:

- Heat transfer

- Fluid flow

- Distribution of electric or magnetic potential

Biomechanical engineering problems typically include stress analyses of human spine, skull, heart, eye etc.

2.4.5 Key Points in Preparing for an FEA

- Mesh Density and Partitioning

The mesh density should be small enough to give usable results yet large enough to reduce computational effort.

Partitioning divides part instances into smaller regions. Partitioning gives greater control over mesh generation – it allows for assigning different mesh sizes and mesh elements on different areas on the same part instance.

Without partitions, the mesh is aligned only along the exterior edges; with partitions, the resulting mesh will have rows or grids of elements aligned along the partitions i.e., the mesh "flows" along the partitions.

- Element Type

The wide range of elements in the ABAQUS element library provides flexibility in modelling different geometries and structures. Each element is characterized by the following:

  o Family

A family of finite elements is the broadest category used to classify elements. Elements in the same family share many basic features. There are many variations within a family.

  o Degree of freedom

An element's number of nodes determines how the nodal degrees of freedom will be interpolated over the domain of the element. ABAQUS includes elements with both first and second-order interpolation

  o Number of nodes

The primary variables that exist at the nodes of an element are the degrees of freedom in the finite element analysis. Examples of degrees of freedom are displacements, rotations, temperature, electrical potential

  o Formulation

This describes the mathematical theory used to define the element's behaviour.

  o Integration

The stiffness and mass of an element are calculated numerically at sampling points called "integration points" within the element. The numerical algorithm used to

integrate these variables influences how an element behaves. ABAQUS includes elements with both "full" and "reduced" integration.

Reduced integration uses a lesser number of Gaussian co-ordinates when solving the integral. The more Gaussian co-ordinates for each element, the more accurate the answer, but the higher the cost of computation time.

Using reduced integration reduces the time to run the analysis but it could have a significant effect on the accuracy of the element for a given problem. The use of fewer integration points produce a less stiff element. Therefore, in some cases, particularly non-linear problems, it is advisable to use reduced integration instead of full integration. The slight loss of accuracy is counteracted by the improvement in approximation to real-life behavior [79]

- Boundary Conditions

Boundary conditions are applied to those regions of the model where the displacements and/or rotations are known. Boundary conditions are step dependent; the step or steps in which they become active must be specified.

- Load Application

In ABAQUS the term load refers to anything that induces a change in the response of a structure from its initial state, including concentrated forces, pressures, nonzero boundary conditions, body loads, and temperature.

- Interactions

Interactions are step-dependent objects. ABAQUS does not recognize mechanical contact between part instances or regions of an assembly unless that contact is specified in the Interaction module; the mere physical proximity of two surfaces in an assembly is not enough to indicate any type of interaction between the

surfaces. Interaction module defines contact interactions, tie constraints, coupling constraints etc.

- Obtaining and Interpreting Results

Graphical postprocessing is important because of the great volume of data created during a simulation. The Visualization module of ABAQUS/CAE allows the viewer to view the results graphically using a variety of methods, including deformed shape plots, contour plots, vector plots, animations, and X–Y plots.

2.4.6 Riks Analysis in ABAQUS – A Detailed Example

Consider the example of a rectangular hollow section (RHS) compressed between wearpads as shown in Figure 23 below. A Riks analysis is carried out to calculate the maximum load carrying capacity of the RHS. As an input, a displacement is applied at the reference point RP-1. Since the displacement is compressive, its value is negative.
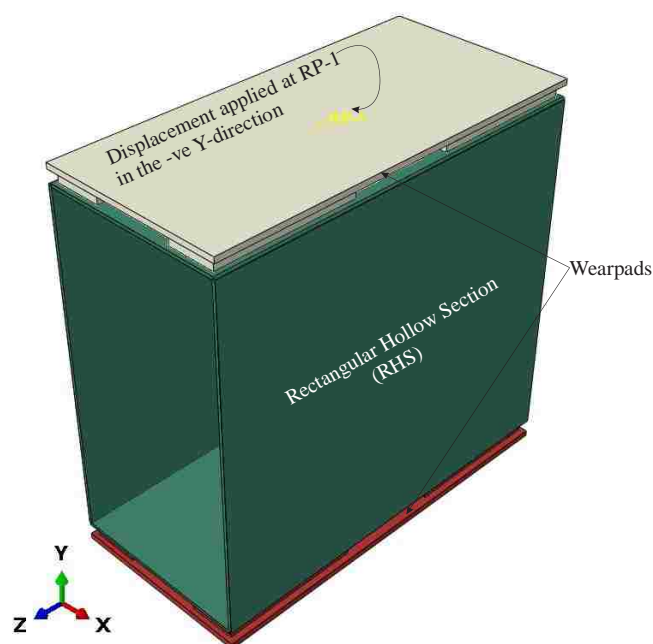
Figure 23: RHS assembly and loading pattern

In the Riks step, the following inputs are to be given:

- An initial increment in arc length, Δl_{in}

- The total arc length scale factor, l_{period}

- The minimum and maximum arc length increments, Δl_{min} and Δl_{max}

- Maximum number of increments

- Stopping criteria
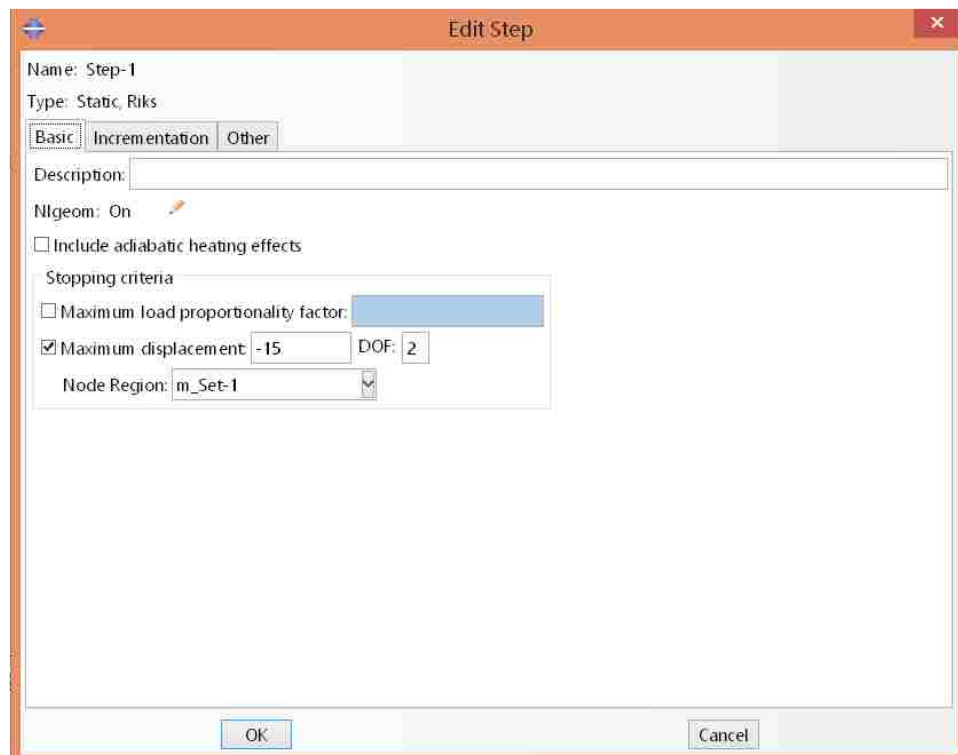
Figure 24: Riks step - basic tab
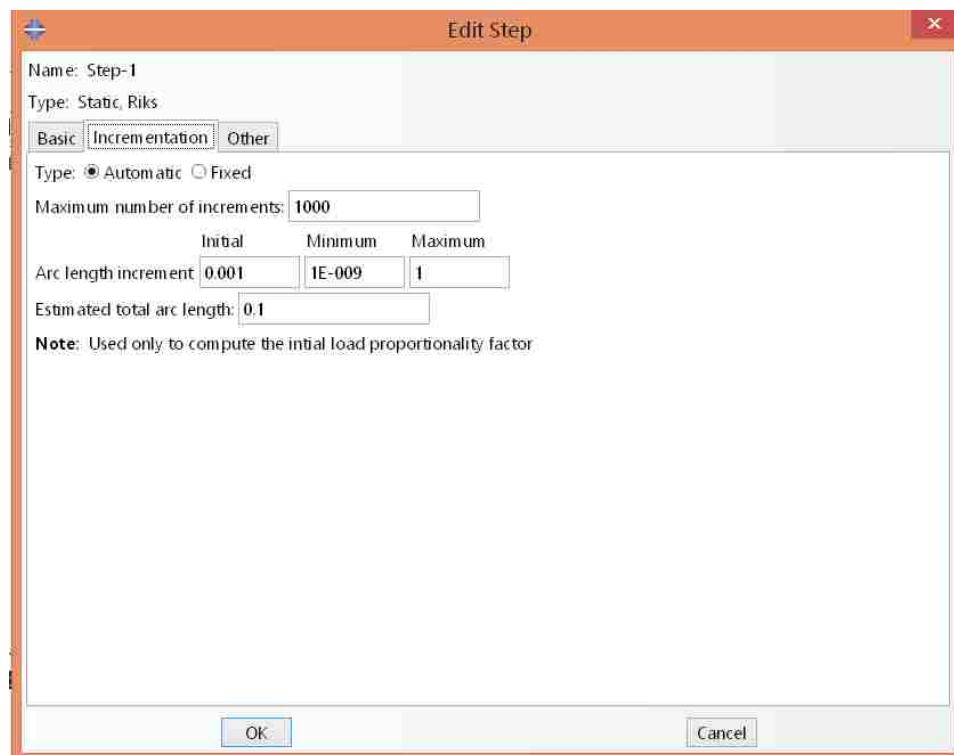
Figure 25: Riks step - incrementation tab

From the initial increment in arc length, Δl_{in}, provided, the initial load proportionality factor, $\Delta\lambda_{in}$, is computed as [80]:

$$\Delta\lambda_{in} = \frac{\Delta l_{in}}{l_{period}} \tag{3.20}$$

where l_{period} is a user-specified total arc length scale factor (typically set equal to 1). The value of $\Delta\lambda_{in}$ is used during the first iteration of a Riks step. For subsequent iterations and increments the value of λ is computed automatically. The value of λ is part of the solution. Minimum and maximum arc length increments, Δl_{min} and Δl_{max}, can be used to control the automatic incrementation. Direct user control of the increment size is also provided; in this case the incremental arc length, Δl, is kept constant. The increment tab in the Riks step is shown Figure 25.

Since the loading magnitude is part of the solution, a method needs to be specified when the step is completed. A maximum value of the load proportionality factor, λ_{end}, or a maximum displacement value at a specified degree of freedom can be used as a stopping critereon. The step will terminate when either value is crossed. If neither of these finishing conditions is specified, the analysis will continue for the number of increments specified in the step definition.

The stopping criteria shown in Figure 24 shows that the analysis will stop if a displacement of -15 in the 2-DOF i.e Y-direction, is reached at the m-set-1 node (defined as RP-1 in model assembly).

2.5 Experimental Design

Product design has the greatest impact on product quality. It is essential to consider all aspects of design (including factors built into the product) that affect the deviation of functional characteristics of the product from target values [81]. When the goal is to design a product (or process) with high stability, parameter design is the most important step [82]. Parameter Design helps ascertain the optimal levels for the parameters of each element in the system so that the functional deviations of the product are minimized [81]. The major usefulness of experimental design in finding the optimal combination of parameter values [82].

Planning and implementation of experiments can be broken down into the seven step procedure shown [83]:

- State Objective: The objective of the experiment needs to be clearly stated. In a work environment, all stakeholders should provide input.
- Choose Response: The response is the experimental outcome or observation. There may be multiple responses in an experiment. The

response should be chosen to increase the understanding of the mechanisms and physical laws involved in the problem

- Choose Factors and Levels: A factor is a variable that is studied in the experiment. In order to study the effect of a factor on the response, two or more values of the factor are used. These values are referred to as levels or settings. A treatment is a combination of factor levels. In choosing factors and levels, cost and practical constraints must be considered.

- Choose experimental Plan: Use the fundamental principles to enable suitable choice of the experimental plan.

- Perform Experiment: The use of a planning matrix is recommended. The matrix describes the experimental plan in terms of actual values or settings of the factors.

- Analyze data: An analysis appropriate for the design used to collect the data needs to be carried out. This includes model fitting and assessment of the model assumptions through an analysis of residuals.

- Draw conclusions and Make Recommendations: Based on the data analysis, conclusions are presented which include the important factors and a model for the response in terms of important factors. Recommended settings or levels for the important factors may also be given. The conclusions should refer back to the stated objectives of the experiment. A confirmation experiment is worthwhile, to conform the recommended settings.

2.5.1 Screening Experiments

In any experimental investigation, one may find that there can be many factors that can contribute to a specific structural phenomena/ behavior. To segregate the

influencing from the less influencing factors, it would be better to conduct a small experiment for a particular response/ output. Such designs/ experiments determine which factors are essential for making improvements [84]. Such designs involve sifting through a large number of potentially important factors to search, as economically and effectively as possible, for the few active/ influencing factors [85]. When the objective of the experiment is factor screening, the number of factor levels is kept low.

Generally, two levels work very well in factor screening studies [84],[85]. In classical screening, knowledge gained from a main effects design can be improved by investigating, in a second stage of experimentation, interaction between factors whose main effects are identified as important at the first stage [86]. The main effect of a certain factor, is the mean of the effect by that factor on the experimental values, taken over the various levels of the other factors [87]. An interaction between factor A and factor B exists, when the effect of A (on the response) differs according to the levels of B, or in other words, when the effect of one factor (on the response) depends upon the value of the other [87].

In a factor screening situation, it is more important not to exclude an active factor than it is to conclude that inactive factors are important [84].

Taguchi's orthogonal L_{12} array [88] is widely used for screening experiments [89], [90]. Orthogonal array is only one way of planning for DOE, yet the most flexible to conduct and easy for non-statistically oriented engineers to execute in practice [21]. An orthogonal array provides a balanced set of experimentation runs such that the conclusions are drawn in a balanced fashion [91]. In Table 11, the numbers 1 to 12 are called experiment runs or numbers [92]. Each vertical column of the array contains six 1s and six 2s. The 1s and 2s represent the coded levels for each

factor. For a given experiment, in any two columns there are four possible combinations: (1,1),(1,2),(2,1),(2,2) If each of these four combinations appears the same number of times in a pair of columns, the columns are said to be balanced or orthogonal [82]. The L_{12} design is among a group of specially designed arrays in which interactions are distributed more or less uniformly to all columns; making it possible to focus on main effects and therefore increase the efficiency and reproducibility of small scale experimentation [87]. Eleven main effects can be studied using this design. The array is given in Table 11.

Table 11: Orthogonal L_{12} array

Run	Factors										
	1	2	3	4	5	6	7	8	9	10	11
1	1	1	1	1	1	1	1	1	1	1	1
2	1	1	1	1	1	2	2	2	2	2	2
3	1	1	2	2	2	1	1	1	2	2	2
4	1	2	1	2	2	1	2	2	1	1	2
5	1	2	2	1	2	2	1	2	1	2	1
6	1	2	2	2	1	2	2	1	2	1	1
7	2	1	2	2	1	1	2	2	1	2	1
8	2	1	2	1	2	2	2	1	1	1	2
9	2	1	1	2	2	2	1	2	2	1	1
10	2	2	2	1	1	1	1	2	2	1	2
11	2	2	1	2	1	2	1	1	1	2	2
12	2	2	1	1	2	1	2	1	2	2	1

Experimental design according to Taguchi has one prerequisite: not all interaction of factors need to be recognize and analysed. If complete relationships are needed, a full factorial experiment is necessary [93].

Once the active factors are identified from the analysis of the screening experiment results, an in-depth investigation is carried out.

2.5.2 Response Surface Methodology

Response surface methodology, or RSM, is a collection of mathematical and statistical techniques useful for the modeling and analysis of problems in which a response of interest is influenced by several variables and the objective is to optimize this response [94]. In a RSM, unlike in screening experiments, in order to assess curvature (non-linear effects) for a particular factor, it is necessary to study more than two levels of the factor [87].

According to Myers and Montgomery [95] Response Surface Methodology (RSM) consists of the following:

- Experimental strategy for exploring the space of the process or independent variables

- Empirical statistical modelling to develop an appropriate approximating relationship between the yield and the process variables and

- Optimization methods for finding the levels or values of the process variables that produce the desirable values of the response.

In simple terms, the response surface is an approximate mathematical model of the response or yield in terms of the active factors identified in the screening experiment. Thus, the response surface can be represented by the model:

$$\eta = f(x_1, x_2 \ldots \ldots \ldots \ldots x_n) \tag{3.21}$$

where η is the response and $(x_1, x_2 \ldots \ldots \ldots x_n)$ are active or influencing factors from the screening experiment.

A second order model is widely used in RSM for several reasons [95]. A general second order model takes the form

$$\eta = \beta_0 + \sum_{j=1}^{k} \beta_j x_j + \sum_{j=1}^{k} \beta_{jj} x_j^2 + \sum \sum_{i<j} \beta_{ij} x_i x_j \qquad (3.22)$$

Finding the values for the βs is called the building of the model. The model is built using an experimental design and the response values obtained by carrying out the experiment. Any prediction made from the polynomial about the response outside the region should be verified by experiments before putting reliance on it [96].

Quadratic polynomials in n variables have $(n+1)(n+2)/2$ coefficients. To fit quadratic response surfaces at least that many points are needed and each factor should have at least three levels. For example, a quadratic polynomial in 6 variables has 24 coefficients. But a three level full factorial design would have 3^6 = 729 runs or trials which is unaffordable. Central composite design is a popular compromise which reduces the number of experiments to close to the 2-level full factorial design.

The central composite design is composed of the 2^n points of the full-factorial two-level design, with all the variables at their extremes, plus a number of repetitions of the nominal design (center point), plus the 2n axial points obtained by changing one design variable at a time by an amount α. Thus, if two variables are considered, the central composite design can be visualized as shown in the planar in Figure 26. The vertices of the square show the runs in the factorial design (2^2=4). The center points are repeated a certain number of times (in this case 2 times). The axial points are generated by changing one factor in the center point along each axis.
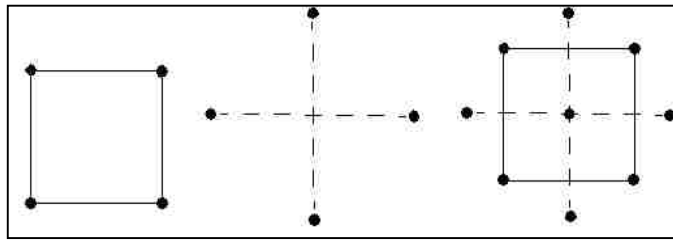
Figure 26: Standard central composite design for two variables

Let the two levels of the factorial design be coded with +1 and -1. Then the full factorial design can be given in the following way:

$$\begin{bmatrix} \text{Factor 1} & \text{Factor 2} \\ -1 & -1 \\ -1 & 1 \\ 1 & -1 \\ 1 & 1 \end{bmatrix}$$

The center point for this design is $\begin{bmatrix} \dfrac{-1+1}{1} & \dfrac{-1+1}{2} \end{bmatrix} = \begin{bmatrix} 0 & 0 \end{bmatrix}$

The axial or star points are developed by changing one factor at a time in the center point and thus the points are $[(\alpha,0),(-\alpha,0),(0,\alpha),(0,-\alpha)]$. Putting it all together the standard design is obtained in the following way where α is assumed to be 1.414. The full design will look like the following:

$$\begin{bmatrix} \text{Factor 1} & \text{Factor 2} \\ -1 & -1 \\ -1 & 1 \\ 1 & -1 \\ 1 & 1 \\ 1.414 & 0 \\ -1.414 & 0 \\ 0 & 1.414 \\ 0 & -1.414 \\ 0 & 0 \\ 0 & 0 \end{bmatrix}$$

Chapter 3: Exploratory FEA and Experiments

This chapter describes the exploratory analyses carried out on a telescopic cantilever beam and the experimental work carried out on RHS rings and RHS pieces. The results obtained here and the findings from the literature survey formed the basis for the theoretical developments explained in Chapter 4.

3.1 Exploratory FEA

In this section, a candidate telescope shown in Figure 27 was analyzed and the results were compared with those obtained from theoretical calculations.
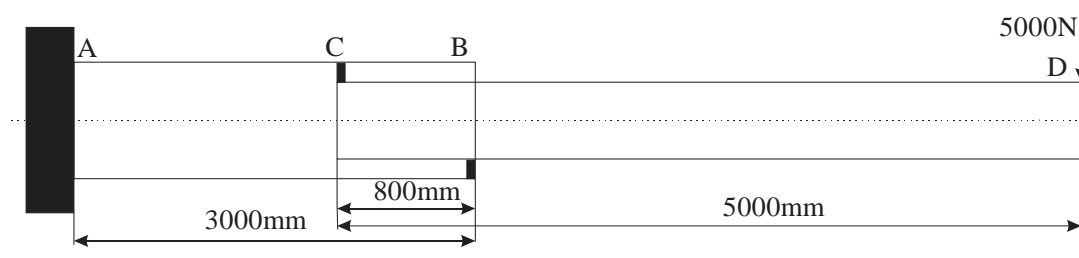
Figure 27: Candidate telescopic beam assembly

The inner beam is made up of a 3 mm thick RHS beam with the outside cross section of 350 mm height and 150 mm width. The two beams are separated by two sets of two wearpads each with a dimension of 10 mm height, 25 mm width and 50 mm length. The outer beam is also made up of a 3 mm thick RHS beam with an inside cross section of 370 mm height and 170 mm width.

An FE model was built for a static analysis in ABAQUS to represent the assembly shown in Figure 27. As the behavior of the inner beam is the area of interest, only the inner beam was modelled and analyzed. The effect of the outer beam however was accounted for by the boundary conditions applied on the inner beam assembly.

Details of the study are described in the following three sub-sections for easy comprehension.

3.1.1 Modelling and Analysis

The inner beam assembly, consisting of four wearpads and the inner beam, is subjected to a linear static analysis using ABAQUS Standard Version 2017. The assembly is shown in Figure 28.

- Assembly Details – The interactions are modelled in the following way:

  o Top surface of top wearpads - Encastred, completely arresting any movement of these surfaces of the wearpads.

  o Bottom surface of top wearpads - Stuck to the inner beam thereby warrantying a tie constraint between the bottom face of the top wearpads and the top surface of the inner beam.

  o Top of bottom wearpads - Frictional interaction is assigned between the top of bottom wearpads and the bottom surface of the inner beam.

  o Bottom surface of bottom wearpads - Encastred, completely arresting any movement of these surfaces of the wearpads.

  Figure 29 illustrates the above interactions.
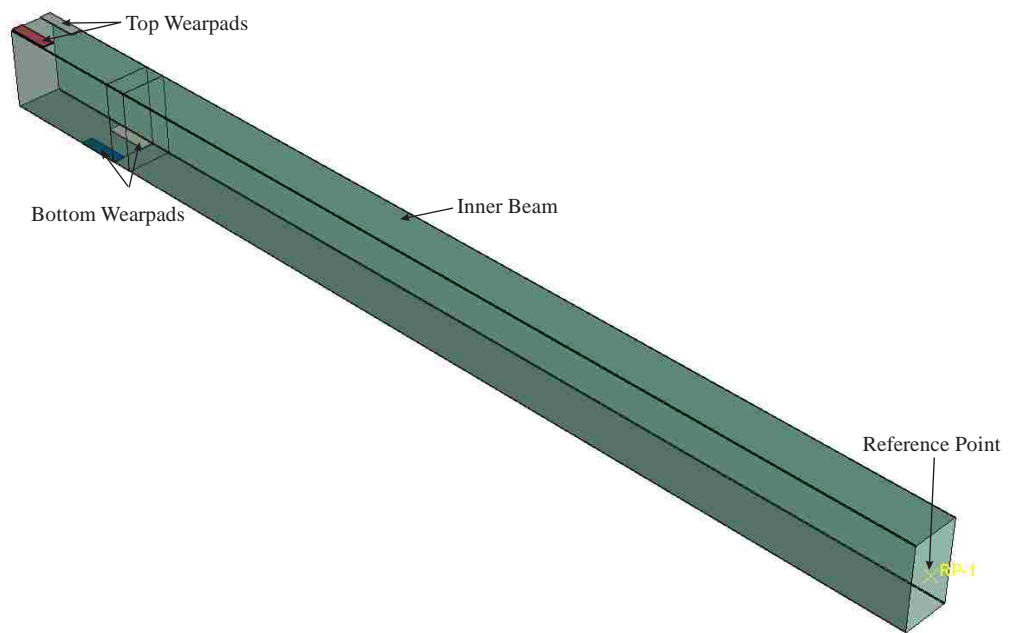
Figure 28: Inner beam assembly
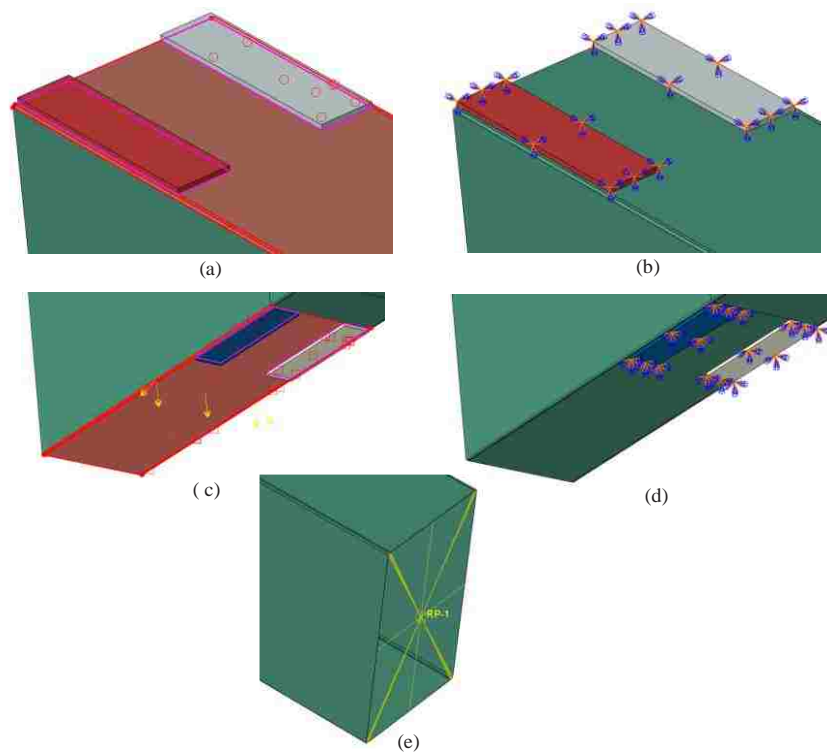
Figure 29: (a) Inner beam-top wearpad frictional interaction (b) Top wearpad encastre (c) Inner beam-bottom wearpad frictional interaction (d) Bottom wearpad encastre (e) reference point coupling with inner beam tip

- For a finer analysis, three partitions have been created in the vicinity of the wearpads.

  o Overlap Partition – the overlap partition is aimed to make sure that the bottom wearpads are located at a specific overlap distance and that a mesh is present at the overlap distance.

  o Distance partition – This is located at a distance of 30 mm from the top flange of the inner beam so that a mesh is created at this distance allowing for stresses to be extracted at this exact distance. By changing the distance value, a partition and hence mesh can be created at any particular distance.

  o Mesh size partition – ''Mesh Size partition' is located at a distance of 200 mm from the overlap partition. As the overlap area is considered critical, the inner beam in the overlap area and in its vicinity upto the mesh partition is assigned a finer mesh of 5 mm. The remaining length of the beam beyond this partition is deemed non-critical and a larger mesh size of 10 mm is assigned.

Figure 30 shows an exploded view of the inner beam to illustrate the partitions.
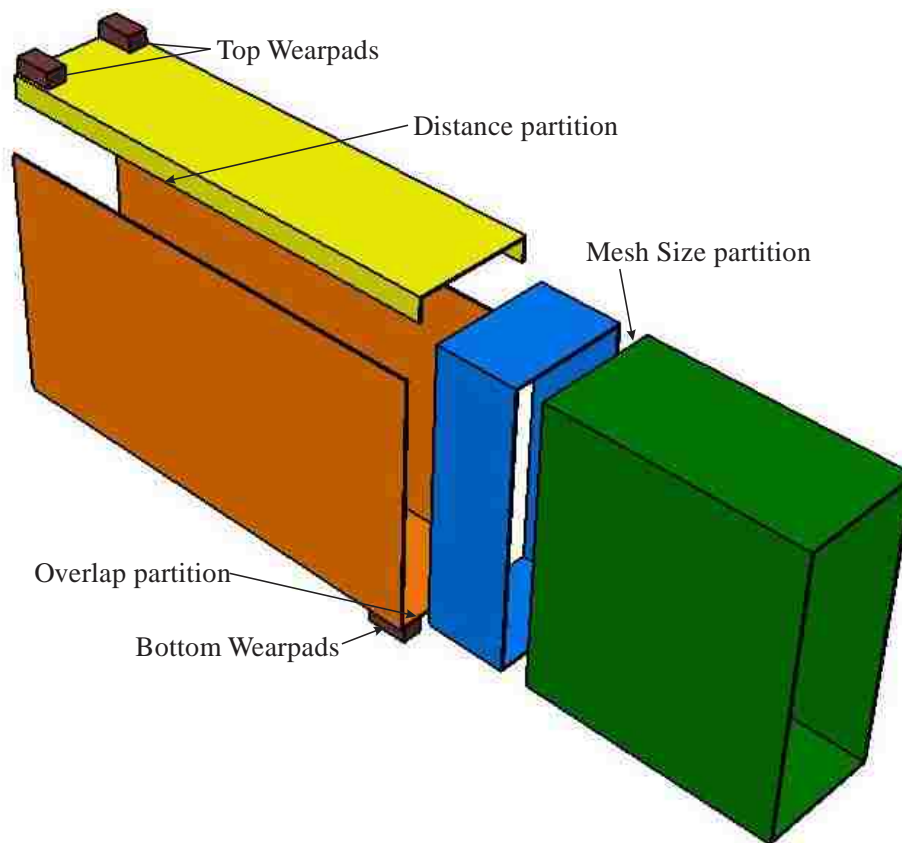
Figure 30: Partitions in the inner beam

Reference point - The reference point RP-1 is located at the center of the free end of the inner beam for load application. RP-1 was kinematically coupled with the nodes of the outermost cross-section of the inner beam allowing for uniform application of the load at the tip of the inner beam.

Figure 31 illustrates the reference point and the mesh sizes.
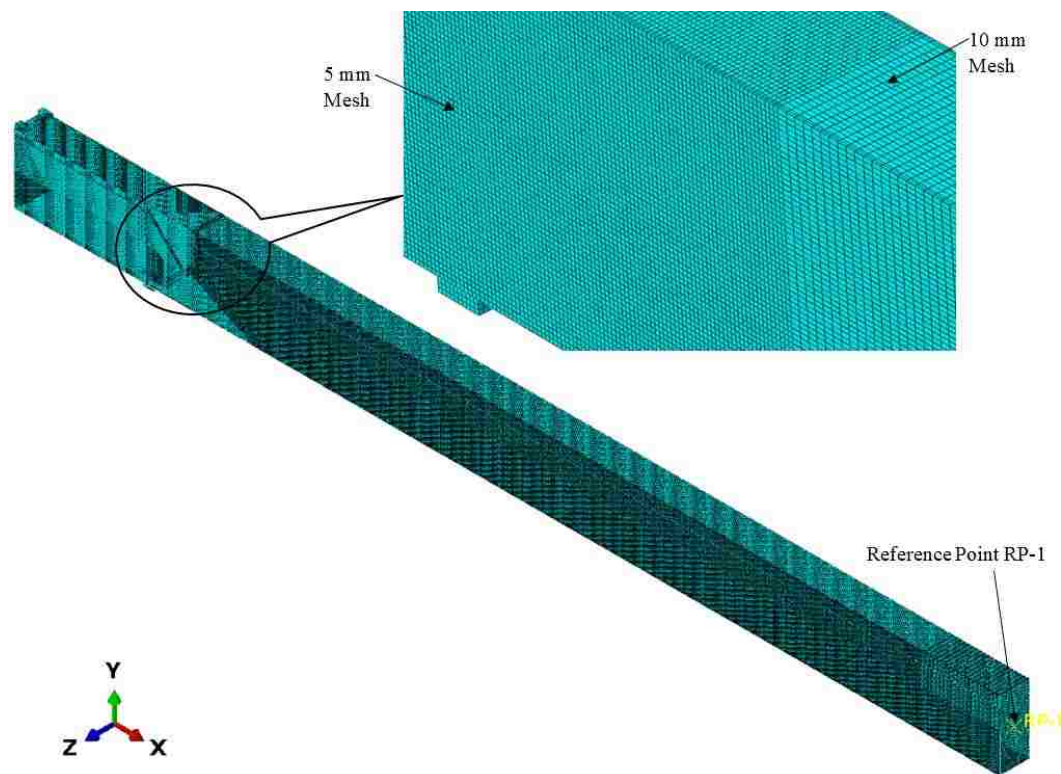
Figure 31: Reference point on candidate inner beam assembly of telescope

- Mesh size and elements

The wearpads were assigned the solid element C3D8R and the beam was assigned the shell element S4R. The S4R element is a general purpose element, with reduced integration [97]. Due to the reduced integration, the locking phenomenon observed in the S4R element does not show. However, due to the reduced integration, the element tends not to be stiff enough in bending.

A mesh analysis was carried out to determine an acceptable mesh size. It resulted in determining a size of 5 mm for the wearpads. For the inner beam, in the overlap area upto the mesh partition, a 5 mm mesh size was found to be suitable, whereas for the remaining length of the beam a 10 mm mesh size was assigned (Refer Figure 31).

- Material Properties

All the parts were assigned the same material, mild steel with a density of 7.89E-09 tonne/ mm^3, Young's Modulus E=210,000 N/mm^2, and Poisson's ratio 0.3.

To represent the elasto-plastic behavior of the material, yield stress values along with the corresponding plastic strain values are given. The initial yield stress is 300 MPa, and the yield stress increases to 400 MPa at a plastic strain of 35%, after which it is perfectly plastic. This defines an elastic-plastic material model.

The plastic properties entered in ABAQUS are given in Table 12.

Table 12: Elasto-plastic properties

True Stress (MPa)	True Plastic strain
300	0.0
350	0.025
375	0.1
394	0.2
400	0.35

- Loading

Tip load applied at RP-1. For the purpose of simplicity, self-weight is not considered in the FE model.

Figure 32 represent the FBD, SFD and BMD for the inner beam assembly of 5000 mm length and 800 mm overlap. At B, the SFD shows that the reaction force R_B = 33,166.6 N and the BMD shows moment M_B = 21,125,000 N-mm. Figure 32 shows that the shear force and the moment are the highest at B (underneath the bottom wearpads).
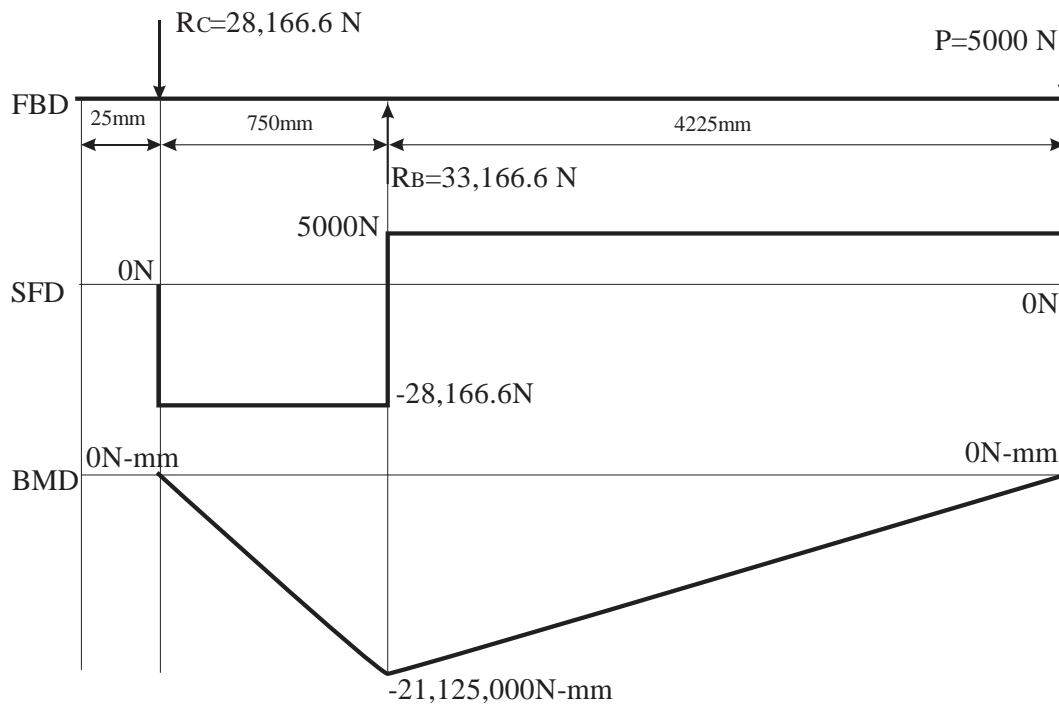
Figure 32: Inner beam without self-weight

The shear flow caused by the compressive force R_B is shown in Figure 36 and highlights the maximum shear stress appears at the center of the web of the section. However, the behavior of the web is also influenced by the bending stress caused by the tip-load and the bending stresses caused by the corner moments. These additional stresses will cause the web of the section to show non-uniform deformation as shown in Figure 40(b).

The shear stress calculation of the inner beam under the bottom wearpads is given below. The cross-section of the beam for which the shear stress is calculated is shown in Figure 33.
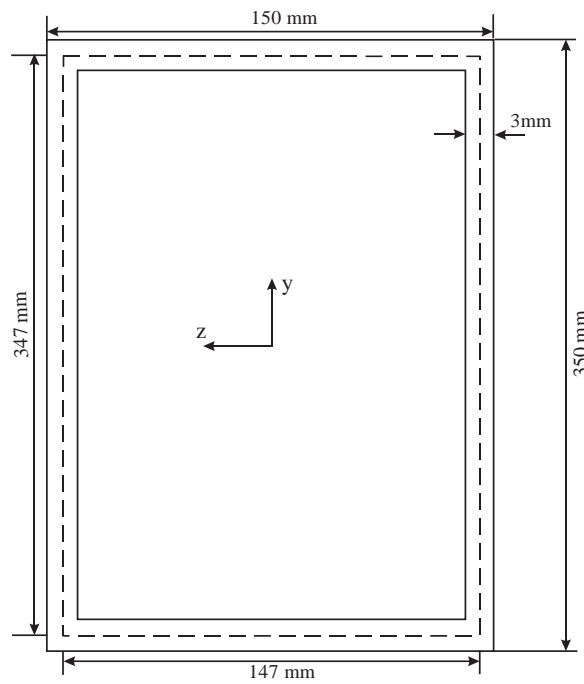
Figure 33: Cross-section of the telescopic beam

For a thin-walled section, the shear stress is given by:

Shear Stress $\tau = \dfrac{VQ}{I(2t)}$

From Figure 32, for a tip load of 5000N, the shear force V = 33,166.6 N at the section of the inner beam under the bottom wearpads.

For the inner beam,

$$I_{yy} = \frac{1}{12}\left[bh^3 - b_1 h_1^3\right]$$
$$= \frac{1}{12}\left[(150 \times 350^3) - (144 \times 344^3)\right]$$
$$= 47,446,492 mm^4$$

Shear stress distribution in the top flange:
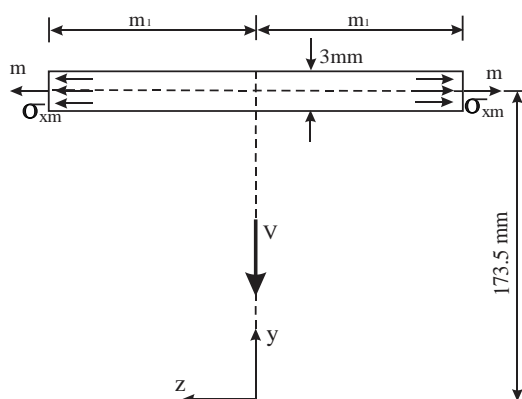
Figure 34: Symmetrical double cut to determine shear stresses in the flange

From Figure 34, the first moment of area 'Q' for the flange is calculated as:

$$Q = 2 \times m_1 \times 3 \times 173.5$$
$$= 1041 m_1 \ mm^3$$

At the top flange $\tau_{(TopFlange)} = \dfrac{33,166.6 \times 1041 m_1}{47,44,492 \times 2 \times 3} = 0.1213 m_1 \ N/mm^2$

This is a linear distribution. All shear stresses act in the positive m direction.

A number of values:

$$m_1 = 0; \tau_{(TopFlange)} = 0$$
$$m_1 = 73.5 mm; \tau_{(TopFlange)} = 8.91 N/mm^2$$

Shear stress distribution in the webs:
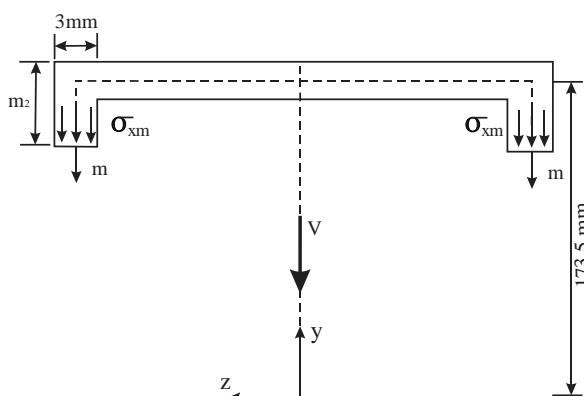
Figure 35: Symmetrical double-cut for determining shear stresses in the webs of the section

From Figure 35, the first moment of area 'Q' for the webs are calculated as:

$$Q = (173.5 \times 3 \times 147) + (2 \times 3 \times m_2 \times (173.5 - m_2/2))$$
$$= 76513.5 + 1041m_2 - 3m_2^2$$

At the top flange $\tau_{(TopFlange)} = -\dfrac{33,166.6 \times (76513.5 + 1041m_2 - 3m_2^2)}{47,44,492 \times 2 \times 3}$

$$= -8.91 - 0.121m_2 + 0.00035m_2^2 N/mm^2$$

This is a parabolic distribution. All shear stresses act in the positive m direction.

A number of values:

$$m_1 = 0; \tau_{(TopFlange)} = -8.91N/mm^2$$
$$m_1 = 173.5mm; \tau_{(TopFlange)} = -19.37N/mm^2$$
$$m_1 = 347.0mm; \tau_{(TopFlange)} = -8.91N/mm^2$$

Combining the results from the shear stress distribution of the flanges and webs gives the overall shear stress distribution across the section as shown in Figure 36.
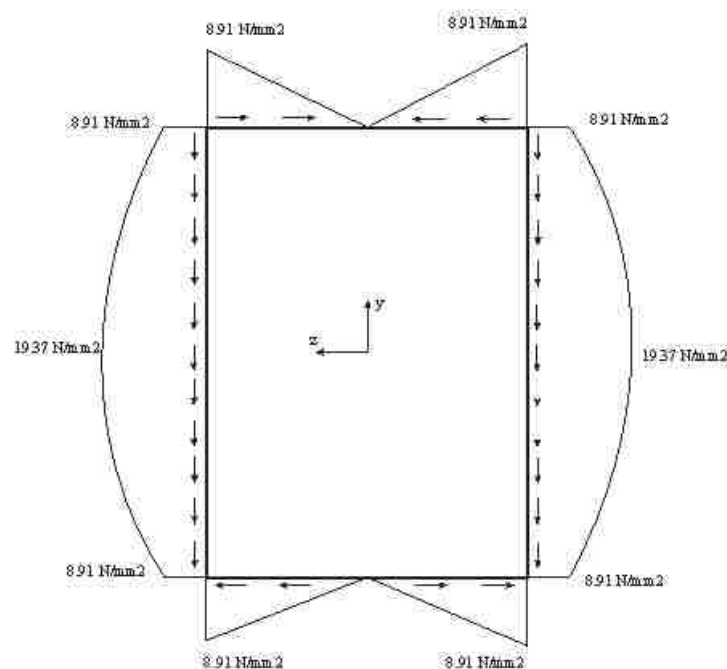
Figure 36: Shear stress diagram for the whole cross-section

Although it is possible to calculate the shear stress due to the reaction forces on the inner beam assembly, calculating the overall stress over the section due to the combination of bending stresses caused by the corner moments and tip load are complicated and hence, for this research FE models are relied upon for deductions on the behavior of the inner beam assembly of the telescope.

3.1.2 Results from the Analysis

Consider the section under wearpads shown in Figure 13. The two sections under the wearpads shown in Figure 37 are isolated for further understanding of the behavior of the inner beam. Four lines - Line AA, Line BB, Line CC and Line DD are drawn along the center of the two sections. All discussions in this section pertain to the behavior of the inner beam along these four lines.
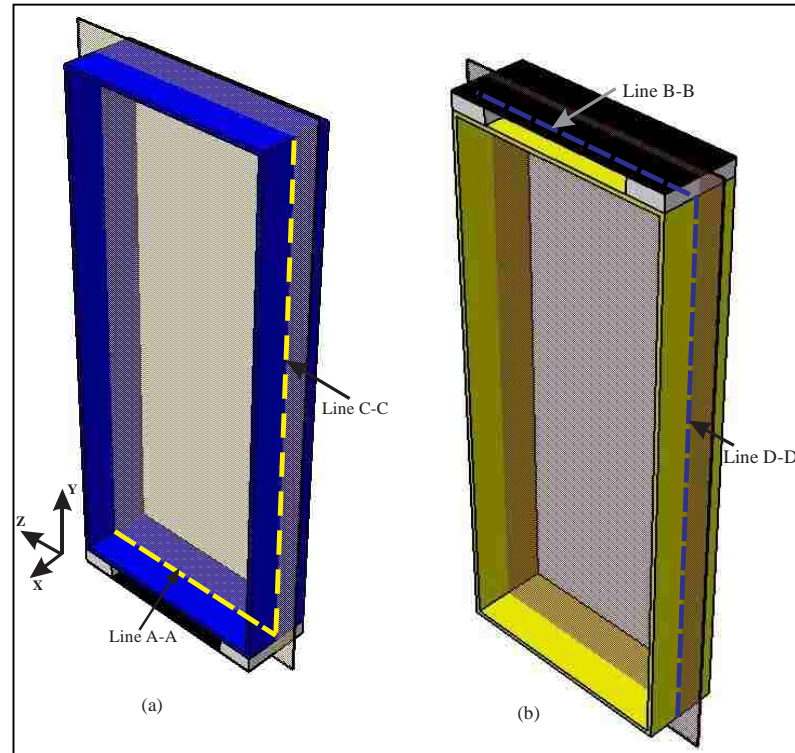
Figure 37: Center lines along areas of inner beam under (a) Bottom wearpads (b) Top wearpads

The following results were collected from the preliminary FEA

a) Stress values under the wearpads:

- Line A-A

Two direct bending stresses, σ_{xx} and σ_{zz} act along this line. σ_{xx} is due to the bending moment caused by the tip load and σ_{zz} is caused by the corner moment caused by the load from the outer beam (refer Figure 13).

Figure 38 shows a plot of the stresses obtained along Line A-A at a 5000 N tip-load. The Mises stress curve peaks in the distance corresponding to the wearpad width and its vicinity (0-30 mm and 120-150 mm) indicating maximum stress concentration in the area.
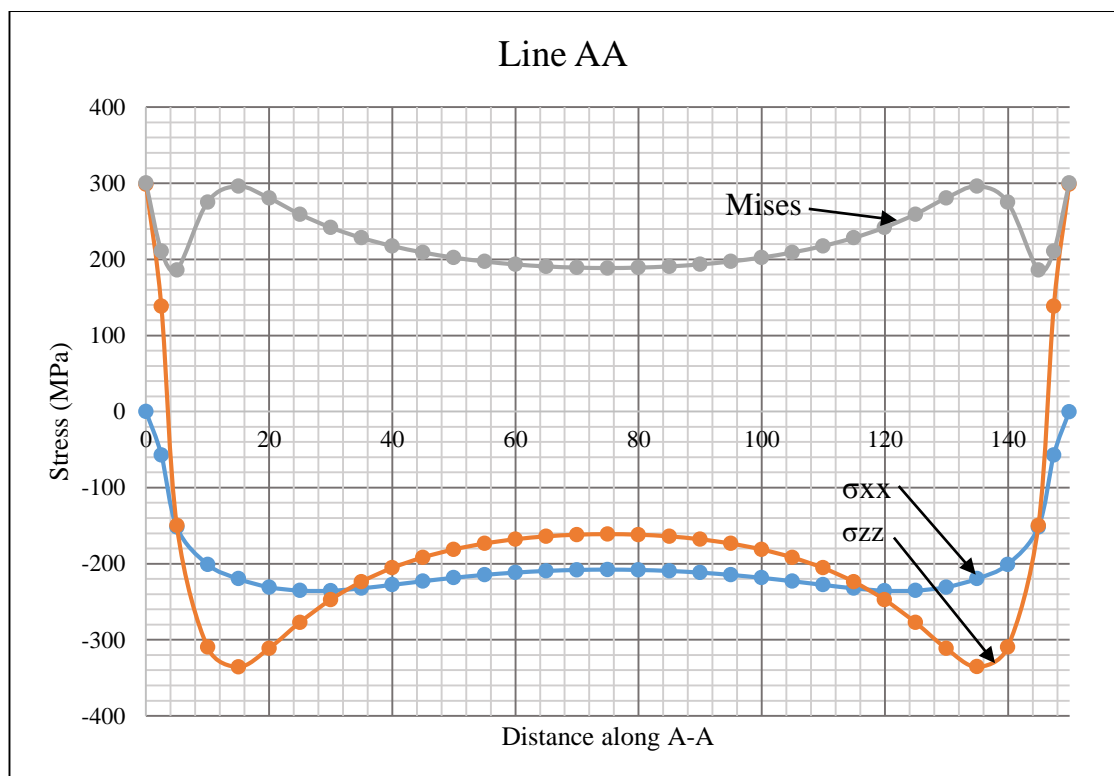
Figure 38: Stresses along line A-A (from the FEA)

- Line C-C

Stresses acting along line C-C is complicated to calculate as the load acting along C-C is non-uniform. It is expected that the entire load acting from the outer beam is taken up by the webs. Line C-C takes up half this load. Also, again the load through the wearpads causes a corner moment to act on the web. In addition, the moment caused by the tip load causes compression on the lower half of the web and tension on the upper half.

As the vertical force acting on Line C-C is compressive in nature, and the moment caused due to the tip load is also compressive at the bottom half of Line C-C, it is expected that maximum stress is induced in the bottom half of the Line C-C as compared to the rest of the Line.

- Line B-B

Unlike Line A-A, along Line B-B only σ_{zz} acts, as the moment due to the tip-load is zero at B-B (Refer the BMD in Figure 32). Here again, σ_{zz} is caused by a corner moment due to the load acting through the wearpads from the outer beam. Because of this, the stress induced in this area is much lesser than in Line A-A and is non-critical.

- Line D-D

Again, the vertical load from the outer beam acting on the top wearpad (lesser than the vertical load acting on the bottom wearpad – refer the SFD in Figure 32) is taken up entirely by the web (Line D-D). σ_{xx} is zero as the moment due to the tip load is zero. Again σ_{zz} acts along D-D because of the corner moment generated by the load

acting from the outer beam on the wearpads. For these reasons, stress is expected to be maximum at the top end of Line D-D.

b) Total reactions at the wearpads

At the bottom wearpad, for a tip load of 5000 N, the total reaction force from the FE Model is 32,789.16 N as shown in Figure 39. From the theoretical calculation, as shown in the FBD in Figure 32, the reaction force value is 33,166 N. This is considered as in agreement and validates the inner beam assembly FE model.
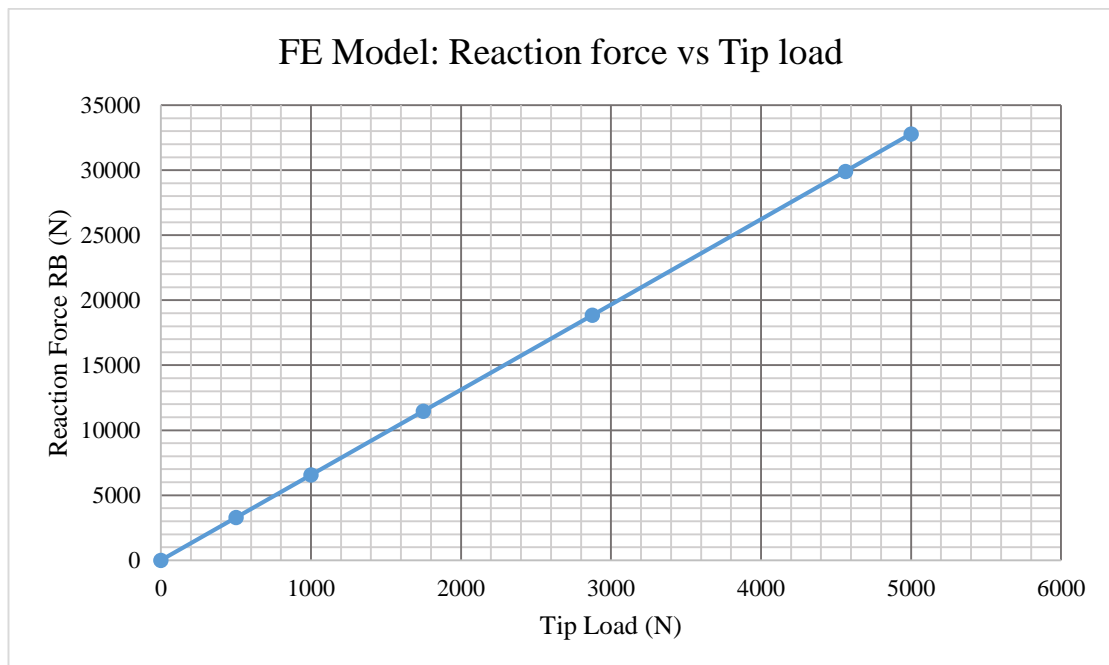
Figure 39: R_B from FE model for inner beam assembly

c) Physical shape (deflections) of the rings under the wearpads

For an inner beam subjected to a tip-load of 5000 N, Figure 40 represents sections of the deformed FE model of the inner beam taken under the top and bottom wearpads. Figure 40 shows the deflection in the section under the bottom wearpads is much more than deflection under the top wearpads. Line A-A exhibits greater hogging than the sagging exhibited by Line B-B. Also, major deflection is observed on the

lower part of Line C-C which is much greater than the deflection observed along Line D-D.
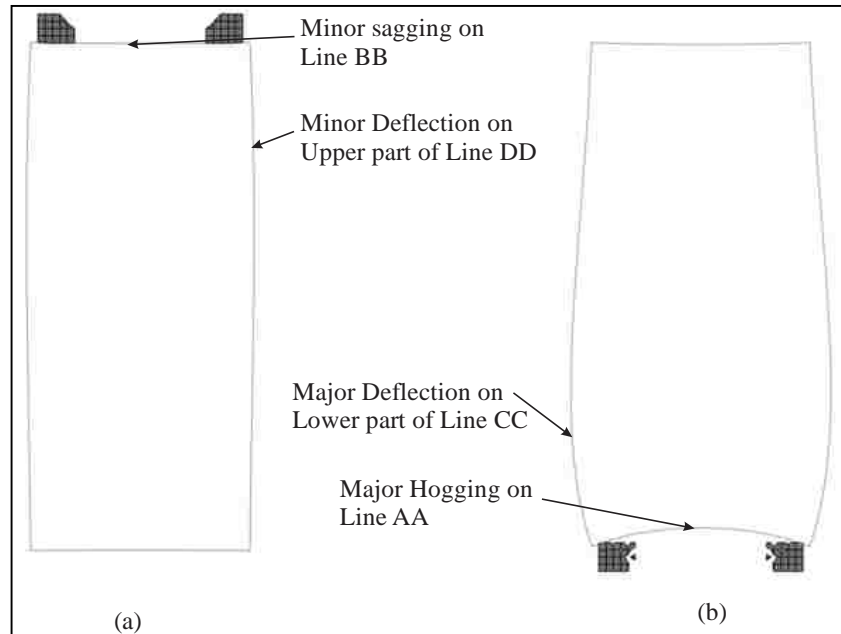
Figure 40: Deflection of inner beam section under (a) Top wearpads (b) Bottom wearpads

d) Deflection Curve:

Figure 40 shows that Line A-A experiences major hogging. Figure 41 shows the displacement curve along the length of A-A which shows that a maximum deflection (hogging) of 1.13 mm occurs at the middle of the bottom flange for a 5000 N tip load.
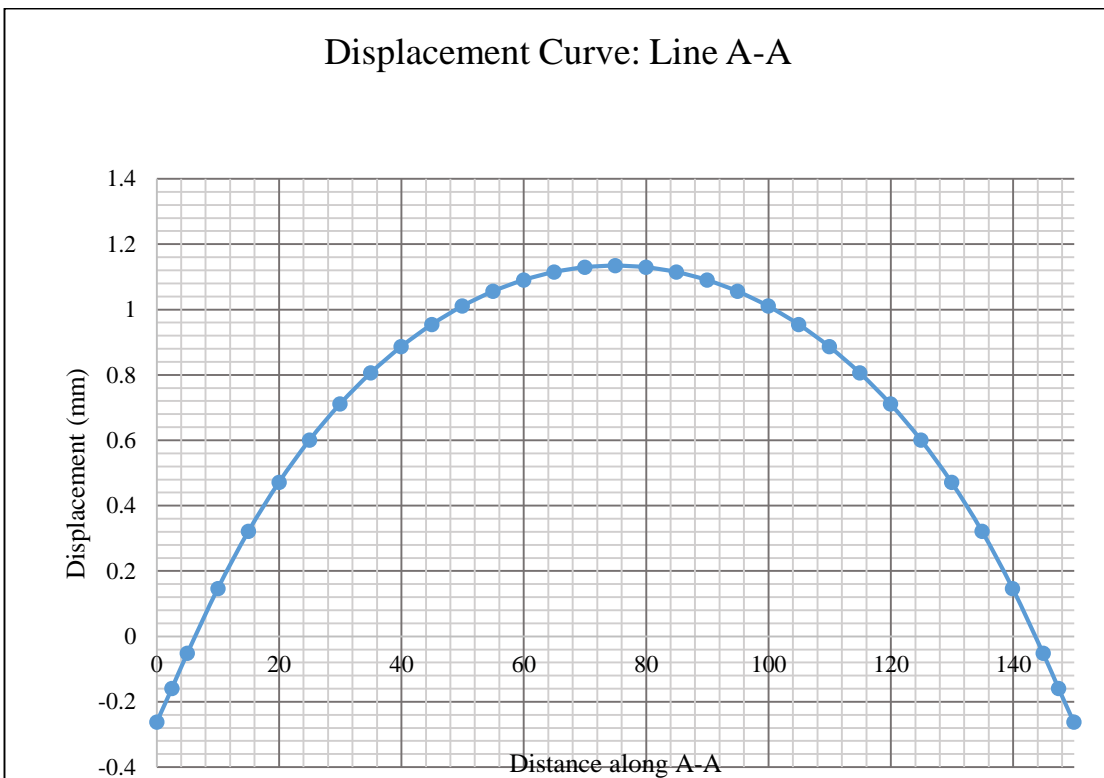
Figure 41: Displacement curve at line AA
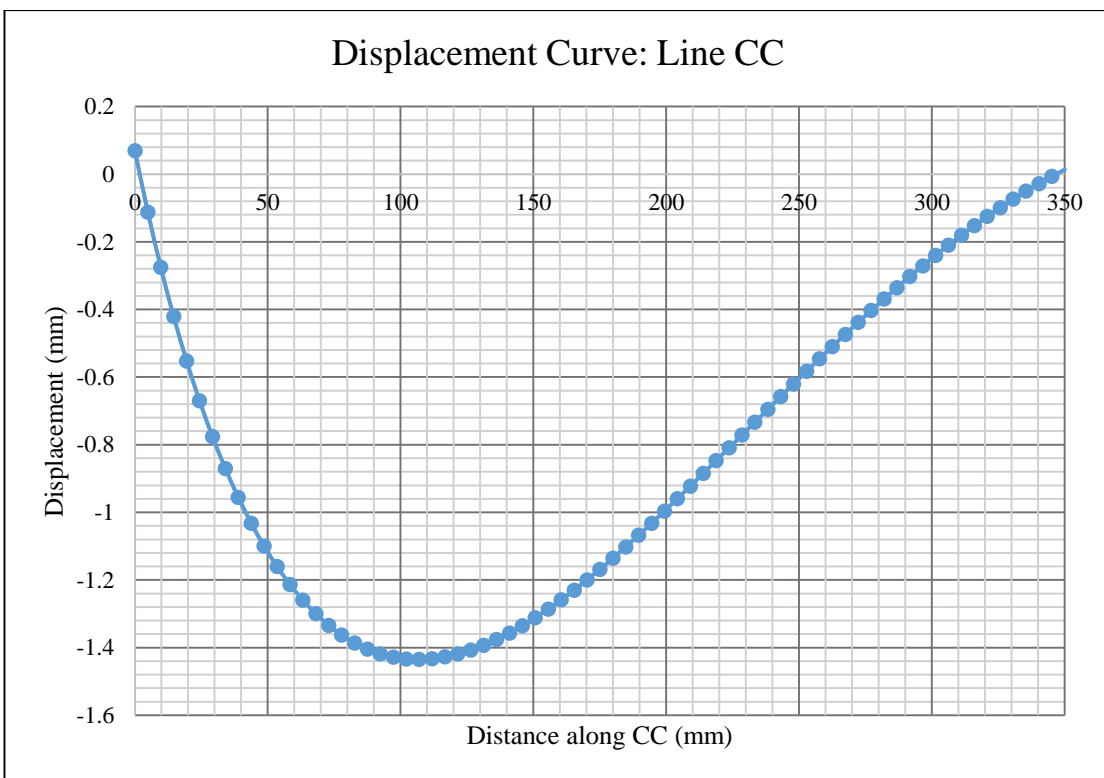
Figure 42: Displacement curve at line CC

Line C-C also exhibits a heavy deflection with the largest deflection equal to 1.43 mm corresponding to the lower part of C-C. The displacement curve for Line C-C is shown in Figure 42.

Lines B-B and D-D exhibit maximum deflections of 0.04 mm and 0.34 mm respectively and are hence considered less significant.

3.1.3 Analysis of the results

The following observations can be made from the above analysis.

- The section under the Top wearpads (Lines B-B and D-D) do not suffer major deformation or stresses.

- The flange (Line A-A) of the section under the bottom wearpads suffers major hogging because of the bending moment due to the tip load and the corner moments from the loads through the wearpads.

- The flange (Line A-A) of the section under the bottom wearpads suffers from bending stresses caused by the tip load (along the axis) and the bending stress across the cross-section due to the corner moment. This region therefore is expected to be the critical area with potential for buckling.

- The web (Line C-C) under the bottom wearpads also suffer major deformation on its lower part due to the vertical load from the wearpads, moment due to the tip load, and the corner moment due to load from the wearpads and can therefore also be an area with potential for buckling.

The observations above suggest that the region of the inner beam under the bottom wearpads induces the most stresses and deflections. This region is equivalent to a RHS Ring if the wearpad is short and a RHS piece if the wearpad is long. This led to the investigation of RHS rings under compressive transverse loading through

experimentation described in sections 3.2 and 0 and the succeeding investigations on the RHS pieces described in sections 3.4 and 0.

3.2 Experiment 1 – Compression of RHS Rings between Platens

A ring is made up of strips whose width and thickness are small compared to their lengths.

- *Description of the Machine*:

An MTS machine (model: 20/H) was used for this experiment. The downward head movement was maintained at a velocity of 0.5 mm/min to apply the load in all the trials. The MTS machine had a capacity of 1000 kN and is equipped with various load heads (Head capacity: 5 kN, 100 kN, 1000 kN) for different load capacities. The load head was changed to a 5 kN capacity for more accurate readings as the maximum load capacity of the Rings was expected to be 1.04 kN (from the initial FEA data). On completion of each experiment, the output was obtained as load-displacement graphs in excel format. The bottom platen of the machine had a 150 mm diameter while the load was applied at the top through a 50 mm diameter cylinder (Refer Figure 45).

- *The specimen*:

RHS rings with cross sectional dimensions 350 mm x 150 mm with a length of 10 mm, corner radius of 5 mm and a uniform thickness of 3 mm were subjected to compressive loads in these experiments. CRCA (Cold Rolled Cold Annealed) MS strips with 3 mm thickness and 10 mm width were bent on a press brake to form the RHS Ring sections. A single center weld on the top flange of each section closed the ring section. The thickness measurement taken using a Vernier calipers at points A-J shown in Figure 43 are listed for RHS rings compressed between platens in Table 13.
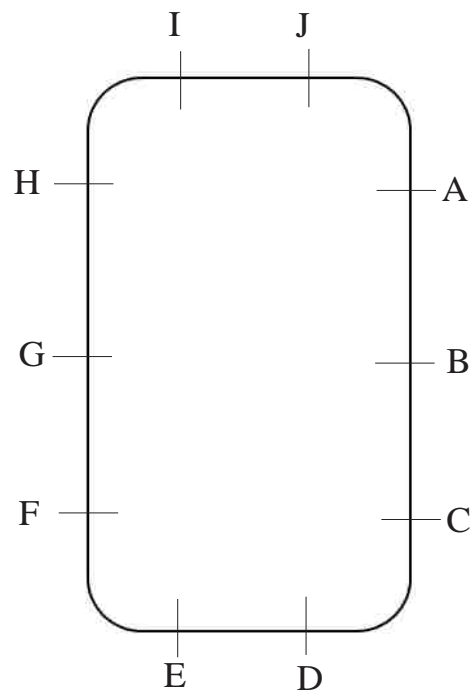
Figure 43: Thickness measurement points

Table 13: Thickness measurements of RHS rings between platens

Specimen	Thickness (mm)									
	A	**B**	**C**	**D**	**E**	**F**	**G**	**H**	**I**	**J**
SR1	2.97	2.97	3.01	2.94	2.99	2.97	3.03	3.09	3.05	3.02
SR2	2.94	2.96	2.90	2.83	2.89	2.89	2.88	2.85	2.82	2.88
SR3	2.83	2.77	2.86	2.81	2.83	2.75	2.81	2.82	2.74	2.79

- *Description of the process*:

The assembly of the RHS ring loaded between platens is as shown in Figure 44. The assembly consists of a RHS ring placed between the top and bottom platens. The top platen has a shallow groove on its upper surface to accommodate the load distributor. The load distributor has a spherical upper surface (in contact with the machine load-applying platen) and a flat lower surface (in contact with the platen on

top of the RHS ring). This arrangement allows for a better, more uniform distribution of load on the RHS ring.
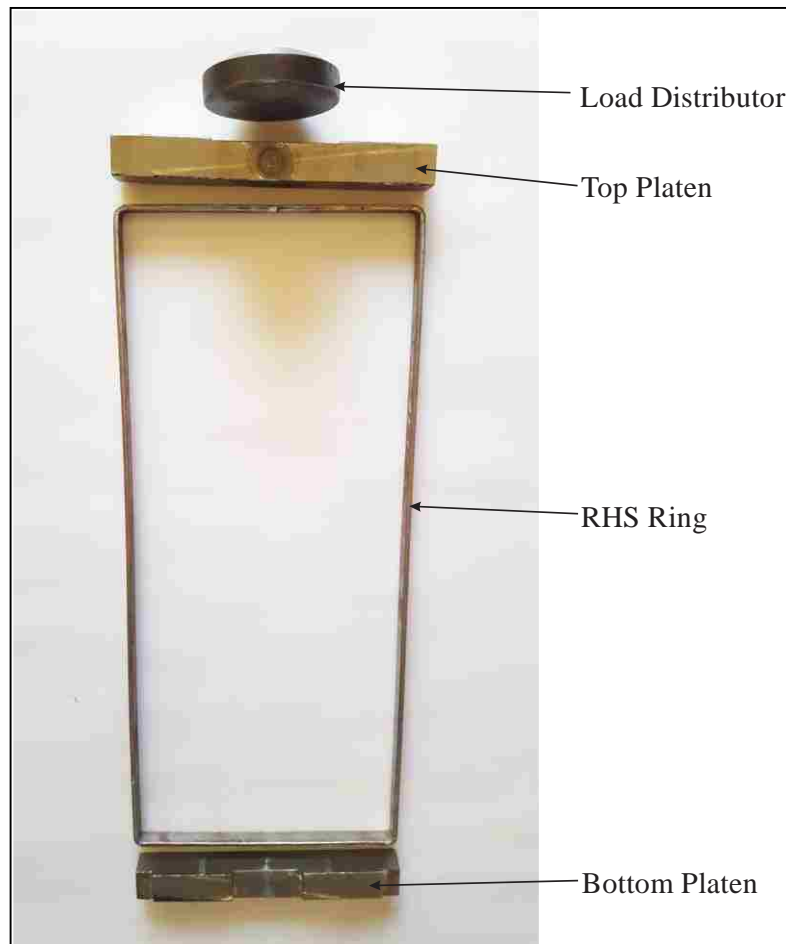
Figure 44: Assembly of RHS ring between platens

The assembly was placed on the MTS machine lower platen while the load was applied by the machine top cylinder. The load was continuously applied till the maximum load value was reached after which the load was released and the load-displacement plot obtained as an output.

- *Characteristics of Loading between platens*

Platens are flat surfaces and they apply a uniformly distributed load on the flat, top and bottom flanges of the RHS ring placed between them. But if the top flange starts sagging and the bottom flange starts hogging, the load distribution will

concentrate on the peripheral areas which are still in contact with the platens. In short, the platens will transmit forces through the areas that maintain contact with them. This point is explained further in the following way:

  o *Initial Stage – Uniform loading under the platen*

The flanges and the webs at the beginning showed no deflection and were at right angles to each other as shown in Figure 45. The platens were in full surface contact with the RHS flanges at this stage.
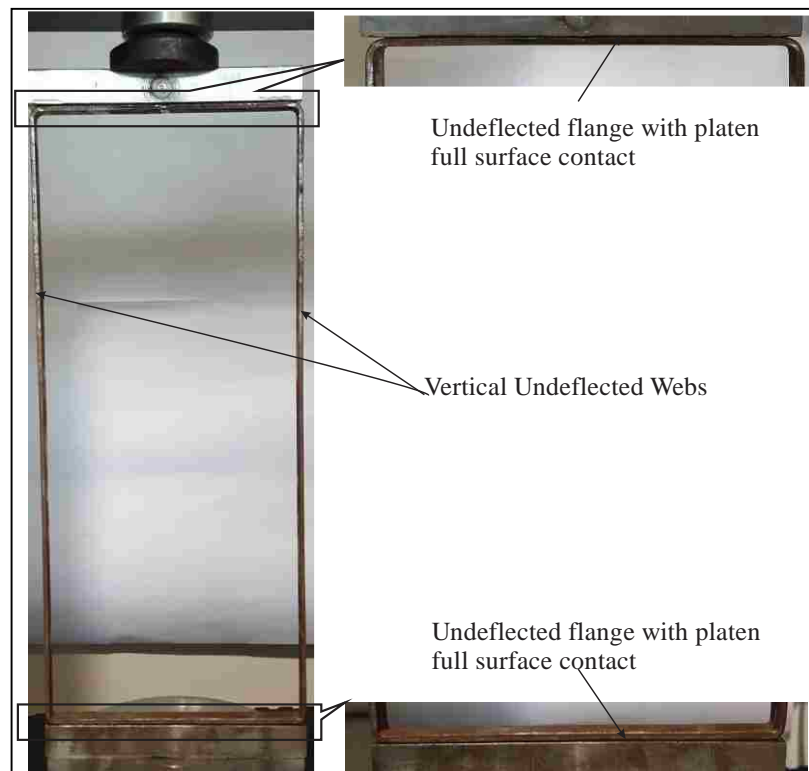
Figure 45: RHS ring between platens at the initial stage

  o *Progress into the process – Bending of the flange with no contact at the center*

Figure 46 shows that as the load is increased, the top flange begins to sag (like a beam under transverse loading) and the bottom flange begins to hog causing the

flanges to lose contact with the platens in the middle. The webs also begin to bulge outwards.
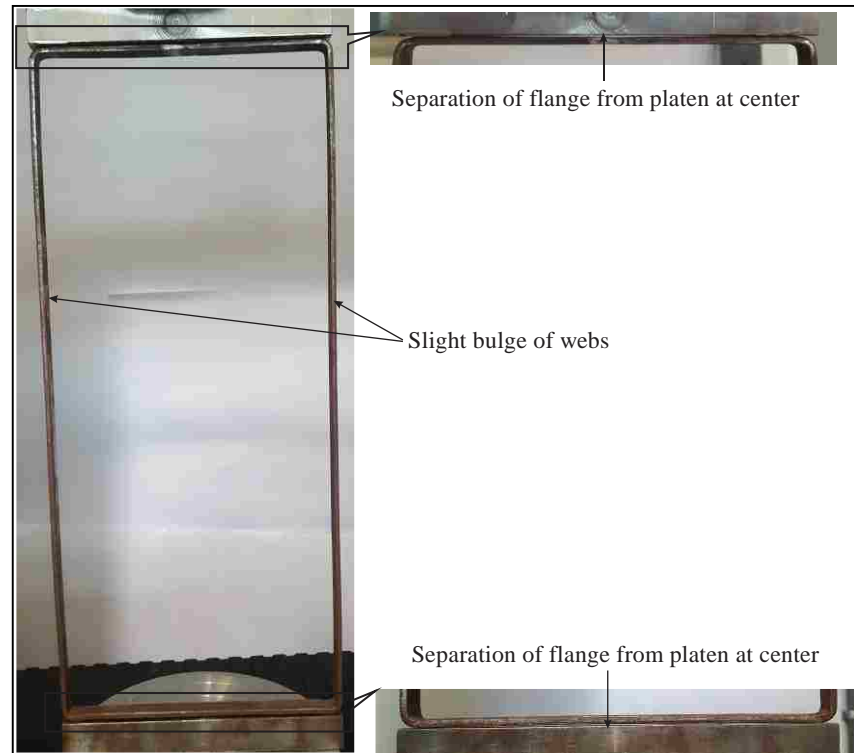
Figure 46: Loss of contact between RHS ring flange and platen

o *Sufficient Progress into the process – Visible deformations of the flanges and the webs with significant loss of contact area*

This stage is marked by an obvious and exaggerated deformation on all four strips of the RHS ring – the two flanges and the two webs. The shape of the RHS ring is shown in Figure 47 below.
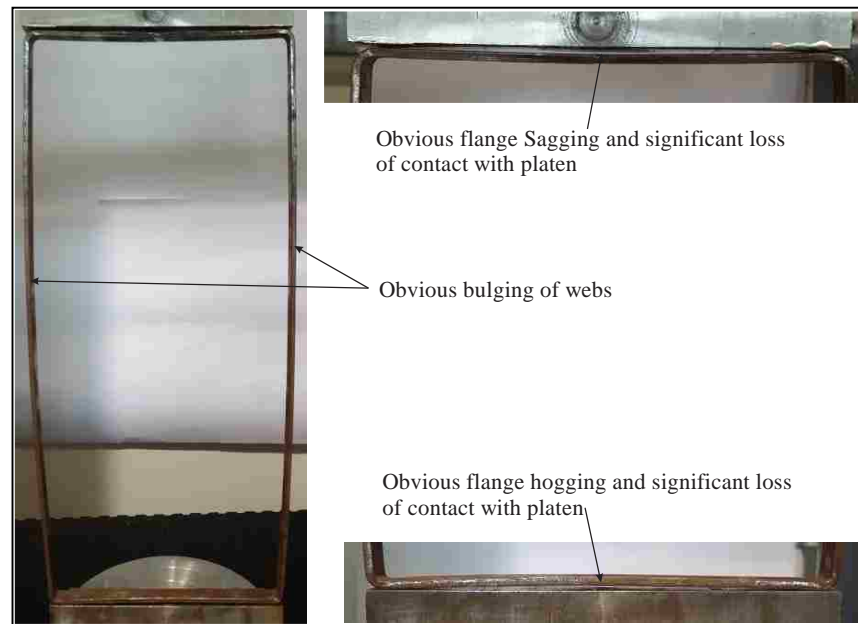
Figure 47: Obvious deformation of webs and flanges of RHS ring between platens

At this stage, consider the right web. The bent shape is like the one showed in Figure 48(a). If this is cut by an imaginary plane at the middle, the free body diagram of the upper half will be as shown in Figure 48(b). The entire cross section will experience the same compressive stress P/A. In addition, the outermost fiber on the outer side will have maximum tensile stress while the outermost fiber on the inner side will have the compressive stress caused due to the bending moment 'Py'. This will result in a bigger compressive stress at the outermost fiber on the inner side. Yielding therefore can be expected to begin at the inner sides of the flanges at the mid-height where 'y' is maximum.
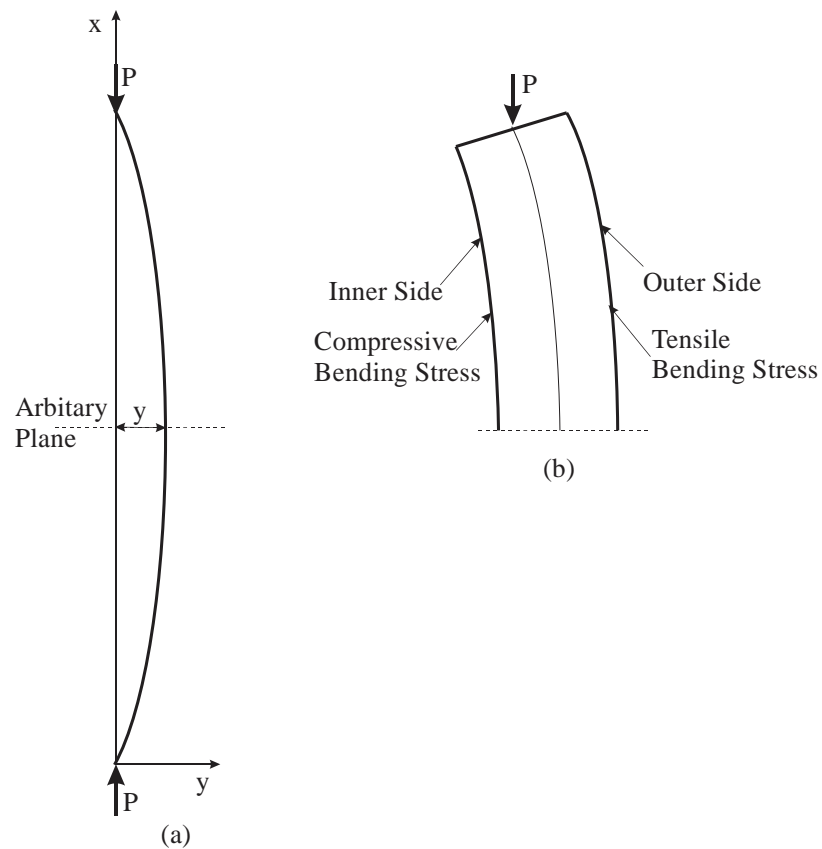
Figure 48: (a) Bent shape and (b) Difference in stresses in right web

    o   *Final stage – Hinged webs and bent flanges*

The outer fibers on the inside of the webs have started yielding at this stage while the platens are still closing in and thus increasing the bending. This causes increasing bending stresses and progressive yielding continues. This form two hinges at the mid-height of the webs. The RHS ring now consists of webs hinged at mid-height and bent flanges as shown in Figure 49.

Figure 49: Hinged webs and bent flanges of RHS ring between platens

- Load Displacement curve:

Each sample was loaded until the load-displacement curve begun to assume a downward negative slope after the RHS ring reached its maximum load carrying capacity. Throughout this process the load deflection behavior was recorded.

Figure 50(a) shows a typical load-displacement curve as obtained from the MTS machine for a RHS ring (sample SR1) compressed between platens.

Figure 50(b) shows the corrected load-displacement curve for the sample SR1.
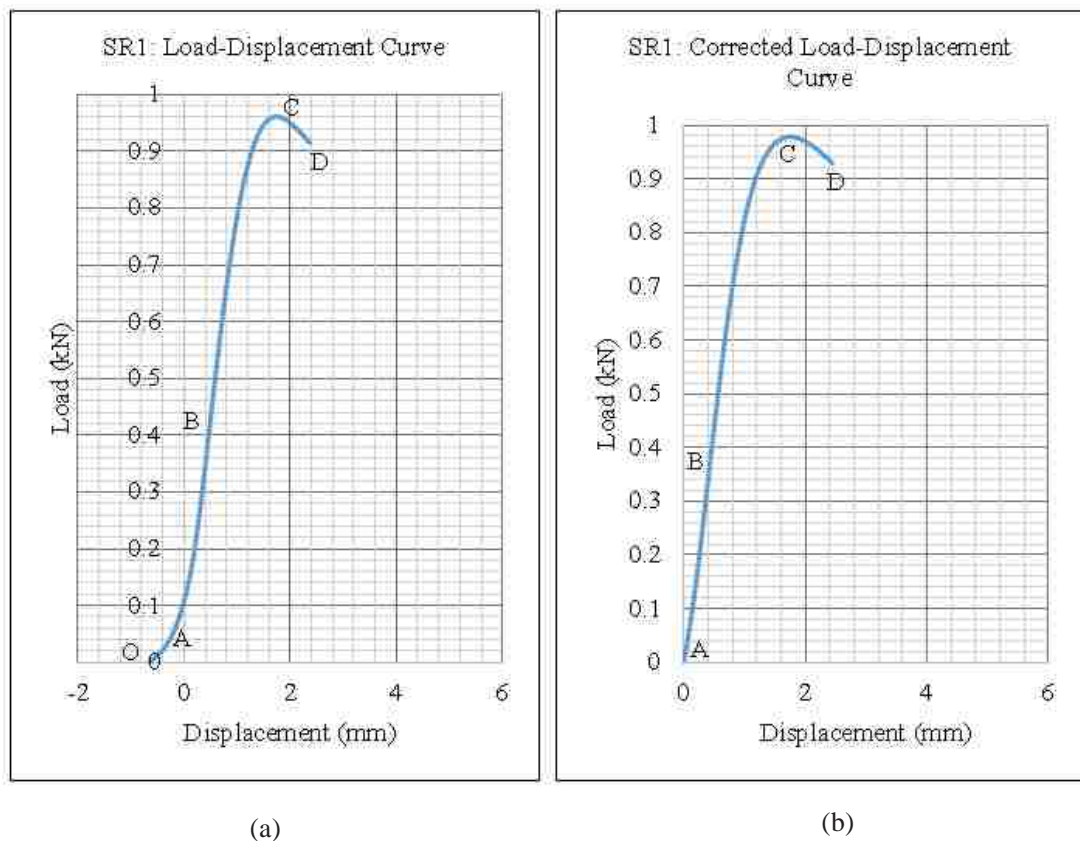
Figure 50: Typical RHS ring load displacement curve (a) As obtained (b) Corrected

The sample considered here is SR1 which was loaded for 292 seconds. The load-displacement curve obtained from the MTS machine has an initial irregularity marked by the region OA shown in Figure 50(a). In this region, the MTS machine top platen has still not established contact with the RHS Ring top flange thereby displaying a negative displacement. Since contact is established only when the displacement value equals zero, the load value corresponding to zero displacement value is taken to be the zero load. Therefore, this load value is subtracted from the remaining load values.

In Figure 50(a), the maximum load value equals 945.54 N but in Figure 50(b), the corrected maximum load value is 934.79 N. This is because at the displacement

value of 0 mm, the load value is 10.75 N and this value is then subtracted from the succeeding load values.

In sections 2.3, 2.4 and 2.5, only the corrected load-displacement curves will be shown and discussed. The load-displacement curve shown in

Figure 50(b) is now used to explain the behavior of RHS ring compressed between platens. Initially, the curve shows a linear load deflection shape (AB in the graph). This is the elastic region of the graph within which the RHS ring retains its capacity to fully regain its original shape if the load is removed. At B, the slope of the graph begins to reduce and gradually flattens out at C where it reaches its maximum load carrying capacity. Region BC is the elasto-plastic region of the RHS ring where yielding (plasticity) begins at the outermost fiber on the innermost side and progresses in the thickness direction gradually as the load increases. After reaching a load value at C, the load starts decreasing while the deflection continues to increase (CD in the graph) before the loading was stopped. Region CD is the post-yield stage.
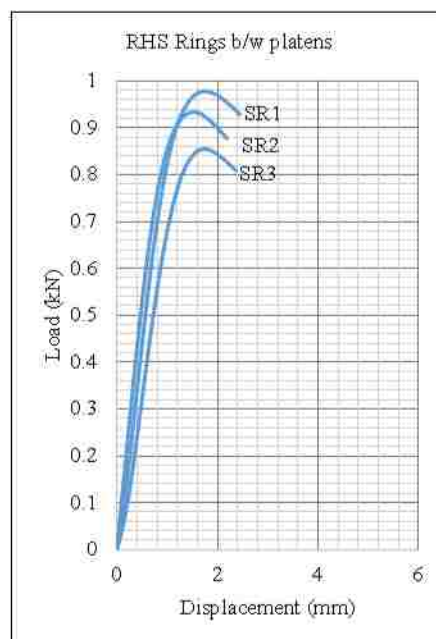
Figure 51: Load-displacement curve for RHS rings between platens

Figure 51 shows the load-displacement curves for the three RHS rings SR1 - SR3 compressed between platens. All three curves display the same trend explained above. Table 14 below shows the maximum load values of each of the three samples.

Table 14: Maximum load of RHS rings between platens

RHS Ring #	Maximum Load (kN)
SR1	0.978
SR2	0.934
SR3	0.900

3.3 Experiment 2 – Compression of RHS Rings between Wearpads

- *Description of the Machine*

    As explained in section 3.2

- *The specimen*:

    Specimen specifications and method of manufacturing are the same as in section 3.2. The thickness measurement taken using a Vernier calipers at points A-J shown in Figure 43 are listed for RHS rings compressed between wearpads in Table 15.

Table 15: Thickness measurements of RHS rings between wearpads

Specimen	Thickness (mm)									
	A	**B**	**C**	**D**	**E**	**F**	**G**	**H**	**I**	**J**
SRW1	3.03	3.08	3.07	3.05	3.03	3.01	3.06	3.07	3.09	3.00
SRW2	3.00	3.10	2.95	2.95	2.94	3.09	3.02	2.97	3.00	3.00
SRW3	3.00	3.06	3.03	3.00	2.99	296	3.05	3.03	3.01	3.02

- *Description of the process*

    The assembly of the RHS ring loaded between wearpads is as shown in Figure 52 below. The assembly shown is very similar to that explained in Section 3.2, except

that the platens in section 3.2 are replaced by wearpads in this section. Here again, the top wearpad has a shallow groove on its upper surface to accommodate the load distributor for a better, more uniform distribution of load on the RHS ring.

Figure 52: Assembly of RHS ring between wearpads

The assembly is placed on the lower platen of the MTS machine while the load is applied by the machine top cylinder. The load is continuously applied till the maximum load value is reached after which the load is released and the load-displacement plot is obtained as an output.

- *Characteristics of Loading between wearpads*

Wearpads are flat cut out surfaces that apply 'patch loads' on portions of the flat, top and bottom flanges of the RHS rings in contact with them.

Once the load application is started, the top flange starts sagging and the bottom flange starts hogging causing the load distribution to move towards, and eventually concentrate on the outer edges of the wearpads. In short, as the load increases, the wearpads will transmit forces through the areas which maintain contact with the RHS ring flanges.

o *Initial Stage – Uniform loading under the wearpads*

The flanges and the webs at the beginning showed no deflection and were at right angles to each other as shown in Figure 53. The flanges maintained area contact only with the regions of the wearpad.
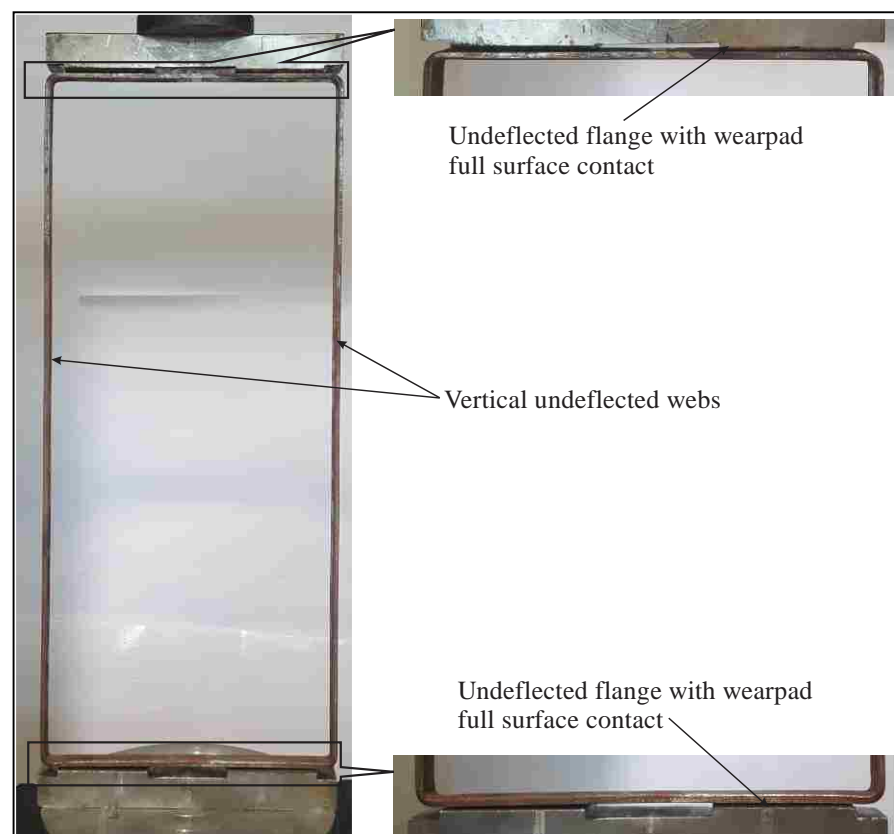
Figure 53: RHS ring between wearpads at the initial stage

- *Progress into the process – Bending of the flange with no contact at the centre*

Figure 54 shows that as the load is increased, the top flange begins to sag (like a beam under transverse loading) and the bottom flange begins to hog causing the flanges to lose contact with the wearpads in the middle. At this stage, the flanges still maintain surface contact with the wearpads. The webs also begin to bulge outwards.
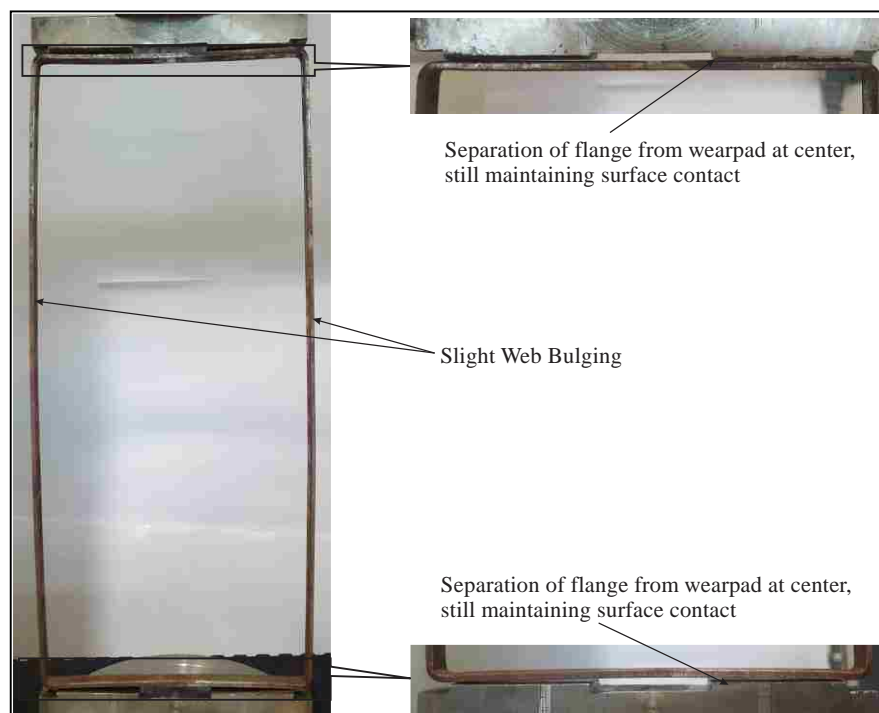
Figure 54: Initial flange separation from wearpads

- *Sufficient Progress into the process – Visible deformations of the flanges and the webs with significant loss of contact area*

This stage is marked by an obvious and exaggerated deformation on all four strips of the RHS ring – the two flanges and the two webs as shown in Figure 55 below. Contact between the flanges and the wearpads is almost reduced to a line/ edge contact at the outer edges of the wearpads.

Figure 55: Obvious deformation of webs and flanges of RHS ring between wearpads

At this stage, consider right web. The bent shape will be like the one showed in Figure 56(a). If this is cut by an imaginary plane at the middle, the free body diagram of the upper half will be as shown in Figure 56(b). The entire cross section will experience the same compressive stress P/A. In addition, bending stresses are caused by moment due to web deflection 'Py' and moment due to load eccentricity 'Pe'. This will result in a bigger compressive stress at the outer fiber on the inner side. Yielding therefore can be expected to begin at the inner sides of the flanges at the mid-height at lower load values compared to when loaded between platens.
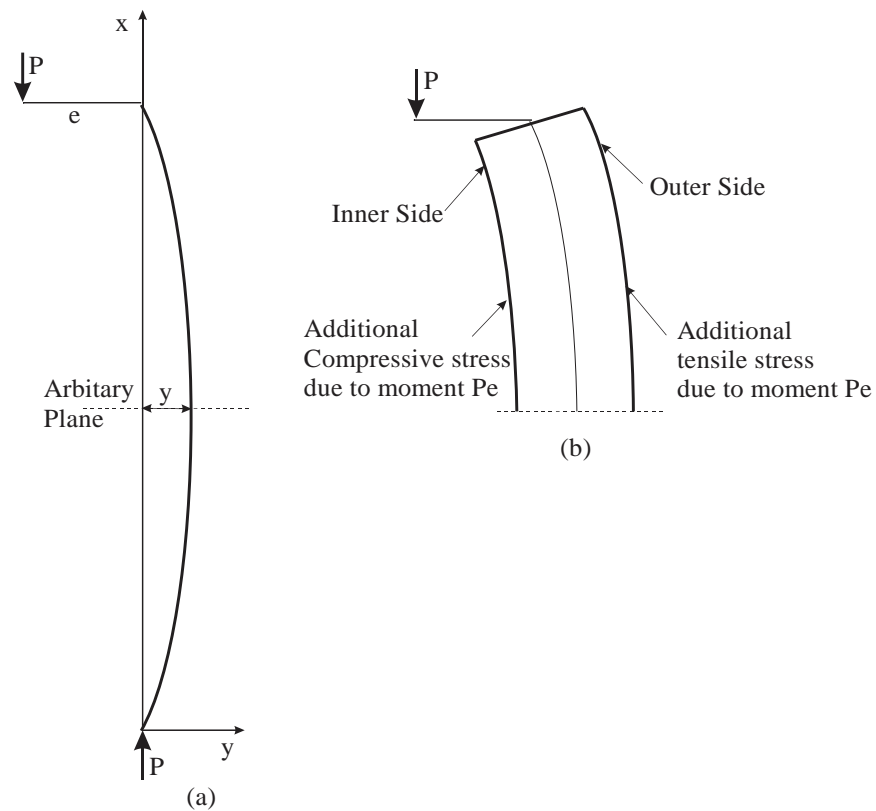
Figure 56: (a) Eccentric load acting of web (b) Resultant stresses on web

o *Final stage – Hinged webs and bent flanges*

The outer fibres in the inside of the webs have started yielding at this stage while the wearpads are still closing in and thus increasing the bending. This causes more bending stresses and progressive yielding continues. This form two hinges at the mid-height of the webs. The RHS ring now consists of webs hinged at the mid-height and bent flanges as shown in Figure 57.

Figure 57: Hinged webs at web center and bent flanges due to compression between wearpads

- Load Displacement curve:

As in section 2.2, each sample was loaded until the load-displacement curve begun to assume a downward negative slope after the RHS ring reached its maximum load carrying capacity. Throughout this process the load deflection behavior was recorded.

Figure 58 shows a typical corrected load-displacement curve obtained for a RHS ring (sample SRW1) compressed between wearpads. Like Figure 51(b) in section 2.2, the load-displacement curve is marked by points A, B, C, and D as shown in Figure 58. Again, the three main regions are the elastic area (OA), the elasto-plastic region of the reduced slope BC and the post-yield region CD after the maximum load at C.

On comparison with Figure 51(b), it is observed that the maximum load carrying capacity of RHS rings between wearpads is smaller than that of RHS rings compressed between platens. Also, at the maximum load, the displacement in the RHS ring compressed between wearpads is higher than that observed in RHS rings compressed between platens. The reasons for both these observations can be attributed to the additional moment caused by the distance of the wearpads from the vertical webs of the RHS rings.
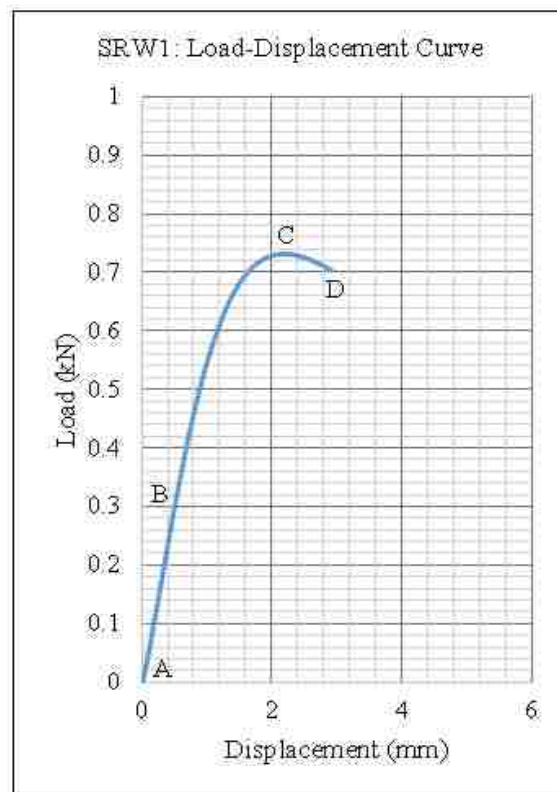
Figure 58: Typical load-displacement curve of RHS ring between wearpads

Figure 59 shows the load-displacement curves for the three RHS rings SRW1-SRW3 compressed between wearpads. All three curves display the same trend explained above.
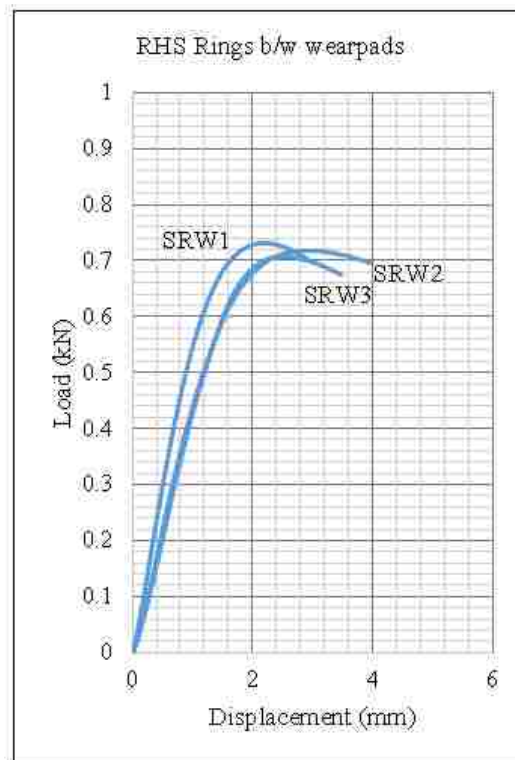
Figure 59: Load displacement curves of RHS rings between wearpads

Table 16 below shows the maximum load values of each of the three samples.

Table 16: Maximum load of RHS rings between wearpads

RHS Ring #	Maximum Load (kN)
SRW1	0.731
SRW2	0.716
SRW3	0.706

- Conclusions:

    o Buckling is indicated by the rapid outward bulging of the webs

    o The flanges of the RHS ring bend in a concave manner.

    o Visually, the shape of the RHS ring when loaded between wearpads
    follows a similar pattern as the RHS ring loaded between platens with
    the outward bulging of the webs and inward bending of the flanges.

o However, Table 14 and Table 16 show that for a given set of geometrical factors, the maximum load value of a RHS ring compressed between wearpads is lower than when compared to a RHS ring compressed between platens.

o As the load increases, the flanges of the RHS ring separate from the platen or the wearpads.

o In the limiting condition, contact between the RHS ring flanges and the platen or wearpad reduces to a line contact.

o The load deflection curves are characterized by three distinct areas; the elastic region, the elasto-plastic region and a post-yield stage.

3.4 Experiment 3 – Compression of RHS Pieces between Platens

In this experiment, RHS pieces are subjected to compressive loads between platens. In the 'rings', the webs and flanges have cross sections with significantly small dimensions compared to the third dimension. But the RHS pieces have webs and flanges, which have only one dimension, the thickness, significantly smaller than the other two. If the rings are constituted with strips, the RHS pieces are constituted with plates. Consider the overlap region explained in and reproduced in Figure 60 here. If the wearpad is long then the region taking up the load will be an RHS piece, while the region taking up the load will be a ring if the wearpad is short.
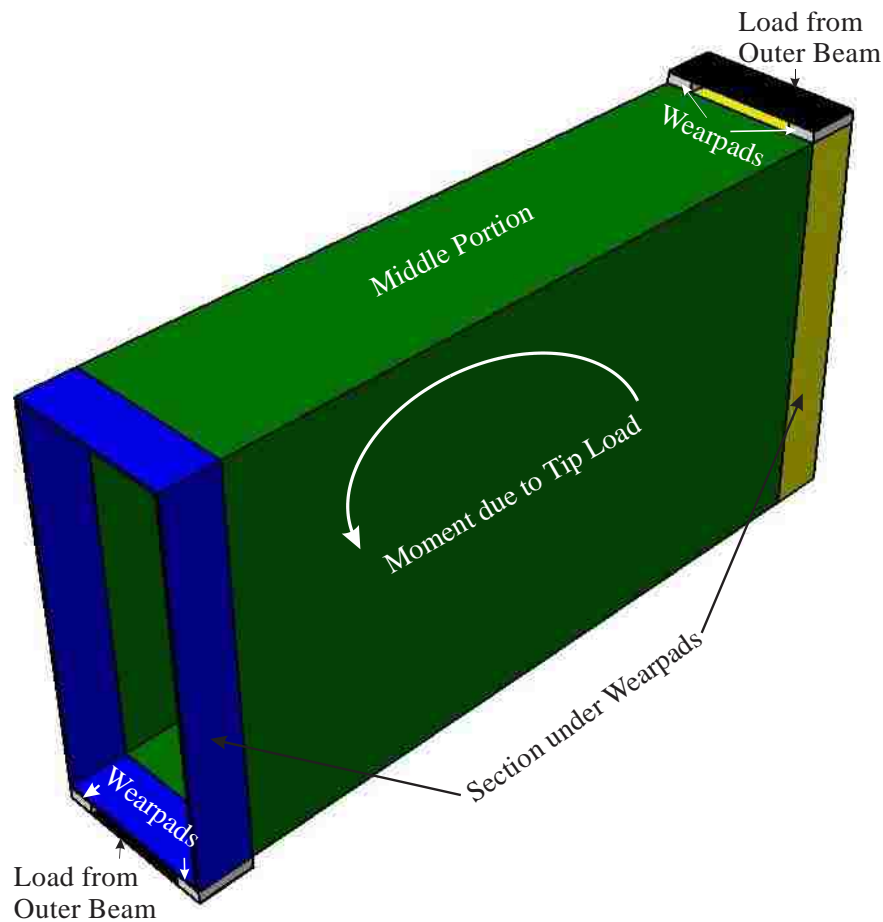
Figure 60: (Repeated) Division of the overlap section

- *Description of the Machine*

Two machines were used for testing two sets of RHS pieces in sections 3.4 and 3.5. The shorter sections with the smaller height of 150 mm were tested on the MTS machine (model 20/H) described in section 3.2.

The taller sections of 350 mm height were tested in an MTS machine (model: SANS SHT 4106) with a capacity of 1000 kN. The machine was equipped with servo valve for automatic load control and had a load measurement resolution of 1/300000 of its capacity. The test output was available as load-displacement graphs in excel format and the load was applied at a speed of 1 mm/min. The samples were placed on compression platens of 200 mm x 200 mm square.

- *The specimen*

  RHS pieces of the following dimensions were tested:

  - 350 mm height, 150 mm width with a length of 150 mm and thickness of 3.2 mm

  - 150 mm height, 100 mm width, with a length of 100 mm and thickness of 3 mm

  For the taller sections, CRCA (Cold Rolled Cold Annealed) MS plates with 3 mm thickness and 150 mm width were bent on a press brake to form the RHS pieces. A single center weld on the top flange of each section closed the section.

  For the shorter sections, two C-sections were bent from a 3 mm MS plate and welded along the center line of the top and bottom flanges to form the section.

  The thickness measurement taken using a Vernier calipers at points A-J shown in Figure 43 are listed for RHS pieces compressed between platens in Table 17 and Table 18.

Table 17: Thickness measurements of tall RHS pieces between platens

Specimen	Thickness (mm)									
	A	**B**	**C**	**D**	**E**	**F**	**G**	**H**	**I**	**J**
SL1	3.19	3.21	3.19	3.11	3.16	3.20	3.21	3.19	3.19	3.18
SL2	3.17	3.18	3.18	3.17	3.15	3.19	3.18	3.18	3.17	3.19
SL3	3.19	3.17	3.16	3.18	3.18	3.18	3.19	3.17	3.16	3.16

Table 18: Thickness measurements of short RHS pieces between platens

Specimen	Thickness (mm)									
	A	**B**	**C**	**D**	**E**	**F**	**G**	**H**	**I**	**J**
SL4	3.03	3.04	3.02	3.01	3.0	3.04	3.02	3.00	3.04	3.03
SL5	3.01	3.01	3.02	2.99	3.01	3.03	2.99	3.02	3.02	2.98
SL6	3.01	3.00	3.02	3.03	2.99	3.01	2.98	3.00	3.01	2.99

- *Description of the process*

The RHS piece is placed on bottom platens of the MTS machine while the load is applied by the top platen at a speed of 1 mm/min. The load is continuously applied till the maximum load value is reached after which the load is released and the load-displacement curve is obtained as an output.

- *Characteristics of Loading between platens*

As explained in section 3.2, platens are flat surfaces and they apply a uniformly distributed load on the flat, top and bottom flanges of the RHS piece placed between them. But if the top flange starts sagging and the bottom flange starts hogging, the load distribution will concentrate on the peripheral areas which still are in contact with the platens. In short, the platens will transmit forces through the areas which maintain contact with them.

- *Initial Stage – Uniform loading under the platen*

The flanges and the webs at the beginning showed no deflection and were at right angles to each other as shown in Figure 61 below. The platens were in full surface contact with the RHS piece flanges at this stage.
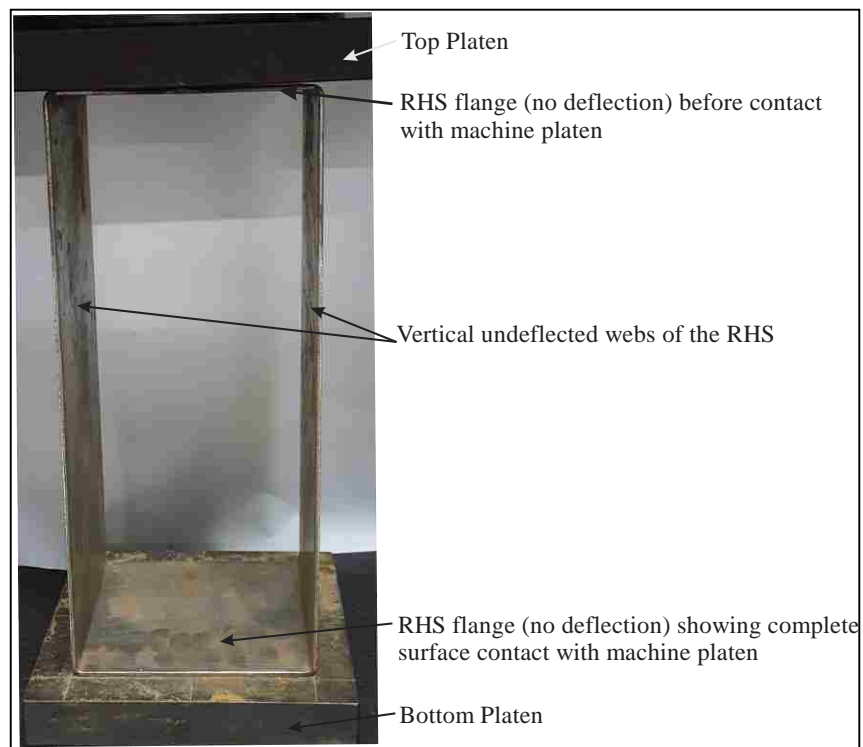
Figure 61: Undeflected webs and flanges of RHS piece between platens

    o *Progress into the process – Bending of the flange with no contact at the centre*

   Figure 62 shows that as the load is increased, the top flange begins to sag (like a plate under transverse loading) and the bottom flange begins to hog causing the flanges to lose contact with the platens in the middle. The webs also begin to bulge outwards.

Figure 62: Initiation of bending of flanges and bulging of webs of RHS piece between platens

o *Sufficient Progress into the process – Visible deformations of the flanges and the webs with significant loss of contact area*

This stage is marked by an obvious and exaggerated deformation on all four plates of the RHS piece – the two flanges and the two webs. The RHS piece at this stage is shown in Figure 63.
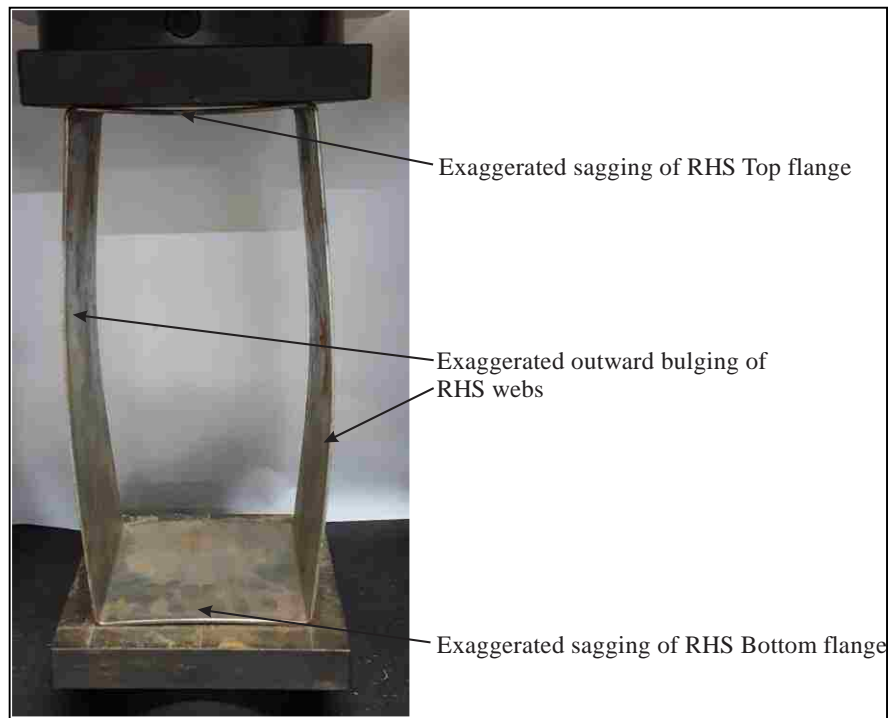
Figure 63: Obvious deflected webs and flanges of RHS piece between platens

Again, as explained in section 3.2 and Figure 48, yielding can be expected to begin at the inner sides of the flanges at the mid-height.

o *Final stage – Hinged webs and bent flanges*

The outer fibres on the inner side of the webs have started yielding at this stage while the platens are still closing and thus increasing the bending. This causes more bending stresses and progressive yielding continues. This form two hinges at the mid-height of the webs. The RHS piece now consists of webs hinged at the mid-height and bent flanges as shown in Figure 64.

Figure 64: RHS piece with hinged webs and bent flanges between platens

- Load Displacement curve:

 Each sample was loaded until the load-displacement curve begun to assume a downward negative slope after the RHS reached its maximum load carrying capacity. Throughout this process the load deflection behavior was recorded.

Figure 65(a) shows a typical load-displacement curve obtained for a RHS piece of height 350 mm (sample SL1) compressed between platens. Figure 65(b) shows a typical load-displacement curve obtained for the shorter RHS piece of height 150 mm (sample SL4) compressed between platens.

Both the graphs display a similar trend. Figure 65(a) representing the taller sections is marked by five regions and six points. Figure 65(b) representing the shorter sections is marked by four regions and five points. The region OA in both graphs

represents the part of the curve where the platens are still establishing complete surface contact with the RHS piece. For the shorter RHS pieces between platens, the load-displacement curve (Refer Figure 65(b)) is like that explained in sections 3.2 and 3.3. AB marks the elastic region, BC the elasto-plastic region and CD the post-yield region.

However, for the taller RHS pieces between platens, the elasto-plastic region is divided into two areas BC and CD.

(a)   (b)
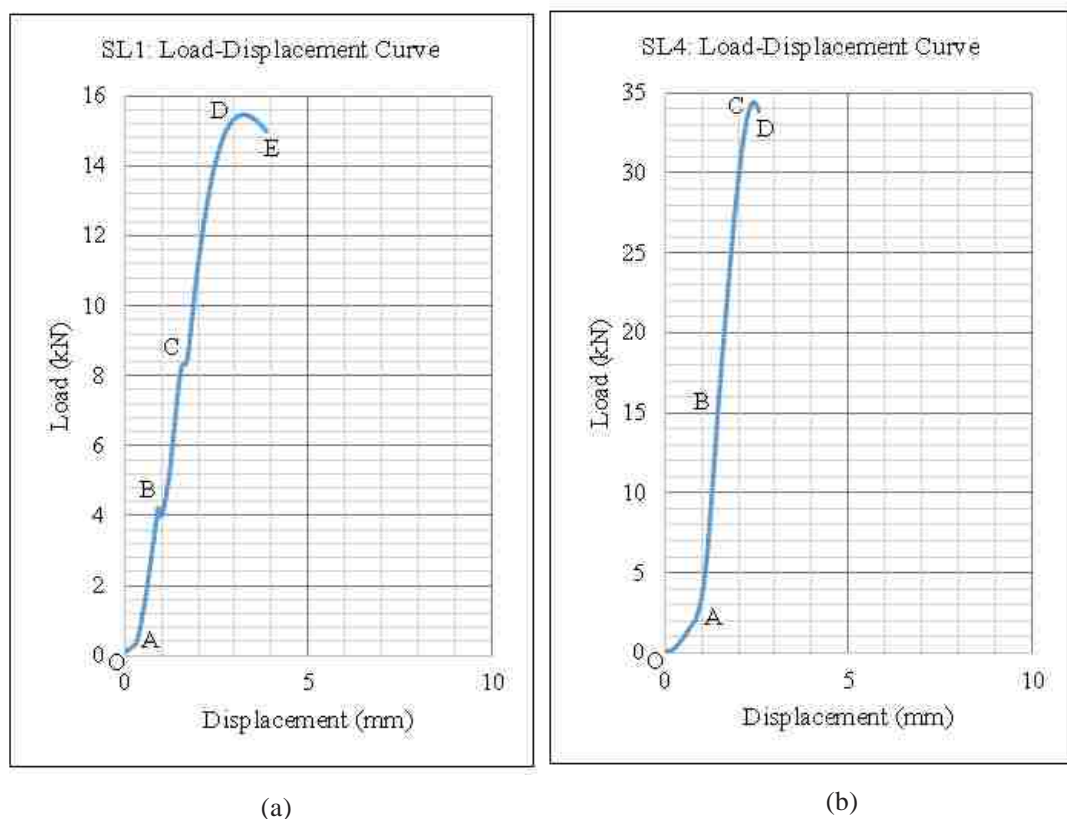
Figure 65: Typical load displacement of (a) Tall (b) Short RHS piece between platens

Figure 66 shows the load-displacement data acquired for the six RHS pieces compressed between platens. Figure 66(a) represents the taller RHS pieces and Figure 66(b) represents the shorter RHS pieces.

The graphs for all six samples display similar load-displacement patterns.

(a)   (b)
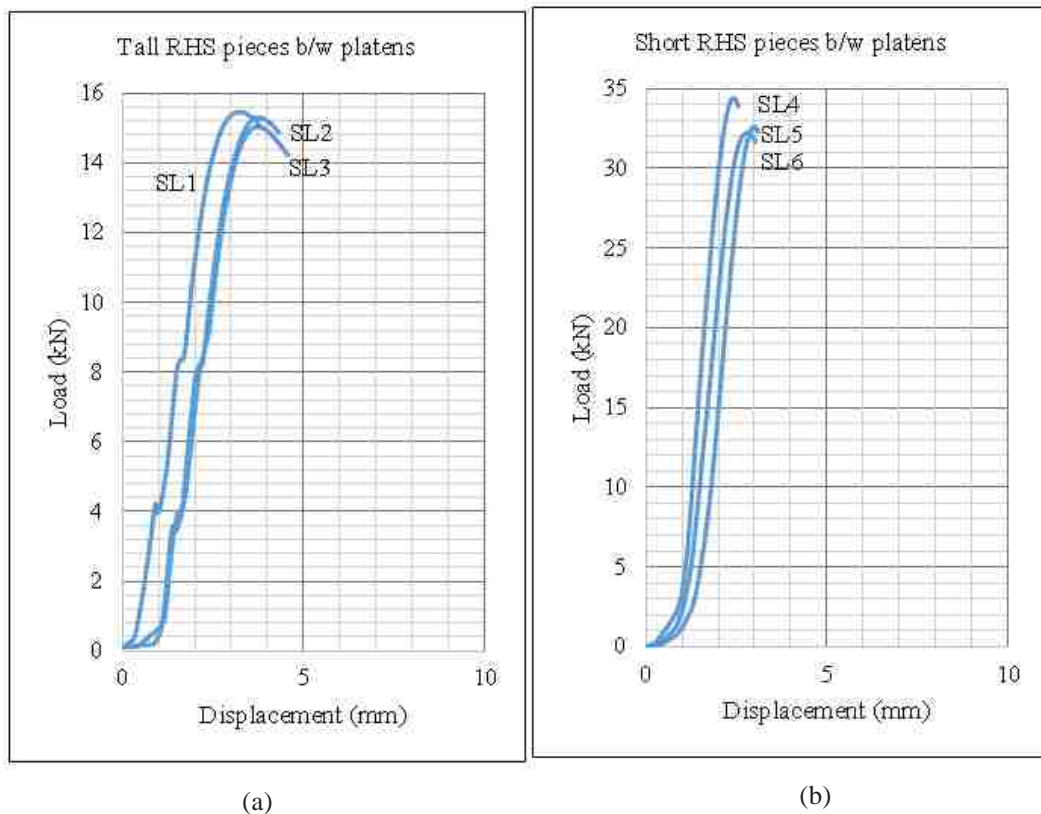
Figure 66: Load-displacement curves for (a) Tall (b) Short RHS pieces between
platens

Table 19 below summarizes the maximum load of the six RHS pieces
compressed between platens. The taller RHS pieces show significantly lower load-
carrying capacities than the shorter ones.

Table 19: Maximum load of RHS pieces between platens

RHS piece #	Maximum Load (kN)
SL1	15.48
SL2	15.28
SL3	15.02
SL4	34.39
SL5	32.58
SL6	32.24

3.5 Experiment 4 – Compression of RHS Pieces between Wearpads

- Description of the Machine

  As explained in section 2.4

- Description of the specimen

Specimen specifications and method of manufacturing are the same as in section 3.4. The thickness measurements taken using a Vernier calipers at points A-J shown in Figure 43 are listed for RHS pieces compressed between wearpads in Table 20 and Table 21.

Table 20: Thickness measurements of tall RHS pieces between wearpads

Specimen	Thickness (mm)									
	A	B	C	D	E	F	G	H	I	J
SLW1	3.18	3.17	3.19	3.15	3.18	3.16	3.19	3.18	3.19	3.19
SLW2	3.16	3.16	3.15	3.15	3.19	3.16	3.17	3.15	3.18	3.17
SLW3	3.14	3.16	3.16	3.17	3.16	3.15	3.15	3.16	3.17	3.15

Table 21: Thickness measurements of short RHS pieces between wearpads

Specimen	Thickness (mm)									
	A	B	C	D	E	F	G	H	I	J
SLW4	3.01	3.04	3.02	3.00	3.01	3.01	3.02	3.00	3.00	3.00
SLW5	300	3.01	3.01	3.03	3.02	3.00	3.01	3.01	3.02	3.02
SLW6	3.00	3.01	3.02	3.02	3.01	3.00	3.00	3.02	3.01	3.02

- Description of the process

The assembly of RHS piece loaded between wearpads is very similar to the assembly explained in section 3.3 where the RHS ring is placed between the top and bottom wearpads.

o For the taller RHS piece, the assembly is shown in Figure 67 and is explained as follows:

The wearpads comprises of an assembly of four rectangular cubes welded onto a square platen of 150 mm length and 150 mm width. Each rectangular cube has a c/s of 25 mm x 15 mm. The wearpads are placed on the RHS piece such that the 25 mm length is parallel to the length of the web. Also, the wearpads are welded at a distance of 10 mm from the square platen edges.

The top wearpad has a shallow groove on its upper surface to accommodate the load distributor. As explained in section 3.2, the load distributor allows for a better, more uniform distribution of load on the tall RHS piece.

Figure 67: Loading assembly of RHS piece (height = 350 mm) between wearpads

o   For the shorter RHS piece, the assembly is shown in Figure 68 and is

explained as follows:

The wearpads comprises of an assembly of four rectangular cubes welded onto a square platen of 100 mm x 100 mm cross-section. Each rectangular cube has a c/s of 10 mm x 10 mm. Also, the wearpads are welded at a distance of 10 mm and 7.5 mm from the square platen edges. The wearpads are placed on top of the RHS piece flange such that the distance of the rectangular cubes from the RHS piece web is 7.5 mm.
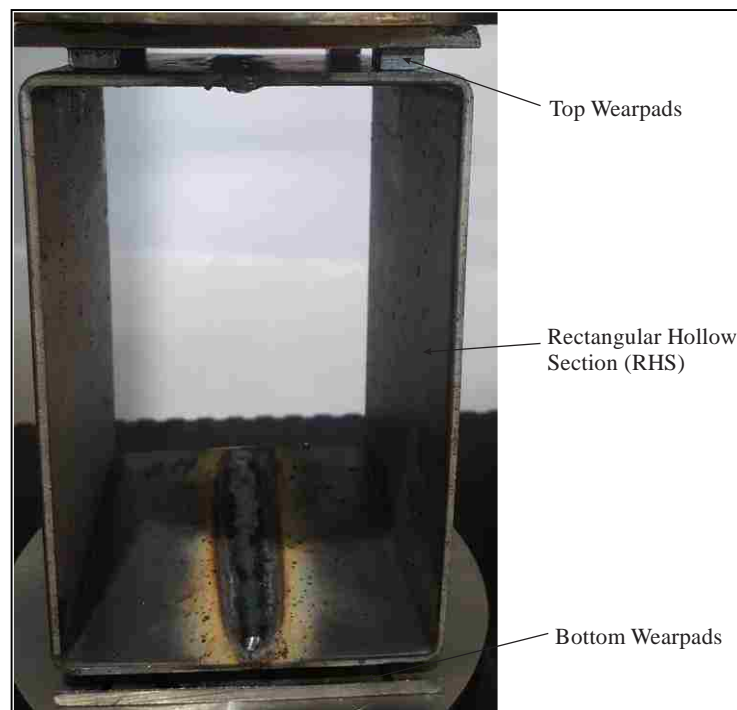
Figure 68: Loading assembly of RHS piece (height = 150 mm) between wearpads

- Characteristics of Loading between wearpads

As explained in section 3.3, wearpads apply 'patch loads' on portions of the flat, top and bottom flanges of the RHS pieces in contact with them.

Once the load application is started, the top flange starts sagging and the bottom flange starts hogging causing the load distribution to move towards and eventually

concentrate on the outer edges of the wearpads. In short, the wearpads transmit forces through the four areas which maintain contact with the RHS piece flanges.

- o *Initial Stage – Uniform loading under the wearpads*

Each flange of the RHS piece is in contact with four wearpads. In the initial stage, contact between the flange and the wearpads show full surface contact. Therefore, effectively on each flange, load acts on it in the form of patch loads at four different locations. The RHS piece webs remain undeflected and at right angles to the flanges as shown in Figure 69 below.
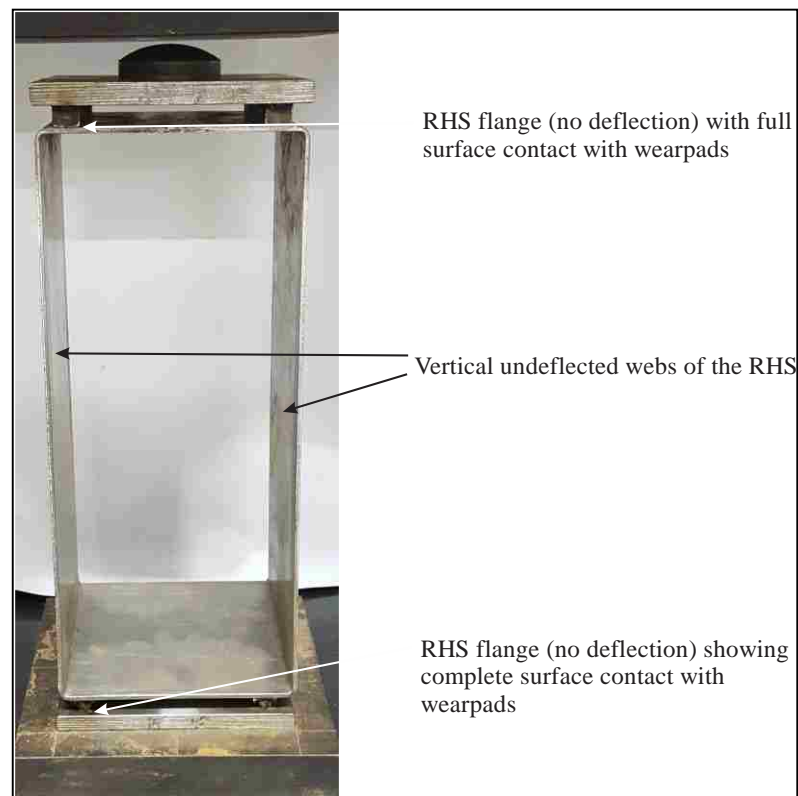
Figure 69: Initial stage of RHS piece between wearpads

- o *Progress into the process – Bending of the flange with no contact at the centre*

On increasing the load, the top flange begins to sag and the bottom flange hog. Contact between the wearpads and the flanges fast moves from full surface to part-

surface due to the bending of the flanges. The webs too begin to bulge outwards in this stage as shown in Figure 70.
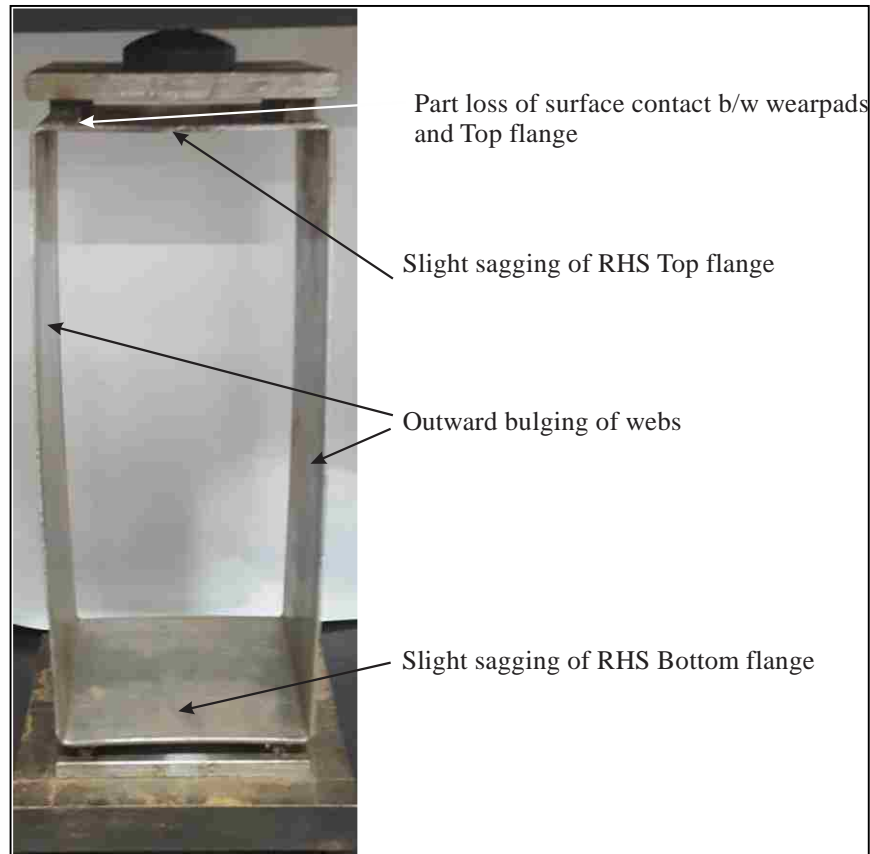
Figure 70: Initiation of flange bending and web bulging of RHS piece between wearpads

- o *Sufficient Progress into the process – Visible deformations of the flanges and the webs with significant loss of contact area*

This stage is marked by an obvious and exaggerated deformation on all four plates of the RHS pieces – the two flanges and the two webs. Contact between the flanges and the wearpads is almost reduced to a line/ edge contact at the outer edges of the wearpads as shown in Figure 71.
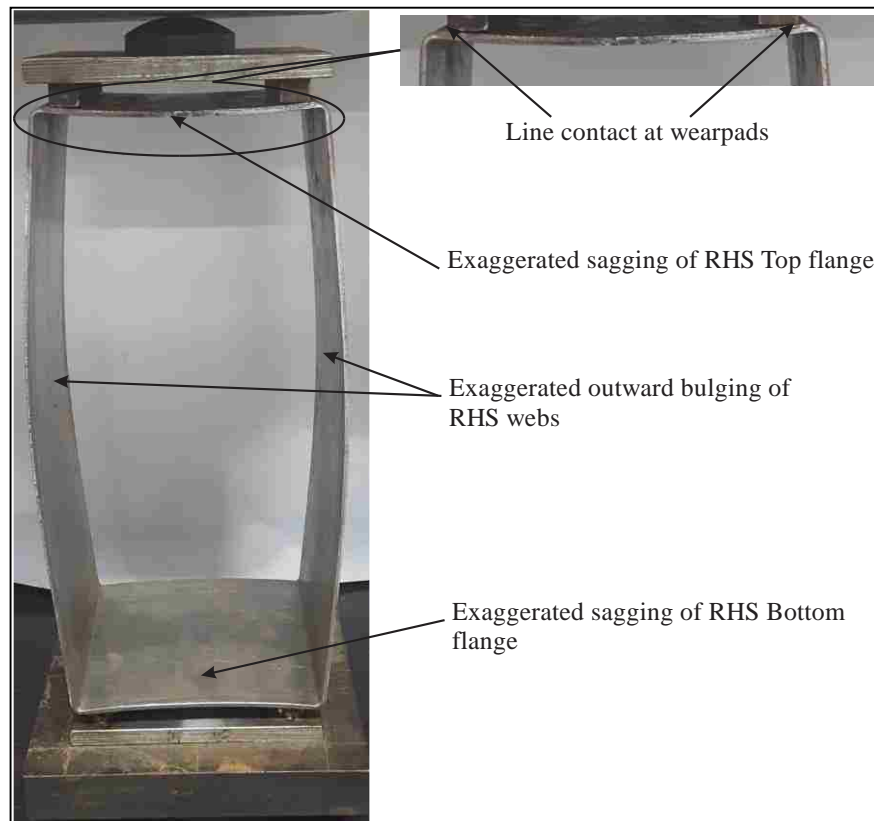
Figure 71: Exaggerated web and flange deflection RHS piece between wearpads

o *Final stage – Hinged webs and bent flanges*

The outer fibers on the inner side of the webs have started yielding at this stage while the wearpads are still closing and thus increasing the bending. This causes more bending stresses and progressive yielding continues. This form two hinges at the mid-height of the webs. The RHS piece now consists of webs hinged at the mid-height and bent flanges as shown in Figure 72.

Figure 72: Hinged webs and bent flanges of RHS piece between wearpads

- Load Displacement curve

Like the RHS piece loaded between platens, Figure 73(a) shows a typical load-displacement curve obtained for a RHS piece of height 350 mm (sample SLW1) compressed between wearpads. Figure 73(b) shows a typical load-displacement curve obtained for the shorter RHS piece of height 150 mm (sample SLW4) compressed between wearpads.

Both the graphs display a similar trend. Figure 73(a) representing the longer sections is marked by five regions, the region OA where complete contact between the wearpads and RHS piece is being established, the elastic region AB, the elasto-plastic regions BC and CD, and the post-yield region DE. Figure 73(b) representing the

shorter sections is similar to Figure 73(a), except that the elasto-plastic area has only one region BC.
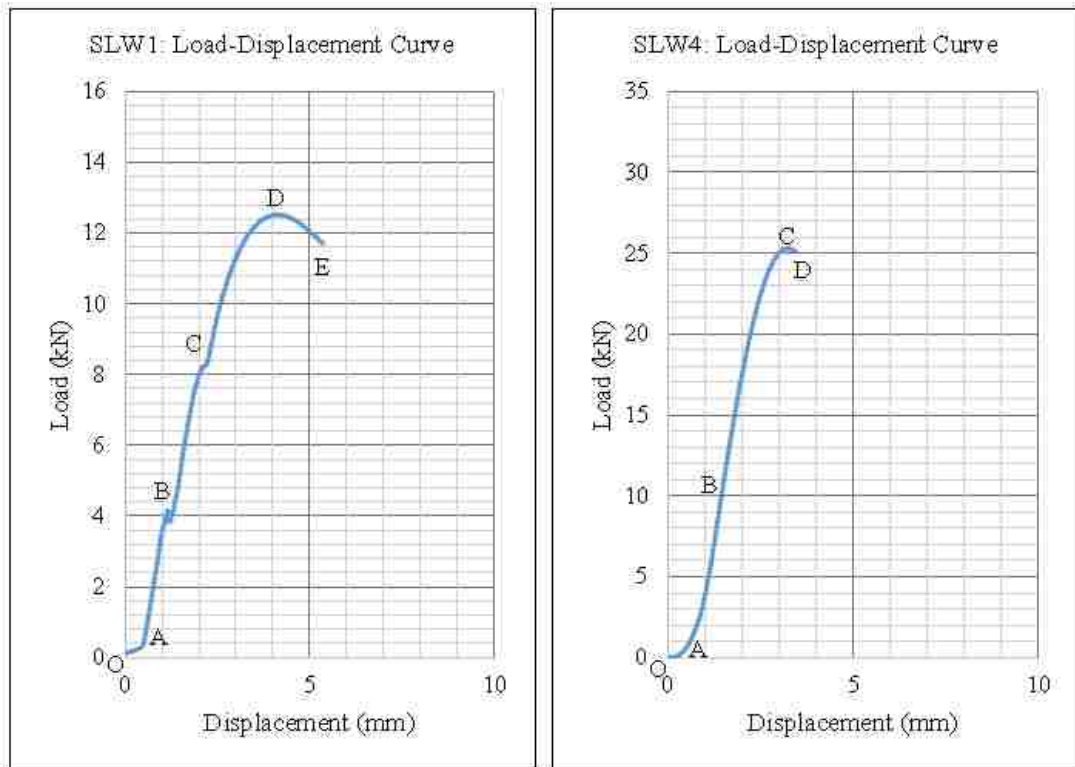
Figure 73: Typical load-displacement curve of (a) Tall (b) Short RHS piece between wearpads

Figure 74(a) represents the load-displacement curves for the taller RHS pieces and Figure 74(b) represents the load-displacement curves for the shorter RHS pieces. The graphs for all six RHS pieces display similar load-displacement patterns.

(a)   (b)
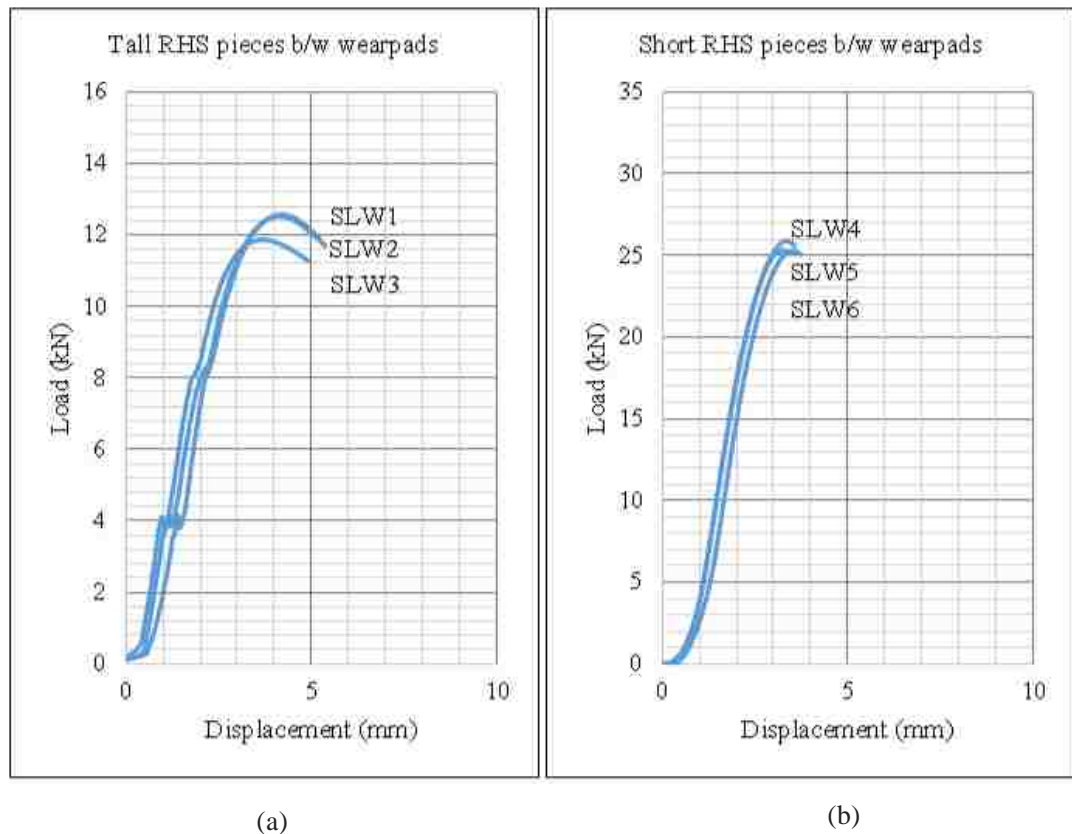
Figure 74: Load-Displacement curves for (a) Tall (b) Short RHS pieces between wearpads

Table 22 below summarizes the maximum load of the six RHS pieces compressed between wearpads.

Table 22: Maximum load of RHS pieces between wearpads

RHS piece #	Maximum Load (kN)
SLW1	12.57
SLW2	12.50
SLW3	11.88
SLW4	25.84
SLW5	25.29
SLW6	25.26

- Conclusions and Observations

  - Buckling is indicated by the rapid outward bulging of the webs

  - The flanges of the RHS piece bend in a concave manner.

  - Visually, the shape of the RHS piece when loaded between wearpads follows a similar pattern as the RHS piece loaded between platens with the outward bulging of the webs and inward bending of the flanges.

  - However, Table 19 and Table 22 show that for a given set of geometrical parameters, the maximum load value of a RHS piece compressed between wearpads is lower than when compared to a RHS piece compressed between platens.

  - As the load increases, the flanges of the RHS piece separate from the platen or the wearpads.

  - In the limiting condition, contact between the RHS piece flanges and the platen or wearpad reduces to a line contact.

  - Similar to sections 3.2 and 3.3, the load-displacement curves for loading between platens and wearpads is defined by an elastic region, an elasto-plastic region and a post-yield region.

  - The load-displacement curves are slightly different for the taller and shorter sections, with the taller section showing a longer elasto-plastic region.

Chapter 4: Theoretical Development

The main tasks of this research are to explain '*how the overlap region of a telescopic beam behaves under a tip load*' and '*the development of a new generic approach to the design of telescopic beams based on parametric studies using FEA and statistical optimization*'. The task was explored further with a finite element analysis of a candidate telescopic beam and the evaluation of the results. The overlap area was further investigated and subdivided into two RHS rings or longer RHS pieces and a connecting middle part. Exploratory experiments were then carried out on RHS rings and longer RHS pieces. These were described in Chapter 3. The literature on relevant topics was reviewed and the salient points of the review are described in Chapter 2. With the findings from (a) the exploratory studies and (b) literature review, it is now possible to form a rough idea of the behavior of the overlap region and a methodology for the telescopic cantilever design for verification and validation. This chapter explains these two tasks. In order to do that, the behavior of the RHS rings, behavior of the RHS pieces and the results of the telescopic beam, together with the literature review were analyzed and evaluated as described in the sub sections.

4.1 Rectangular Ring between Platens

A rectangular ring is made up of two flanges and two webs as shown in Figure 75(a). The load is applied by the platens on the flanges. At the beginning, this can be considered as a uniformly distributed load. This load has to be taken up by the webs. This means that the top flange will have two upward reactions from the webs. If a beam is supported at the ends and a distributed or pressure load is applied, the result will be a bent beam as shown in Figure 75(b). This bending will increase as the load applied increases. The platen is a flat surface and because of the bending the middle

of the platen will lose contact with the middle of the beam as shown in Figure 75(c). In the limiting condition, the platen will have contacts at the extreme points only, i.e. near the webs, and there will only be a line contact (represented by a point in the 2D representation as shown in Figure 75(d). It is therefore safe to assume that the webs directly take up the load and the flanges are free from the load. This explanation is in agreement with the behavior of the rings compressed between platens in the exploratory experiments in section 3.2.
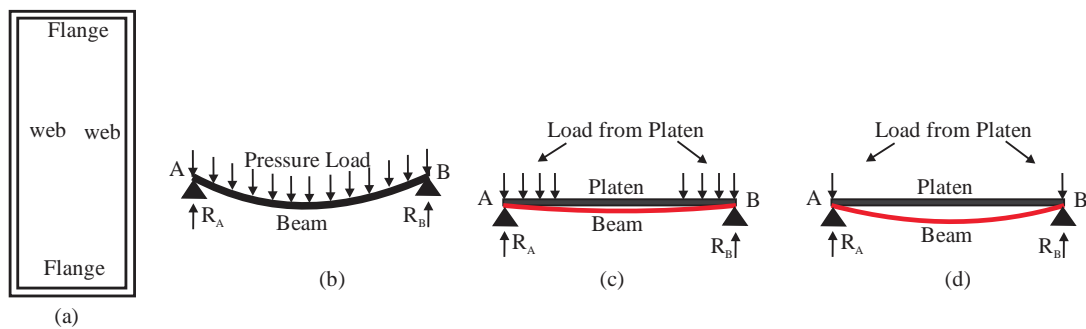
Figure 75: (a) RHS ring assembly (b) Pressure load on RHS ring top flange (c) Loss of contact in platen loading (d) Line contact in limiting condition of platen loading

Further, the sagging of the top flange will try to rotate the flange at the ends. But the webs will resist this rotation and create reaction moments at the joints. In the limiting condition, the loading in the top flange can be assumed to be as shown in Figure 76(a). Considering the webs, the reaction moments in the flanges have to be balanced for equilibrium, in the corners where the flanges meet the webs. To meet this requirement the webs will have reaction moments acting in the opposite directions to those in the flange. The loadings in the right web are shown in Figure 76(b).

Moment Balancing
Rotation Resisting Moment

Moment Balancing
Rotation Resisting Moment

Web Reaction

Web Reaction

(a)

Load from Platen

Moment Resisting
Rotation

Moment Resisting
Rotation

Load from Platen

(b)
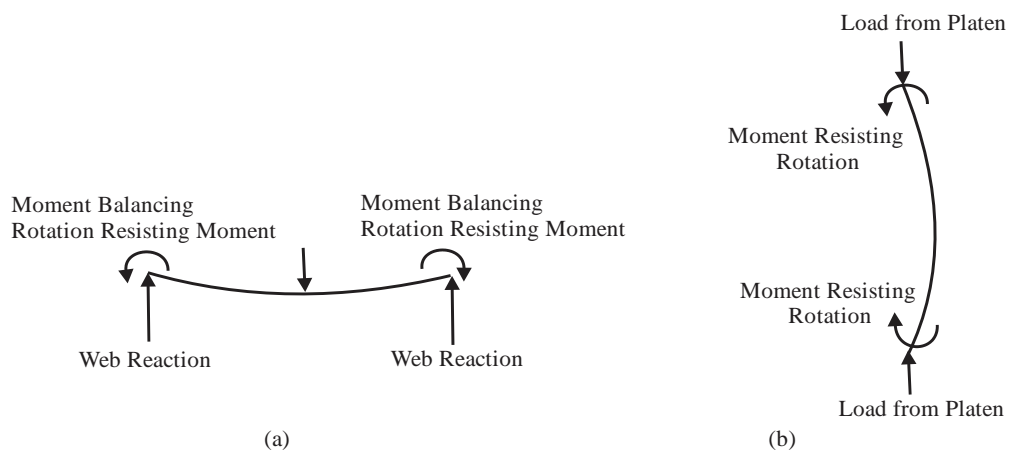
Figure 76: Loadings in the top flange and right web of a ring

In summary when a rectangular ring is loaded between platens, the flanges will behave like beams subjected to end moments and forces. The webs will behave like columns subjected to compressive loads and end moments. This is similar to a column with eccentric loading. Figure 77 schematically represents the ring under loading between platens.

Moment Balancing
Rotation Resisting Moment

Load from
Platens

Web
Reactions

Moments resisting
rotation

(a)

(b)

(c)
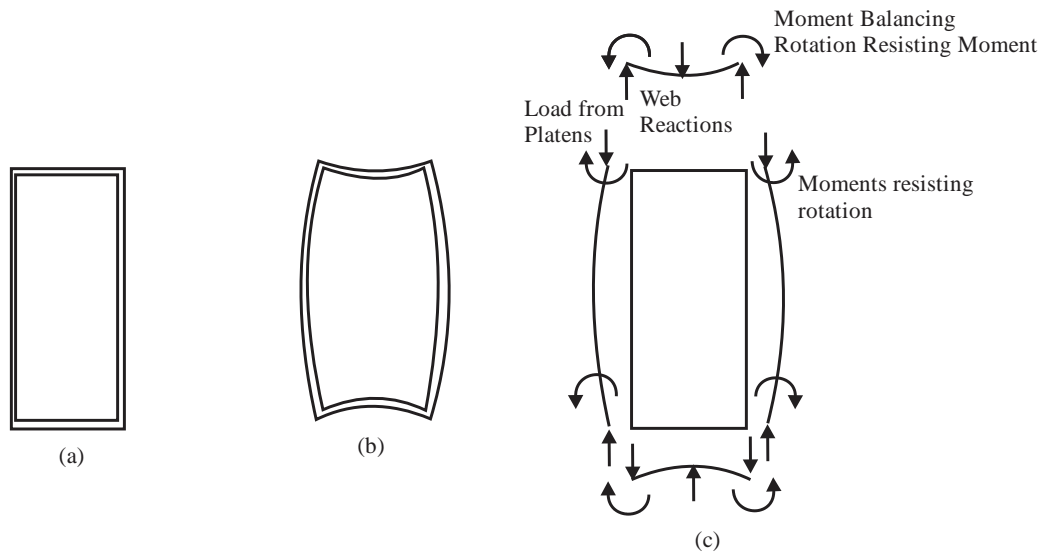
Figure 77: (a) Unloaded RHS ring (b) Deformed RHS ring shape(c) Force diagram of RHS ring under loading between platens

4.1.1 Analysis of the Web of a Rectangular Ring

Now consider the left web in the slightly bent position as shown in Figure 78. This web takes half of the load from the platens at both ends. Figure 78(a) represents the left web.
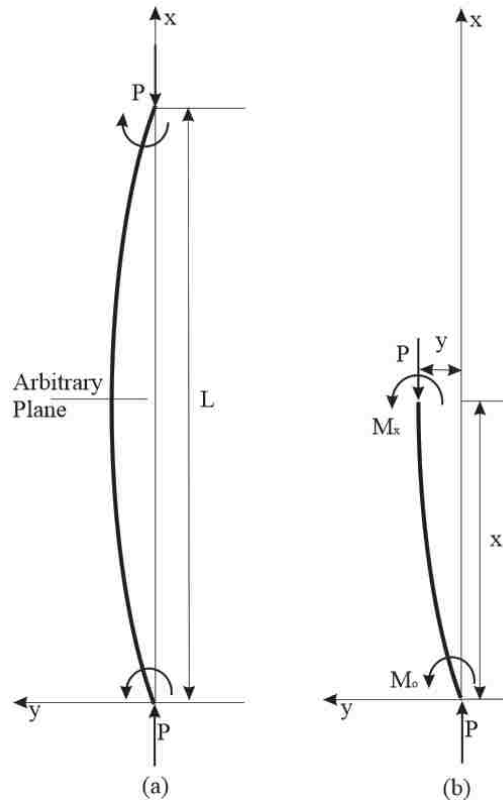
Figure 78: (a) Deformed left web (b) Forces and moments on section of left web

The free body diagram shown in Figure 78(b) shows the bending moment in a section at a distance x from the y axis along the x axis. The bending moment is

$$M_x = -M_0 - Py \qquad (4.1)$$

The governing differential equation is

$$EI \frac{d^2 y}{dx^2} + Py = -M_0 \qquad (4.2)$$

Substituting $k^2 = \dfrac{P}{EI}$ in (4.2), the differential equation is

$$\frac{d^2 y}{dx^2} + k^2 y = -\frac{M_0}{EI} \tag{4.3}$$

Its boundary conditions are $y = 0$ when $x = 0$ and $x = L$

The general solution for this differential equation is

$$y = A\cos kx + B\sin kx \tag{4.4}$$

Its particular solution can be of the form $y_p = C$ and the complete solution is

$$y = A\cos kx + B\sin kx + C$$

Substituting for y_p and its derivatives in (4.3) gives

$$k^2(C) = -\frac{M_0}{EI}$$

$$\therefore C = -\frac{M_0}{EI \times k^2} = -\frac{M_0}{P} \quad \left(\because k = \sqrt{\frac{P}{EI}} \right)$$

The full solution is

$$y = A\cos kx + B\sin kx - \frac{M_0}{P} \tag{4.5}$$

Substituting the boundary conditions gives

$$A = \frac{M_0}{P} \text{ and } B = \frac{M_0}{P}\left(\frac{1 - \cos kL}{\sin kL} \right) = \frac{M_0}{P}\tan\left(\frac{kL}{2} \right)$$

The full solution is

$$y = \frac{M_0}{P}\left(\cos kx + \tan\left(\frac{kL}{2} \right)\sin kx - 1 \right) \tag{4.6}$$

Differentiating once gives

$$y' = \frac{M_0}{P}\left(-k\sin kx + k\tan\left(\frac{kL}{2} \right)\cos kx \right) \tag{4.7}$$

When $x = 0$, $y' = \frac{M_0}{P}\left(k\tan\left(\frac{kL}{2} \right) \right)$

4.1.2 Analysis of the Bottom Flange of a Rectangular Ring
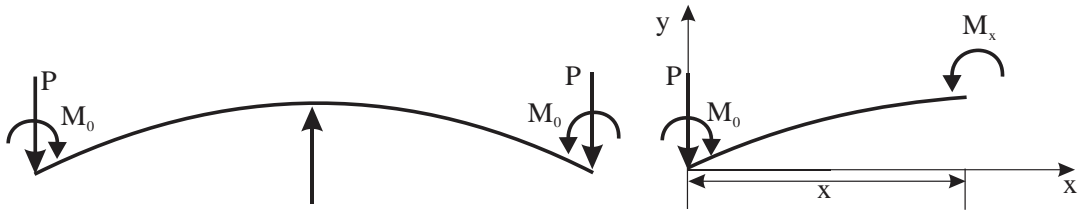
Figure 79: Forces and moments in the bottom flange

Consider a beam with both ends simply supported.

The bending moment is

$$M_x = M_0 - Px \tag{4.8}$$

The governing differential equation is

$$EI \frac{d^2 y}{dx^2} = M_0 - Px \tag{4.9}$$

Integrating once gives

$$EI \frac{dy}{dx} = M_0 x - \frac{Px^2}{2} + C \tag{4.10}$$

Integrating again gives $EIy = \dfrac{M_0 x^2}{2} - \dfrac{Px^3}{6} + Cx + D$

Therefore,

$$y = \frac{1}{EI} \left[\frac{M_0 x^2}{2} - \frac{Px^3}{6} + Cx + D \right] \tag{4.11}$$

Substituting $x = 0$, $y = 0$ in (4.11) gives

$$D = 0 \tag{4.12}$$

Substituting $x = \dfrac{l_1}{2}$, $\dfrac{dy}{dx} = 0$ in (4.10) gives

$$C = \frac{1}{8} \left[P l_1^2 - 4 M_0 l_1 \right] \tag{4.13}$$

Substituting (4.12) and (4.13) in (4.11) gives

$$y = \frac{1}{EI} \left[\frac{M_0 x^2}{2} - \frac{Px^3}{6} + \frac{1}{8} \left[P l_1^2 - 4 M_0 l_1 \right] x \right] \tag{4.14}$$

$$\text{Deflections at mid-point, } \delta_1 = \frac{1}{EI}\left[\frac{M_0(l_1/2)^2}{2} - \frac{P(l_1/2)^3}{6} + \frac{1}{8}\left[Pl_1^2 - 4M_0l_1\right]\frac{l_1}{2}\right]$$

$$\therefore \delta_1 = \frac{1}{8EI}\left[-M_0l_1^2 + \frac{1}{3}Pl_1^3\right] \tag{4.15}$$

4.2 Rectangular Ring between Wearpads

The load in this setup is applied by the wearpads on the flanges. At the beginning, this can be considered as uniformly distributed loads on two sections of a beam as shown in Figure 80(a). As the load increases the bending will also increase and separation between the wearpads and the flange will begin as shown in Figure 80(b).
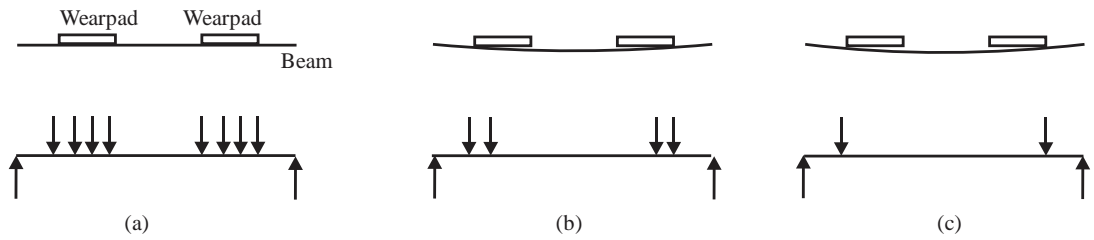
Figure 80: Loading through wearpads

The bending will increase further as the load applied increases and in the limiting condition the wearpads will have contacts at the extreme points only, i.e. near the webs, and there will only be a line contact. The forces will be similar to those shown in Figure 80(c). This explanation is in agreement with the behavior of the RHS Rings compressed between wearpads in the exploratory experiments in section 3.3.
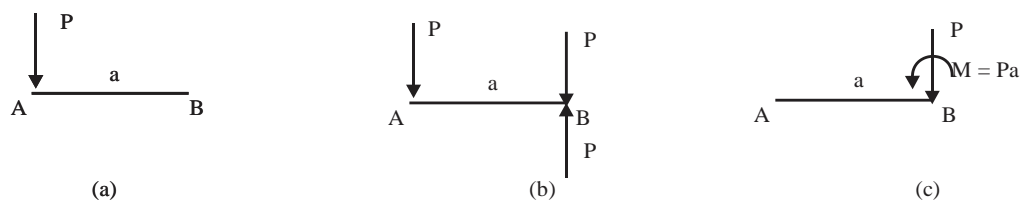
Figure 81: Force acting at a point in a structure

Now consider the force system in Figure 81(a) where a single force P is acting at point A at a distance a from point B in a body. If two forces of the same magnitude as P and opposite in direction are acting on point B as shown in Figure 81(b) they would not make any difference to the system. Now consider the force in A and the force opposite in direction acting at point B they form a couple. The force system can now be represented as a force in B and a moment as shown in Figure 81(c). Thus a force acting at a point in a structure can be represented by a force of the same magnitude and direction, and a moment acting at a different point in the structure.

Now consider the force system in Figure 82(a) where two forces P act at A and B at a distance a from the flange ends C and D. If two forces of the same magnitude as P, and opposite in direction act at each of the flange ends at C and D as shown in Figure 82(b), they would not make any difference to the system. Now, the force at A and the force opposite in direction at point C form a couple. Similarly, the force at B and the force opposite in direction at point D form a couple. Therefore, the forces acting at A and B in Figure 82(a) can be represented by forces and moments acting at C and D in the direction shown in Figure 82 (c). The two vertical forces at C and D shown in Figure 82(c) can be replaced by a single vertical force 2P acting at the flange center shown in Figure 82(d). This force 2P is balanced by the reaction forces at C and D shown in Figure 82(d). The moments caused by the wearpads shown in Figure 82

(c) cause counter reaction moments of the same magnitude from the flange as shown in Figure 82(d).
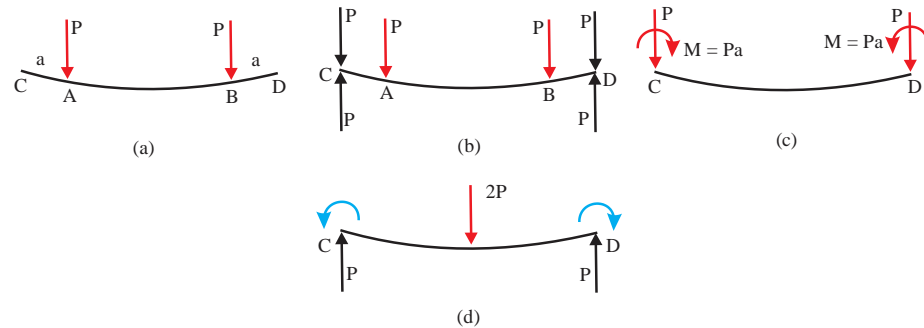
Figure 82: Load on the RHS ring top flange

Thus mathematically, loading through the wearpads is equivalent to creating an additional moment to the system compared to when loading is through the platens. These additional moments cause reaction moments that act in the same directions as the moments created when loading is through platens. Since the webs and flanges are connected, these reaction moments also have to come from the web and will be in the opposite direction to the reaction moments at the flanges. Figure 83 schematically represents the loading under wearpads.
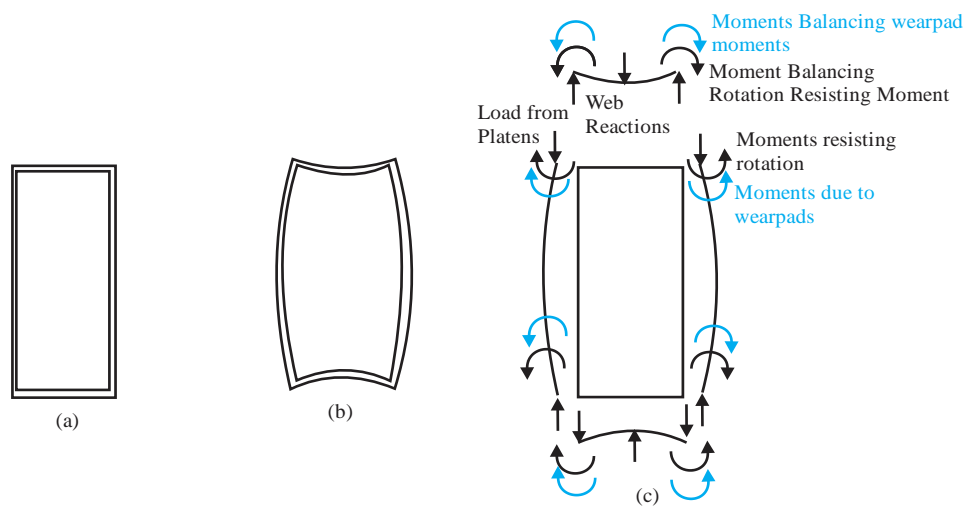
Figure 83: Unloaded RHS ring (b) Deformed RHS ring shape(c) Force diagram of RHS ring under loading between wearpads

4.3 Concluding Remarks on the Behavior of Rectangular Rings

The preceding sections and sub-sections provide in-depth analyses that can be used to hypothesize the behavior of a RHS ring under transverse loading in the following way:

1. The ring can be considered as an assemblage of two webs and two flanges. The behavior of the ring can be studied by analyzing the individual webs or flanges.

2. The free body diagrams of RHS rings show end reaction forces and end reaction moments as shown in Figure 77(c) and Figure 83(c).

3. The web in a ring can therefore be considered as a column under eccentric loading (because of the end reaction moments). This means that the buckling of the web will be due to yielding at the inner side (compressive side) of the webs at the mid-height.

4. The boundary conditions for the web under axial compression is neither pinned nor fixed. This means that the value for k_1 in the equation $P_{cr} = \dfrac{k_1 \pi^2 EI}{L^2}$ is between 1 and 4.

5. Stresses at the mid-height of the web are due to (a) the axial compression and (b) bending as a beam. Axial compressive stress is uniform throughout the cross section. The bending stress is compressive maximum at the inner fiber and tensile maximum at the outer fiber.

6. The magnitudes of the stresses are $\left(-\dfrac{P}{A} - \sigma_b \right)$ compressive in the innermost fiber and $\left(-\dfrac{P}{A} + \sigma_b \right)$ tensile at the outer most fiber. This means that yielding will start at the inner fibre and progress outwards.

7. The flanges in a RHS ring can be considered as a beam under end moments. It will have bending stresses and can yield at the mid span. This depends on the magnitude of the load and the dimensions of the flange.

8. Loading through wearpads will cause similar behavior as loading through platen except, with an additional end moment.

9. The ability of the material is used to accommodate the axial stress and the bending stress as explained in 6 above. This means that the additional end moment due to the wearpads would reduce the magnitude of load P before the RHS ring starts yielding. This has been the behavior observed in the exploratory experiments.

10. For a given value of the applied load, an RHS ring compressed between platens will show smaller lateral displacement at the web center as compared to when loaded between wearpads. This is again because of the additional moment caused by the wearpads. This has also been the behavior observed in the exploratory experiments.

4.4 RHS Pieces under Compression between Platens and Wearpads

Experimental investigations with rings gave the clues for the 10 observations explained in section 4.3. However, the load carrying capacity was reduced because of the small length of the ring. Exploratory experimentation with short and tall RHS pieces were carried out to find any difference in behavior.

In the exploratory investigation, an RHS piece was placed between platens and the load was applied by the platens on the flanges. The behavior was found to be similar to that of the ring excepting that the magnitude of the maximum load was much higher. At the beginning, the applied load can be considered as a uniformly distributed load. This load has to be taken up by the webs. This means that the top flange will have

two upward reactions from the webs and the load that would make it bend. This bending will increase as the load applied increases. The platen is a flat surface and as in the ring, because of the bending the middle of the flange will lose contact with the platen. In the limiting condition, the platen will have contacts at the extreme points only, ie near the webs, and there will only be a line contact. As considered in the rings, it is safe to assume that the webs directly take up the load and the flanges are free from the load. This explanation is in agreement with the behavior of the RHS pieces of two different sizes compressed between platens in the exploratory experiments. Compression between wearpads also showed a similar behavior.

4.5 Theoretical Analyses of Rings and RHS Pieces

Theoretical analysis is based on the assumption that a ring can be represented as an assemblage of two columns and beams and an RHS piece can be represented as an assemblage of two plates under transverse and another two under axial loadings. Analysis of the webs in the rings as columns reveal that ideally it would have a buckling load as $P_{cr} = \dfrac{k_1 \pi^2 EI}{L^2}$ as explained in section 1.3.4. The values of k_1 for some known boundary conditions are given in Table 4. However, the condition of the web of a rectangular ring has not been included in the table. The boundary condition here is neither simply supported nor fixed-fixed. This means k_1 for the current condition can lie within 1 and 4. However, it is not possible to find this value at present.

In the case of RHS piece, which is considered as an assemblage of plates the critical stress, is found to be $(\sigma_x)_{cr} = k_2 \dfrac{\pi^2 E}{12(b/t)^2 (1 - \upsilon^2)}$ in Chapter 2. Here again the

value of k_2 for the boundary conditions has to be known. At present, it is not possible to find this value.

In summary, the RHS ring can be represented as an assemblage of two columns and beams, and an RHS piece can be represented as an assemblage of two plates under transverse and another two under axial loadings. Although their analysis gave an insight on their behavior, the findings cannot be used in real life applications. Because of these reasons, a finite element method with statistical experimental design is proposed in section 4.6 below.

4.6 Methodology for Designing Telescopic Beams

Exploratory analysis of a telescopic beam and the analysis of the preceding sections, show that the overlap area of the inner beam of a telescopic cantilever is the vulnerable area for buckling. The overlap area can be analysed as a combination of two RHS rings or RHS pieces, and a connecting middle portion. The behavior of the RHS rings and RHS pieces has been explained in section 4.5. Also, it is known that buckling behavior is a case dependent occurrence. Considering all these, a seven stepped methodology for the design of the inner beam of a telescopic cantilever was derived. The steps are as follows:

i.   Consider the influencing factors for maximum load of a RHS ring and RHS piece and the assembly of the inner beam of a telescopic cantilever.

ii.   Design and conduct a screening experiment to identify the influencing factors for maximum load of the inner beam assembly

iii. Design and conduct a CCD experiment and fit the response surface for maximum load

iv.   Carry out a confirmation FE analysis to validate the response surface.

v. Consider significant factors and interactions in the fitted response surface

vi. Propose various combinations of the significant parameters that are essentially different conceptual designs and choose and optimize the design in terms of manufacturability.

vii. Conduct a validating analysis.

Figure 84 explains the methodology with a schematic diagram.
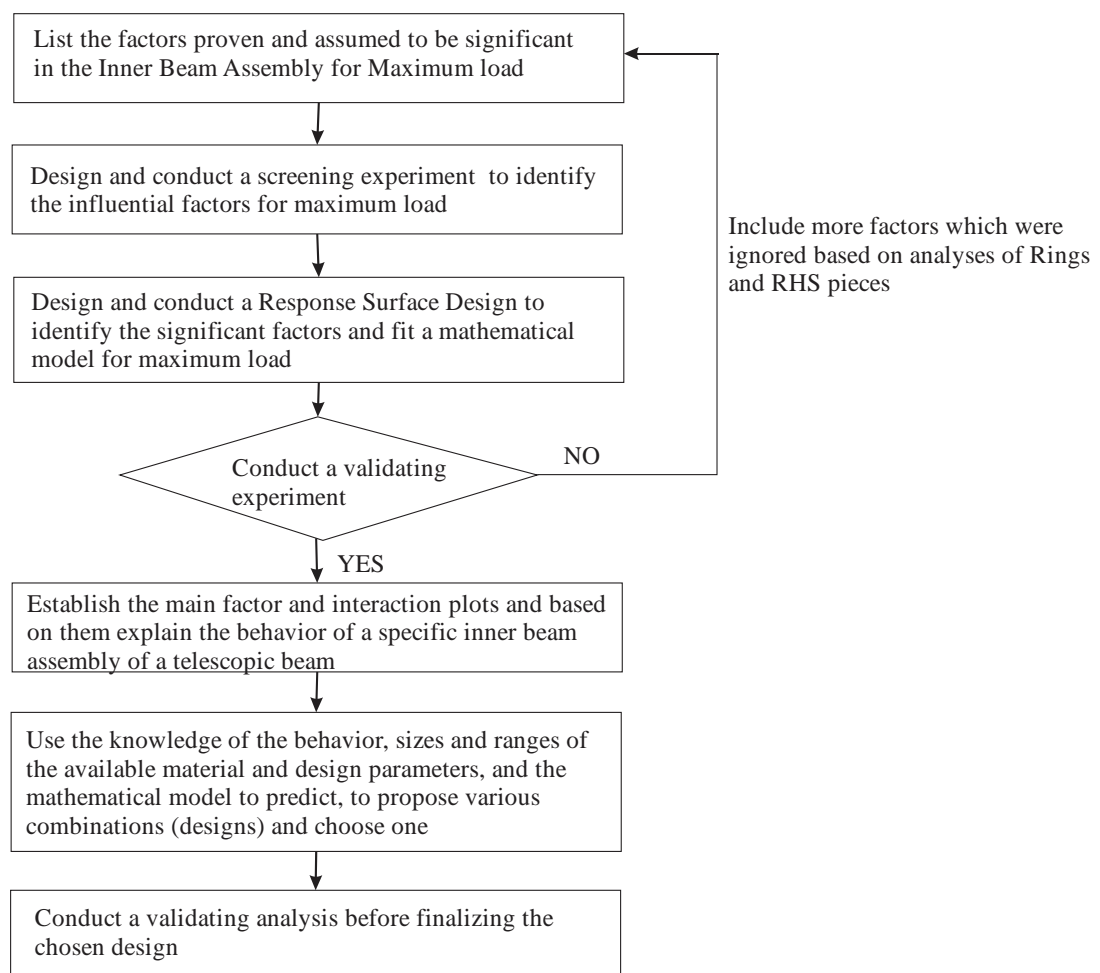
Figure 84: Methodology for designing telescopic cantilever beams

Chapter 5: Parametric Studies on RHS Rings

The previous chapter highlighted that completer theoretical calculations could not be made to calculate the behavior of the overlap region in telescopic beams because of unknown boundary conditions of the constituent webs and flanges. Hence section 4.6 in Chapter 4 highlights the methodology for the design of the inner beam assembly of the telescope using FEA and DOE. The design methodology includes the factors influencing the maximum load capacity of RHS rings and pieces compressed between wearpads. Therefore, this chapter aims to determine the geometric factors that affect the behavior of RHS rings under compressive loads between wearpads with FE models and experimental designs.

FE models for both RHS ring between (a) platens and (b) wearpads are built and validated against the experiments on RHS rings shown in sections 3.2 and 3.3. Validation is done against the RHS deformed shape, maximum load value of the RHS rings, and load-displacement curves between experiments and FEA.

Experimental designs were conducted using Minitab software. In the experimental design for the RHS rings between platens, only the Taguchi L_{12} screening experiment is carried out and the influencing parameters obtained here are compared to that obtained from the Taguchi L_{12} for RHS rings between wearpads to better understand the RHS ring behavior between wearpads.

The procedure in this chapter involves (a) FE Model validation- use validated model for further design of experiments (b) Taguchi L_{12} design – to identify influencing factors (c) CCD analysis – to confirm the factors influencing the maximum load capacity of the RHS rings and to generate a mathematical model for the maximum load (d) Confirmatory Experiment – to verify the mathematical model.

5.1 RHS Rings between Platens

FE Model: The FE model comprising of three parts—the top platen, the bottom platen, and the RHS ring is subjected to a Riks analysis using ABAQUS Standard Version 2017. A typical FE model representing RHS ring compression between platens is shown in Figure 85.
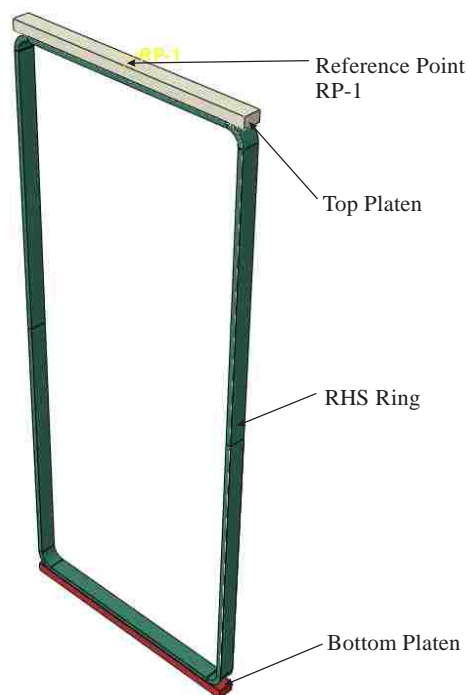
Figure 85: RHS ring between platens

- Assembly Details

The assembly consisting of the three parts were assigned the following interactions:

- o Bottom outer face of the RHS ring: assigned a frictional interaction with the bottom platen (Refer Figure 86(e))

- o Bottom Platen: encastred, thereby restricting all degrees of freedom (Refer Figure 86(c))

    o   Top outer face of the RHS ring: assigned a frictional interaction with the underside of the top platen (Refer Figure 86(d)).

    o   Top Platen: All degrees of freedom of the top platen were restrained apart from the vertical translation, thereby allowing for compression (Refer Figure 86(a)).

- Reference point

A reference point RP-1 was created at the center of the top face of the top platen and kinematically coupled with the top platen top surface for uniform application of the load on the Top Platen (Refer Figure 86(b)).

A displacement of -15 was applied through a reference point, RP-1.

<div align="center">(a)   (b)   (c)</div>

<div align="center">(d)   (e)</div>
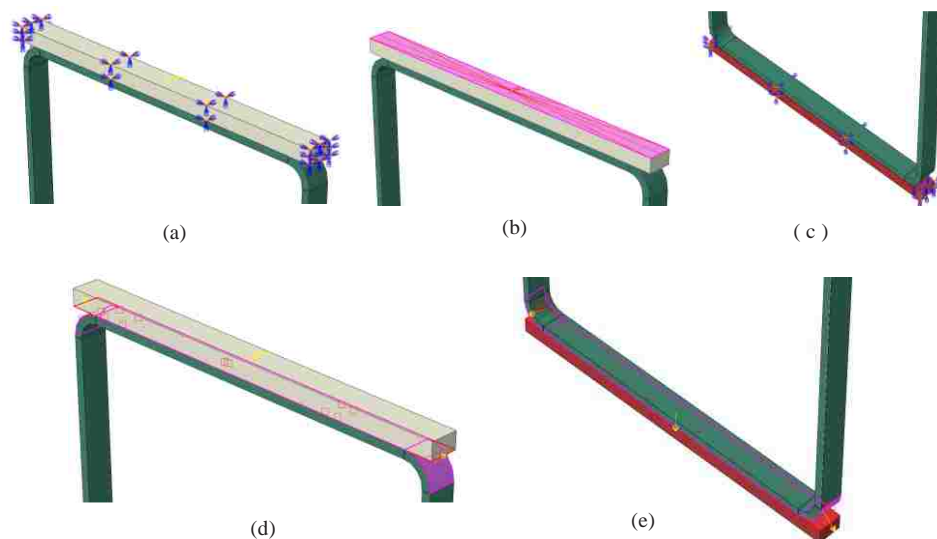
Figure 86: (a) Top platen constraints (b) Reference point coupling (c) Bottom platen encastre (d) Top platen interaction (e) Bottom platen interaction

- Mesh size and elements

The platens were assigned the solid element C3D8R and the RHS ring was assigned the shell element S4R where 'R' at the end of an element name in ABAQUS indicates an element with reduced integration [97].

A mesh analysis was carried out to determine an acceptable mesh size. A mesh size of 5 mm was determined for all three parts of the assembly.

- Material Properties

A test coupon from the sheet used to fabricate the RHS rings gave the material properties shown in Table 23. The test report is shown in Figure 121 of Appendix I.

The material of the RHS rings in the FE Model was assigned the properties shown in Table 23.

Table 23: Material properties of rings

Property	Value
Modulus of Elasticity	125,946 N/mm^2
Yield Stress	211.88 N/mm^2
Ultimate Stress	317.35 N/mm^2

- Dimensions

The FE model was built to the dimensions shown in Table 24.

Table 24: FE model part dimensions for RHS ring assembly

Part	Dimensions
RHS Ring	Height = 350 mm, Width = 150 mm, Corner Radius = 5 mm, Length = 10 mm, Thickness = 3 mm
Platens	150 mm width with 10 mm length

- Loading

Displacement of -15 applied at RP-1

- Validation of FE Model

o Load Validation

Table 25 shows a comparison of the maximum load values obtained from the experiments and the FE model. The load values are in agreement and hence the FE model is considered validated.

Table 25: Maximum load values comparison for RHS rings between platens

Sr. No.	Maximum Load (kN)	
	Experiment	FEA
Sample SR1	0.934	
Sample SR2	0.900	0.905
Sample SR3	0.978	

- Shape Validation

Shape Validation of the RHS ring is done by comparison and agreement of the RHS ring shape obtained from experiments and FEA as shown in Figure 87.
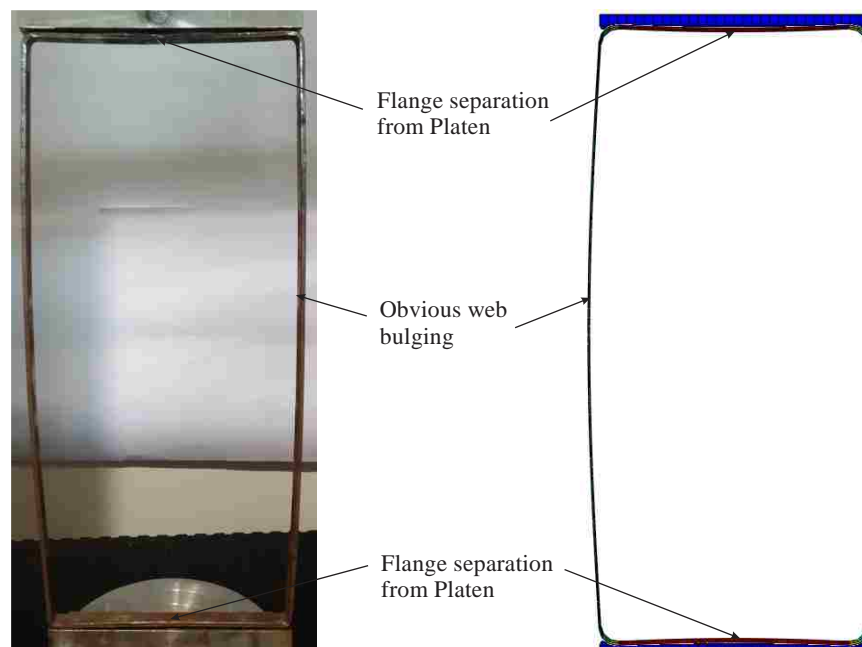
Figure 87: Deformed shape of RHS ring between platens in (a) Experiments (b) FEA

- Load-Displacement curve

The comparison of the load-displacement curves between the three experimental samples and the FE Model is shown in Figure 88.
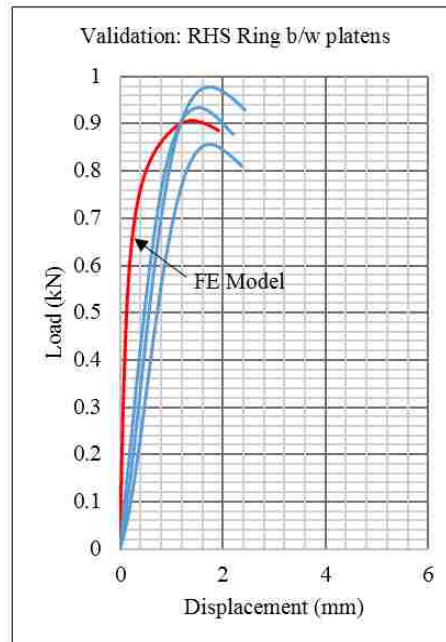
Figure 88: Load-Displacement curve validation for RHS rings between platens

The red curve indicates the load-displacement curve for the FE Model, while the three blue curves are the load-displacement curves experimentally obtained in section 3.2. Agreement between plots from the two methods validates the FE model.

Design of Experiments:

- Taguchi L_{12} design:
  - Possible Parameters

For the RHS ring between platens, the factors with their given levels shown in Table 26 were considered in the Taguchi L_{12} experiment.

Table 26: Factors and factor levels for L_{12} of RHS ring between platens

Factor No.	Factor	Level 1 (mm)	Level 2 (mm)
1	Corner Radius	2	4
2	RHS Thickness	3	4
3	RHS Height	350	450
4	RHS Width	200	250

As the FE model is now validated, its material properties can now be modified for the experimental design. The model properties were modified to that shown in section 3.1.1 for the sake of uniformity. The validated RHS ring model compressed between platens was modified to fit each run of the L_{12} matrix shown in Table 49 of Appendix II. Table 49 also includes the maximum load (response) corresponding to each run.

    o   Influencing Parameters

Figure 89 shows the factor plot obtained from the maximum load results in Table 49.
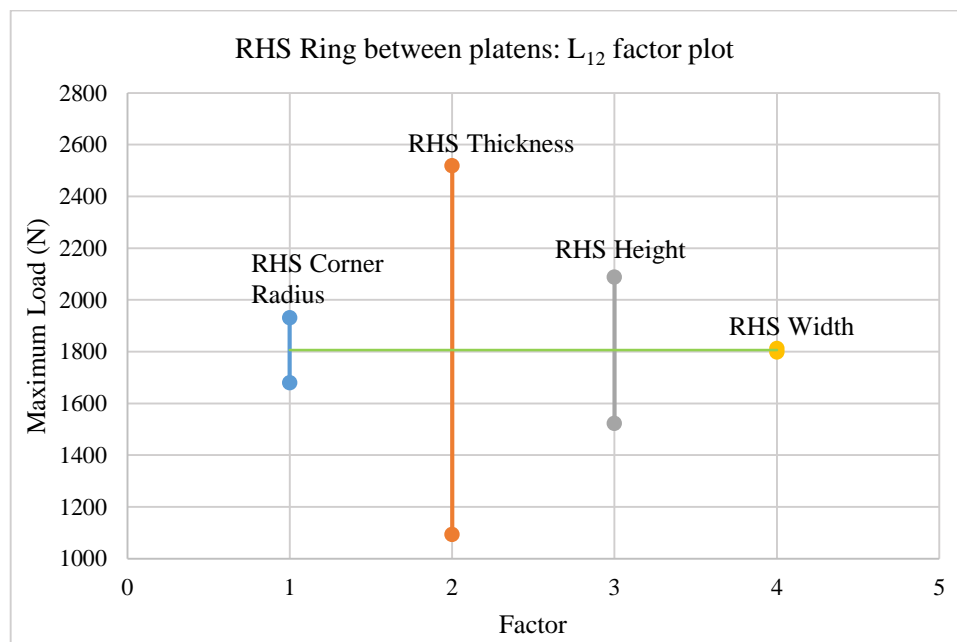
Figure 89: Factor plot for RHS rings between platens

The factors with the most influence have the largest effect on the maximum load. 'RHS Thickness' has the highest influence on the maximum load. Other influencing factors are the 'RHS Height' and 'RHS Corner Radius' determined from Figure 89.

5.2 RHS Rings between Wearpads

FE Model: The platens in section 5.1 are replaced by the top and bottom wearpads in this section. The top wearpads are built by extruding two rectangular cubes from the wearpad platens as shown in Figure 90(b). The RHS ring assembly is subjected to a Riks analysis using ABAQUS Standard Version 2017. A typical FE model representing RHS ring compression between wearpads is as shown in Figure 90(a).
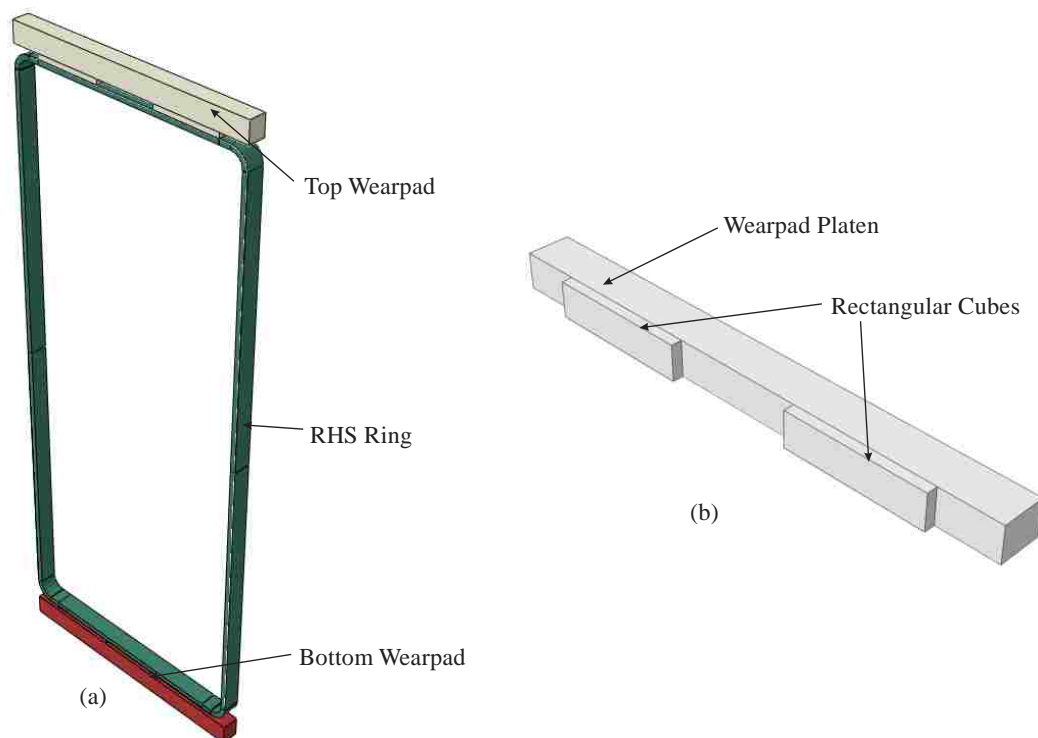
Figure 90: (a) RHS ring between wearpads assembly (b) Wearpad parts

- Assembly Details

    The assembly consisting of the three parts were assigned the following interactions:

    - o Bottom face of the RHS ring: assigned a frictional interaction with the two extrusions of the bottom wearpad (Refer Figure 91(e))

    - o Bottom Wearpad platen: is encastred, thereby restricting all degrees of freedom (Refer Figure 91(c))

    - o Top outer face of the RHS ring: assigned a frictional interaction with the two extrusions of the top wearpad (Refer Figure 91(d)).

    - o Top Wearpad platen: All degrees of freedom of the top wearpad platen were restrained apart from the vertical translation, thereby allowing for compression (Refer Figure 91(a)).

- Reference point

    Similar to section 5.1, a reference point RP-1 was created at the center of the top face of the top wearpad platen. RP-1 was kinematically coupled with the top platen top surface for uniform application of the load on the top Platen.

    Again, a displacement of -15 was applied through a reference point, RP-1.
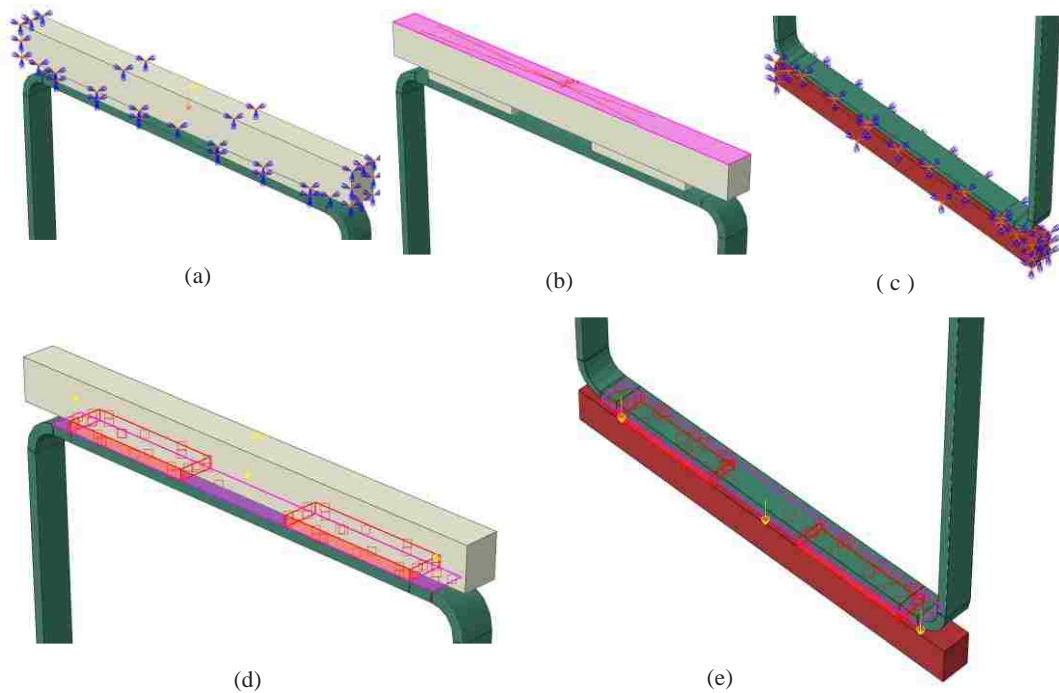
Figure 91: (a) Top wearpad platen constraints (b) Reference point coupling (c) Bottom wearpad platen encastre (d) Top wearpad interaction (e) Bottom wearpad interaction

- Mesh size and elements

  Same as in section 5.1

- Material Properties

  Same as in Table 23 of section 5.1

- Dimensions

  The FE model was built to the dimensions shown in Table 27.

Table 27: FE model part dimensions for RHS ring between wearpads

Part	Dimensions
RHS Ring	Height = 350 mm, Width = 150 mm, Corner Radius = 5 mm, Length = 10 mm, Thickness = 3 mm
Wearpads	Wearpad platen: 150 mm width with 10 mm length Rectangular pieces: Width = 55 mm, Length = 10 mm, WP Distance from edge = 10 mm

- Loading

  Displacement of -15 applied at RP-1

- Validation of FE Model

  o Load Validation

Table 28 shows a comparison of the maximum load values from the experiments and FEA. Agreement between the values validates the FE models.

Table 28: Maximum load values comparison for RHS ring between wearpads

Sr. No.	Maximum Load (kN)	
	Experiment	FEA
Sample SRW1	0.716	
Sample SRW2	0.706	0.738
Sample SRW3	0.731	

- Shape Validation

  Deformed shapes of the RHS Ring between wearpads is shown in Figure 92. Identical deformed shapes from experiments and FEA validates the FE model.
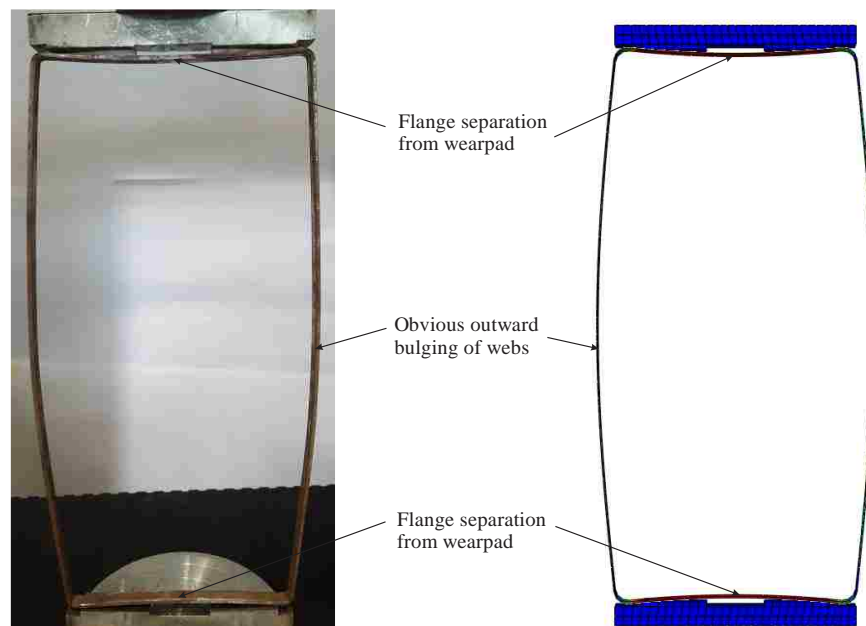
Figure 92: Deformed shape of RHS ring between wearpads in (a) Experiments (b) FEA

- Load-Displacement Curve

The load-displacement comparison plot between the three experimental samples and the FE Model is shown in Figure 93. Agreement between them validates the FE model.
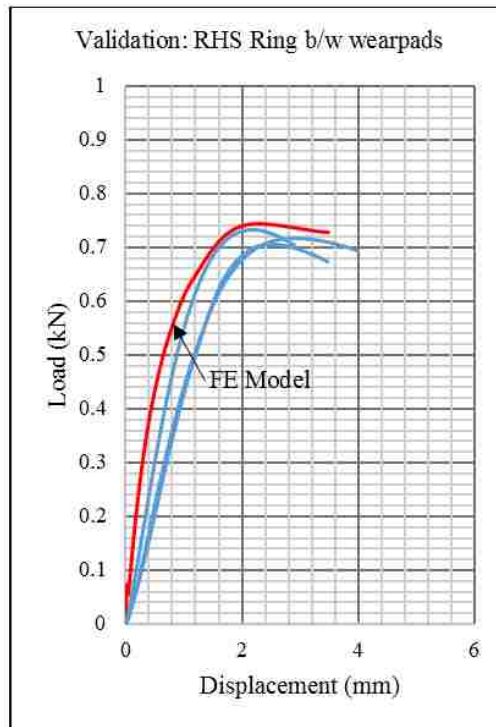
Figure 93: Load-displacement curve validation for RHS ring between wearpads

Design of Experiment

- Taguchi L_{12} design:
  - Possible Parameters

Table 29 shows the factors and levels considered for the L_{12} experiment of the RHS Rings between wearpads.

Table 29: Factors and factor levels for L_{12} of RHS ring between wearpads

Factor No.	Factor	Level 1 (mm)	Level 2 (mm)
1	WP-Web Distance	5	10
2	WP Width	50	70
3	RHS Corner Radius	2	4
4	RHS Thickness	3	4
5	RHS Height	350	450
6	RHS Width	200	250

Table 50 in Appendix II shows the maximum load values corresponding to each run of the L_{12} design matrix for RHS rings between wearpads.

o   Influencing Parameters

Figure 94 shows the factor plot obtained from the data in Table 50. Again, like in section 5.1, 'RHS Thickness' has the highest influence on the maximum load. Other influencing factors from Figure 94 are 'RHS Height' and 'WP-Web Distance'.
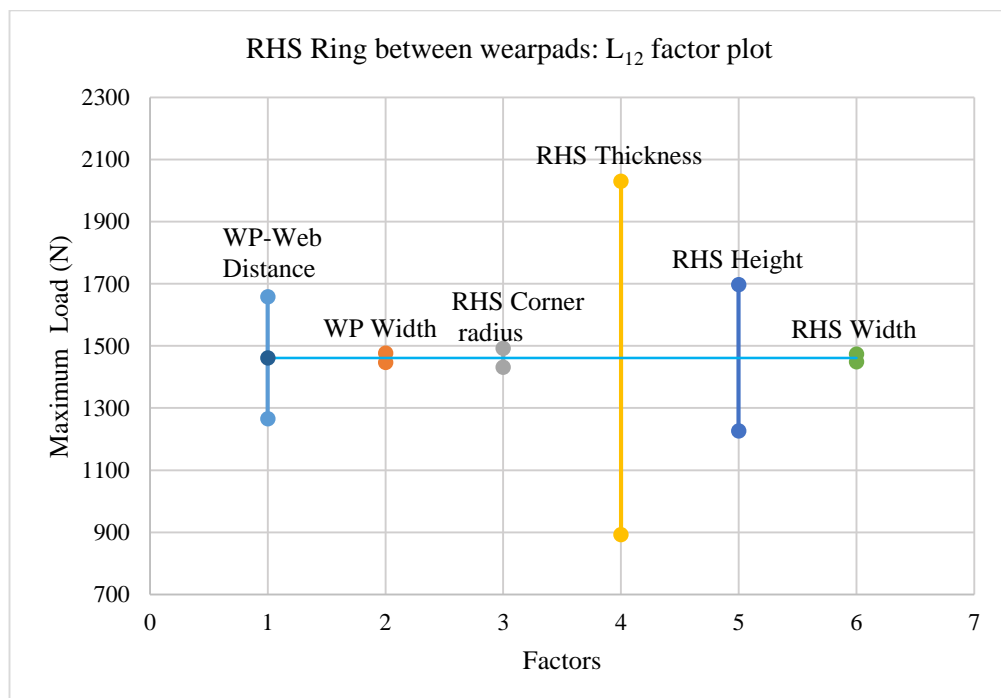
Figure 94: Factor plot for RHS rings between wearpads

- CCD

Minitab software was used to develop a CCD to conduct computer experiments and fit a response surface for the maximum load with the main aim of verifying the CCD model and hence validating the influencing factors obtained for the RHS rings between wearpads to be considered further in Chapter 7. For this design, the value for α was kept at 2. The values of the coded levels for the three most influencing factors selected from Figure 94 are given in Table 30.

Table 30: Values for the coded factor level for RHS ring between wearpads

Coded value	-2	-1	0	1	2
RHS Thickness	3	3.25	3.5	3.75	4
RHS Height	350	375	400	425	450
WP-Web Distance	6	7	8	9	10

The validated RHS Ring model compressed between wearpads was modified to fit each run shown in Table 51 of Appendix II. Table 51 also includes the maximum load (response) corresponding to each run.

- Statistical Analyses of the Results and Evaluations

The results from the CCD are given in the form of a mathematical model, main effect plots and interaction plots.

  o The Response Surface:

Let the following parameters to be named in the way expressed below.

Maximum Load   p

RHS thickness x_1

RHS Height x_2

WP-Web Distance x_3

From the CCD analysis, the model is represented by:

$$p = 1276.65 + 257.56x_1 - 90.31x_2 - 56.51x_3 + 18.10x_1^2 + 7.26x_2^2 + 3.32x_3^2$$
$$- 25.89x_1x_2 - 10.59x_1x_3 + 12.39x_2x_3$$

(5.1)

Equation (5.1) can be mathematically manipulated to get the value combination of the parameters x_1, x_2, x_3 to obtain a target maximum load p.

For the three selected factors, the model has $\frac{1}{2}(3+1)(3+2) = 10$ terms. The degree of contribution varies for each factor. The Pareto Chart shown in Figure 95 indicates the significant main factors and interactions from the CCD.
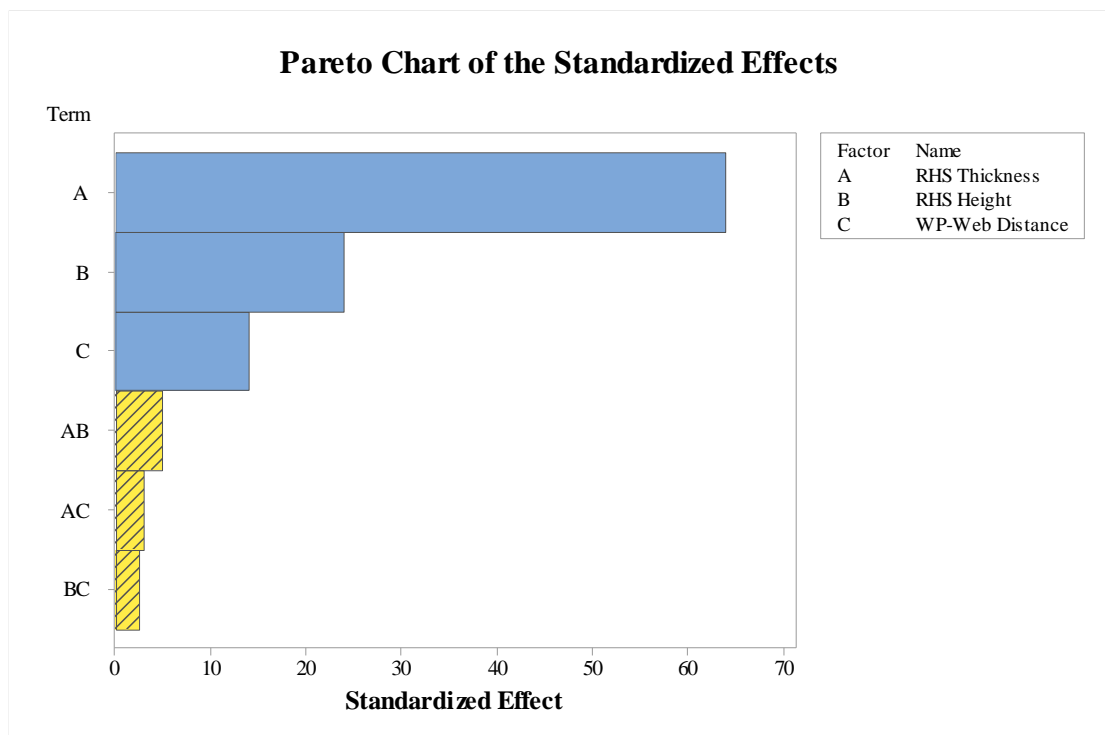
Figure 95: Pareto chart for RHS ring between wearpads

The p-values for all the factors and interactions are shown in Table 31. For a 95% confidence interval, any factor with a p-value ≤ 0.05 is considered significant. Only the factors and interactions with p-value ≤ 0.05 are shown in Figure 95.

Table 31: P-value for CCD model of RHS ring between wearpads

Term	P-value
Linear	
RHS Thickness	0.000
RHS Height	0.000
WP-Web Distance	0.000
Square	
RHS Thickness* RHS Thickness	0.000
RHS Height*RHS Height	0.000
WP-Web Distance * WP-Web Distance	0.001
2-Way Interaction	
RHS Thickness*RHS Height	0.000
RHS Thickness* WP-Web Distance	0.000
RHS Height* WP-Web Distance	0.000

o   Validating mathematical model

For a target maximum load value *p* of 2000 N and restricting the 'RHS Height'

at 350 mm, Minitab gave the following results:

Maximum load = 1998.36 N

RHS thickness = 3.89 mm

WP-web distance = 7.98 mm

An ABAQUS model built for the parameter values obtained from the Minitab

optimization study, gave a maximum load of 2029.2 N.

Agreement of the maximum load values from Minitab and the FE model

validates the mathematical model.

o   Main Factor Effects

Figure 96 shows the effect of three factors considered in the CCD analysis. The

maximum load increases as the thickness of the RHS ring is increased. The RHS

thickness also has the highest effect on the maximum load.
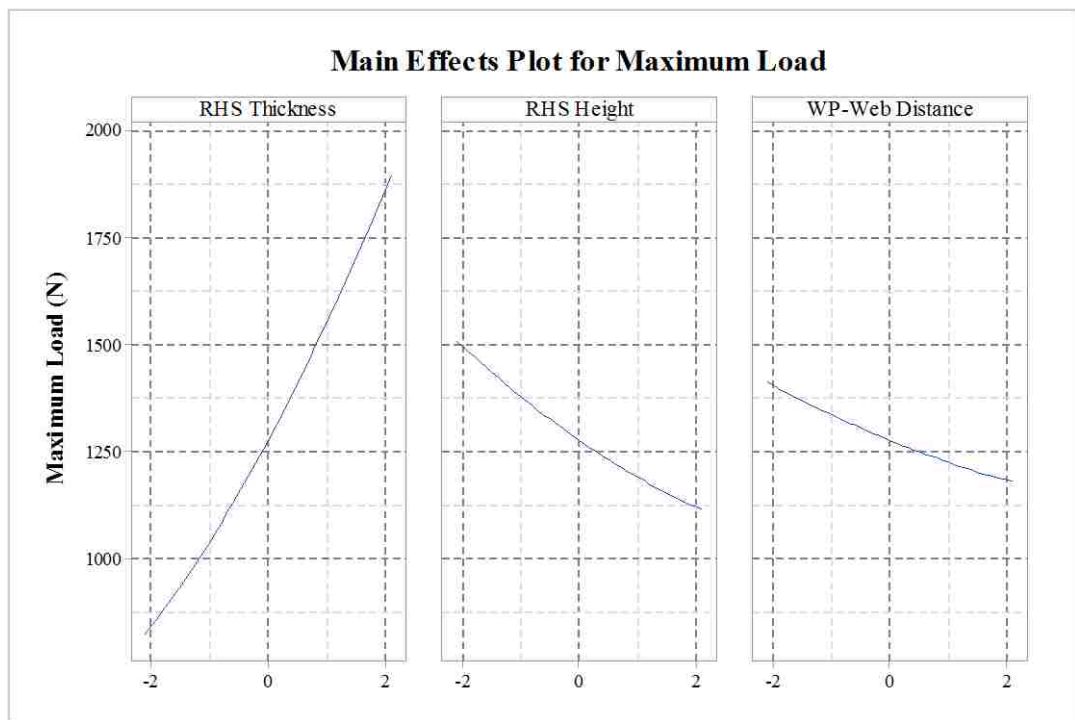
Figure 96: Main effects plot for maximum load of RHS ring between wearpads

The maximum load reduces as the RHS height or WP-web distance is increased. From an engineering point of view, as the thickness increases or the height reduces, the slenderness ratio reduces, thereby increasing the maximum load capacity of the RHS ring.

When the WP-web distance is increased, it results in an increase in the moment load acting on the webs of the RHS ring which results in reducing the maximum load carrying capacity of the RHS ring. This is as observed by experiments in section 3.2 and 3.3.

o   Interaction factors

Three interactions were identified as significant as shown in Figure 97 to Figure 99. While interpreting interaction plots, if the curves are almost parallel, it does not indicate a strong interaction.

Consider Figure 97 showing the variation of maximum load when the RHS Thickness is varied from level -2 (3 mm) to level 2 (4 mm). As the RHS thickness increases, the distance between the RHS height curves increases. This means that the difference in the RHS ring behaviour with height 375 mm and 425 mm increases as the thickness increases.

Similar observations can be made for the interaction plots shown in Figure 97 to Figure 99.
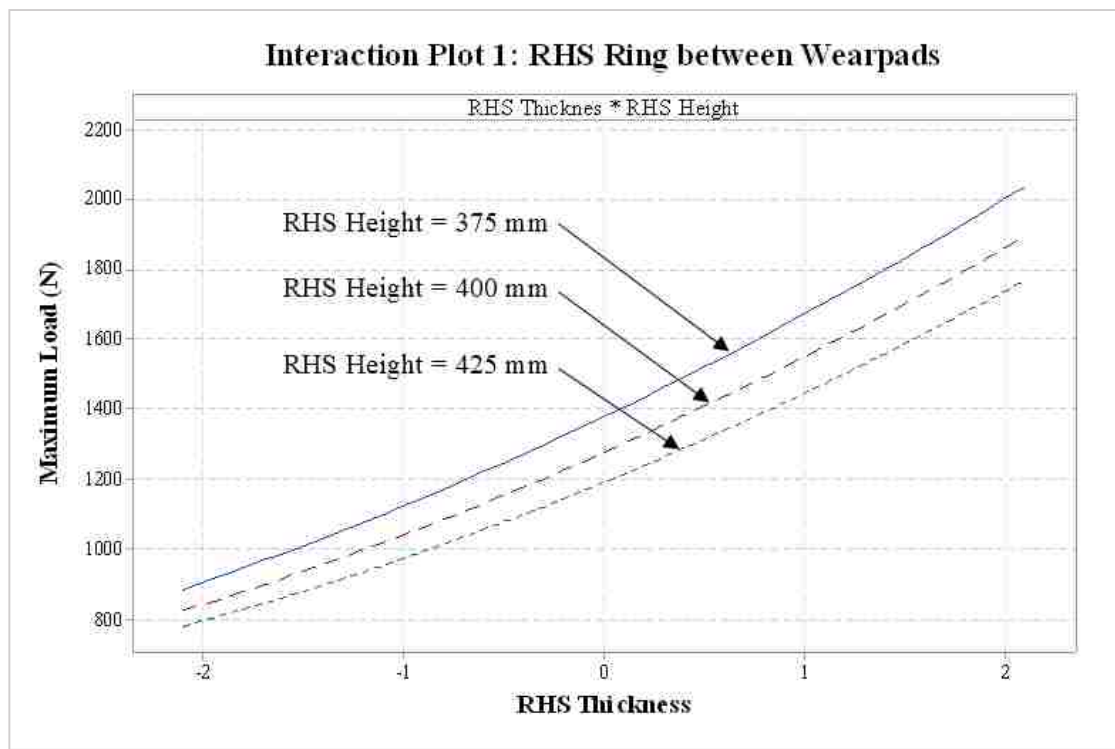
Figure 97: Effect of interaction between RHS thickness and RHS height on maximum load
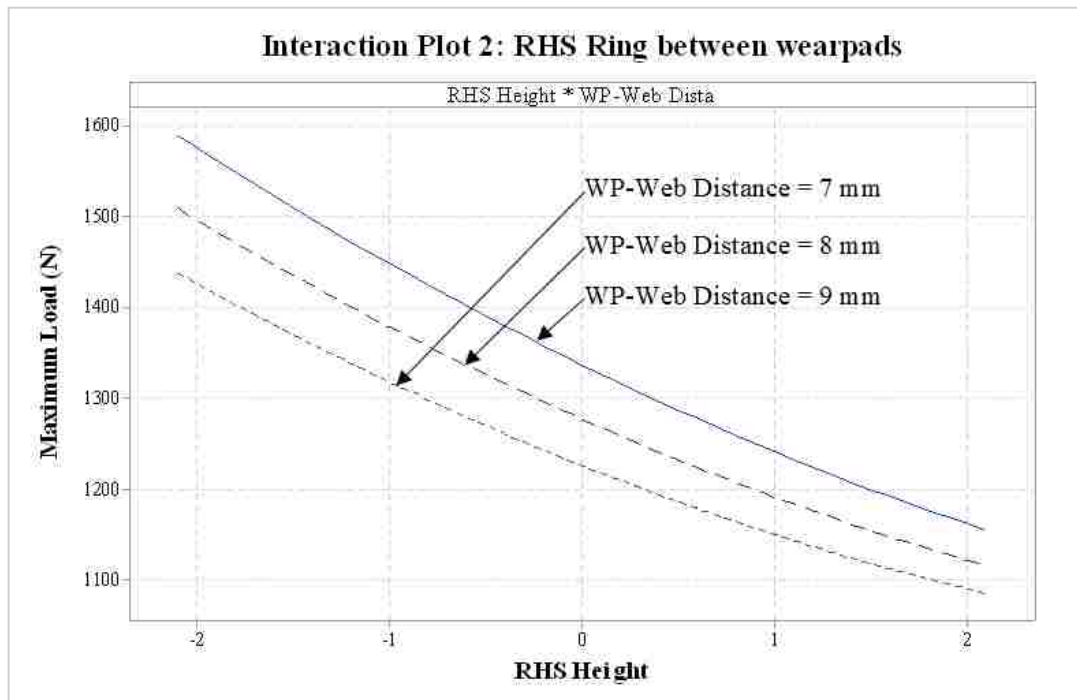
Figure 98: Effect of interaction between RHS height and WP-web distance on
maximum load
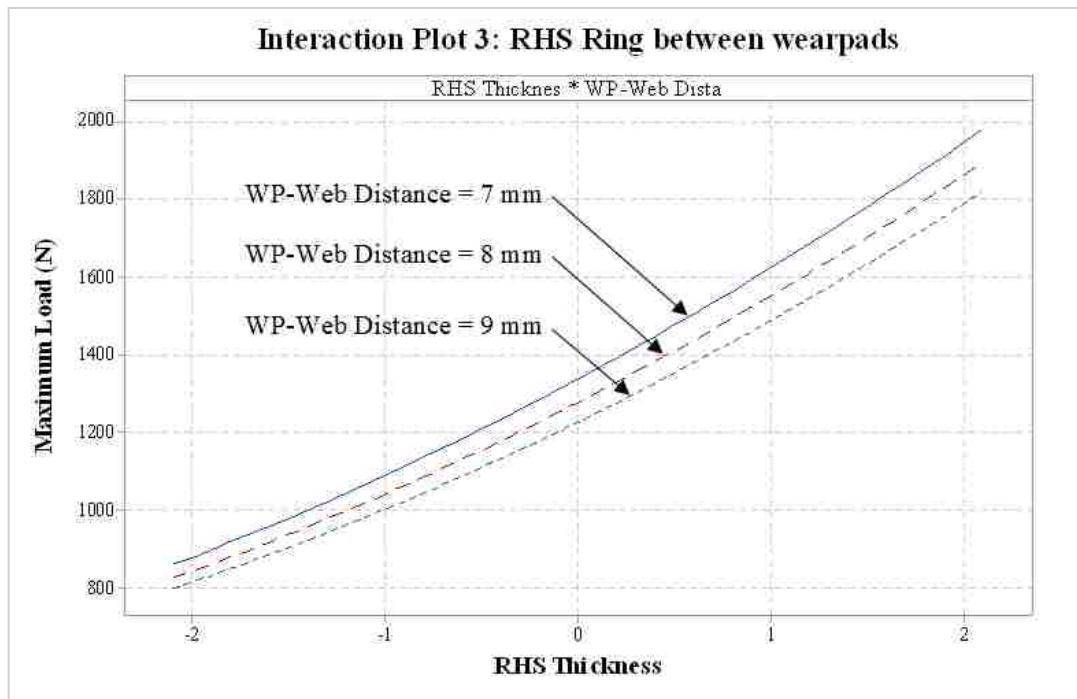
Figure 99: Effect of interaction between RHS thickness and WP-web distance on
maximum load

- Conclusions:

  - FE model for RHS rings between platens was validated

  - FE model for RHS rings between wearpads was validated

  - For the same factor ranges of the RHS ring, the Taguchi L_{12} for:

    - RHS ring between platens suggests the influencing factors are: 'RHS Thickness', 'RHS Height', 'RHS Corner Radius'

    - RHS Ring between wearpads suggests the influencing factors are: 'RHS Thickness', 'RHS Height', 'WP-Web distance'

    The substitution of the RHS corner radius by the WP-web distance in the influencing factors for RHS ring between wearpads indicates that the effect of both these factors is the same i.e. to move the load away from the web. When compressed between wearpads, the effect of the RHS corner radius therefore becomes redundant.

  - A mathematical model was obtained for the RHS ring between wearpads from the CCD and hence the influencing factors obtained for the RHS rings between wearpads were verified

  - The mathematical model was validated by FEA

  - Main factors and interactions were obtained and explained to better understand the behavior of the RHS ring between wearpads.

  - The lower maximum loads of the RHS ring compressed between wearpads is attributed to the additional moment induced due to the position of the wearpads causing the load to act away from the webs. This is confirmed by the interaction between the 'RHS Height' and 'WP-Web Distance'.

Chapter 6: Parametric Studies on RHS pieces

Chapter 5 determined the factors influencing the maximum load capacity of RHS rings between wearpads. This chapter aims to determine the geometric factors that affect the maximum load of RHS pieces under compressive loads between wearpads

Similar to Chapter 5, FE models of RHS pieces compressed between (a) platens and (b) wearpads are validated against the experiments on RHS pieces shown in sections 3.4 and 3.5. Validation is done against the RHS piece deformed shape, maximum load carrying capacity, and load-displacement curves of the RHS pieces.

In this chapter, a detailed analysis of RHS pieces using experimental design is shown. Like in Chapter 5, for the RHS pieces between platens, only the Taguchi L_{12} screening experiment is done and the influencing factors obtained are compared to that obtained from the Taguchi L_{12} for RHS pieces between wearpads to better understand the behavior of RHS pieces between wearpads. The RHS pieces are used further in a CCD to confirm the factors most influencing the maximum load of RHS pieces between wearpads. These factors are then considered in the L_{12} experiment of the inner beam assembly of the telescope in Chapter 7.

The procedure in this chapter involves (a) FE model validation - use validated model for further design of experiments (b) Taguchi L_{12} design − to identify influencing factors (c) CCD analysis - to establish the optimal settings using a mathematical model with the influencing factors (d) Confirmatory Experiment − to verify mathematical model.

6.1 RHS Pieces between Platens

FE Model:

The FE model comprising of three parts—the top platen, the bottom platen, and the RHS piece is subjected to a Riks analysis using ABAQUS Standard Version 2017. A typical FE model representing RHS piece compression between platens is as shown in Figure 100.

Two models were built for the two sets of RHS pieces tested. The assembly shown in Figure 100 is true for both models. For the shorter sections with 150 mm height, the RHS piece was built with solid elements whereas for the taller sections with the 350 mm height, shell elements were assigned to the RHS piece. The material properties for both models varied. All other features including interactions, mesh size, load application, boundary conditions etc. remained the same for both models.
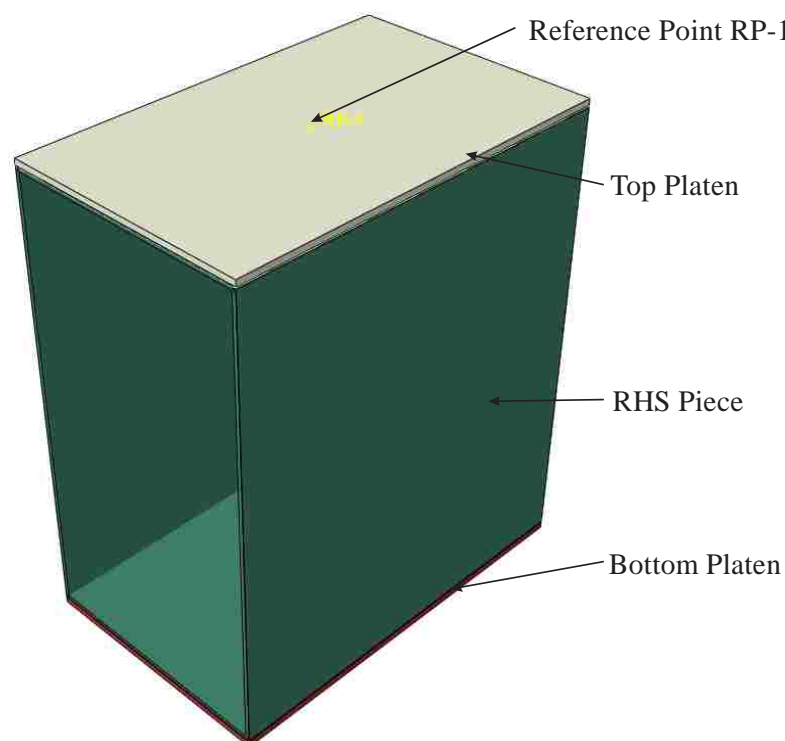
Figure 100: RHS piece between platens

- Assembly Details

The assembly consisting of the three parts were assigned the following interactions:

- o Bottom outer face of the RHS piece: assigned a frictional interaction with the bottom platen (Refer Figure 101(d))

- o Bottom Platen: is encastred, thereby restricting all degrees of freedom (Refer Figure 101(b))

- o Top outer face of the RHS piece: assigned a frictional interaction with the underside of the top platen (Refer Figure 101(c)).

- o Top Platen: All degrees of freedom of the top platen were restrained apart from the vertical translation, thereby allowing for compression (Refer Figure 101(a)).

- Reference point

A reference point RP-1 was created at the center of the top face of the top platen. RP-1 was kinematically coupled with the top platen top surface for uniform application of the load on the Top Platen.

A displacement of -15 was applied through a reference point.
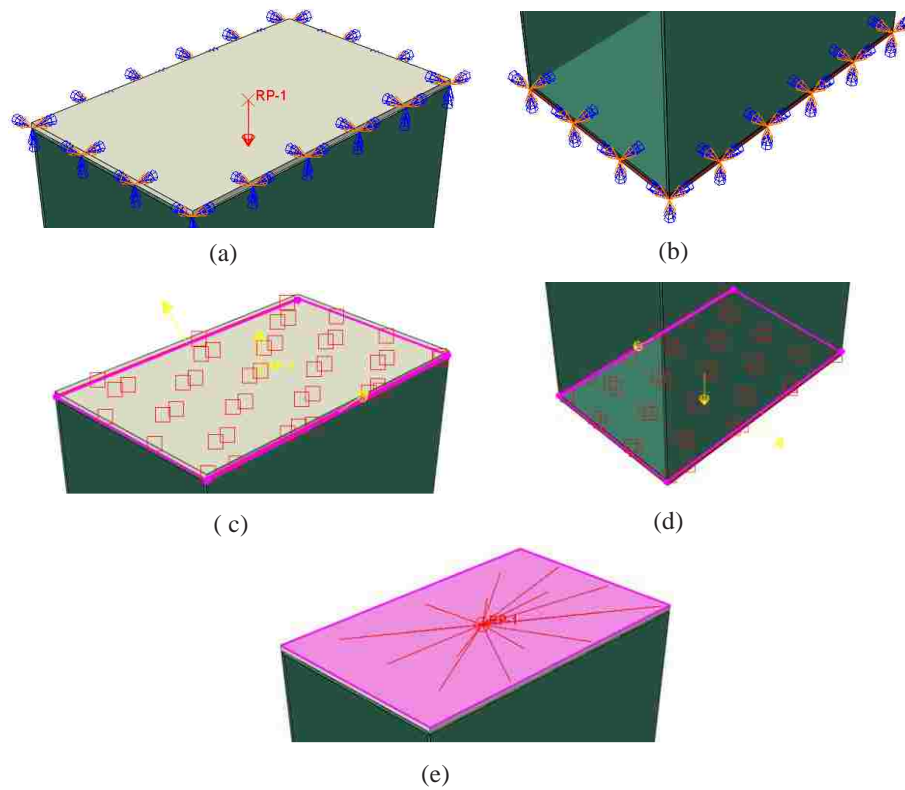
Figure 101: (a) Top platen constraints (b) Bottom platen encastre (c) Top platen interaction (d) Bottom platen interaction (e) Reference point

- Mesh size and elements

For both models, the platens were assigned the solid element C3D8R.

For the taller RHS piece, the RHS piece was assigned the shell element S4R. A mesh analysis resulted in determining a size of 5 mm for all three parts.

The shorter RHS piece was assigned the solid element C3D8R. The C3D8R element is also a brick element, with reduced integration [15]. Due to the reduced integration, the element tends not to be stiff enough in bending. Therefore, four elements were assigned through the thickness of the RHS piece. A mesh analysis resulted in determining a size of 5 mm × 5 mm for the RHS piece and platens.

- Dimensions

The FE model for the tall and short RHS pieces was built to the dimensions shown in Table 32 and Table 33 respectively.

Table 32: FE model part dimensions for tall RHS piece between platens

Part	Dimensions
RHS piece	Height = 350 mm, Width = 150 mm, Corner Radius = 5 mm, Length = 150 mm, Thickness = 3.2 mm
Platen	150 mm width and 150 mm length

Table 33: FE model part dimensions for short RHS pieces between platens

Part	Dimensions
RHS piece	Height = 150 mm, Width = 100 mm, Corner Radius = 5 mm, Length = 100 mm, Thickness = 3 mm
Platen	100 mm width and 100 mm length

- Loading

Displacement of -15 applied at RP-1

- Validation of FE Model:
  o Load Validation

Table 34 and Table 35 show the comparison of the maximum load values between the experiments and the FEA. Agreement of maximum load values between both methods validates the FE models.

Table 34: Maximum load value validation for tall RHS pieces between platens

Sr. No.	Maximum Load (kN)	
	Experiment	FEA
Sample SL1	15.02	
Sample SL2	15.28	14.63
Sample SL3	15.48	

Table 35: Maximum load value validation for short RHS pieces between platens

Sr. No.	Maximum Load (kN)	
	Experiment	FEA
Sample SL4	32.24	
Sample SL5	34.39	34.64
Sample SL6	32.58	

- Shape Validation:

    Agreement between the deformed shape from experiments and FEA of a RHS

piece shown in Figure 102(a) and Figure 102(b) validates the FE model.
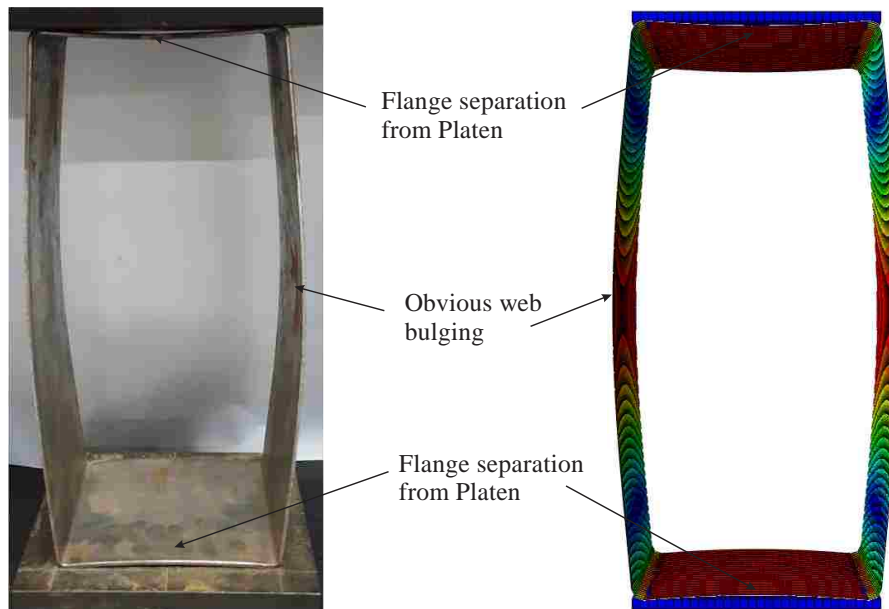
Figure 102: Deformed shape of RHS piece between platens in (a) Experiments (b)
FEA

- Load-Displacement Curve

The load-displacement curves for the experiments and FE models for the tall and short RHS pieces between platens is shown in Figure 103(a) and Figure 103(b) respectively. The blue curves indicate the load-displacement curves for the experiments in section 3.4 and the red curve indicates the load-displacement curves from the FE model. Agreement in the load-displacement curves from the experiments and FE models validates the FE models.

(a)   (b)
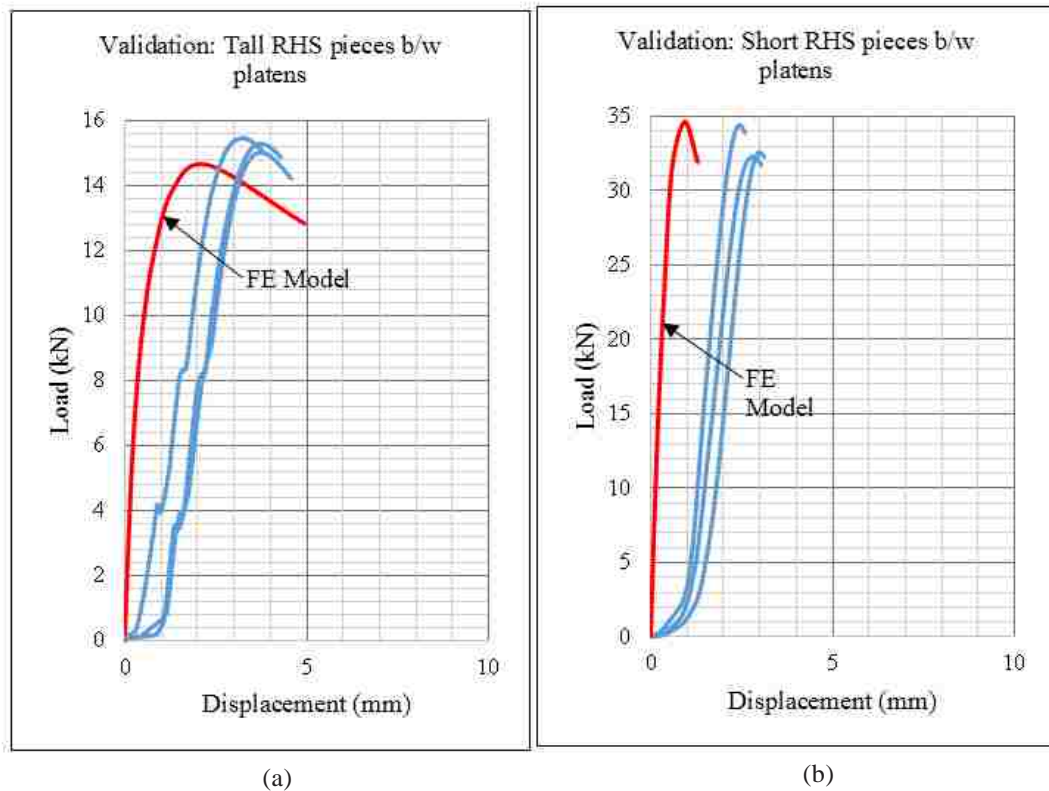
Figure 103: Load-displacement graph for (a) Tall RHS piece (b) Short RHS piece

Design of experiments

- Taguchi L_{12} design:

  o Possible Parameters

Using the validated FE model of the tall RHS piece, the L_{12} experiment was executed with the listed five factors and their levels shown in Table 36.

Table 36: Factors and factor levels for L_{12} of RHS piece between platens

Factor No.	Factor Name	Level 1 (mm)	Level 2 (mm)
1	RHS Thickness	3	4
2	Corner radius	2	5
3	RHS Height	350	450
4	RHS Width	200	250
5	RHS Length	400	450

Like in the case of the RHS ring in Chapter 5, the material properties for the FE models in the experimental design were modified to that shown in section 3.1.1 for the sake of uniformity. The validated tall RHS piece model compressed between platens was modified to fit each run shown in Table 52 in Appendix III. Table 52 also includes the maximum load (response) corresponding to each run.

- Influencing Parameters
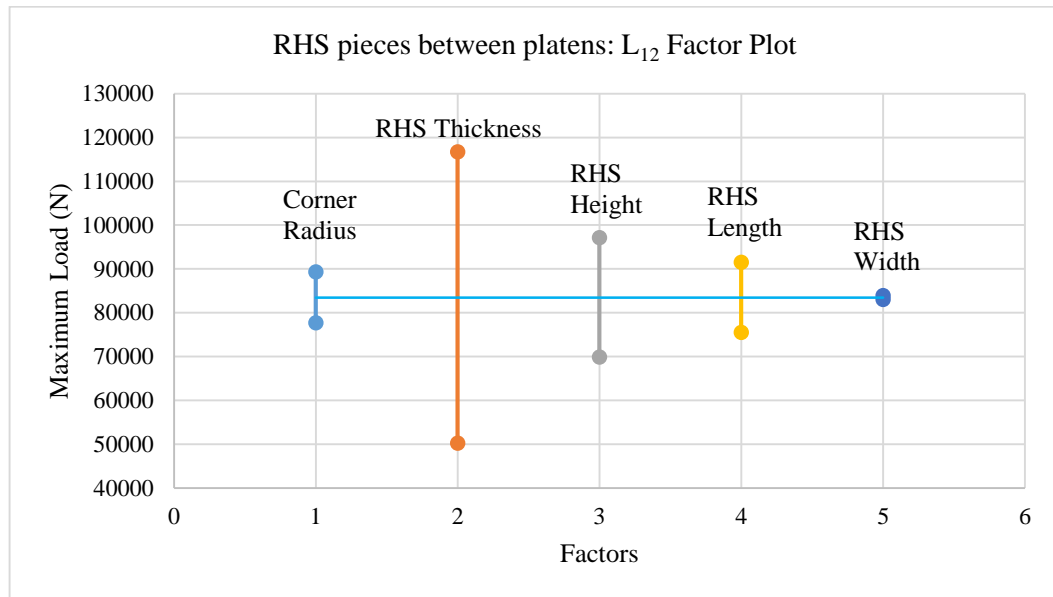
Figure 104: Factor plot for RHS pieces between platens

Figure 104 shows the Factor Plot from the results shown in Table 52. From Figure 104, again the 'RHS Thickness' has the highest influence on the maximum load. Other influencing factors include the 'RHS Height', 'RHS Length' and 'Corner Radius'.

6.2 RHS Pieces between Wearpads

FE Model: The FE model comprising of three parts—the top wearpad, the bottom wearpad, and the RHS piece is subjected to a Riks analysis using ABAQUS Standard Version 2017. A typical FE model representing RHS compression between wearpads is as shown in Figure 105(a). For this section, the platens shown in section 6.1 are replaced by the top and bottom wearpads. The top wearpads are built by extruding four rectangular cubes from a flat platen as shown in Figure 105(b). A typical FE model representing RHS piece compression between wearpads is as shown in Figure 105(a).

Like in section 6.1, two models were built for the two sets of samples tested. The assembly shown in Figure 105(a) is true for both models. Again, for the shorter sections with 150 mm height, the RHS piece was built with solid elements whereas for the taller sections with the 350 mm height, shell elements were assigned to the RHS piece. The material properties for both models varied. All other features including interactions, mesh size, load application, boundary conditions etc. remained the same for both models.
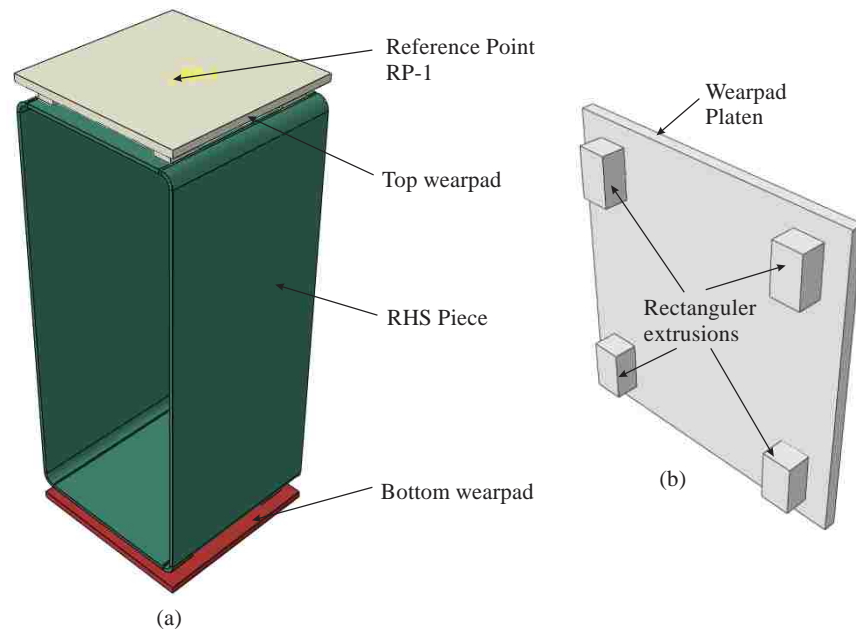
Figure 105: (a) RHS ring between wearpads assembly (b) Wearpad parts

- Assembly Details

The assembly consisting of the three parts were assigned the following interactions:

- o Bottom outer face of the RHS piece: assigned a frictional interaction with the four extrusions of the bottom wearpad (Refer Figure 106(d))

- o Bottom Wearpad platen: is encastred, thereby restricting all degrees of freedom(Refer Figure 106(b))

o   Top outer face of the RHS piece: assigned a frictional interaction with the four extrusions of the top wearpad (Refer Figure 106(c))

o   Top Wearpad platen: All degrees of freedom of the top wearpad platen were restrained apart from the vertical translation, thereby allowing for compression (Refer Figure 106(a)).

- Reference point

As explained in section 5.2, a reference point RP-1 was created at the center of the top face of the top wearpad. RP-1 was kinematically coupled with the top platen top surface for uniform application of the load on the top platen (Refer Figure 106(e)).

Again, a displacement of -15 was applied through a reference point.

(a)

(b)

(c)

(d)

(e)
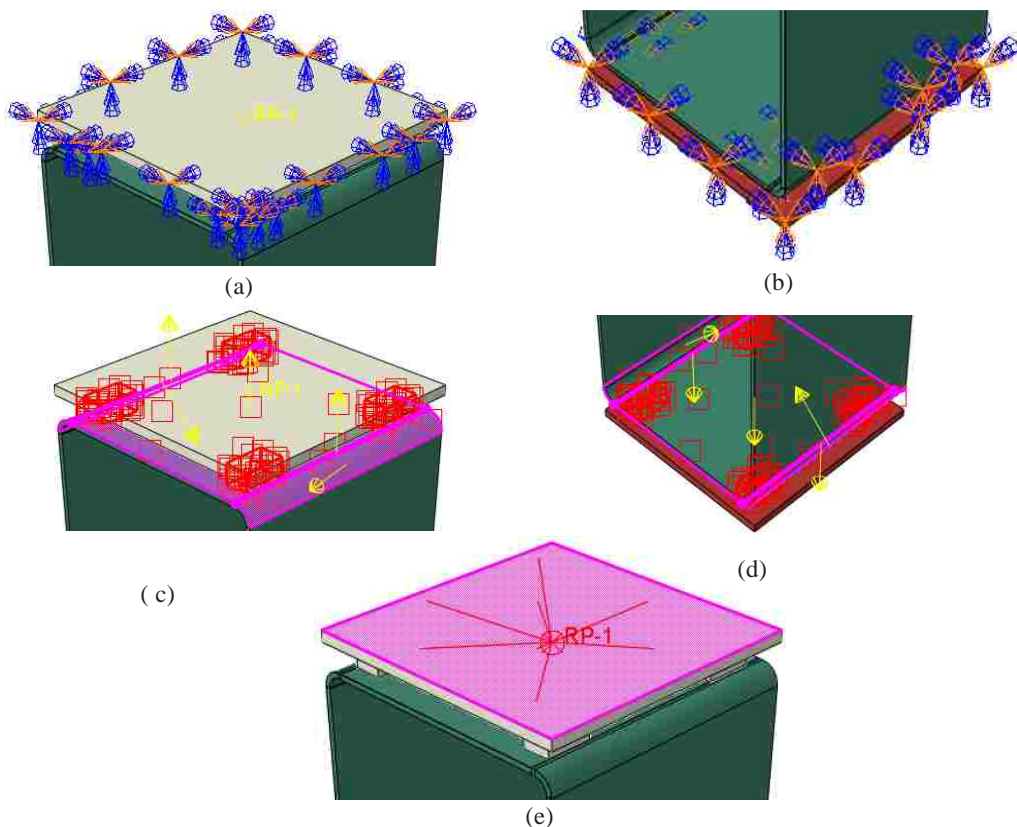
Figure 106: (a) Top wearpad platen constraints (b) Bottom wearpad platen encastre (c) Top wearpad interaction (d) Bottom wearpad interaction (e) Reference point coupling

- Mesh size and elements

  Same as section 5.1

- Dimensions

  The FE model for the tall and short RHS pieces was built to the dimensions shown in Table 37 and Table 38 respectively.

Table 37: FE model part dimensions for tall RHS piece between wearpads

Part	Dimensions
RHS piece	Height = 350 mm, Width = 150 mm, Corner Radius = 5 mm, Length = 150 mm, Thickness = 3.2 mm
Wearpads	Wearpad Platen: 150mm length x 150 mm width Rectangular pieces: Width = 15 mm, Length = 25 mm, WP distance from both edges = 10 mm

Table 38: FE model part dimensions for short RHS pieces between wearpads

Part	Dimensions
RHS piece	Height = 150 mm, Width = 100 mm, Corner Radius = 5 mm, Length = 100 mm, Thickness = 3 mm
Wearpads	Wearpad Platen: 100 mm length x 100 mm width Rectangular pieces: Width = 15 mm, Length = 25 mm, WP Distance from web edge = 7.5 mm, WP Distance from front edge = 10 mm

- Loading

  Displacement of -15 applied at RP-1

- Validation of FE Model:

  o Load Validation

  Table 39 and Table 40 show an agreement in the maximum load values between the experiments and the FEA. This validates the FE model.

Table 39: Maximum load validation for tall RHS pieces between wearpads

Sr. No.	Maximum Load (kN)	
	Experiment	FEA
Sample SLW1	11.88	
Sample SLW2	12.57	12.42
Sample SLW3	12.50	

Table 40: Maximum load validation for short RHS pieces between wearpads

Sr. No.	Maximum Load (kN)	
	Experiment	FEA
Sample SLW4	25.285	
Sample SLW5	25.263	27.03
Sample SLW6	25.840	

- Shape Validation

Agreement between the deformed shape of RHS piece compressed experimentally and in the FE model between wearpads as shown in Figure 107(a) and Figure 107(b) validates the FE model.
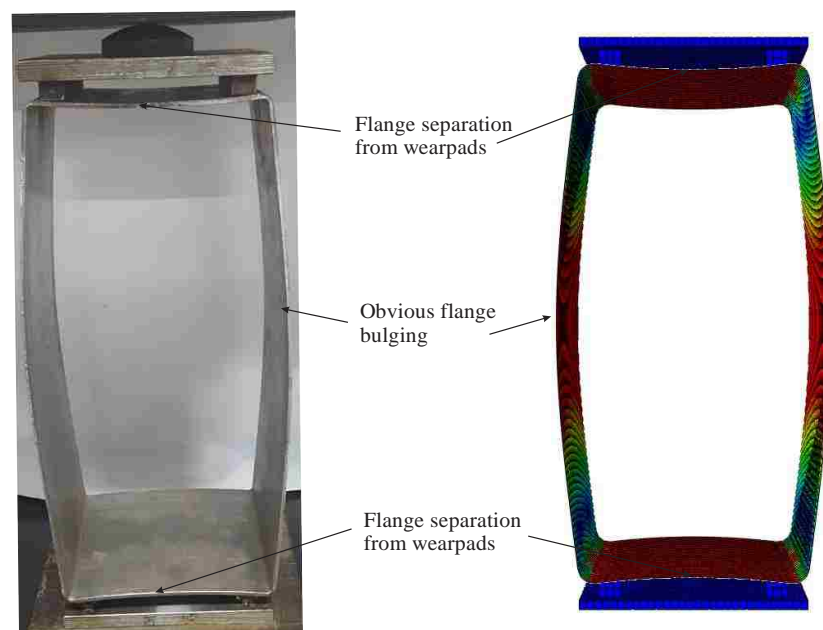
Figure 107: Deformed shape of RHS piece between wearpads in (a) Experiments (b) FEA

- Load-Displacement Curve:

Figure 108 shows the load-displacement curves for the two sets of RHS pieces between wearpads. Agreement between the curves from both methods validates the model.
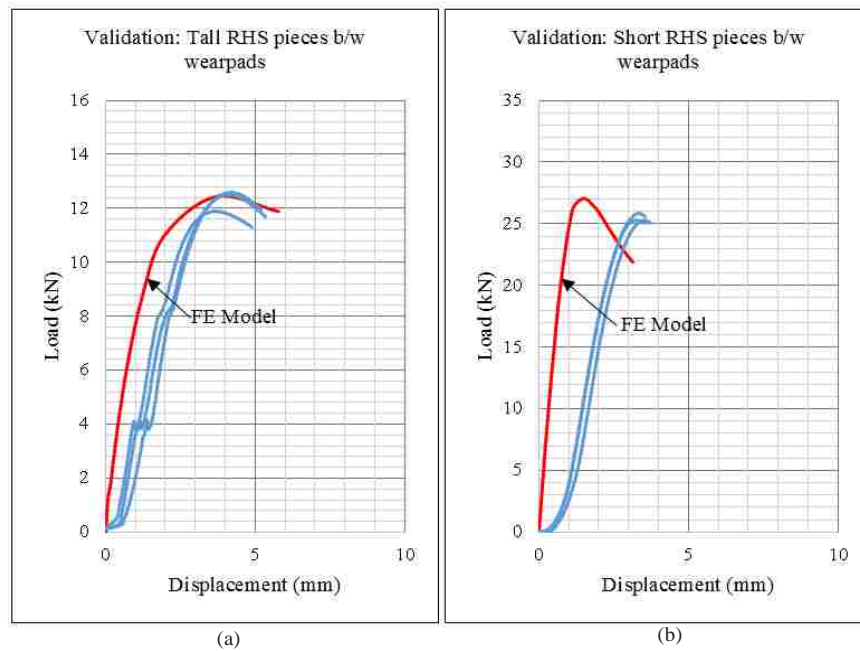
Figure 108: Load-displacement curve for (a) Tall RHS piece (b) Short RHS piece between wearpads

Design of Experiments

- Taguchi L_{12} design:

  o Possible Parameters

Table 41 lists the nine factors and their levels considered for the L_{12} design of RHS pieces between wearpads.

Table 41: Factors and factor levels for L_{12} of RHS piece between wearpads

Factor No.	Factor	Level 1 (mm)	Level 2 (mm)
1	RHS Thickness	3	4
2	RHS Corner Radius	2	4
3	RHS Height	350	450
4	RHS Width	200	250
5	RHS Length	400	450
6	WP Length	150	175
7	WP Width	50	75
8	WP-Web Distance	5	10
9	WP-End Distance	5	10

Again, the material properties for the FE models in the experimental design were modified to that shown in section 3.1.1 for the sake of uniformity. The validated tall RHS piece model compressed between wearpads was modified to fit each run shown in Table 53. Table 53 also includes the maximum load (response) corresponding to each run.

o   Influencing Parameters

Figure 109 shows the factor plot for the maximum load obtained from the data shown in Table 53. The most influencing factors are the 'RHS Thickness', 'RHS Height', 'WP-Web Distance' and 'RHS Length'.
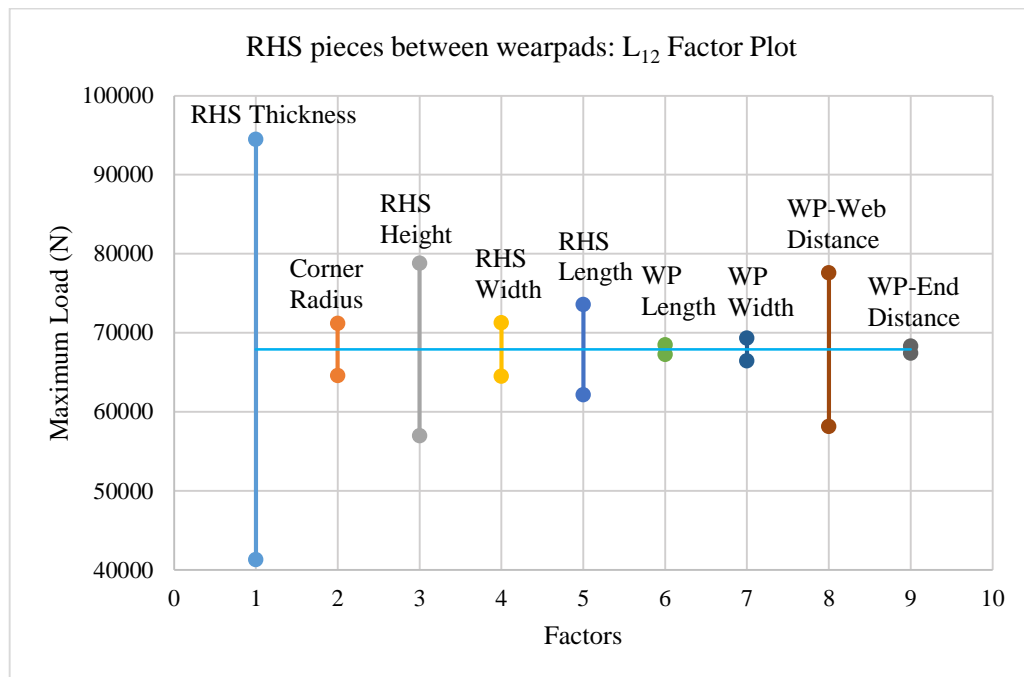
Figure 109: Factor plot for RHS pieces between wearpads

- CCD

In Minitab, for this design, the value for α was kept at 2. The values of the coded levels are given in Table 42. The values of the coded levels for the four most influencing factors selected from Figure 109 are given in Table 42.

Table 42: Values for the coded factor levels for RHS pieces between wearpads

Coded Value	-2	-1	0	1	2
RHS Thickness	3	3.25	3.5	3.75	4
RHS Height	350	375	400	425	450
RHS Length	400	410	420	430	440
WP-Web Distance	5	6	7	8	9

The validated tall RHS piece model compressed between wearpads was modified to fit each run shown in Table 54 of Appendix III. Table 54 also includes the maximum load (response) corresponding to each run.

- Statistical Analyses of the Results and Evaluations:

The results from the CCD are given in the form of a mathematical model, main effect plots and interaction plots. The main aim of the CCD is to validate the mathematical model and hence the influential factors of the RHS pieces between wearpads.

  o The Response Surface:

Let the following parameters to be named in the way expressed below:

Maximum Load p

RHS thickness x_1

RHS Height x_2

RHS Length x_3

WP-Web Distance x_4

The response surface is a mathematical model using these parameters. From the analysis the model is given by:

$$\begin{aligned} p &= 64760 + 12837x_1 - 4690x_2 + 1592x_3 - 2026x_4 + 899x_1^2 + \\ & 395x_2^2 + 118x_3^2 - 487x_4^2 - 911x_1x_2 + 399x_1x_3 - 385x_1x_4 \\ & -158x_2x_3 + 691x_2x_4 + 16x_3x_4 \end{aligned} \qquad (6.1)$$

This model given by equation (6.1) can be mathematically manipulated to get the value combination for the geometric factors to get a target value of the maximum load p.

The model has $\frac{1}{2}(4+1)(4+2) = 15$ terms. Some of these have marginal contributions while some have major contributions. The Pareto Chart in Figure 110 shows the significant main factor effects and interactions.
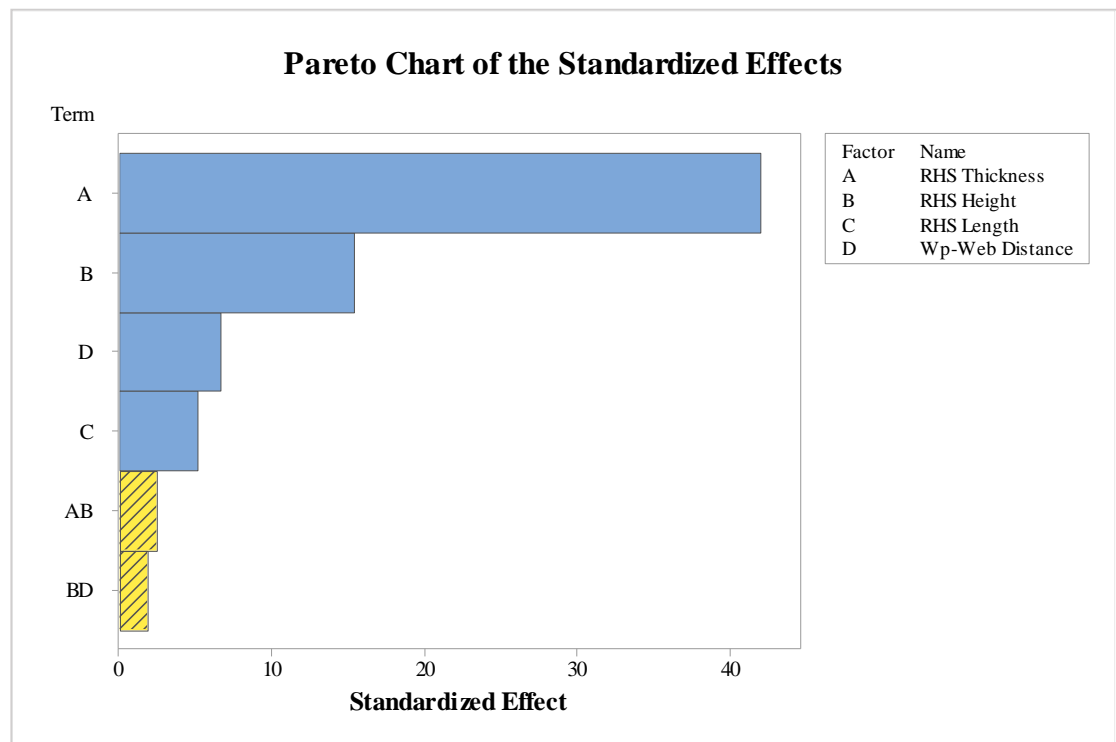
Figure 110: Pareto chart for RHS pieces between wearpads

The p-values for all the factors and interactions are shown in Table 43. Again, only factors with a p-values ≤ 0.05 are considered significant. The pareto chart in Figure 110 shows only the significant factors and interactions.

Table 43: P-value for all factors/ interactions of RHS pieces between wearpads

Source	P-Value
Linear	
RHS Thickness	0.000
RHS Height	0.000
RHS Length	0.000
Wp-Web Distance	0.000
Square	
RHS Thickness*RHS Thickness	0.000
RHS Height*RHS Height	0.025
RHS Length*RHS Length	0.473
Wp-Web Distance*Wp-Web Distance	0.008
2-Way Interaction	
RHS Thickness*RHS Height	0.001
RHS Thickness*RHS Length	0.081
RHS Thickness*Wp-Web Distance	0.090
RHS Height*RHS Length	0.470
RHS Height*Wp-Web Distance	0.005
RHS Length*Wp-Web Distance	0.942

o   Validating mathematical model

For a target maximum load value p of 55,000 N, with a fixed RHS Height of 350 mm, the multiple response prediction is given in Table 44. The maximum load obtained from Minitab was 55,002 N.

Table 44: Multiple response prediction for RHS piece between wearpads

Variable	Setting	Value
RHS Thickness	-1.6803	3.08
RHS Height	-2	350
RHS Length	1.9023	439.023
Wp-Web Distance	-1.6768	5.3232

With parameter values in Table 44, an ABAQUS model was built and run and a maximum load of 58933.3 N was obtained. The higher value of maximum load from

ABAQUS can be attributed to the fact that the thickness value was rounded up to a higher value of 3.1 mm.

Agreement of the maximum load values from both Minitab and the FE model validates the mathematical model.

o   Main Factor Effects:

Figure 111 and Figure 112 shows the effect of the four factors considered in the CCD analysis. The maximum load increases as the thickness and length of the RHS piece is increased. The RHS thickness also has the highest effect on the maximum load.
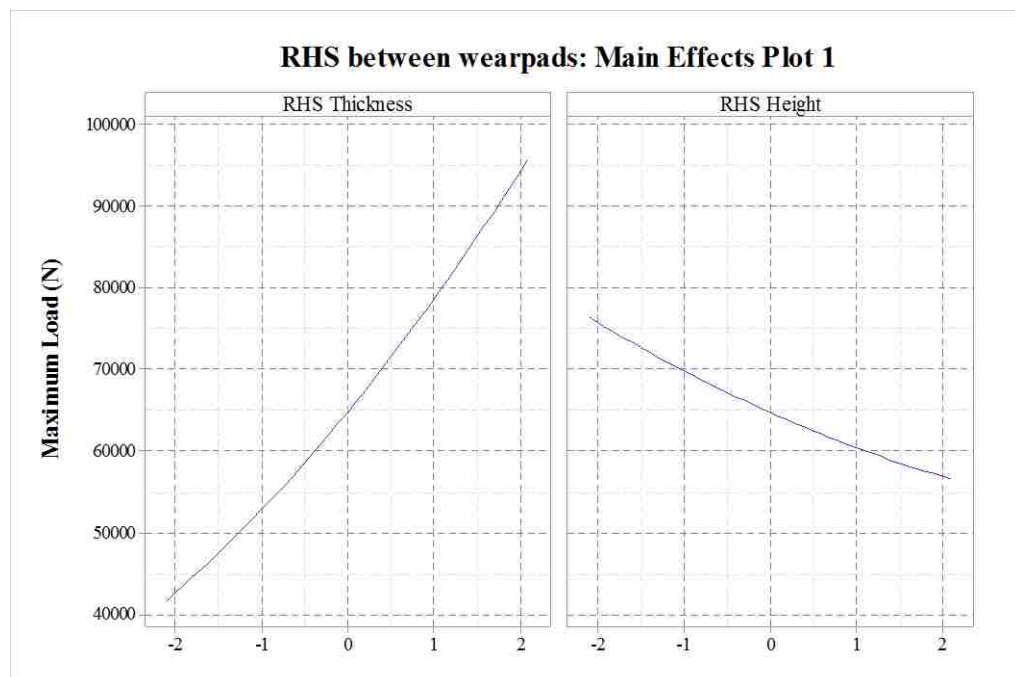
Figure 111: Main effects plot 1 for RHS piece between wearpads
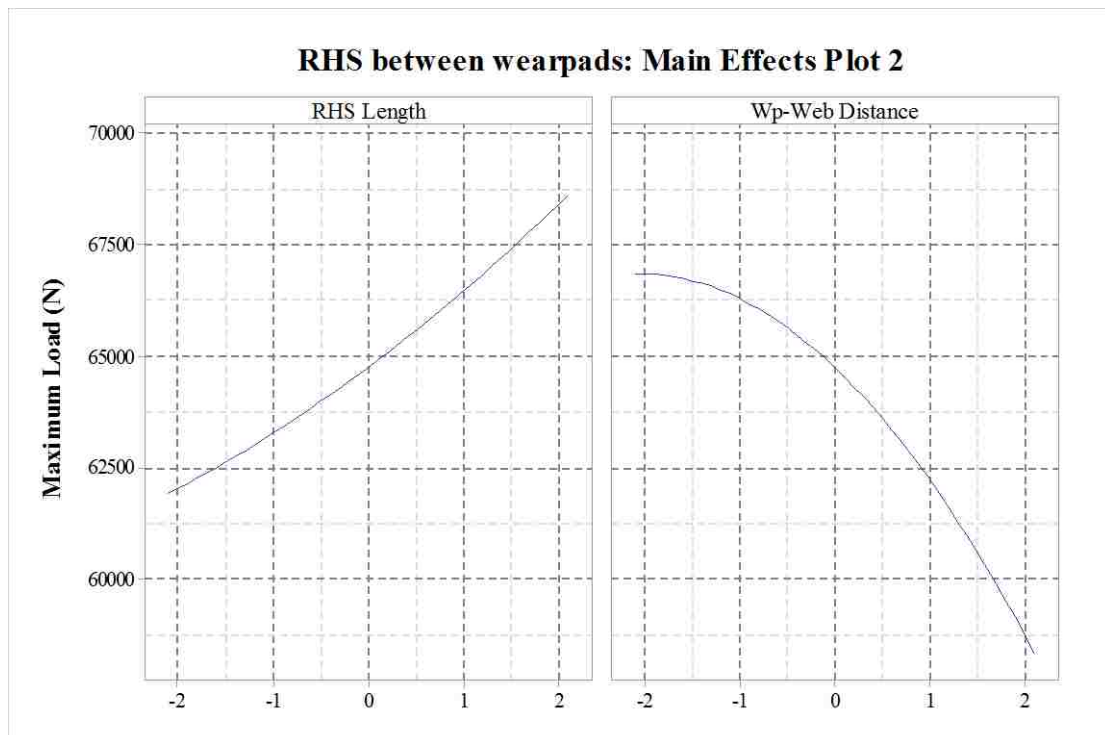
Figure 112: Main effects plot 2 for RHS piece between wearpads

The maximum load reduces as the RHS height or WP-Web distance is increased. From an engineering point of view, for a given thickness value, if the RHS height increases, the slenderness ratio increases making the RHS more prone to failure. When the WP-web distance is increased, it results in an increase in the moment load acting at the web of the structure which results in lower maximum load capacity of the RHS piece.

o   Interaction factors

Two interactions have been identified as significant and they are shown in Figure 113 and Figure 114. As explained in section 5.2, while interpreting interaction plots, if the curves are almost parallel, it does not indicate a strong interaction.

Consider Figure 113 showing the variation of maximum load when the RHS height is varied from level -2 (350 mm) to level 2 (450 mm). As the RHS height

increases, the distance between the WP-web distance curves decreases. This means that the difference in the RHS piece behaviour with WP-web distance 7 mm and 10 mm increases as the RHS height reduces.

A similar explanation can be given for the interaction plot shown in Figure 114.
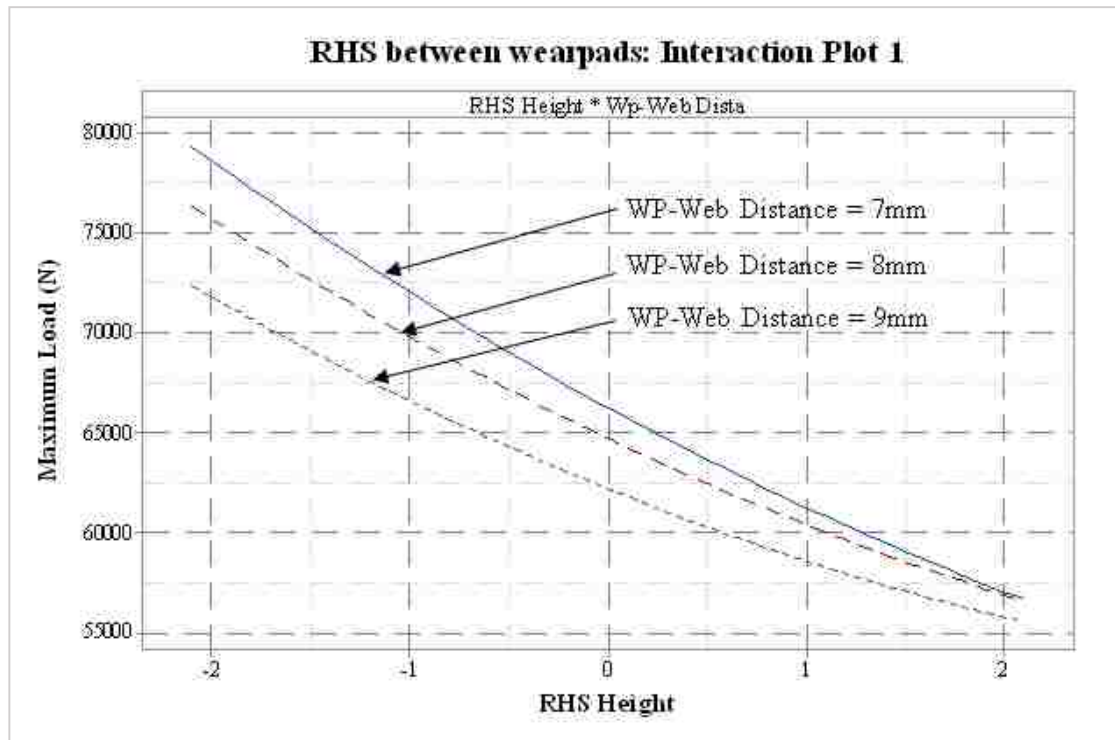
Figure 113: Effect of interaction between RHS height and WP-Web distance on maximum load of RHS piece between wearpads
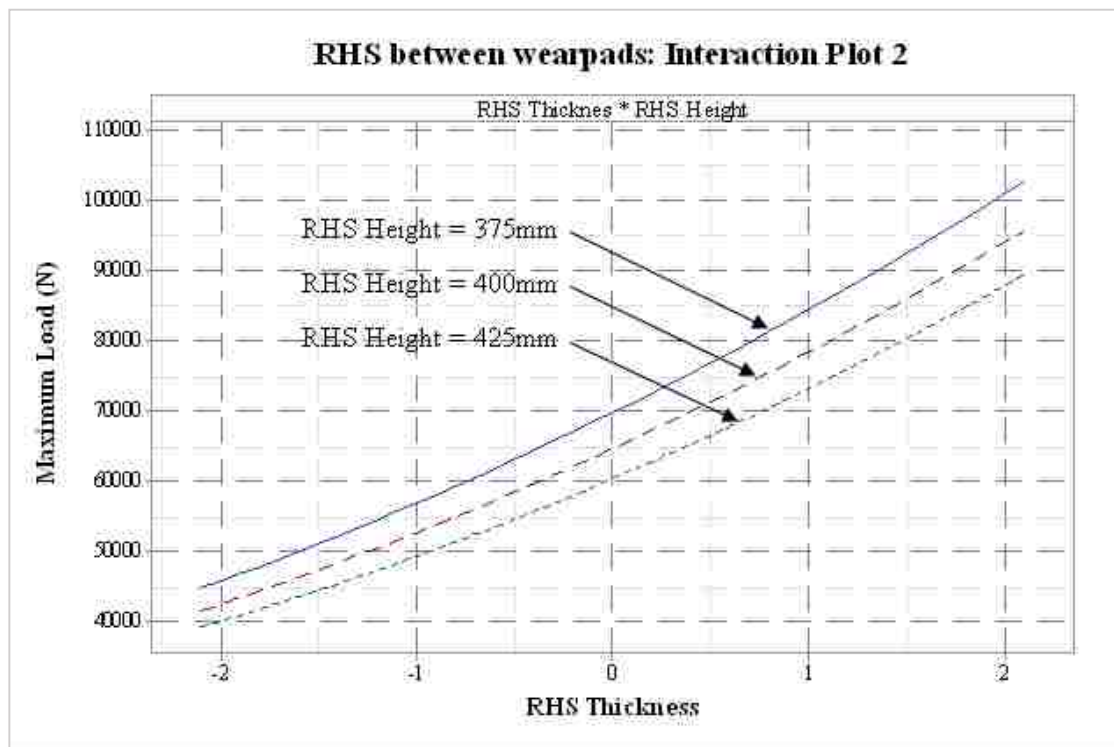
Figure 114: Effect of interaction between RHS thickness and RHS height on maximum load of RHS piece between wearpads

- Conclusions:

    o FE model for RHS pieces between platens was validated

    o FE model for RHS pieces between wearpads was validated

    o For the same parameter range of the RHS piece, the Taguchi L_{12} for:

        ▪ RHS piece between platens suggests the influencing factors are – 'RHS Thickness', 'RHS Height', 'RHS Length', 'RHS corner Radius'

        ▪ RHS piece between wearpads suggests the influencing factors are – 'RHS Thickness', 'RHS Height', 'RHS Length', 'WP-Web distance'

            Similar to the conclusions drawn in Chapter 5, the substitution of the RHS corner radius with the WP-Web

distance in the influencing factors for RHS piece between wearpads indicates that the purpose of both these factors is to move the load away from the web. When compressed between wearpads, the RHS corner radius therefore becomes redundant.

o A mathematical model was obtained from the CCD of the RHS piece between wearpads

o The mathematical model was validated by FEA

o The validated mathematical model confirmed the influencing factors of the RHS pieces between wearpads

o Main factors and interactions were obtained and explained to better understand the behavior of the RHS piece between wearpads.

o The lower maximum loads of the RHS piece compressed between wearpads is attributed to the additional corner moment induced due to the position of the wearpads causing the load to act away from the webs. This is confirmed by the interaction between the 'RHS Height' and 'WP-Web Distance'.

Chapter 7: Parametric Studies on Inner Beam Assembly of Telescope

Chapter 7 entails the implementation of the design methodology of the inner beam assembly in section 4.6 on a case study. It aims to generate a response surface or mathematical model for the maximum load capacity of an inner beam assembly in order to be able to optimize the design for a given set of constraints valid for a given factor range.

In this chapter, the FE model explained and validated in chapter 3 is used here for further experimental designs. Validation of the FE model in chapter 3 was done against the reaction force obtained at the bottom wearpads from theory and analysis.

Section 1.5 in Chapter 1 highlighted that in the overlap area of a telescope, the inner beam sections under the wearpads (Refer Figure 13) act as either RHS rings or RHS pieces, depending on the length of the wearpads. With this in mind, and the design methodology established in section 4.6, the factors considered in this Chapter include the influencing factors obtained from chapters 5 and 6 for the RHS rings and RHS pieces between wearpads. In addition, overall assembly factors were also considered.

The procedure in this chapter involves (a) Taguchi L_{12} design – to identify influencing factors (b) CCD analysis - to establish the optimal settings using a mathematical model with the influencing factors (c) Confirmatory Experiment – to verify mathematical model.

FE Model

- Modelling and analysis

As explained in section 3.1

- Validation of FE Model

  Reaction force agreement between theory and analysis (Refer section 3.12)

  Design of Experiments

- Taguchi L_{12} design

  o   Possible Parameters

The listed factors and their levels shown in Table 45 were used to carry out the L_{12} experiment. The factors considered are a combination of influencing factors borrowed from chapters 5 and 6, and overall assembly factors of the inner beam assembly.

Table 45: Factors and factor levels for L_{12} of inner beam assembly

Factor No.	Factor Name	Level 1	Level 2
1	IB Length	3000	4000
2	IB Overlap	600	700
3	IB Height	350	450
4	IB Width	200	250
5	IB Thickness	3	4
6	WP Length	75	250
7	WP Width	50	75
8	WP-Web Distance	5	10
9	Corner radius	2	5

The maximum load (response) corresponding to the L_{12} runs are given in Table 55 in appendix IV. The validated inner beam assembly model was modified to fit each run shown in Table 55.

o   Influencing Parameters

Figure 115 below shows the Factor Plot for the maximum load for the factors shown in Table 45. The six most influencing factors are: 'IB Thickness', 'IB Length', 'IB Overlap', 'IB Height', 'WP Length', 'WP- Web distance'.
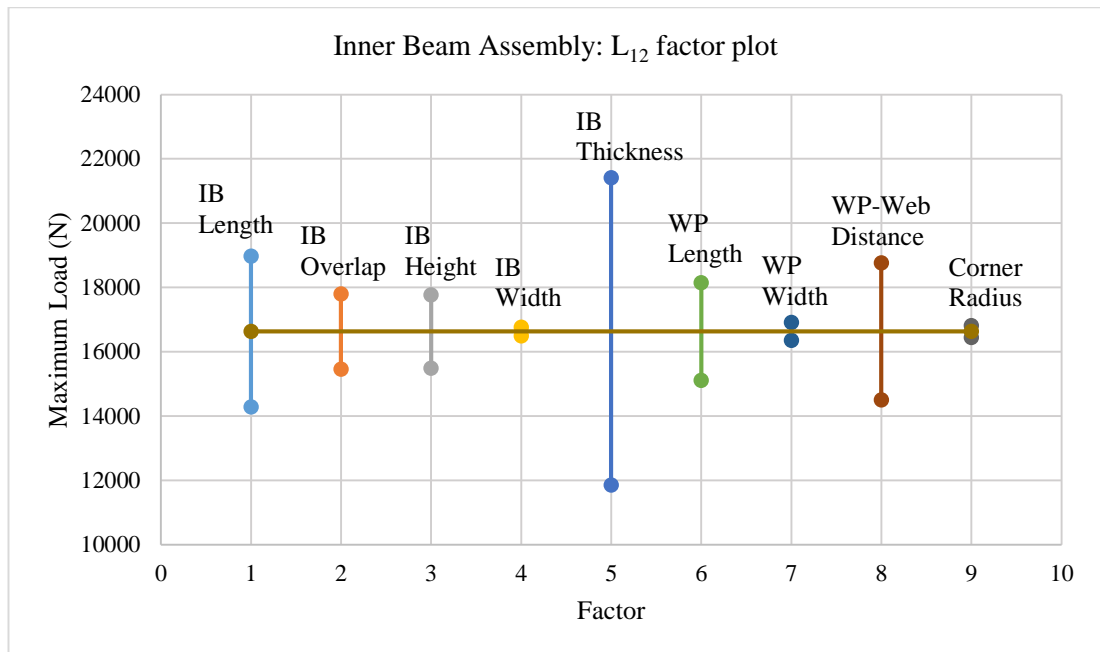
Figure 115: Factor plot for inner beam assembly of telescope

Of the six influencing factors, three influencing factors ('IB Thickness', 'IB Height', 'WP-Web Distance') were common to RHS rings and RHS pieces between wearpads from chapters 5 and 6. The wearpad length in Figure 115 represents the RHS piece length shown in Figure 109 in Chapter 6. In addition, overall inner beam (IB) dimensions; 'IB Length' and 'IB Overlap' also showed relevance.

- CCD

Using the CCD in Minitab, a response surface was fitted for the maximum load of the telescope. For the design, the value for α was kept at 2. The values of the coded levels of the six influencing factors selected from Figure 115 are shown in Table 46. The main of the CCD is to generate a mathematical model or response surface to optimize the inner beam assembly for a given set of constraints within a set factor range.

Table 46: Values for the coded factor level for inner beam assembly

	-2	-1	0	1	2
IB Length	3000	3250	3500	3750	4000
IB Overlap	600	625	650	675	700
IB Height	350	375	400	425	450
IB Thickness	3	3.25	3.5	3.75	4
WP Length	200	210	220	230	240
WP-Web Distance	5	6	7	8	9

The validated inner beam assembly model was modified to fit each run shown in Table 54 of Appendix IV. Table 54 also includes the maximum load (response) corresponding to each run.

- Statistical Analyses of the Results and Evaluations

The results from the response surface methodology are given in the form of a mathematical model and factor plots.

- o The Response Surface

Let the following parameters to be named in the way expressed below:

Maximum Load $\quad$ p

IB Length $\quad x_1$

IB Overlap $\quad x_2$

IB Height $\quad x_3$

IB Thickness $\quad x_4$

WP Length $\quad x_5$

WP-Web Distance $\quad x_6$

The response surface is a mathematical model using these parameters. From the CCD analysis, the model is given by:

$$p = 18404.7 - 1485.76x_1 + 841.41x_2 + 20.61x_3 + 3042.08x_4$$
$$+ 123.28x_5 - 1271.53x_5 + 113.77x_1^2 - 11.04x_2^2 - 39.96x_3^2$$
$$+ 125.29x_4^2 - 16.80x_5^2 + 95.41x_6^2 - 66.62x_1x_2 - 9.73x_1x_3$$
$$- 231.98x_1x_4 - 11.56x_1x_5 + 113.97x_1x_6 + 31.20x_2x_3 + 111.46x_2x_4 \qquad (7.1)$$
$$+ 25.83x_2x_5 - 59.33x_2x_6 + 51.36x_3x_4 - 14.87x_3x_5 + 11.92x_3x_6$$
$$+ 33.17x_4x_5 - 246.23x_4x_6 + 11.59x_5x_6$$

The model has $\frac{1}{2}(6+1)(6+2) = 28$ terms. Some of these have marginal contributions while some have major contributions. Pareto Chart shown in Figure 116 shows all the factors and interactions. Factor D (IB thickness) has the highest influence with a standardized effect of around 160. Considering this, only factors and interactions with a standardized effect of more than 5 are considered as important. These factors and interactions and discussed in the main effect and interaction plots.
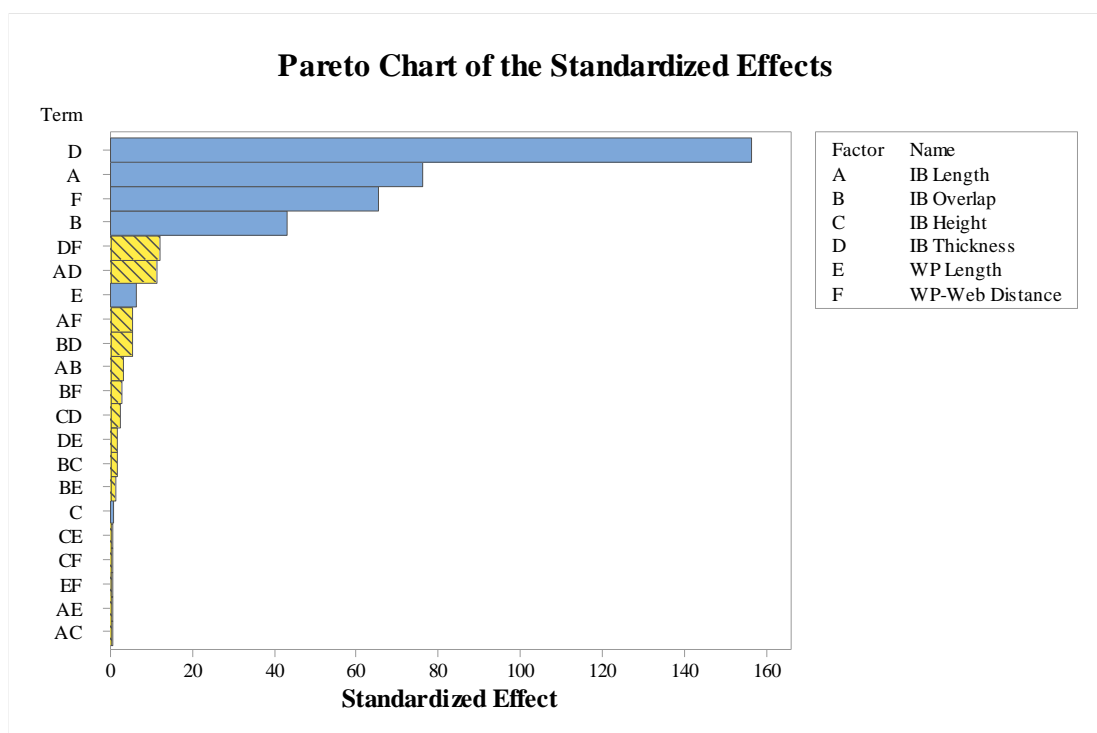
Figure 116: Pareto chart for all factors and interactions

The p-values for all the factors and interactions are shown in Table 47 below. For a 95% confidence interval, any factor with a p-value ≤ 0.05 is considered statistically significant.

Table 47: P-value for the whole model

Source	P-Value
IB Length	0.000
IB Overlap	0.000
IB Height	0.000
IB Thickness	0.000
WP Length	0.000
WP-Web Distance	0.000
Square	
IB Length*IB Length	0.000
IB Overlap*IB Overlap	0.143
IB Height*IB Height	0.000
IB Thickness*IB Thickness	0.000
WP Length*WP Length	0.028
WP-Web Distance*WP-Web Distance	0.000
2-Way Interaction	
IB Length*IB Overlap	0.000
IB Length*IB Height	0.083
IB Length*IB Thickness	0.000
IB Length*WP Length	0.040
IB Length*WP-Web Distance	0.000
IB Overlap*IB Height	0.000
IB Overlap*IB Thickness	0.000
IB Overlap*WP Length	0.000
IB Overlap*WP-Web Distance	0.000
IB Height*IB Thickness	0.000
IB Height*WP Length	0.009
IB Height*WP-Web Distance	0.035
IB Thickness*WP Length	0.000
IB Thickness*WP-Web Distance	0.000
WP Length*WP-Web Distance	0.040

o   Validating mathematical model

For a target maximum load value p of 20,000 N and for the variable range given, the multiple response prediction is as given in Table 48 below:

Table 48: Multiple response prediction for inner beam assembly

Variable	Setting	Value
IB Length	-1.90674	3023.315
IB Overlap	0.128002	353.2
IB Height	2	450
IB Thickness	-0.227464	3.443
WP Length	2	240
WP-Web Distance	0.802204	7.802

Using the factor values obtained in Table 48 from the Minitab optimization study, the ABAQUS model was run and a maximum load of 21,223 N was obtained.

Agreement of the maximum load values from both Minitab and the FE model validates the mathematical model.

The validated mathematical model can be used further to explore various combinations of factors for a desired maximum load value. The best design, keeping in mind manufacturing or facility constraints, can be chosen. The chosen design can be confirmed again with an FE model.

o   Main Factor Effects

Figure 117 and Figure 118 shows the effect of six parameters considered in the CCD analysis.
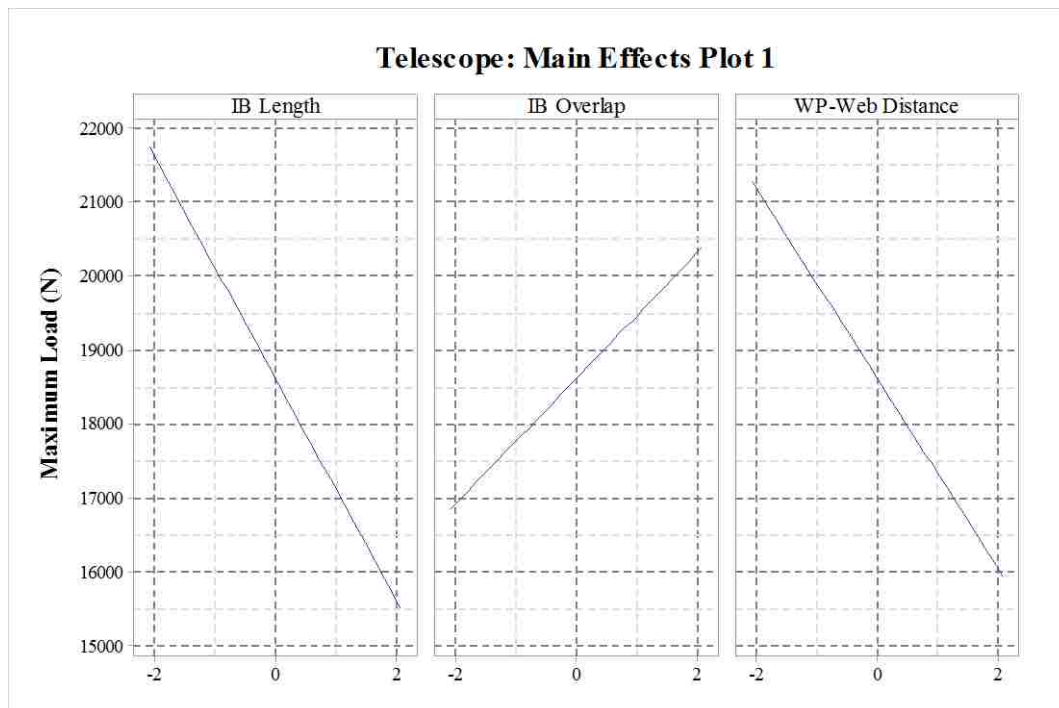
Figure 117: Main effects plot 1 for telescope
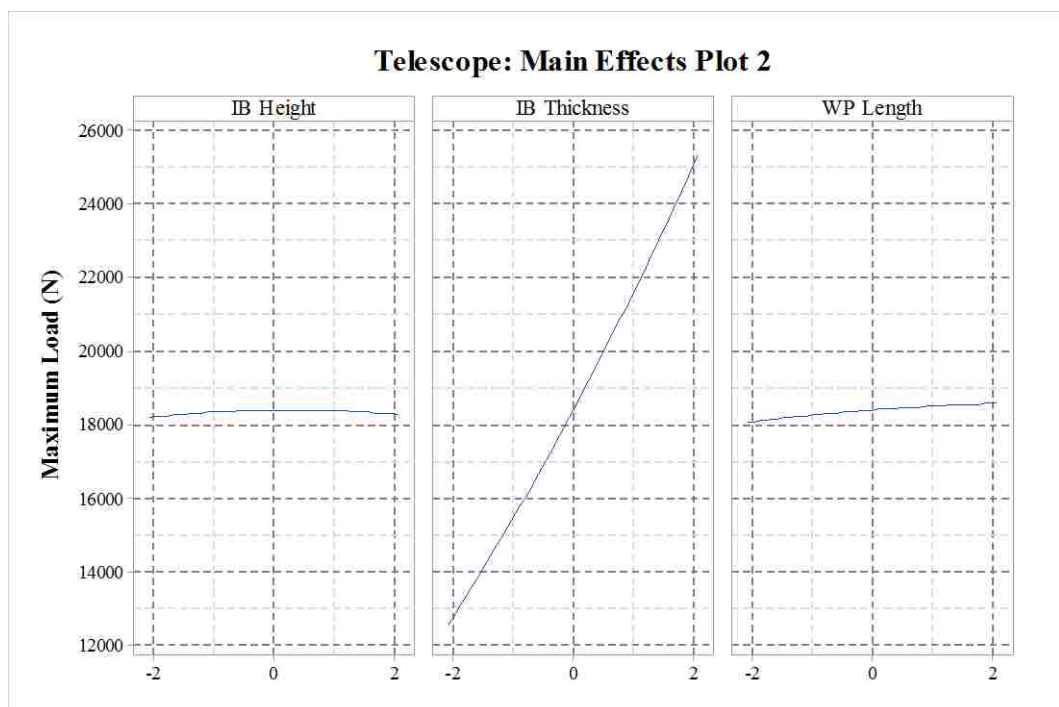
Figure 118: Main effects plot 2 for telescope

The maximum load increases as the thickness of the inner beam is increased. The 'IB Thickness' also has the highest effect on the maximum load. Increasing the 'IB overlap' also increases the maximum load. However, increasing the IB Length and the 'WP-Web distance' reduces the maximum load. The 'IB Height' and the 'WP Length' has almost no impact on the maximum load.

From an engineering point of view, the main factor effects can be explained as follows:

o   As the thickness value increases, the slenderness ratio decreases, increasing the maximum load capacity of the inner beam.

o   As the WP-web distance is increased, it results in an increase in the moment load acting at the web of the structure which reduces the maximum load of the inner beam

o   Increasing the IB length or reducing the overlap length has the effect of increasing the moment at the bottom wearpad, thereby reducing the maximum load capacity of the inner beam.

o   The greater the wearpad length, the greater the contact length and therefore the larger the area on which the force is distributed. This increases the maximum load of the inner beam.

o   The IB Height has a very small effect on the maximum load. It can be said that for the current factor ranges, the overall assembly factors have a greater influence on the maximum load than part geometric factors.

o   Interaction factors

Two interactions have been identified as significant and they are shown in Figure 119 and Figure 120.

Consider Figure 119 showing the variation of maximum load when the IB Thickness is varied from level -2 (3 mm) to level 2 (4 mm). As the IB Thickness increases, the distance between the WP-Web Distance curves increase i.e. the difference between what happens to the inner beam with WP-Web Distance 6 mm and 8 mm increases as the IB thickness increases.

A similar explanation can be given for the interaction shown in Figure 120.
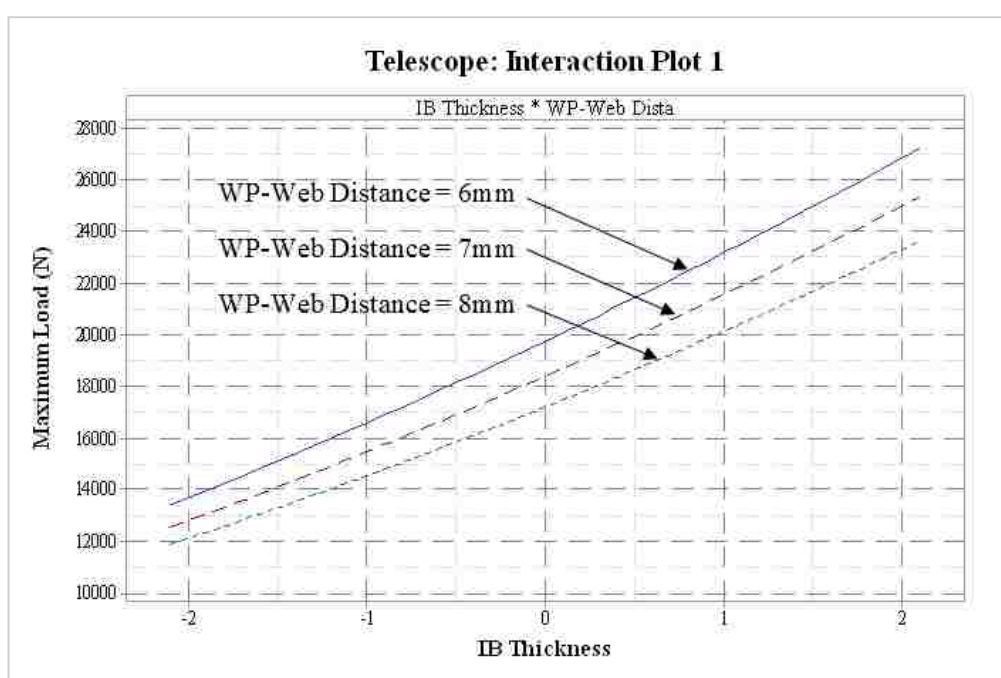
Figure 119: Effect of interaction between IB thickness and WP-web distance on maximum load
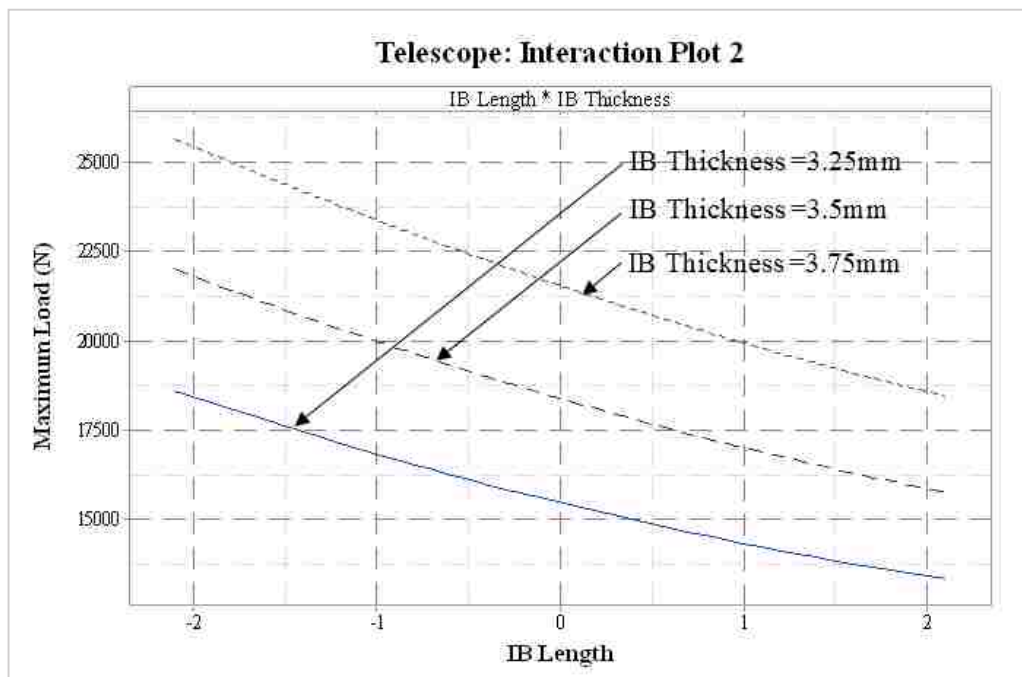
Figure 120: Effect of interaction between IB length and IB thickness on maximum load

- Conclusions:

  o The factors considered for the Taguchi L_{12} design included the influencing factors obtained from chapters 5 and chapter 6. Other factors considered included overall inner beam assembly factors

  o The influencing factors obtained for the inner beam assembly included all the influencing factors obtained for RHS rings and RHS pieces.

  o From the factor plot, the six influencing factors from the Taguchi L_{12} were: 'IB Length', 'IB Overlap', 'IB Height', 'IB Thickness', 'WP-Web Distance', 'WP Length'.

  o As IB Height$_{telescope}$ = RHS ring height = RHS piece height, and WP Length$_{Telescope}$ = RHS ring length = RHS piece length, the hypothesis that the portion of the inner beam beneath the wearpads can be studied as RHS rings or RHS pieces is correct

- o From the CCD, the mathematical equation of the model was obtained and validated and optimized.

- o The main effect plot showed the contribution of the RHS height was minimal. This maybe because for this factor range combination, the overall assembly factors had a greater influence than the part geometric factors.

Chapter 8: Conclusions

8.1 Summary

In telescopic cantilevers, the overlap area is identified as crucial based on the findings from the tip-reaction model and exploratory analysis which motivated the investigation of the overlap area in detail.

Analysis indicated that it was easier to divide the overlap area into an assemblage of two sections made of RHS rings or pieces and a connecting middle section. RHS rings and RHS pieces were analyzed as assemblages of beams and columns, and horizontal and vertical plates respectively. Theoretical analyses of the webs of the RHS rings showed that the webs behave like a column with eccentric loading which leads to the formation of the hinges at the middle of the webs. The RHS rings when compressed between wearpads behaved in a similar manner to the loading between platens except that they had an additional corner moment because of the eccentric nature of the loading. This resulted in a reduction in the maximum load that the ring could carry. Similar observations were made for the vertical plates of the RHS pieces. Experiments and FEA conducted on RHS rings and RHS pieces confirmed this.

Screening computer experiments with RHS rings between wearpads in the case study identified 'RHS Thickness', 'RHS Height' and 'WP-Web Distance' as the influencing factors. However, because of the buckling behaviors dependence on the dimensions of the individual case, in general, all factors should be included for screening experiments.

For the RHS pieces between wearpads, screening computer experiments in the case study identified 'RHS Length' in addition to the three factors listed above for the RHS rings between wearpads. Again, because of the buckling behaviors dependence

on the dimensions of the individual case, in general, it is recommended that all factors be included in the screening experiments.

For the inner beam assembly of the telescope, the factors included the 'IB Length', 'IB overlap', 'IB Height', 'IB Width', 'IB Thickness', 'IB corner radius', 'WP Length', 'WP Width', 'WP-Web Distance'. Of these factors, four factors were borrowed from the influencing factors of the RHS rings and pieces. As the overlap area was considered as an assembly of RHS rings or pieces and a middle section, the 'RHS Length' in the screening experiment for the RHS pieces is equivalent to the 'WP Length' in the inner beam assembly of the telescope. The findings from the case study conducted on the inner beam assembly identified the 'IB Length', 'IB overlap', 'IB Height', 'IB Thickness', 'WP Length' and 'WP-Web Distance' as the influencing factors.

A mathematical model generated from a CCD with the identified influencing factors was then used to generate an optimal factor combination for a specific target maximum load.

In reality, manufacturers often face multiple constraints on the geometric factors. For instance, a manufacturer may only be able to manufacture beam sections with 3 mm thickness and with a maximum height constraint of 350 mm. The mathematical model generated can therefore by used to acquire the best possible factor value combinations, given the mentioned constraints.

Based on this a methodology was developed as explained in Figure 84 in Chapter 4.

8.2 Contribution to knowledge

The key contribution of this work to knowledge are summarized below:

- Identifying the area of the inner beam in the vicinity of the bottom wearpads as the area most susceptible to buckling.

- Understanding the behavior of the overlap area by looking at it as an assembly of RHS rings and a middle section or RHS pieces and a middle section.

- Explanation of the RHS ring behavior by treating it as an assemblage of horizontal beams and vertical columns which when subjected to transverse compressive loads result in the beams and columns experiencing corner moments

- Explanation of the RHS piece behavior by treating it as an assemblage of horizontal and vertical plates which when subjected to transverse compressive loads result in each of the plates experiencing corner moments

- Establishing that RHS pieces and rings experience additional corner moments when compressed between wearpads as compared to when compressed between platens

- Establishing a design methodology of an inner beam assembly that can be applied to any range of geometric parameters to obtain an optimal model with specific geometric constraints (if necessary)

8.3 Recommendation for future developments

The following areas of interest could offer opportunities for further development:

- Extensive experimental investigation of RHS rings and RHS pieces subjected to transverse compressive loading to obtain k_1 and k_2.

- Experimental investigation of RHS pieces subjected to a combined loading of transverse compression and bending

- Introduction of errors into the FE models used in DOE studies to better represent real-life situations

8.4 Conclusion

This research enhances the understanding of the telescopic cantilevers. It also helps relate structural analysis and experimental design as tools to accurately design telescopic booms. Therefore, this research investigates the question of:

'How the overlap region of a telescopic cantilever behaves under tip load' and establishes a new generic approach to the design of telescopic beams based on parametric studies using FEA and statistical optimization.

References

[1] J. M. Gere and B. J. Goodno, Mechanics of Materials, 8 edition. Stamford, CT: CL Engineering, 2012.

[2] T. H. G. Megson, Aircraft Structures for Engineering Students. Butterworth-Heinemann, 2016.

[3] O. A. Bauchau and J. I. Craig, Eds., Structural Analysis, vol. 163. Dordrecht: Springer Netherlands, 2009.

[4] T. R. Chandrupatla and A. D. Belegundu, Introduction to Finite Elements in Engineering, 4 edition. Upper Saddle River,NJ: Pearson, 2011.

[5] S. Singh, Applied Stress Analysis. Delhi: Khanna Publishers, 2000.

[6] J. S. Rao, Simulation Based Engineering in Solid Mechanics. Springer, 2016.

[7] S. Timoshenko and J. N. Goodier, Theory of Elasticity. McGraw-Hill Book Company, 1951.

[8] S. A.C and S. P.K, Engineering Mathematics : Volume 1. PHI Learning Pvt. Ltd., 2010.

[9] M. H. Sadd, Elasticity: Theory, Applications, and Numerics. Academic Press, 2014.

[10] J. A. Collins, Failure of Materials in Mechanical Design: Analysis, Prediction, Prevention, 2nd Edition, 2 edition. New York: Wiley-Interscience, 1993.

[11] D. W. A. Rees, Basic Solid Mechanics, 1997 edition. Basingstoke: Palgrave, 1997.

[12] J. Marin, Mechanical behavior of engineering materials. Prentice-Hall, 1962.

[13] M. L. Gambhir, Fundamentals of Solid Mechanics: A Treatise on Strength of Materials. PHI Learning Pvt. Ltd., 2009.

[14] C. H. Yoo and S. Lee, Stability of Structures: Principles and Applications. Elsevier, 2011.

[15] Y. M. Tseytlin, Structural Synthesis in Precision Elasticity. Springer Science & Business Media, 2007.

[16] Srinath, Advanced Mechanics Of Solids. Tata McGraw-Hill Education, 2009.

[17] Beer and J. & Dewolf, Mechanics Of Materials (In Si Units). Tata McGraw-Hill Education, 2004.

[18] Y. M. Desai, Finite Element Method with Applications in Engineering. Pearson Education India, 2011.

[19] K. H. Huebner, The Finite Element Method for Engineers. John Wiley & Sons, 2001.

[20] S. O. Mobasseri, "Developing a QFD-Based design-integrated structural analysis methodology," Thesis, Brunel University School of Engineering and Design PhD Theses, 2012.

[21] P. J. Ross, Taguchi Techniques for Quality Engineering: Loss Function, Orthogonal Experiments, Parameter and Tolerance Design. McGraw Hill Professional, 1996.

[22] F. Betz, Managing Science: Methodology and Organization of Research. Springer Science & Business Media, 2010.

[23] M. Brindhamani and K. Marisamy, Comparitive Education.

[24] S. Sivaloganathan, O. G.A, and W. Y.H, "Design and Conduct Experiments, Analyze and Interpret Data: Learning Experience In the Design and Manufacture Lab Course," presented at the 122nd ASEE Annual Conference & Exposition, Seattle, WA.

[25] T. H.K. Kang, K. A. Biggs, and C. Ramseyer, "Buckling Modes of Cold -Formed Steel Columns," International Journal of Engineering and Technology, vol. 5, no. 4, Aug. 2013.

[26] F. Yui, "A Geometrically Exact Thin-walled Theory considering in-plane cross-section Distortion," Cornell University, 2005.

[27] S. P. Timoshenko and J. M. Gere, Theory of Elastic Stability. Courier Corporation, 2012.

[28] V. Silva, "Structural Stability," in Mechanics and Strength of Materials, Springer Berlin Heidelberg, 2006, pp. 389–464.

[29] J. G. Abraham, "A deflection, buckling and stress investigation into telescopic cantilever beams," Thesis, Brunel University School of Engineering and Design PhD Theses, 2012.

[30] M. Nedelcu, "GBT formulation to analyse the behaviour of thin-walled members with variable cross-section," Thin-Walled Struct., vol. 48, no. 8, pp. 629–638, Aug. 2010.

[31] S. Adamy and B. Schafer, "Buckling Mode Classification of Members with Open Thin-walled Cross-sections," presented at the Fourth International Conference on Co upled Instabilities in Metal Structures, Rome, Italy, 2004.

[32] E. Ventsel and T. Krauthammer, Thin Plates and Shells: Theory: Analysis, and Applications. CRC Press, 2001.

[33] T. K. Vardan and K. Bhaskar, Analysis of Plates: Theory and Problems. London: Narosa Publishing House, 1999.

[34] Q. Q. Liang, Analysis and Design of Steel and Composite Structures. CRC Press, 2014.

[35] T. Kubiak, Static and Dynamic Buckling of Thin-Walled Plate Structures, 2013 edition. Cham: Springer, 2013.

[36] Timoshenko, Theory Of Plates & Shells, 2 edition. New Delhi: Mc Graw Hill India, 2010.

[37] R. D. Ziemian, Guide to Stability Design Criteria for Metal Structures. John Wiley & Sons, 2010.

[38] X.-Z. Zhang, S. Liu, M.-S. Zhao, and S.-P. Chiew, "Comparative experimental study of hot-formed, hot-finished and cold-formed rectangular hollow sections," Case Stud. Struct. Eng., vol. 6, pp. 115–129, Dec. 2016.

[39] F. R. Mashiri, A. M. Paradowska, B. Uy, Z. Tao, M. Khan, and P. Dayal, "Residual Stresses Distribution Measured by Neutron Diffraction in Fabricated Square High Strength Steel Tubes," Material Science forum, vol. 777, pp. 249–254.

[40] Y. Chen, R. Feng, and L. Wang, "Flexural behaviour of concrete-filled stainless steel SHS and RHS tubes," Eng. Struct., vol. 134, pp. 159–171, Mar. 2017.

[41] O. Zhao, L. Gardner, and B. Young, "Buckling of ferritic stainless steel members under combined axial compression and bending," J. Constr. Steel Res., vol. 117, pp. 35–48, Feb. 2016.

[42] O. Zhao, B. Rossi, L. Gardner, and B. Young, "Behaviour of structural stainless steel cross-sections under combined loading – Part II: Numerical modelling and design approach," Eng. Struct., vol. 89, pp. 247–259, Apr. 2015.

[43] M. Bock, I. Arrayago, and E. Real, "Experiments on cold-formed ferritic stainless steel slender sections," J. Constr. Steel Res., vol. 109, pp. 13–23, Jun. 2015.

[44] F. Zhou and B. Young, "Tests of cold-formed stainless steel tubular flexural members," Thin-Walled Struct., vol. 43, no. 9, pp. 1325–1337, Sep. 2005.

[45] B. Zheng, G. Shu, L. Xin, R. Yang, and Q. Jiang, "Study on the Bending Capacity of Cold-formed Stainless Steel Hollow Sections," Structures, vol. 8, Part 1, pp. 63–74, Nov. 2016.

[46] Y. Huang and B. Young, "Experimental and numerical investigation of cold-formed lean duplex stainless steel flexural members," Thin-Walled Struct., vol. 73, pp. 216–228, Dec. 2013.

[47] M. Theofanous, N. Saliba, O. Zhao, and L. Gardner, "Ultimate response of stainless steel continuous beams," Thin-Walled Struct., vol. 83, pp. 115–127, Oct. 2014.

[48] B. Zheng, G. Shu, L. Xin, R. Yang, and Q. Jiang, "Study on the Bending Capacity of Cold-formed Stainless Steel Hollow Sections," Structures, vol. 8, Part 1, pp. 63–74, Nov. 2016.

[49] Y. Huang and B. Young, "Experimental and numerical investigation of cold-formed lean duplex stainless steel flexural members," Thin-Walled Struct., vol. 73, pp. 216–228, Dec. 2013.

[50] M. Theofanous and L. Gardner, "Experimental and numerical studies of lean duplex stainless steel beams," J. Constr. Steel Res., vol. 66, no. 6, pp. 816–825, Jun. 2010.

[51] M. Bock, I. Arrayago, and E. Real, "Experiments on cold-formed ferritic stainless steel slender sections," J. Constr. Steel Res., vol. 109, pp. 13–23, Jun. 2015.

[52] L. Gardner and D. Nethercot, "Experiments on stainless steel hollow sections—Part 2: Member behaviour of columns and beams," Journal of Constructional Steel Research, 2004.

[53] M. Theofanous, N. Saliba, O. Zhao, and L. Gardner, "Ultimate response of stainless steel continuous beams," Thin-Walled Struct., vol. 83, pp. 115–127, Oct. 2014.

[54] L. Gardner and D. A. Nethercot, "Experiments on stainless steel hollow sections—Part 2: Member behaviour of columns and beams," J. Constr. Steel Res., vol. 60, no. 9, pp. 1319–1332, Sep. 2004.

[55] J. Wang, S. Afshan, N. Schillo, M. Theofanous, M. Feldmann, and L. Gardner, "Material properties and compressive local buckling response of high strength steel square and rectangular hollow sections," Eng. Struct., vol. 130, pp. 297–315, Jan. 2017.

[56] J. Wang, S. Afshan, N. Schillo, M. Theofanous, M. Feldmann, and L. Gardner, "Material properties and compressive local buckling response of high strength steel square and rectangular hollow sections," Eng. Struct., vol. 130, pp. 297–315, Jan. 2017.

[57] I. Arrayago, E. Real, and E. Mirambell, "Experimental study on ferritic stainless steel RHS and SHS beam-columns," Thin-Walled Struct., vol. 100, pp. 93–104, Mar. 2016.

[58] O. Zhao, L. Gardner, and B. Young, "Behaviour and design of stainless steel SHS and RHS beam-columns," Thin-Walled Struct., vol. 106, pp. 330–345, Sep. 2016.

[59] T. Y. Reddy and S. R. Reid, "Phenomena associated with the crushing of metal tubes between rigid plates," Int. J. Solids Struct., vol. 16, no. 6, pp. 545–562, Jan. 1980.

[60] D. K. Sinha and N. R. Chitkara, "Plastic collapse of square rings," Int. J. Solids Struct., vol. 18, no. 9, pp. 819–826, Jan. 1982.

[61] N. K. Gupta and P. Ray, "Collapse of thin-walled empty and filled square tubes under lateral loading between rigid plates," Int. J. Crashworthiness, vol. 3, no. 3, pp. 265–285, Jan. 1998.

[62] N. K. Gupta and A. Khullar, "Collapse load analysis of square and rectangular tubes subjected to transverse in-plane loading," Thin-Walled Struct., vol. 21, no. 4, pp. 345–358, Jan. 1995.

[63] N. K. Gupta and S. K. Sinha, "Lateral compression of crossed layers of square-section tubes," Int. J. Mech. Sci., vol. 32, no. 7, pp. 565–580, Jan. 1990.

[64] N. K. Gupta and S. K. Sinha, "Collapse of a laterally compressed square tube resting on a flat base," Int. J. Solids Struct., vol. 26, no. 5, pp. 601–615, Jan. 1990.

[65] N. K. Gupta and A. Khullar, "Lateral collapse of orthogonal and non-orthogonal cross-layered arrays of square and rectangular tubes," Int. J. Mech. Sci., vol. 36, no. 5, pp. 449–467, May 1994.

[66] N. K. Gupta and A. Khullar, "Lateral compression of a square or rectangular tube between two parallel narrow width indenters placed non-orthogonally," Thin-Walled Struct., vol. 22, no. 1, pp. 9–23, Jan. 1995.

[67] N. K. Gupta and A. Khullar, "Lateral crushing of square and rectangular tubes by non-orthogonally placed narrow width indenters," Int. J. Mech. Sci., vol. 37, no. 1, pp. 31–50, Jan. 1995.

[68] N. K. Gupta and S. K. Sinha, "Transverse collapse of thin-walled square tubes in opposed loadings," Thin-Walled Struct., vol. 10, no. 3, pp. 247–262, Jan. 1990.

[69] N. K. Gupta, G. S. Sekhon, and P. K. Gupta, "A study of lateral collapse of square and rectangular metallic tubes," Thin-Walled Struct., vol. 39, no. 9, pp. 745–772, Sep. 2001.

[70] T. N. Tran and T. N. T. Ton, "Lateral crushing behaviour and theoretical prediction of thin-walled rectangular and square tubes," Compos. Struct., vol. 154, pp. 374–384, Oct. 2016.

[71] M. R. Bambach, H. Jama, X. L. Zhao, and R. H. Grzebieta, "Hollow and concrete filled steel hollow sections under transverse impact loads," Eng. Struct., vol. 30, no. 10, pp. 2859–2870, Oct. 2008.

[72] J. Liu and N. Jones, "Experimental investigation of clamped beams struck transversely by a mass," Int. J. Impact Eng., vol. 6, no. 4, pp. 303–335, Jan. 1987.

[73] Y. Jilin and J. Norman, "Further experimental investigations on the failure of clamped beams under impact loads," Int. J. Solids Struct., vol. 27, no. 9, pp. 1113–1137, Jan. 1991.

[74] M. J. Fagan, Finite Element Analysis: Theory and Practice. Longman Scientific & Technical, 1992.

[75] D. L. Logan, A First Course in the Finite Element Method, Student international ed of 4th revised ed edition. Stamford, CT: Nelson Engineering, 2010.

[76] S. S. Bhavikatti, Finite Element Analysis. New Age International, 2005.

[77] "Abaqus Analysis User's Manual (6.10)." [Online]. Available: https://www.sharcnet.ca/Software/Abaqus610/Documentation/docs/v6.10/books /usb/default.htm?startat=pt03ch06s02at02.html. [Accessed: 20-Jan-2017].

[78] J. G. Abraham, "A deflection, buckling and stress investigation into telescopic cantilever beams," Thesis, Brunel University School of Engineering and Design PhD Theses, 2012.

[79] "What is reduced integration in the context of finite element analysis?" TWI. [Online]. Available: http://www.twi-global.com/technical-knowledge/faqs/faq-what-is-reduced-integration-in-the-context-of-finite-element-analysis/. [Accessed: 11-Sep-2017].

[80] "Unstable collapse and postbuckling analysis," in Abaqus Analysis User's Manual (6.10)

[81] G. Taguchi, E. A. Elsayed, and T. C. Hsiang, Quality Engineering in Production Systems. New York: McGraw-Hill Inc.,US, 1988.

[82] G. Taguchi, An Introduction to Quality Engineering, Illustrated edition edition. Tokyo: Asian Productivity Organization, 2001.

[83] C. F. J. Wu and M. Hamada, Experiments: Planning, Analysis and Parameter Design Optimization. Wiley India Private Limited, 2009.

[84] G. S. Peace, Taguchi methods: a hands-on approach. Addison-Wesley, 1993.

[85] D. Draguljić, D. C. Woods, A. M. Dean, S. M. Lewis, and A.-J. E. Vine, "Screening Strategies in the Presence of Interactions," Technometrics, vol. 56, no. 1, pp. 1–1, Jan. 2014.

[86] F. H. Dar, J. R. Meakin, and R. M. Aspden, "Statistical methods in finite element analysis," J. Biomech., vol. 35, no. 9, pp. 1155–1161, Sep. 2002.

[87] N. Logothetis and H. P. Wynn, Quality Through Design: Experimental Design, Off-line Quality Control and Taguchi's Contributions, New edition edition. Oxford: Clarendon Press, 1994.

[88] N. Logothetis and H. P. Wynn, Quality through design: experimental design, off-line quality control and Taguchi's contributions. Oxford: Clarendon Press, 1994.

[89] A. A. Alnaqi, S. Shrestha, D. C. Barton, and P. C. Brooks, "Optimisation of Alumina Coated Lightweight Brake Rotor," ResearchGate, vol. 2014, Sep. 2014.

[90] J. P. Rath, A. Bankar, G. Unnikrishnan, and T. Thomas, "Optimisation of Tire Design and Construction Parameters for Handling," CEAT, India, 2012.

[91] G. Taguchi and S. Chowdhury, Robust Engineering: Learn How to Boost Quality While Reducing Costs & Time to Market. New York: McGraw-Hill Education, 1999.

[92] D. C. Montgomery, Design and Analysis of Experiments, 8 edition. Hoboken, NJ: Wiley, 2012.

[93] J. Krottmaier, Optimizing Engineering Designs. London ; New York: McGraw-Hill Publishing Co., 1993.

[94] D. C. Montgomery, Design and Analysis of Experiments, 8 edition. Hoboken, NJ: Wiley, 2012.

[95] R. H. Myers, D. C. Montgomery, and C. M. Anderson-Cook, Response Surface Methodology: Process and Product Optimization Using Designed Experiments. John Wiley & Sons, 2009.

[96] W. G. Cochran and G. M. Cox, Experimental Designs, New ed of 2 Revised ed edition. New York: John Wiley & Sons, 1992.

[97] "Abaqus Analysis User's Manual (6.12)." [Online]. Available: http://abaqus.software.polimi.it/v6.12/books/usb/default.htm?startat=pt06ch28s01ael03.html. [Accessed: 22-Dec-2016].

Appendix I: Material Test Report

ST/QF/2301

Certificate No. T-0629,T-0630
NABL Accredited Laboratory
As per ISO / IEC – 17025 (2005)

Subodh
Precise Analysis, Proficient Results
Subodh Technologists
MATERIAL SCIENCE CENTER

TEST REPORT
Page 1 of 1

Report No.	**I9498**
Party's Name & Add.	**M/s ARIECKAL INDUSTRIES**

Date: 09-08-2017

Plot No. 1, Panvel Industrial Co-operative Industrial Estate
Panvel-410206

Reference Ch. No.	AI-08/17-25
Sample Received on	03-08-2017
Specification	**IS 513:2008 Gr.CR2**
Sample Described As	3mm Thk x 150mm Long x 73mm Width CRCA Sheet
ID Mark	AI-08/17-25-01

Date: 03-08-2017

Tensile Test
Test Method : IS 1608:2005 (RA 2010)

	Result
Width (mm)	12.50
Thk. (mm)	3.02
Area (mm²)	37.75
Gauge Length (mm)	50.00
0.2% Proof Load (kN)	7.998
Ultimate Load (kN)	11.98
Final Gauge Length (mm)	72.20
0.2% Proof Strength (N/mm²)	211.88
U.T.S (N/mm²)	317.351
Elongation (%)	44.40
Youngs Modulus (N/mm²)	125.946
Fracture	W.G.L.

Chemical Analysis
Test Method : ASTM E 415:2014/IS 8811:1998

	Result	R/V
Carbon (C)%	0.045	0.12 max.
Manganese (Mn)%	0.20	0.50 max.
*Silicon(Si)%	0.013	
Sulphur (S)%	0.011	0.035 max.
Phosphorus (P)%	0.015	0.040 max.
Remarks	Satisfactory	

Remark: The Test Result(s) are within specified limits of IS 513:2008 Gr.CR2.

In absence of specified values / criteria in the specification, test result(s) are for information.

-------------End of Report-------------

For SUBODH TECHNOLOGISTS

V.D. Bhaskar / Ankush Pratapure / Anita Goilkar
QAM / GM / Senior Chemist

Figure 121: Material test report for RHS Ring

Figure 122: Typical Mild Steel Stress-Strain Curve

A typical stress-strain curve for a mild steel sample is shown in Figure 122. The curve shows a yield stress value of 397.6 N/mm^2 and an ultimate stress of 640.2 N/mm^2.

Appendix II: DOE Tables for the RHS Rings

Table 49: L_{12} matrix for RHS ring between platens

Run #	RHS Corner radius	Thickness	Height	Width	Maximum Load (N)
1	1	1	1	1	1437.76
2	1	1	1	1	1437.76
3	1	1	2	2	904.5
4	1	2	1	2	3248.85
5	1	2	2	1	2362.28
6	1	2	2	2	2198.51
7	2	1	2	2	804.79
8	2	1	2	1	860.342
9	2	1	1	2	1115.66
10	2	2	2	1	2008.63
11	2	2	1	2	2522.54
12	2	2	1	1	2769.2

Table 50: L_{12} matrix for RHS ring between wearpads

Run#	WP Web Distance	WP width	RHS Corner Radius	RHS Thickness	RHS Height	RHS Width	Maximum Load (N)
1	1	1	1	1	1	1	1184.13
2	1	1	1	1	2	2	798.02
3	1	1	2	2	1	1	2697.56
4	1	2	1	2	1	2	2548.03
5	1	2	2	1	2	1	862.39
6	1	2	2	2	2	2	1856.31
7	2	1	2	2	1	2	1918.64
8	2	1	2	1	2	2	678.14
9	2	1	1	2	2	1	1582.45
10	2	2	2	1	1	1	940.04
11	2	2	1	2	2	1	1577.62
12	2	2	1	1	1	2	895.16

Table 51: CCD matrix for RHS ring between wearpads

Run #	RHS Thickness	RHS Height	WP-Web Distance	Maximum Load (N)
1	-1	-1	-1	1180.54
2	1	-1	-1	1756.27
3	-1	1	-1	1017.38
4	1	1	-1	1500.89
5	-1	-1	1	1082.24
6	1	-1	1	1594.63
7	-1	1	1	942.06
8	1	1	1	1393.89
9	-2	0	0	840.50
10	2	0	0	1867.69
11	0	-2	0	1495.70
12	0	2	0	1125.74
13	0	0	-2	1407.85
14	0	0	2	1185.69
15	0	0	0	1278.33
16	0	0	0	1278.33
17	0	0	0	1278.33
18	0	0	0	1278.33
19	0	0	0	1278.33
20	0	0	0	1278.33

Appendix III: DOE Tables for the RHS Pieces

Table 52: L_{12} matrix data for RHS piece between platens

Run #	Corner Radius	RHS Thickness	RHS Height	RHS Length	RHS Width	Maximum Load (N)
1	1	1	1	1	1	62129.3
2	1	1	1	1	1	62129.3
3	1	1	2	2	2	44520.8
4	1	2	1	2	2	157968
5	1	2	2	1	2	94661.8
6	1	2	2	2	1	114343
7	2	1	2	2	1	42895.9
8	2	1	2	1	2	34900.8
9	2	1	1	2	2	54848.8
10	2	2	2	1	1	87741
11	2	2	1	2	1	134354
12	2	2	1	1	2	111216

Table 53: L_{12} matrix for RHS piece between wearpads

Run #	RHS Thickness	Corner radius	RHS Height	RHS Width	RHS Length	WP Length	WP Width	WP-Web Distance	WP-End Distance	Maximum Load (N)
1	1	1	1	1	1	1	1	1	1	51825
2	1	1	1	1	1	2	2	2	2	41398
3	1	1	2	2	2	1	1	1	2	39590.5
4	1	2	1	2	2	1	2	2	1	44733.5
5	1	2	2	1	2	2	1	2	1	35588
6	1	2	2	2	1	2	2	1	2	34813.6
7	2	1	2	2	1	1	2	2	1	65665
8	2	1	2	1	2	2	2	1	1	96928.8
9	2	1	1	2	2	2	1	2	2	92343.9
10	2	2	2	1	1	1	1	2	2	69460
11	2	2	1	2	1	2	1	1	1	110043
12	2	2	1	1	2	1	2	1	2	132611

Table 54: CCD matrix for RHS piece between wearpads

Run #	RHS Thickness	RHS Height	RHS Length	WP-Web Distance	Maximum Load (N)
1	-1	-1	-1	-1	57195.9
2	1	-1	-1	-1	85062.8
3	-1	1	-1	-1	49083.1
4	1	1	-1	-1	72036.0
5	-1	-1	1	-1	59978.0
6	1	-1	1	-1	89187.3
7	-1	1	1	-1	50939.3
8	1	1	1	-1	75999.1
9	-1	-1	-1	1	53874.5
10	1	-1	-1	1	79106.8
11	-1	1	-1	1	47390.6
12	1	1	-1	1	70156.4
13	-1	-1	1	1	56602.3
14	1	-1	1	1	83590.5
15	-1	1	1	1	49688.6
16	1	1	1	1	73625.2
17	-2	0	0	0	42011.6
18	2	0	0	0	94054.4
19	0	-2	0	0	75240.5
20	0	2	0	0	56801.0
21	0	0	-2	0	61782.8
22	0	0	2	0	68036.0
23	0	0	0	-2	68283.5
24	0	0	0	2	56697.4
25	0	0	0	0	64759.9
26	0	0	0	0	64759.9
27	0	0	0	0	64759.9
28	0	0	0	0	64759.9
29	0	0	0	0	64759.9
30	0	0	0	0	64759.9
31	0	0	0	0	64759.9

Appendix IV: DOE Tables for the Inner Beam Assembly of the Telescope

Table 55: L_{12} matrix for inner beam assembly of the telescope

Run #	IB Length	IB Overlap	IB Height	IB Width	IB Thickness	WP Length	WP Width	WP-Web Distance	Corner radius	Maximum Load (N)
1	1	1	1	1	1	1	1	1	1	12693.5
2	1	1	1	1	1	2	2	2	2	11359.9
3	1	1	2	2	2	1	1	1	2	24719.7
4	1	2	1	2	2	1	2	2	2	19125.4
5	1	2	2	1	2	2	1	2	1	26845.3
6	1	2	2	2	1	2	2	1	1	19144
7	2	1	2	2	1	1	2	2	1	6399.38
8	2	1	2	1	2	2	2	1	2	21943.1
9	2	1	1	2	2	2	1	2	1	15692.5
10	2	2	2	1	1	1	1	2	2	7613.19
11	2	2	1	2	1	2	1	1	2	13936.1
12	2	2	1	1	2	1	2	1	1	20166.2

Table 56: CCD matrix for inner beam assembly of the telescope

Run #	IB Length	IB Overlap	IB Height	IB Thickness	WP Length	WP-Web Distance	Maximum Load (N)
1	-1	-1	-1	-1	-1	-1	17154.9
2	1	-1	-1	-1	-1	-1	14627.4
3	-1	1	-1	-1	-1	-1	18736.1
4	1	1	-1	-1	-1	-1	15950.0
5	-1	-1	1	-1	-1	-1	17025.6
6	1	-1	1	-1	-1	-1	14395.8
7	-1	1	1	-1	-1	-1	18744.0
8	1	1	1	-1	-1	-1	15932.2
9	-1	-1	-1	1	-1	-1	23780.3
10	1	-1	-1	1	-1	-1	20309.8
11	-1	1	-1	1	-1	-1	25846.5
12	1	1	-1	1	-1	-1	22059.8
13	-1	-1	1	1	-1	-1	23921.3
14	1	-1	1	1	-1	-1	20397.9
15	-1	1	1	1	-1	-1	26157
16	1	1	1	1	-1	-1	22258.1
17	-1	-1	-1	-1	1	-1	17340.4
18	1	-1	-1	-1	1	-1	14746.2
19	-1	1	-1	-1	1	-1	18903.2
20	1	1	-1	-1	1	-1	16203.4
21	-1	-1	1	-1	1	-1	17119.0
22	1	-1	1	-1	1	-1	14529.8
23	-1	1	1	-1	1	-1	18930.6
24	1	1	1	-1	1	-1	16080.3
25	-1	-1	-1	1	1	-1	24090.2
26	1	-1	-1	1	1	-1	20546.3
27	-1	1	-1	1	1	-1	26306.0
28	1	1	-1	1	1	-1	22325.1
29	-1	-1	1	1	1	-1	24100.1
30	1	-1	1	1	1	-1	20562.0
31	-1	1	1	1	1	-1	26516.1
32	1	1	1	1	1	-1	22561.5
33	-1	-1	-1	-1	-1	1	14957.3
34	1	-1	-1	-1	-1	1	12772.2
35	-1	1	-1	-1	-1	1	16323.7
36	1	1	-1	-1	-1	1	13927.6
37	-1	-1	1	-1	-1	1	14944.3

Table 56: CCD matrix for inner beam assembly of the telescope (Continued)

Run #	IB Length	IB Overlap	IB Height	IB Thickness	WP Length	WP-Web Distance	Maximum Load (N)
38	1	-1	1	-1	-1	1	12726.7
39	-1	1	1	-1	-1	1	16416.0
40	1	1	1	-1	-1	1	13973.5
41	-1	-1	-1	1	-1	1	20598.6
42	1	-1	-1	1	-1	1	17613.5
43	-1	1	-1	1	-1	1	22391.1
44	1	1	-1	1	-1	1	19166.1
45	-1	-1	1	1	-1	1	20746.9
46	1	-1	1	1	-1	1	17755.0
47	-1	1	1	1	-1	1	22637.1
48	1	1	1	1	-1	1	19346.4
49	-1	-1	-1	-1	1	1	15163.1
50	1	-1	-1	-1	1	1	12914.5
51	-1	1	-1	-1	1	1	16604.5
52	1	1	-1	-1	1	1	14197.3
53	-1	-1	1	-1	1	1	15084.4
54	1	-1	1	-1	1	1	12843.3
55	-1	1	1	-1	1	1	16654.2
56	1	1	1	-1	1	1	14165.9
57	-1	-1	-1	1	1	1	20942.4
58	1	-1	-1	1	1	1	17880.0
59	-1	1	-1	1	1	1	22895.3
60	1	1	-1	1	1	1	19567.1
61	-1	-1	1	1	1	1	21016.1
62	1	-1	1	1	1	1	17957.6
63	-1	1	1	1	1	1	23019.4
64	1	1	1	1	1	1	19696.2
65	0	0	0	0	0	0	18401.0
66	0	0	0	0	0	0	18401.0
67	0	0	0	0	0	0	18401.0
68	0	0	0	0	0	0	18401.0
69	0	0	0	0	0	0	18401.0
70	0	0	0	0	0	0	18401.0
71	0	0	0	0	0	0	18401.0
72	0	0	0	0	0	0	18401.0
73	-2	0	0	0	0	0	21847.0

Table 56: CCD matrix for inner beam assembly of the telescope (Continued)

Run #	IB Length	IB Overlap	IB Height	IB Thickness	WP Length	WP-Web Distance	Maximum Load (N)
74	2	0	0	0	0	0	15898.1
75	0	-2	0	0	0	0	16710.0
76	0	2	0	0	0	0	20036.6
77	0	0	-2	0	0	0	18242.2
78	0	0	2	0	0	0	18297.0
79	0	0	0	-2	0	0	12881.0
80	0	0	0	2	0	0	24956.2
81	0	0	0	0	-2	0	18098.4
82	0	0	0	0	2	0	18602.1
83	0	0	0	0	0	-2	21371.7
84	0	0	0	0	0	2	16226.5
85	0	0	0	0	0	0	18401.0
86	0	0	0	0	0	0	18401.0
87	0	0	0	0	0	0	18401.0
88	0	0	0	0	0	0	18401.0
89	0	0	0	0	0	0	18401.0
90	0	0	0	0	0	0	18401.0